NORTHWESTERN UNIVERSITY

# Hierarchical Assembly by Peptide Amphiphiles and Their Use in Cartilage Repair

A DISSERTATION

SUBMITTED TO THE GRADUATE SCHOOL
IN PARTIAL FULLFILLMENT OF THE REQUIREMENTS

for the degree

DOCTOR OF PHILOSOPHY

Field of Biomedical Engineering

By

Jacob A. Lewis

EVANSTON, ILLINOIS

September 2020

# ABSTRACT

**Hierarchical Assembly by Peptide Amphiphiles and Their Use in Cartilage Repair**

**Jacob A. Lewis**

In nature, materials with complex architectures are formed through hierarchical self-assembly. Therefore, the study and design of hierarchically assembling materials is important in producing materials that mimic biological structures and is a key challenge in biomaterials science and engineering. In articular cartilage, hierarchical assembly of extracellular matrix (ECM) components provides mechanical resilience to this musculoskeletal tissue. However, following injury or degradation of adult human cartilage, this critical tissue in joints lacks the intrinsic ability to repair the damaged ECM and regenerate functional tissue. Therefore osteoarthritis, or cartilage degradation, is a leading cause of morbidity, affecting a quarter of a billion people worldwide. This work describes the development of several hierarchically assembling peptide amphiphile (PA) systems to study how these structures form and to apply bioactive superstructures for regeneration of cartilage tissue. PA molecules, comprising a peptide sequence conjugated to a hydrophobic alkyl tail, self-assemble in aqueous media to form filament networks that mimic the topology of ECM, making PAs a valuable tool in producing scaffolds for regeneration. To study how hierarchical assemblies form in peptide systems, the first project explored the formation of supramolecular superstructures by oppositely charged short PAs. In previous work on PA molecules covalently conjugated to DNA segments (DNA-PA), co-assembled PA molecules demonstrated formation of superstructures containing many nanoscale filaments formed due to dynamic exchange of monomers in the supramolecular assemblies. Superstructure formation was triggered by mixing of supramolecular structures containing complementary DNA segments

followed by dynamic exchange of molecules to enhance Watson-Crick pairing in the bundled regions. While this assembly process relied on pairing of complementary sequences to overcome strong cohesive interactions among molecules within the assemblies, it remained unknown if PA superstructures could form from simpler building blocks. Upon mixing aggregates of oppositely charged short PA molecules, the system formed filament bundles over the course of several days as a result of molecular redistribution among the oppositely charged assemblies, producing mixed charge primary assemblies that could form hierarchical bundles. Comparing the short PA supramolecular assemblies to oppositely charged PA mixtures with stronger or with weaker intermolecular cohesion showed that more cohesive structures had a decreased tendency to redistribute and form superstructures, while less cohesive structures were better able to redistribute and quickly formed robust superstructures. To better understand the role that charged groups play in determining how supramolecular systems assemble, the second study focused on a nonionic PA molecule with a decaethylene glycol group replacing the charged residues like glutamic acid and lysine needed for solubility in aqueous conditions. These nonionic PA molecules formed high aspect ratio filaments, but unlike charged PA molecules their assembly was largely independent of buffer pH. Mixing charged and uncharged PA molecules revealed that if only a minority of the PA molecules within the assemblies were charged, the co-assembled filaments had similar morphologies to the completely charged system. X-ray scattering and spectroscopic analysis showed mixing charged and uncharged PA molecules resulted in assemblies with high intermolecular order by decreasing repulsion among assemblies. Previous work indicated that nonionic hydrophilic functional groups in nanomaterials may improve osteogenic differentiation of progenitor cells. Therefore, the study concluded with *in vitro* experiments that nonionic PA filaments increased osteogenesis of human mesenchymal stem cells (hMSCs), suggesting tuning

filament charge may be an important tool for improving musculoskeletal regeneration. The third project aimed to develop PA filaments for cartilage repair and to study the way in which their hierarchical assembly affects their bioactivity. Deamidation of hydrogel forming PA sequences displaying a peptide epitope programmed to bind the chondrogenic cytokine transforming growth factor β-1 was shown to improve retention of the growth factor and chondrogenesis of encapsulated cells. Studying the self-assembly of these systems revealed that without deamidation, PA filaments formed bundled structures which likely masked the growth factor binding peptide sequence. This work established the deamidated sequence as the preferred PA design for chondrogenic applications, while highlighting the implications of superstructure formation on PA bioactivity. In the final study, these improved chondrogenic PA filaments were used for cartilage regeneration in a sheep model. To produce a more resilient material that could withstand the mechanical environment in a large-animal joint, the supramolecular PA assemblies were mixed with particles of the covalent biopolymer hyaluronic acid (HA). Combining the two components produced PA filament bundles with regular order, which was attributed to swelling by the HA component packing the PA filaments into a confined volume. The supramolecular-covalent hybrid was found to support chondrogenesis by encapsulated hMSCs *in vitro*. After implantation in cartilage defects in sheep stifles, the material was well retained and improved the macroscopic appearance of healing cartilage in both the load-bearing femoral condyle and in the less mechanically active trochlear groove at early times, indicating the material had the physical properties needed to remain present in defects long enough to affect healing. After 12 weeks, condyle defects continued to show improved macroscopic appearance due to treatment, while histological staining of trochlear groove defects showed improved regeneration of hyaline-like tissue, demonstrating the PA/HA hybrid superstructures had the biological efficacy to direct

cartilage repair. While treated condyle defects may have developed hyaline-like tissue if evaluated at later times, further improvements in the PA/HA hybrids mechanical properties may still be necessary for comparable healing of the high load-bearing condyle defects to the observed regeneration in the less mechanically active trochlear groove. Together, these studies help explain how superstructures form in natural systems and how their hierarchical assembly can affect their biological performance. Successful regeneration of hyaline-like tissue in the clinically relevant sheep model suggests that through further optimization of hybrid formulation and of bioactive signal presentation, hybrid PA superstructures have the potential to immensely improve the lives of many millions of patients suffering from damaged cartilage.

# ACKNOWLEDGEMENTS

I would like to thank Professor Samuel Stupp for bringing me into his lab and for working hard to provide the guidance and resources I needed to complete a Ph.D. Throughout the last six years, I have always appreciated his attention and insight for every one of us in the lab, and I am particularly grateful the time he spent helping me complete and publish my work. I cannot imagine a better place to train as a scientist than the Stupp Group, and I am immensely appreciative that Professor Stupp made that education possible for me. I would also like to thank Professor Ronit Freeman for her exceptional mentorship to me during her time as a postdoctoral researcher in the group. Ronit spend countless hours teaching me to be the scientists I am today. I greatly appreciate the kindness she showed me and the others she mentored and count her as a true friend. I am also grateful for Professor Liam Palmer for spending an enormous amount of time guiding me over the past years, and spending a great deal of time working with me on my scientific writing. I am also incredibly grateful for the guidance of Dr. Mark McClendon who has been a wonderful mentor, collaborator, and friend for much of my work.

In addition, I would like to thank others who have mentored me during my time at Northwestern. Thank you to my committee members Professor Evan Scott, Professor Erik Luijten, and Professor Milan Mrksich for their wonderful feedback and suggestions. I would especially like to thank Professor Robert Linsenmeier for his exceptional guidance while I served as teaching assistant for his course.

I likewise could not have completed a Ph.D. without those that prepared me for my doctoral work. I am deeply grateful to Professor Christine Wildsoet for her guidance and mentorship while I worked in her group as an undergraduate at UC Berkeley. I also am appreciative of Dr. Mariana

Garcia for the time and energy she spent mentoring me, and showing me how fun lab work could be. Thank you to Professor Dror Seliktar for hosting me in his lab prior to my arrival at Northwestern and to Dr. Olga Kossover for the training and guidance she provided me while I was there.

While working in the Stupp group, I had the opportunity to work alongside wonderful researchers who taught me much. I am very grateful to Dr. Jacqueline Godbe and Dr. Chris Serrano for helping me figure out what to do at every turn, for keeping me sane, and for being friendly faces throughout. Thank you also to the rest of the members of "Team DNA," Professor Nicholas Stephanopoulos, Dr. Dounia Dems, and Stephen Henrich for their collaboration. I am very appreciative of Dr. Hiroaki Sai for being a wonderful teacher and expert collaborator on many projects. Thank you to Dr. Tristan Clemons and Dr. Jake Carrow for their collaboration and guidance as well on key aspects of my dissertation. Thank you also to the rest of the biomaterials subgroup who gave much useful feedback throughout my work. I was also the beneficiary of a successful collaboration with Professor Mark Markel's group at the University of Wisconsin. Thank you to Dr. Markel, to Brett Nemke, and to Yan Lu for their hard work, patience, discussion, guidance, and hospitality throughout our studies in Madison. Finally, thank you to the students for whom I have served as mentor. James Wester has been an exceptional collaborator and a pleasure to work with. Shelby Yuan has proven an incredibly fast learner and dedicated researcher, and I am excited to see all she will accomplish during her thesis work.

I am immensely grateful to my wife Arielle for her enthusiastic support over the past decade. She is an incredible partner, mother to our daughter June, and friend. I owe her more than I can put in words. Thank you also to Arielle's wonderful parents Nadia and Morad Gabai for their love and support, going so far as to come and help take care of June so I could travel to complete

experiments. Finally, thank you to my parents: my father Dr. Jonathan Lewis and my late mother Professor June Cummins-Lewis. They spent their lives carrying for me, for my brothers, and for each other. They taught me to love learning and discovery and made me who I am today. It was their example of commitment to scholarship and to education that led me to pursue a doctorate, and it was their support and encouragement that gave me the will to complete it.

# LIST OF ABBREVIATIONS

| | |
|---|---|
| ACI | Articular chondrocyte implantation |
| ALP | Alkaline phosphatase |
| AMIC | Autologous matrix-induced chondrogenesis |
| BMP-2 | Bone morphogenic protein 2 |
| BSA | Bovine serum albumin |
| CD | Circular dichroism |
| CS | Chondroitin sulfate |
| DIEA | Diisopropylethylamine |
| DLS | Dynamic light scattering |
| DMEM | Dulbecco′s modified Eagle′s medium |
| DMF | Dimethylformamide |
| DMMB | Dimethylmethylene blue |
| ECM | Extracellular matrix |
| EDC | N-(3-Dimethylaminopropyl)-N′-ethylcarbodiimide hydrochloride |
| EDTA | Ethylenediaminetetraacetic acid |
| ELISA | Enzyme-linked immunosorbent assay |
| ESI-MS | Electrospray ionization – mass spectroscopy |
| FBS | Fetal bovine serum |
| FITC | Fluorescein isocyanate |
| Fmoc | 9-fluorenyl methoxycarbonyl |
| FTIR | Fourier transform infrared spectroscopy |

| | |
|---|---|
| GAG | Glycosaminoglycan |
| HA | Hyaluronic acid |
| HBTU | Hexafluorophosphate benzotriazole tetramethyl uronium |
| HPLC | High performance liquid chromatography |
| H&E | Hematoxylin and eosin |
| ICRS | International cartilage regeneration and joint preservation society |
| IL-1 | Interleukin-1 |
| IL-6 | Interleukin-6 |
| IL-8 | Interleukin-8 |
| IL-10 | Interleukin-10 |
| IL-37RA | Interleukin-37 receptor antagonist |
| IGF | Insulin-like growth factor |
| IP-10 | Interferon gamma-induced protein-10 |
| LAP | Latency associated peptide |
| LC-MS | Liquid chromatography – mass spectroscopy |
| MACI | Matrix-assisted articular chondrocyte implantation |
| MCP-1 | Monocyte chemoattractant protein-1 |
| MIP-1α | Macrophage inflammatory protein-1α |
| MSC | Mesenchymal stem cell |
| nHLF | Normal human lung fibroblast |
| PA | Peptide amphiphile |
| PBS | Phosphate buffered saline |

| | |
|---|---|
| PEG | Polyethylene glycol |
| PyBOP | Benzotriazol-1-yl-oxytripyrrolidinophosphonium hexafluorophosphate |
| Q-TOF | Quadrupole time of flight |
| RMSD | Root mean square deviation |
| SAXS | Small-angle x-ray scattering |
| SEM | Scanning electron microscopy |
| TAMRA | TAMRA |
| TBS | Tris-buffered saline |
| TEM | Transmission electron microscopy |
| TGFβ | Transforming growth factor β |
| TFA | Trifluoroacetic acid |
| THF | Tetrahydrofuran |
| TIS | Triisopropylsilane |
| TNF-α | Tumor necrosis factor-α |
| VEGF | Vascular endothelial growth factor |
| WAXS | Wide-angle x-ray scattering |

# TABLE OF CONTENTS

# LIST OF FIGURES

# LIST OF TABLES

# CHAPTER 1

# 1. Introduction

## 1.1. Hierarchical Self-Assembly in Nature

All known life is made up of hierarchical assemblies, where the properties of small individual building blocks determine the structures they form over orders of magnitude longer length scales.[1] These building blocks include a small set of biopolymers—peptides, nucleic acids, lipids, and carbohydrates—where interactions among the chains can program assembly of the polymers into much larger structures.[2] This bottom-up strategy is distinct from top-down strategies in that all the information needed to determine complex architectures is stored within the building blocks themselves.[3,4] In this way, biology limits its needs for diverse instructions put together building blocks into complex structures; only the instructions to build the blocks themselves and the means to make them are needed to build life. Through this efficient approach, the information needed to assemble an entire organisms can be stored in the nucleus of a single cell.[5]

A second major advantage of natural assemblies is that the interactions between the building blocks are dynamic, allowing systems to adapt to their environment.[6] In biological systems, the stability of the hierarchical assembly depends on the strength and kinetics of the dynamic interactions between the parts. Actin filaments disassemble within minutes of forming, allowing cells to dynamically change their shape to move through their environment.[7] Other assemblies are designed to last much longer; for instance, the half-life of collagen fibril assemblies is likely greater than a human lifetime.[8] Some of the most devastating medical pathologies are a result of dysregulation of these dynamic processes. Alzheimer's disease,[9] Parkinson's disease,[10]

and amyotrophic lateral sclerosis[11] are all related to the formation of filamentous protein assemblies that cannot disassemble, killing surrounding cells. Thus, both spatial and temporal control over biological assemblies determine their function.

A diverse group of intermolecular interactions form bonds among self-assembling components in natural systems. These include (in approximate order of descending bond energy): [2,12]

- Ion-ion interactions: Salt-bridges among charged groups are important in protein folding and cell adhesion.
- Ion-dipole interactions: Interactions between ions and dipoles are weaker than ion-ion interactions, but their shorter length scales are important in fixing protein geometry.[13]
- Dipole-dipole interactions: Hydrogen bonds are ubiquitous in proteins due to dipoles in the polyamide peptide backbone. These interactions are the basis of secondary protein structure, α-helix and β-sheet. Hydrogen bonds also bridge complementary bases in nucleic acids, giving rise to the double-helix structure of DNA.
- Hydrophobic interactions: Cell membranes and liposomes assemble by hydrophobic collapse of lipid groups. Hydrophobic interactions among aliphatic peptide sidechains also plays a role in protein folding
- π-π stacking: Stacking of nitrogenous bases is important in nucleic acid structure and stacking of aromatic peptide sidechains affects protein folding.

Once assembled, these primary assemblies can develop superstructures of even greater complexity which in turn influence biological function. For example, proteins can form filaments like actin or collagen fibrils, rings like helicases or nucleases, and cages like clathrins or ferritins.[14]

An important example of hierarchical assembly in nature is the structure of the extracellular matrix (ECM), a fibrous network that physically supports cells in most tissues.[15] Both the

morphology of the ECM and its chemical composition can influence cell behavior and determine cell fate during development.[16] Collagen fibrils—themselves a superstructure of protein triple-helices—are among the most common protein component of the ECM, forming networks with distinct architectures that depend on tissue function. Common collagen types include collagen I which forms thick oriented fibers that give bone and tendon their structural strength and collagen IV which forms sheets that support the basal surface of epithelia.[17] Collagen topography can affect cell phenotype. For example, following injury fibrous collagen I induces scarring that impairs axonal regrowth.[18] The filaments of the ECM bind a variety of signaling molecules that direct the behavior of attached cells. Adhesion proteins like fibronectin and laminin coordinate interactions between ECM fibers and focal adhesions of cells, with the topography of the signals affecting cell survival, migration, and differentiation over both nanoscopic and microscopic length scales.[19] In addition, the ECM sequesters and presents morphogenic signals like growth factors that combine with topographical cues to direct cell differentiation and tissue development.[20]

At longer length scales, hierarchical assembly of pre-assembled components can produce structures with astonishing macroscopic physical properties.[21] For example, hierarchical bundles of protein fibers in spider silk give the material exceptional strength and extensibility, while the orientation of cellulose superstructures allow trees to adapt the mechanical properties of their wood.[22] In skeletal tissues, hierarchical assembly give individual components unique physical properties specific to their function. In bone, collagen superstructures template the growth of a hydroxyapatite mineral phase, producing oriented crystals that give bone its anisotropic mechanics (Figure 1.1).[23] Tendons, on the other hand, become stiffer as they are strained in order to resist over extension and therefore comprise hierarchical fibril assemblies where the lower stiffness is due to the stretching of fibril kinds at larger length scales, while the higher modulus is due to

stretching of collagen triple helices.[24] In cartilage, hierarchical arrangement of proteoglycans gives the material a low friction surface while acting to absorb stress on the underlying bone.[25] Mimicking the complex architectures of these systems is a major goal of bioregenerative approaches repair damaged tissue.[26] At the same time, these systems inspire a wide range of synthetic systems with advances physical properties based on their hierarchical supramolecular assembly.

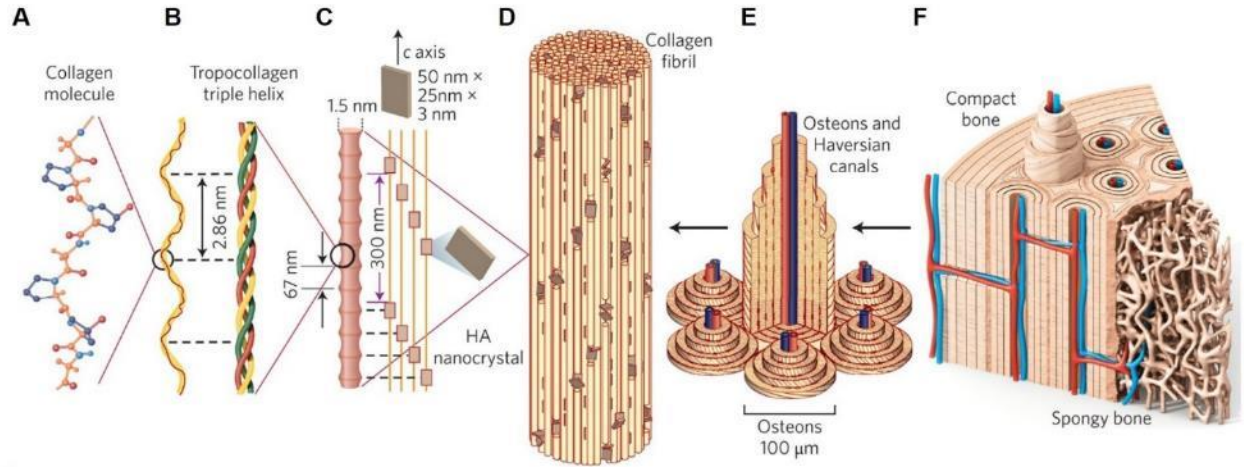


**Figure 1.1: Hierarchical assembly of collagen in bone**
(a) Collagen protein molecules assemble to form a (b) triple helix structure. (c) These helices form fibrils that template mineralization of the tissue. (d) The resulting fiber composite is organized around blood vessels to form (e) osteons, which are the functional unit of (g) cortical bone. Adapted from ref.[27]

## 1.2. Hierarchical Organization, Function, and Degradation of Articular Cartilage

Articular cartilage is a mechanical tissue that covers the surface of bones at the joints, providing a low friction surface while shielding the bone from compressive loads.[28] Unlike other skeletal tissues, cartilage is avascular and has a low cell density. Instead, cartilage comprises mostly water with a small population of native chondrocytes that maintain the ECM. Without

vasculature, nutrients must diffuse through the hydrated space to the embedded cells, primarily from the synovial fluid that bathes the joint.[29] The ECM of cartilage forms an interpenetrating network of two primary components: collagen II and proteoglycans. Collagen II is fibrous like collagen I, but forms thinner fibers with less fiber orientation, providing mechanical support for the tissue.[17] Proteoglycans are glycosylated proteins that assemble to form bottlebrush structures with a protein core and conjugated glycosaminoglycan (GAG) chains. GAGs like hyaluronic acid (HA) or chondroitin sulfate (CS) are hydrophilic carbohydrates that provide the osmotic pressure needed to hydrate the tissue (Figure 1.2).[30]

The hierarchical organization of the ECM components that comprise cartilage give the tissue its material properties, and depend on their location within the joint.[16,31] In the superficial zone furthest from the underlying bone, fibers align parallel align horizontally, producing a smooth articulating surface lubricated by high GAG content. Below the surface, the tissue transitions to a deep zone were fibers align vertically, perpendicular to the compressive forces acting on the joint. Here, the hydrated GAG component adds additional toughness as the osmotic pressure produced by the hydrophilic ECM opposed deformation by compressive loads. Chondrocytes are arranged in vertical columns, following the collagen fibers. Underlying the deep zone is the tidemark which separates the non-mineralized hyaline cartilage from the subchondral bone below.[32] Together, hyaline cartilage and the subchondral bone form an osteochondral unit, and communication across the tidemark is important in regulation and homeostasis of both tissues.[33]

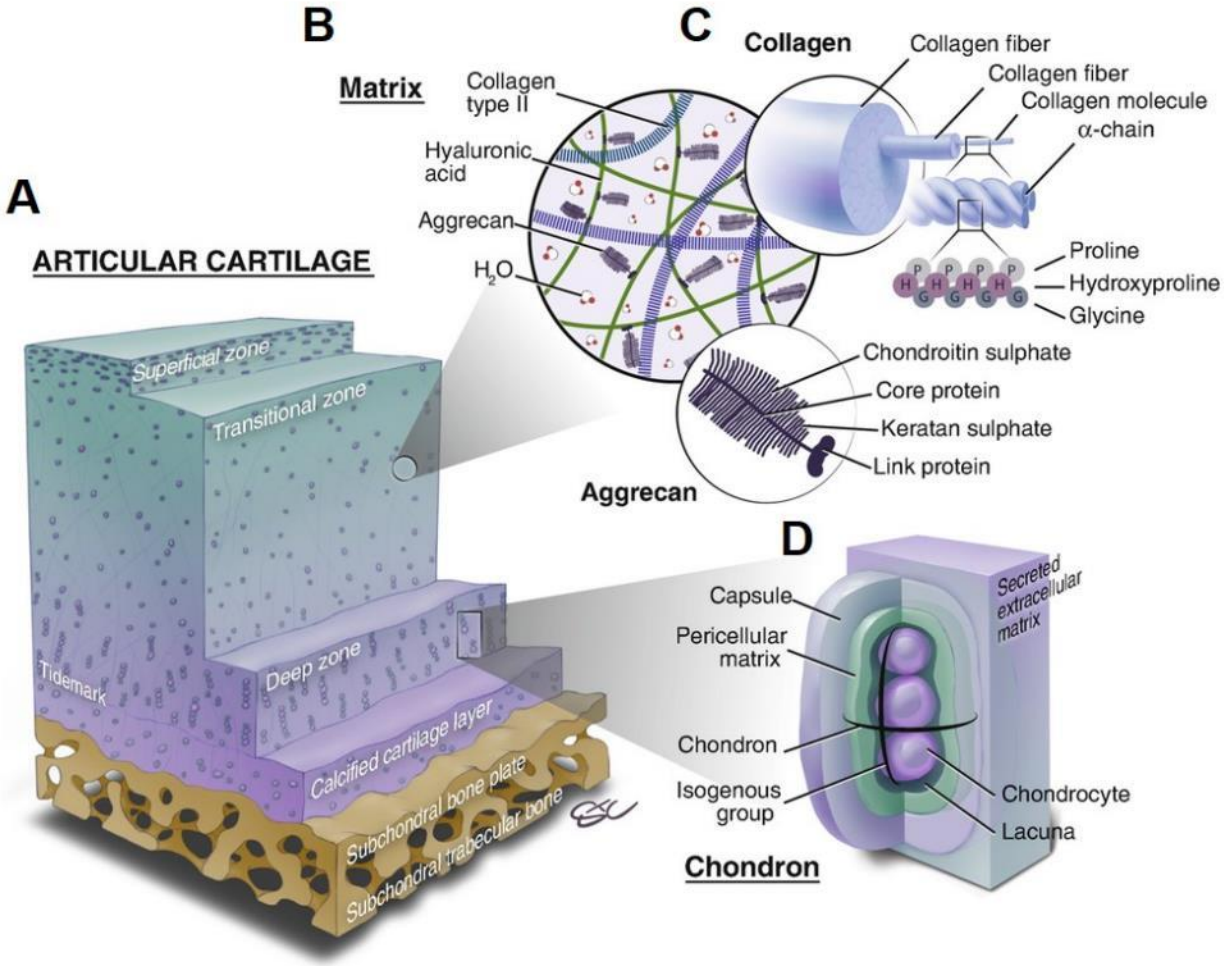


**Figure 1.2: Structure of articular cartilage**

(a) The variable structure of cartilage at different tissue depths where cell and ECM arrangement depends on mechanical function. (b) The ECM of cartilage comprising a network of collagen fibers and proteoglycans like aggrecan. (c) Both collagen and proteoglycans are themselves hierarchical structures. Collagen is made of protein triple helices that assemble into the fibrils that make up fibers. Aggrecan is an assembly of glycoproteins that template a GAG brush. (d) Within the tissue, cells are located within lacunae, with a pericellular matrix extending several microns from the cell surface. Adapted from ref.[32]

Given its critical role in the skeletal system, degradation and injury of articular cartilage can be highly debilitating. As many as 250 million people worldwide suffer from cartilage degeneration in the knee,[34] and the cost associated with these morbidities is estimated to reach 2.5% of gross the gross domestic product of developed countries.[35] However, while bone can self-

heal following injury, hyaline cartilage lacks the ability to regenerate.[36] Instead, the most common approach to address severe cartilage damage is replacement of the entire joint, with the total number of annual knee arthroplasties in the United States expected to reach 3.5 million by 2030.[37] To minimize joint replacements, regenerative therapies aim to address the ways in which the biology, structure, and function of cartilage limit its ability to self-heal.

Most often, cartilage damage is a result of osteoarthritis, a condition in which cartilage is degraded to dysregulation of cellular maintenance of ECM homeostasis.[38] In osteoarthritis, collagen fibers are destabilized while proteoglycan brushes disaggregate and shed associated GAG chains.[39] As a result, the cartilage surface becomes fibrillated and while the tidemark advances as the deeper portions of the tissue undergo endochondral ossification.[35] This process is mediated by inflammatory factors like interluken-1 (IL-1), interluken-6 (IL-6), and tumor necrosis factor-α (TNF-α; Figure 1.3).[40] Increasingly, the condition is considered a systemic disease not localized to the cartilage alone. In addition to structural and genetic factors, co-morbidities that alter inflammatory and metabolic regulation like obesity and diabetes precede the development of osteoarthritis, suggesting that treatment of these underlying factors is as important in treating the disease as regeneration of damaged tissue.[41]

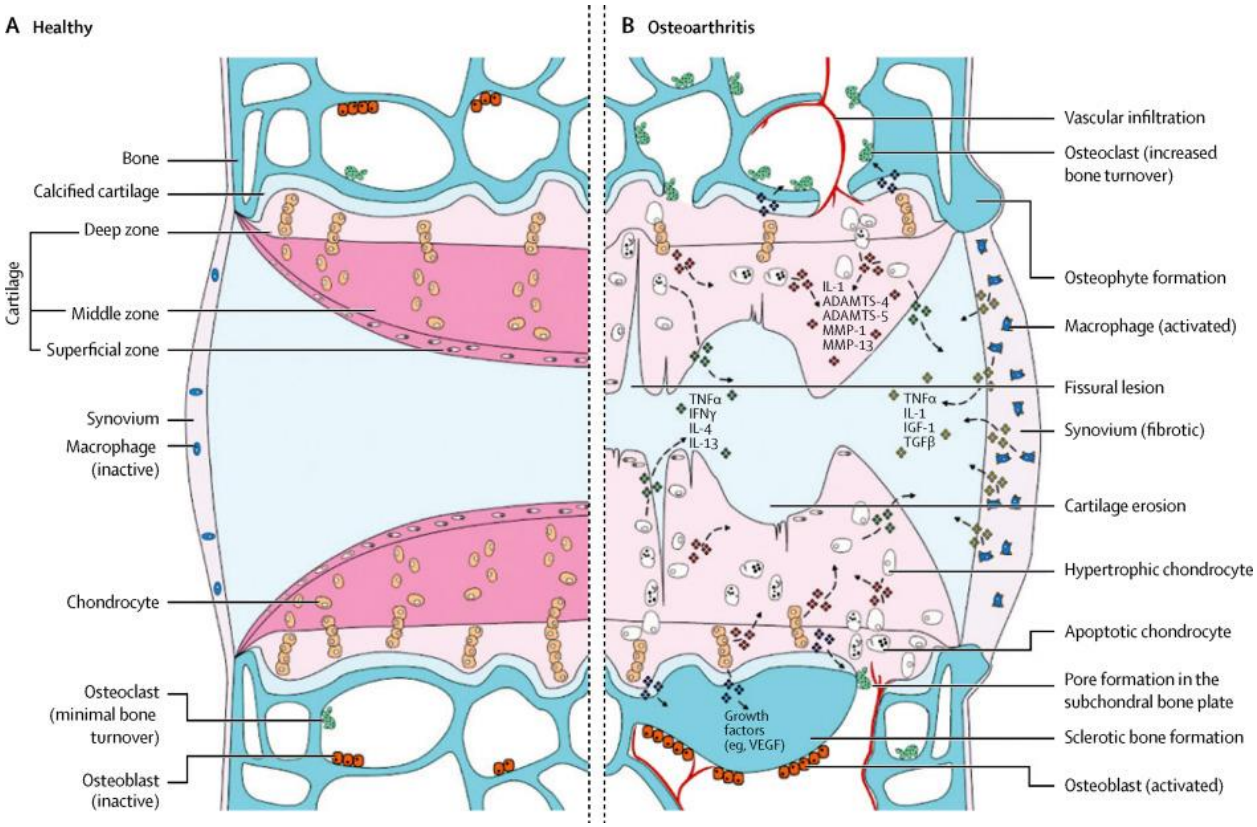


**Figure 1.3: Structural and chemical changes in cartilage degeneration**
Osteoarthritis is a disease of the entire chondral unit. In the cartilage, chondrocytes lose their organized structure and become hypertrophic, while secreting factors that degrade the ECM. The cartilage surface becomes defibrillated. Osteoblasts in the subchondral bone become activated and secrete angiogenic factors, leading to endochondral ossification of the tissue. The synovium secretes inflammatory factors into the joint space, further accelerating degradation and inhibiting repair. Adapted from ref.[35]

A major impediment to regenerating cartilage in osteoarthritis or acute injury is the lack of progenitor cells within the tissue. While the synovium contains mesenchymal stem cells (MSCs) that can differentiate and repopulated damaged skeletal tissue, cartilage itself likely lacks such progenitors.[42] At the same time, joint injuries can initiate infiltration of senescent cells into cartilage and synovial tissue.[43] Recent evidence suggests signaling by these cells intensifies osteoarthritic signals, while their clearance can restore a pro-chondrogenic environment.[44] In addition, cartilage development and homeostasis depends on local concentrations of growth

factors[45] and metabolites.[46] However, factors like age, inflammation, and cellular senescence can influence the response to these signals.[47] In some cases, signals that induce matrix anabolism and homeostasis in healthy tissue can exacerbate degeneration in unhealthy tissue or in high doses.[48] Thus, successful regeneration of cartilage requires delivering or supporting healthy cells in the tissue while controlling local concentrations of morphogenic and metabolic factors. Without this regulation, the ECM structures that give cartilage its mechanical resilience are not produced, resulting pain and loss of function as the articular surface is poorly lubricated and bone lacks shielding from compressive loads.

### 1.3. Biomaterials for Regenerative Medicine and Cartilage Repair

Current clinical techniques to replace damaged cartilage focus filling the defect space with cells that can initiate the regeneration process. In the gold standard procedure, called microfracture, the damaged cartilage is debrided and holes are made extended into the subchondral bone to induce bleeding.[49] The intention is that progenitor cells in the clot differentiate into chondrocytes and produce hyaline tissue; however, about half the time fibrocartilage develops which lacks the hierarchical structure and thus the mechanical function of articular cartilage.[50] In an alternative approach, articular chondrocyte implantation (ACI), chondrocytes or progenitor cells are extracted from the patient, expanded *ex vivo*, and implanted into the defect space.[51] This technique can be augmented with a collagen scaffold to support the chondrocytes in matrix-assisted articular chondrocyte implantation (MACI; Figure 1.4).[52] These techniques are expensive and time consuming, requiring an additional procedure to harvest the cells, extensive laboratory manipulation of cells prior to implanting, and have unclear regulatory status.[53] Therefore, cell-free

implants that can support the production of hyaline cartilage are the most likely approach for widespread clinical use.

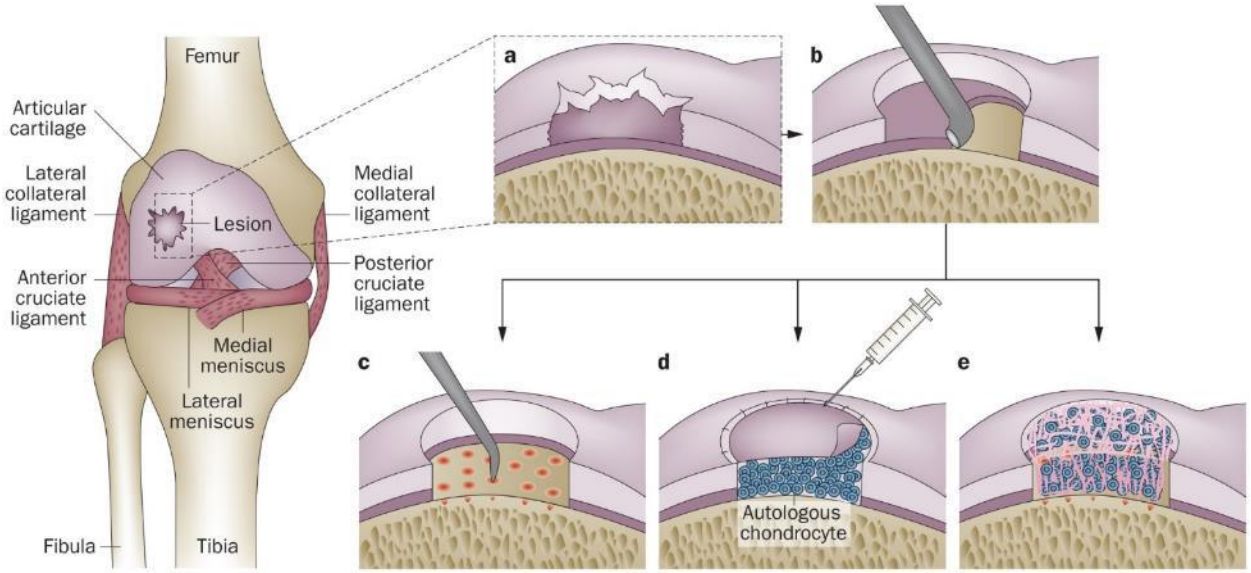


**Figure 1.4: Clinical approaches to induce cartilage repair**
(a) Lesions in the articular cartilage of the knee are often shaped irregularly. (b) The lesion is debrided creating a regularly shaped, full thickness defect that extends to the subchondral bone. (c) In microfracture, holes are made in the subchondral bone to induce clot formation. (d) In ACI, defects are filled with expanded chondrocytes. (e) Chondrocytes are supported by an implanted scaffold in MACI. Figure adapted from ref.[53]

One approach to augment microfracture is autologous matrix induced chondrogenesis (AMIC) where a biomaterials scaffold like collagen I, HA, or fibrin is implanted in the defect following fracturing the subchondral bone.[54] In early clinical models, PEG scaffolds have also been shown to support cartilage regeneration healing.[55] While these technique have shown improvements relative to microfracture alone,[56] the materials poorly mimic the structure and biology of native cartilage, which may limit its ability to produce hyaline tissue over the long term. One possible approach to improve scaffold performance is the delivery of morphogenic signals that induce cartilage production.[57] Due to their importance in cartilage development and ability to induce chondrogenic differentiation *in vitro*,[58] members of the TGFβ family are a frequent target

for delivery by cell free scaffolds.[59] For example, supramolecular peptide amphiphile (PA) hydrogels that specifically bind TGFβ-1 were shown to induce hyaline cartilage regeneration in a rabbit model.[60] Other work points to insulin-like growth factor (IGF) and as important signals to induce cell viability and proliferation during the early healing process.[61,62] In combination, these signals and others may act synergistically to enhance the chondrogenic potential of encapsulated cells.[63] Alternatively, autologous growth factors are present in platelet rich plasma which can be applied directly to a defect or loaded on a scaffold.[64]

In addition to chemical cues, scaffold topologies that mimic the organization of native cartilage may be useful in directing infiltrating cells toward hyaline cartilage lineages.[65] Cartilage progenitor cells are sensitive to mechanical cues from their environment, with recent work demonstrating highly confined scaffolds can limit differentiation toward hyaline cartilage.[66] One approach to produce scaffolds that mimic ECM architecture is to produce hydrogels directly from ECM components, though these materials can initiate immune rejection even when purified.[67] Instead, several synthetic approaches can be used to fabricate materials that mimic the hierarchical architecture of cartilage. Electrospinning can be used to create fibrous networks with tunable diameters and orientation.[68] Work with these systems has shown filaments with micron-scale morphology support chondrogenesis better than those with nanoscale diameters, possibly due to increased gel porosity.[69] To further control spatial organization, fibers can conjugated to GAG binding peptides to produce structural gradients like those in healthy tissue.[70] In one example, Guilak and coworkers produced woven scaffolds with anisotropic fiber alignment that mimicked the mechanics of native cartilage.[71,72] Alternatively, 3D printing can be used to produce porous scaffolds with durable mechanical properties that support cell infiltration.[73] In another approach, assembly of microgels can be used to form porous structures that can support cell encapsulation

and differentiation.[74,75] Finally, synthetic supramolecular systems that mimic the superstructures found in nature are an emerging technique to program complex hierarchical architecture, though improvement in their mechanical performance may be necessary to produce effective cartilage regeneration scaffolds.[76]

### 1.4. Supramolecular Design of Hierarchical Self-Assembly

Inspired by nature, supramolecular chemists work to design self-assembling systems with long range order.[3] By working "beyond the molecule" the study of intermolecular interactions among assemblies can lead to the rational programming of a wide variety of nanoscopic architectures.[77] As in biology, the design of the individual building blocks holds the necessary information for the entire assembly. These building blocks can be made from polymers[78] or small molecules,[79] but often biologically inspired materials like oligonucleotides provide significant control over self-assembly.[80] While the high specificity of DNA base pairing provides precise control over assembly, peptides are highly stable and easy to produce, making them ideal to produce functional self-assembled nanostructures.[81] Self-assembling peptides are especially useful as biomaterials because their composition can mimic the fibrous proteins of the ECM.[82]

The design of self-assembling peptides combines a number of intermolecular interactions to control the morphology of the assemblies. For example, self-complementary designer peptides developed by Zhang and colleagues with repeating form β-sheet among neighboring peptide chains while ion-ion interactions coordinate stacking of peptide sheets.[83,84] In another example, diphenylalanine peptides reported by Gazit bond with neighbors both through hydrogen bonding and π-π stacking.[85] Materials made of self-assembling peptides have been applied in numerous biomedical applications including protein and drug delivery,[86] and as scaffolds for tissue

engineering and regenerative therapies.[87,88] These successes have made self-assembling peptides a promising platform for future clinical applications, and in recent years one example has been the subject a clinical trials to investigate its efficacy in treating tooth decay.[89]

Among the most versatile self-assembling peptide systems are PAs developed by Stupp and co-workers, comprising a peptide conjugated to a fatty acid tail.[90,91] Assembled morphology depends on the peptide sequence used, with a subclass of these molecules are designed to form high-aspect-ratio filaments (Figure 1.5). These PAs generally include three domains: (i) the aliphatic tail group to drive assembly by hydrophobic collapse, (ii) a hydrogen bonding region that directs filament formation, and (iii) a hydrophilic peptide region for solubility, which generally contains ionic groups with formal charge.[92,93] Supramolecular PA assemblies are highly dynamic,[94,95] with molecules consistently exchanging among the assemblies.[96] This also makes PA systems sensitive to processing such as heat treatment and ionic conditions, giving researchers control over the structures that form.[97] Importantly, when anionic groups are used as the hydrophilic domain, hydrogels are formed by the nanofibers when exposed to polyvalent cations like calcium[98,99] or oligolysines.[100]

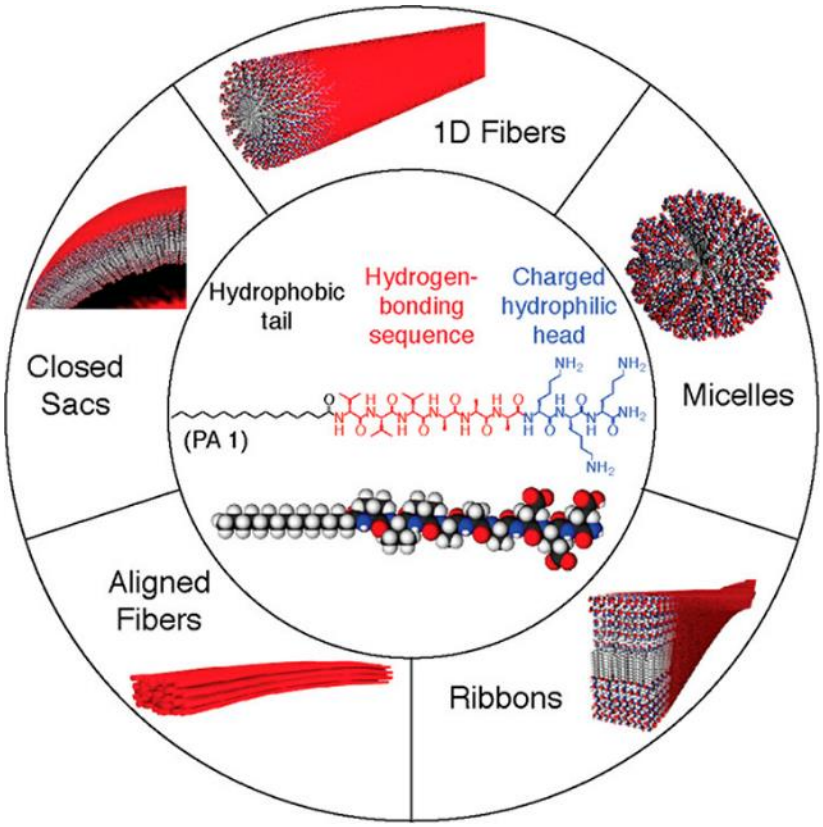


**Figure 1.5: Morphology of PA assemblies**
PA molecules generally comprise an aliphatic tail, a hydrogen bonding peptide region, and a hydrophilic peptide region (center). Rational design of the peptide sequence can be used to form supramolecular structures with a variety of morphologies with long-range order. Figure adapted from ref.[93]

The long filaments formed by PA assemblies are similar in structure to ECM filaments.[82,101,102] Moreover, because these molecules are peptides, a fourth domain comprising a bioactive peptide is easily appended to these molecules, producing nanostructures that present specific peptide epitopes to their surroundings.[103] These sequences can mimic ECM components like fibronectin[104] and laminin;[105,106] bind bioactive signals like TGFβ-1,[60] bone morphogenic protein-2 (BMP-2),[107,108] platelet derived growth factor,[109] and heparin;[110] or mimic bioactive signals like fibroblast growth factor-2,[111] vascular endothelial growth factor (VEGF),[112] brain derived neurotrophic factor,[113] and heparin sulfate.[114] The biomimetic and bioactive properties of

PA assemblies have led to their demonstrated improvement in a number of bioregenerative models including bone regeneration,[107,108,114] cartilage regeneration,[60] spinal cord regeneration,[105] muscle regeneration,[115] and treatment of atherosclerotic plaques.[116]

To develop self-assembling materials with more complex geometries, recent research has focused on the design of hierarchically assembling peptide systems.[117] These materials can better mimic the hierarchical assemblies found in nature and help explain the fundamental interactions that lead to superstructure assemble.[118,119] In one example, Gazit and co-workers showed that short hydrophobic tripeptides can form helices which in turn for bundles of many peptide assemblies.[120] In another study, Chilkoti and co-workers conjugated elastin-like peptide domains to β-sheet forming polyalanine domains, producing thermally-responsive, injectable networks of fractal-like structures.[121]Other studies have sought to establish design rules to determine when hierarchical assembly occurs for instance by manipulating the order of phenolic residues[122] or by coassembling components with varying hydrophobicity.[123] Through hierarchical assembly, researchers can design materials with unique properties, such as an amyloid sequence-based system that is stronger any known protein material.[124]

PA systems have proven a useful platform to study hierarchical assembly as well. Because PA assemblies are dynamic, their structures can adapt as superstructures form. For example, mixing solutions of cationic PA filaments with anionic HA produces membranes at the solution interface with PA fibrils extending into the HA solution.[125] In another example, polymerization of thermo-responsive polymer chains from PA filaments produces gels of oriented polymer brushes that can be 3D printed and act as anisotropic actuators.[126] Others have shown that PA filaments with positively and negatively charged domains can form bundled structures depending on the buffer pH.[127] Recent work reported DNA-conjugated PA molecules where Watson-Crick base-

pairing led to association of PA filaments displaying complementary strands. In these systems, wide bundles of DNA-rich PA filaments developed, while PA-poor filaments did not form hierarchical structures. Computational simulations showed that superstructure formation was a result of dynamic redistribution of PA molecules, where DNA-rich domains were incorporated into growing bundles. Importantly, this work demonstrated that superstructure formation depended on intermolecular cohesion among the PA molecules: If cohesion among the molecules within the assemblies is too strong, molecules are unable to redistribute and bundles cannot form. Superstructure formation could be reversed by the addition of toehold displacement strands, and astrocytes responded to the formation of hierarchical assemblies by switching between reactive and non-reactive states (Figure 1.6).[128]

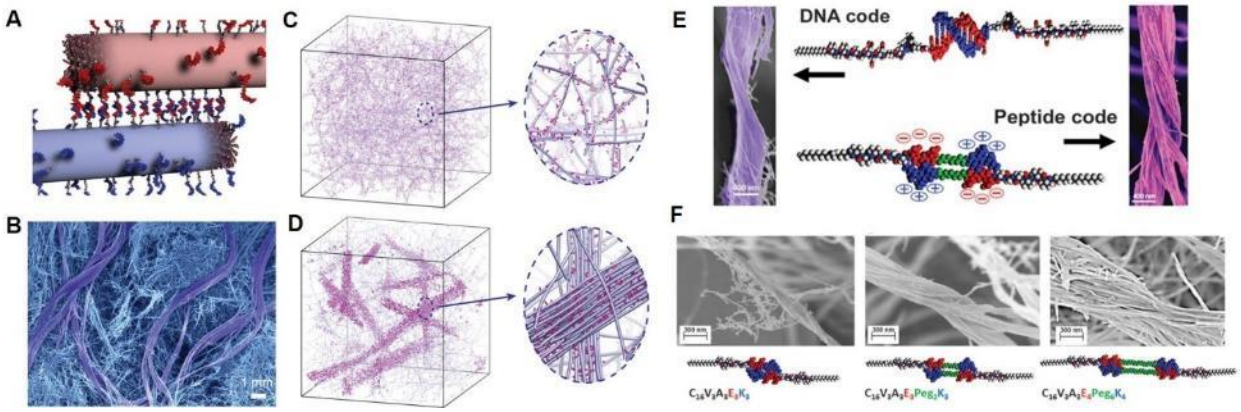


**Figure 1.6: Superstructure formation by DNA-PA conjugates**
(a) Schematic showing hybridization of complementary DNA sequences on adjacent PA filaments (b) SEM micrograph of bundled filaments that form as a result of hybridization. Molecular simulations showed that (c) without monomer reorganization superstructures could not form, but (d) did form when reorganization was allowed. (e) Hierarchical assembly could be programmed with complementary DNA sequences or complementary peptide sequences, with (f) strengthening electrostatic interactions increasing bundling by the peptide systems. (Adapted from ref.[128])

Work on DNA-PA conjugates demonstrated hierarchical assembly by PA based structures could be tuned by rational design, and controlling assembly architecture could be used to influence

biological systems. An advantage of this system was the precise control over inter-assembly interactions through tuning base-pairing between DNA strands. However, these systems are difficult to synthesize and have limited biological stability. These initial results suggested further exploration of how hierarchical assembly occurs in peptide systems would help design simpler and more versatile superstructure platforms for use in an expanded set of applications, including *in vivo* as therapeutic materials. The highly tunable nature of the dynamic assemblies these systems form further indicated that PA superstructures would be particularly useful in mimicking biological environments with hierarchical structures, for example, cartilage.

## 1.5. Thesis Overview

This thesis begins with fundamental studies on the interplay between the cohesive interactions that cause primary self-assembly and the hierarchal interactions that determine how these primary assemblies affect one another. Based on this work, the second part of the thesis focuses on the design of hierarchically assembled systems for use in cartilage repair.

In Chapter 2, a model system of short PA molecules of opposite charge is introduced to study how interactions among molecules within assemblies can dictate the hierarchical structures they form. These studies show that dynamic rearrangement of molecules is key to the development of superstructures. Redistribution of molecules from homogeneous assemblies of either positive or negative charge to heterogeneous mixed charge structures predicted further assembly into fibrous superstructures. Importantly, increased cohesion in the primary assemblies decreased superstructure formation while decreasing cohesion caused the structures to form more quickly. These results clearly demonstrate that the effect of primary and hierarchical interactions on one another is the basis of forming complex architectures.

In a second study to understand PA self-assembly at multiple length scales, Chapter 3 reports an uncharged PA molecule where solubility is derived from a decaethylene glycol group. By eliminating charge from the PA molecule, these systems allow investigation into how electrostatic interactions determine the way in which PA molecules assemble. Without repulsion among charged ionizable groups, PA assembly was pH independent and occurred at relatively low concentrations. Mixing charged and uncharged PA molecules showed that even small amounts of charge in the assemblies can produce morphologies similar to their fully charged counterparts. Charge determined how cells responded to these systems, with charged and uncharged PA assemblies inducing osteogenesis in different media conditions.

Chapter 4 focuses on applying lessons on PA charge to design systems that better deliver morphogenic signals to induce chondrogenesis. A PA system previously reported by Stupp and colleagues to bind the cytokine TGFβ-1[60] was found to undergo a deamidation side reaction during purification which altered the intended binding epitope. Because the deamidation was the result purification conditions necessary for the ionic PA backbone, using a PEGylated PA to present the epitope allowed for purification without deamidation occurring. Surprisingly, comparing the intended epitope to the deamidated epitope revealed that the deamidated sequence improved growth factor retention by the PA material. Improved retention of TGFβ-1 correlated with increased chondrogenesis of cells encapsulated by the PA. The decreased binding of the growth factor by the original sequence was correlated with stronger electrostatic attraction between the binding epitopes on one filament and charged groups on the surfaces of neighboring PA filaments, forming hierarchical structures. This work highlights an example of how forming hierarchical superstructures can affect the bioactivity of self-assembled systems.

Chapter 5 describes the application of the improved TGFβ-1 binding PA system to cartilage repair in a large-animal model. Because cartilage is subjected to significant shear forces, biomaterials scaffolds for cartilage regeneration must have resilient materials properties. Combining the chondrogenic PA system with HA particles produced gels that were better able to withstand the mechanical forces in large-animal joints. Interestingly, combining the two components formed aligned PA superstructures due to special confinement of the PA filaments as the hydrophilic HA component swelled. These hierarchically ordered PA/HA hybrids supported chondrogenic differentiation of progenitor cells and were well retained for short periods in defects made in sheep joints, making them a strong candidate for cartilage repair. The chapter concludes with a series of animal studies to test the efficacy of the material to regenerate healthy cartilage. These studies showed that the when delivering TGFβ-1, the material improved the fill and integration of the new tissue with surrounding cartilage as assessed by macroscopic scoring after four weeks. After twelve weeks, defects treated with the growth factor delivering material formed more hyaline-like tissue than defects treated with TGFβ-1 alone. This work highlights an example of the use of bioactive hierarchical assemblies in an important clinical target for bio-regeneration.

The thesis closes with Chapter 7, which describes future directions for exploring hierarchical supramolecular assemblies for regenerative medicine. These include possible techniques to modulate the physical properties for PA superstructures and possible biological targets of future work.

# CHAPTER 2

# 2. Supramolecular Exchange Among Assemblies of Opposite Charge Leads to Hierarchical Structures

## 2.1. Objectives and Significance

Hierarchical assemblies of proteins into fibrillar structures occur in both physiologic and pathologic extracellular spaces and often involve interactions between oppositely charged peptide domains. However, the interplay between primary structure dynamics and hierarchical structure formation remains unclear. In this work we investigate supramolecular mimics of these systems in which the primary structures are one-dimensional assemblies of small alkylated peptides bearing opposite charge. Exchange dynamics in these systems creates hierarchical superstructures among many assemblies only when their constituent molecules have weak cohesive interactions. This allows the small molecules to escape from their large assemblies and reassemble to optimize electrostatic attraction. Increasing intermolecular cohesion using longer peptide sequences that form stable β-sheets was found to suppress superstructure formation. In contrast, increasing repulsive interactions among the molecules by adding charged residues resulted in faster dynamic exchange of molecules and accelerated inter-assembly formation of hierarchical structures. These results suggest that in peptide systems low internal cohesion could facilitate the conformational rearrangements required to create hierarchical structures.

## 2.2. Background

In nature, hierarchical assembly of proteins leads to the formation of either functional or pathological fibrils. Actin filaments,[129,130] bundled collagen triple helices,[1,131] and silk fibrils[132,133] are hierarchical superstructures of many individual folded proteins. In diseased states, pathological aggregation of mis-folded protein components yields toxic amyloid fibrils, associated with neurodegenerative diseases such as Alzheimer's disease,[134,135] Parkinson's disease,[136,137] and amyotrophic lateral sclerosis.[138,139] Several proposed pathways to explain amyloid fiber formation suggest that the hierarchical assembly depends on the stability of intermolecular interactions within the assembling aggregates.[140,141] The tendency of natural peptides and proteins to achieve hierarchical complexity has inspired the development of synthetic peptide systems that similarly achieve hierarchical morphologies.[2,117] A major goal is to achieve structurally complex assemblies from short peptide building blocks due to their ease of design and preparation.[142] Controlling interactions among primary assemblies of homogeneous short peptide systems has proven useful in programming assembly into hierarchical structures.[122,143-145] Yet a better understanding of how intermolecular interactions among peptides within the assemblies—especially in heterogeneous mixtures—affect superstructure formation can help explain complex assembly of protein and direct design of synthetic peptide systems.[146]

Stupp and co-workers have developed a broad class of PA molecules consisting of a peptide sequence conjugated to a fatty acid that in aqueous solution self-assemble into nanoscale filamentous assemblies.[91,96,97,147-149] These systems can be programmed to form cylindrical nanofibers that mimic extracellular filaments and have emerged as a promising biomaterials platform for regenerative medicine therapies.[60,105,112,114,115,150] Cohesive supramolecular

assemblies can also be formed by co-assembling oppositely charge amphiphiles,[151] with electrostatic attraction increasing β-sheet formation among co-assembled PA molecules[152] or producing crystalline order among neighboring amphiphiles.[153] In a recent report, complementary aromatic groups on oppositely charged molecules provided the cohesive driving force for co-assembly into mixed fibers, which formed hierarchical aggregates due to neutralization of the surface charge in the co-assembled structures.[154] While these previous reports focused on how intermolecular cohesion determines assembly morphology, further work is needed to explain how these primary interactions affect the ability of assemblies to interact with one another.

The Stupp group recently reported the formation of large bundled superstructures of PA nanofibers that were programmed to display complementary DNA oligomers or charged peptide sequences that drove formation of superstructures among nanofibers.[128] The study proposed a model whereby long-range exchange of PA molecules among the assemblies resulted in superstructure formation. The proposed mechanism implied that two energies mediated the process—namely, the cohesive energy among molecules in the assembly and the interaction energy among assemblies through Watson-Crick pairing or electrostatic attraction. In previous work,[128] peptide-only superstructures that contained programmed association of both positively and negatively charged domains in the same PA molecule bundled extensively into superstructures. However, mixtures of PA fibers ionizable to only negative charge and PA fibers ionizable to only positive charge did not have sufficient driving force to form bundles. The hypothesis here was that the energy associated with inter-fiber attractive interactions was lower than the cohesive energy within individual fibers, thus suppressing the exchange necessary to build the hierarchical superstructure.

This work describes the synthesis of PA molecules to create model systems to help us gain further understanding of mechanisms behind the self-assembly of superstructures. The model systems have been investigated using the pH dependent self-assembly of short, negatively and positively charged PA molecules. These molecules were designed without β-sheet forming sequences in order to decrease cohesive energy within the assemblies and thus promote exchange dynamics when oppositely charged assemblies are mixed. The study also compared the behavior of these systems with others formed by molecules with enhanced or diminished intermolecular cohesion. These experiments establish design rules to create hierarchical superstructures with small molecule peptides by controlling the primary structure of the assemblies they form.

## 2.3. Results and Discussion

*Self-assembly of short PA molecules*

The synthesized PA molecules were composed of only a palmitic acid tail and three glutamic acid (**PA1**) or three lysine (**PA2**) residues which lack the β-sheet forming sequences that program self-assembly of long supramolecular nanofibers (Figure 2.1a, Figure 2.23a,b).[97] The initial hypothesis was that the anionic palmitoylated tripeptide would form distinct planar, fibrillar, and spherical nanostructures in a pH-dependent manner similar to the cationic palmitoylated dipeptides previously reported.[155] Titration of 0.1 M sodium hydroxide (NaOH) into a 0.75 mM solution of *N*-palmitoyl-triglutamic acid showed a buffering region from pH 5.9 to 6.9, where the pH changed by about 1 unit as two equivalents of base were added (Figure 2.1b). At pH values below the buffering region, a white precipitate was present (Figure 2.2a). While buffering, a cloudy suspension formed near 6.45, and the solution became fully clear at a pH near 6.9, suggesting

improved solubility due to deprotonation of acidic side chains (Figure 2.2a). At acidic pH, **PA2** dissolved easily forming a clear solution. The titration curve of **PA2** showed a similar buffering region where the pH remained near 9.0 as 2 equivalents of NaOH were added (Figure 2.1b).

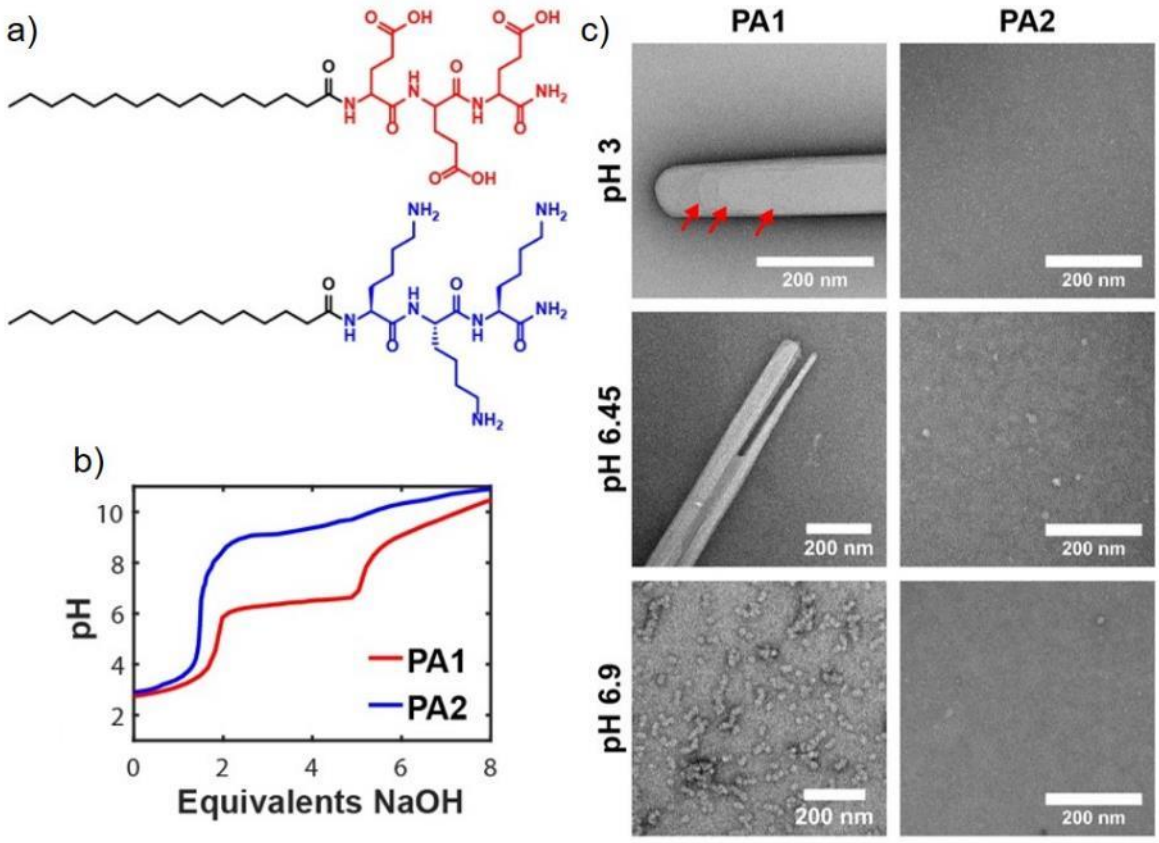


**Figure 2.1: Self-assembly of short PA molecules**
(a) Molecular structures of **PA1** and **PA2**; (b) titration curves for **PA1** and **PA2** demonstrating pH change as 0.1M NaOH was titrated into aqueous solutions; (c) conventional TEM of **PA1** and **PA2** at pH 3, 6.45, and 6.9, negatively stained with uranyl acetate; arrows indicate the edge of lamellar layers within stacked structures.

These results led the the hypothesis that the morphology of the nanostructures would change significantly as **PA1** glutamic acid residues were deprotonated in this buffering region. Negative stained transmission electron microscopy (TEM) imaging for high contrast showed **PA1**

formed wide structures that precipitated out of solution at a pH below the buffering region, with an average width of 248 nm (Figure 2.1c). When pH was increased to 6.45, the additional deprotonation of glutamic acid residues increased repulsion among molecules resulting in thinner ribbons with an average width of 145 nm (Figure 2.1c). As molecules were further deprotonated with additional base, aggregates of spherical micelles formed in a clear solution at pH 6.9 (Figure 2.1c). Cryogenic TEM of PA solutions preserved in vitreous ice revealed similar structures, though individual layers and micelles were not clearly discerned due to the limited contrast of micrographs obtained by this technique (Figure 2.2b).

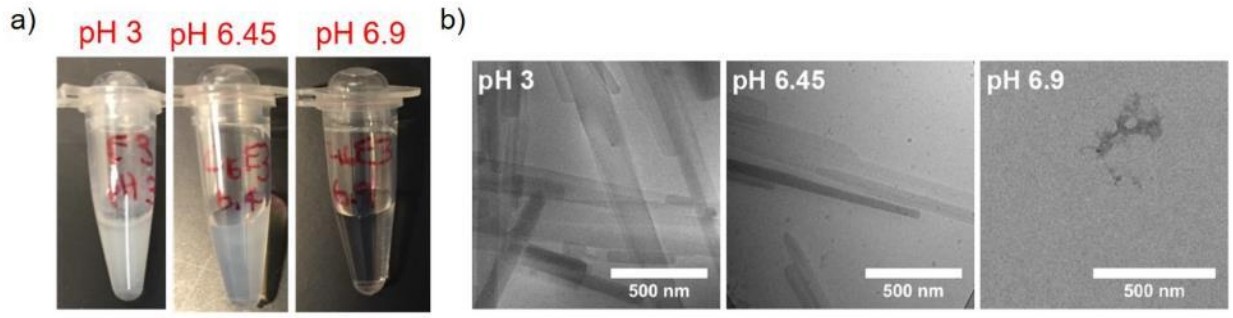


**Figure 2.2: Solution appearance and cryo-TEM for short PA molecules**
(a) Macroscopic appearance and (b) cryo-TEM of **PA1** at pH values 3, 6.45 and 6.9.

To confirm that changes in morphology were caused by changes in protonation state, we synthesized peptides where the one or two glutamic acid residues closest to the palmitic acid group were substituted with the corresponding methyl ester, limiting the total charge in alkaline solution (Figure 2.23c-d). The inner glutamic acid residues were methylated because past reports indicated that the solvent-exposed side chains deprotonate at the lowest pH, given that these side chains are closer to the hydrophilic solvent environment than the hydrophobic alkyl tail. When dissolved at pH 9, the double methylated peptide bearing only one charged residue formed ribbon-like structures while the single methylated peptide with two charges formed spherical micelles (Figure

2.3). These results suggested that the morphological changes observed in **PA1** supramolecular structures over the buffering region from pH 5.9 to 6.9 correspond primarily to deprotonation of the second glutamic acid residue.

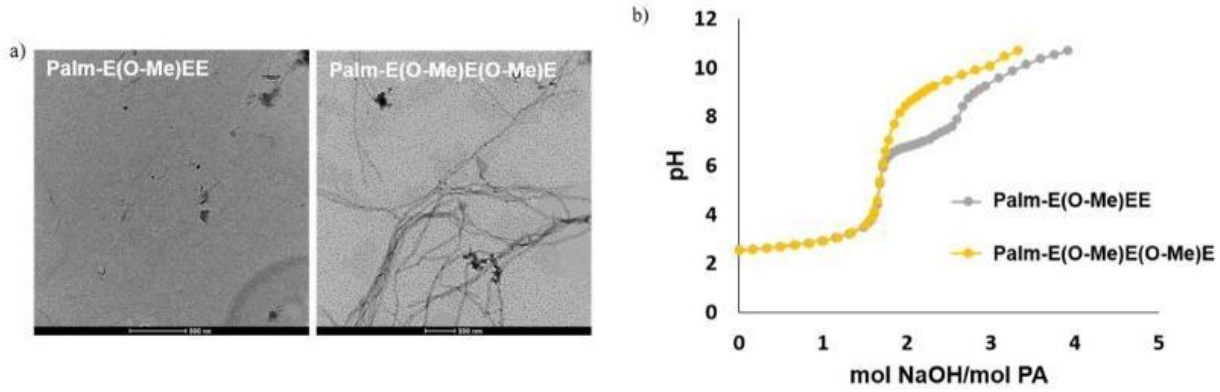


**Figure 2.3: Self-assembly of methyl ester short PA**
(a) Characterization of the O-methylated **PA1** derivatives by conventional TEM at pH 9 and (b) titrations in aqueous solution.

Previously, Stupp and colleagues reported that hierarchical assembly in supramolecular systems depends on dynamic exchange of the molecules among the assemblies.[128] In the systems reported, strong inter-fiber attraction was required to overcome strong inter-molecular cohesive energy within the assemblies, which limited their dynamic exchange. Although the palmitoylated tripeptides reported here lack complementary interdigitating peptide sequences, we hypothesized that without a β-sheet forming sequence increased dynamics would result in superstructure formation when the molecules were mixed.

*Superstructure formation by mixing oppositely charged short PA molecules*

Next studies were mixtures at pH 3, 6.45, and 6.9, where **PA1** lamellae, ribbons, and aggregates of spherical micelles respectively were observed, while **PA2** consistently formed

spherical micelles at all three pH values as indicated by TEM micrographs (Figure 2.1c) and small-angle x-ray scattering (SAXS) patterns (Figure 2.4; see Figure 2.10).

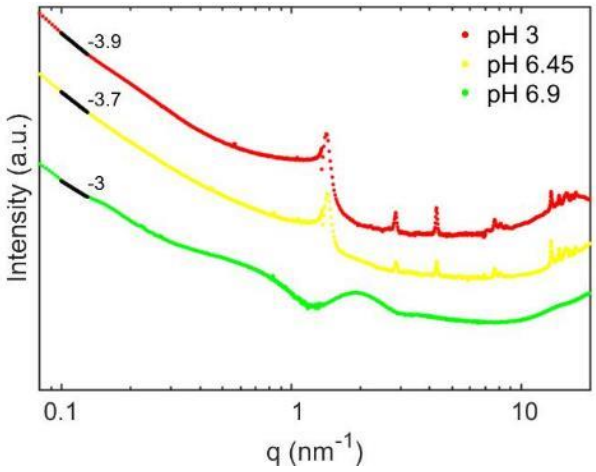


**Figure 2.4: SAXS for short PA molecules at various pH**
SAXS/MAXS/WAXS scattering pattern of **PA1** collected at pH 3, pH 6.45, and pH 6.9. The high slope in the low-q region at pH 6.9 can be attributed to the aggregation of micelles observed by TEM. This prevented fitting the data to a micelle model.

Separate PA solutions of each PA molecule at a desired pH were mixed, followed by adjustment to the pre-mixing pH. TEM of negatively stained samples prepared 1 hour after mixing revealed the formation of flat structures and micelle aggregates at pH 3, ribbons and micelle aggregates at pH 6.45, and exclusively clusters of micelle aggregates at pH 6.9 (Figure 2.5), suggesting little molecular reorganization had occurred. The nanostructures were characterized four days following mixing by negative-stained TEM for high contrast (Figure 2.6a), scanning electron microscopy (SEM, Figure 2.6b) of samples preserved by critical point drying coated on a polystyrene sponge for imaging three-dimensional samples, and cryogenic-TEM to exclude drying effects (Figure 2.7). Interestingly, all three imaging techniques revealed the formation of robust bundled fiber superstructures in pH 6.45 samples, while some fibers but limited superstructures were observed in the more acidic and basic mixtures. These results support the previously reported

model of superstructure formation by molecular redistribution[128]—the high-propensity of these short molecules to exchange among assemblies driven by the establishment of strong interactions. While smaller bundles were observed by TEM, which is limited by small sample thickness, imaging of three-dimensional structures by SEM revealed the largest hierarchical assemblies at pH 6.45 were over 1 μm in diameter (Figure 2.6b). These large structures were highly birefringent when observed under cross-polarizers (Figure 2.8). The confinement of bundling behavior to a narrow pH range indicated superstructure formation was limited by protonation state, likely due to changes in electrostatic repulsion among molecules within the assemblies.

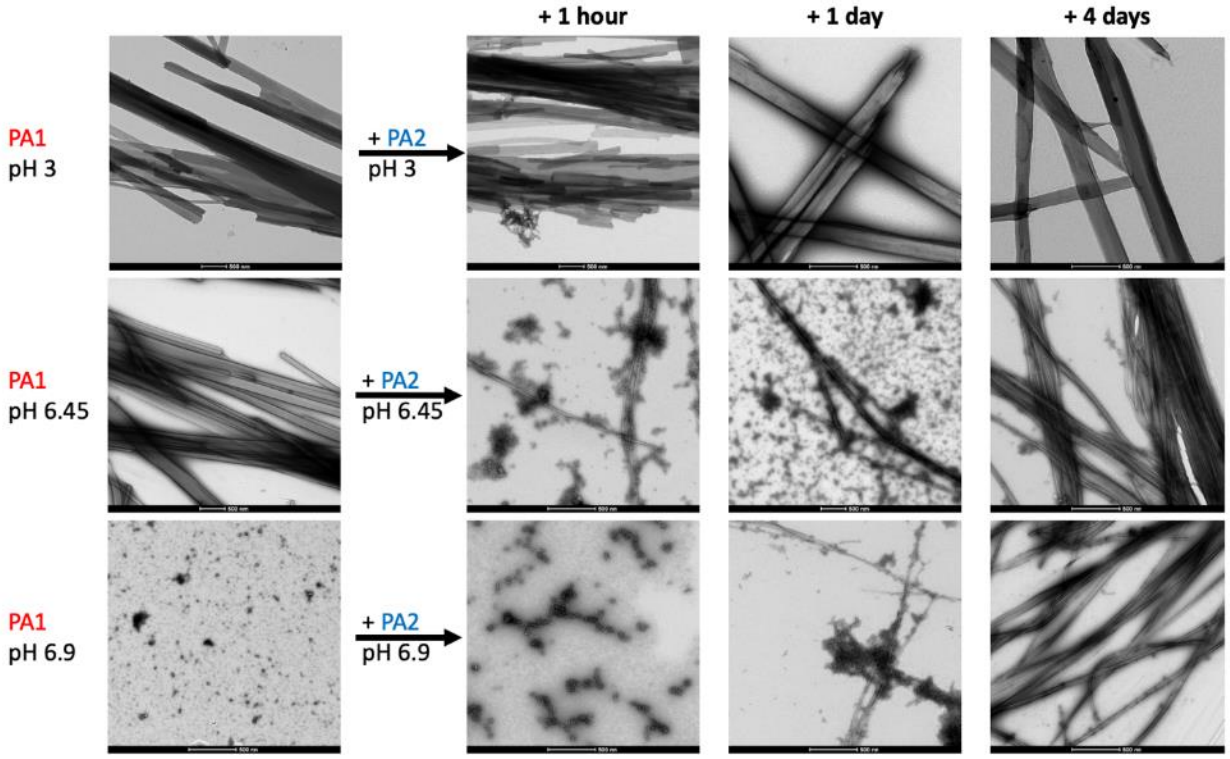


**Figure 2.5: Time-dependent formation of PA superstructures**
TEM characterization of **PA1** at pH 3, 6.45 and 6.9 before mixture, and the **PA1**/**PA2** mixture at the timepoints 1 hour, 1 day, and 4 days after pH adjustment.

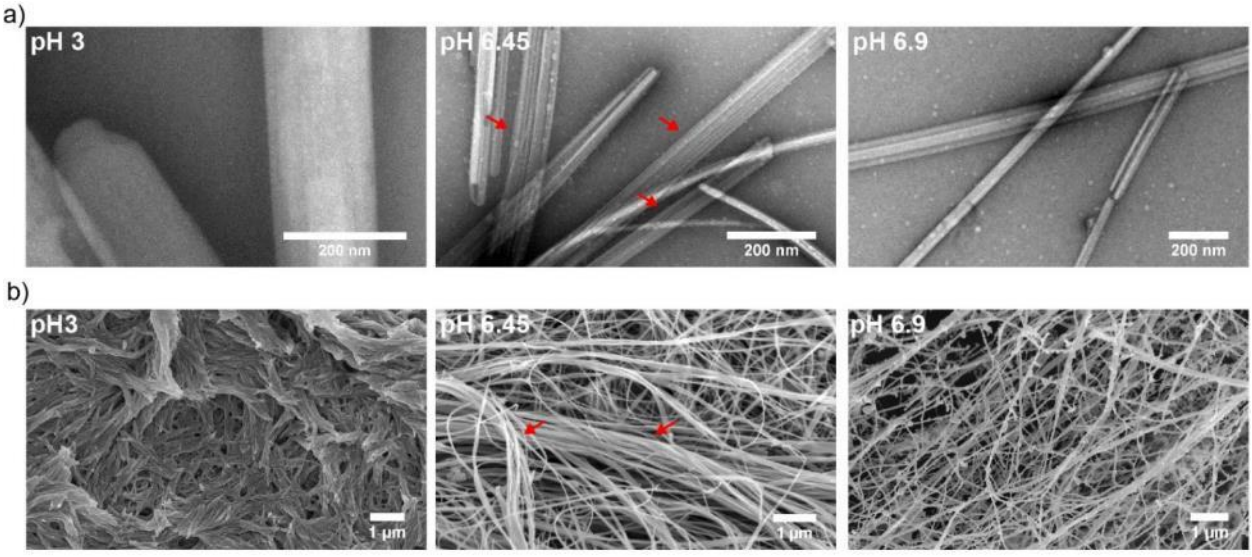


**Figure 2.6: Assembly after mixing short PA molecules of opposite charge**
(a) TEM with uranyl acetate negative-staining and (b) SEM prepared by critical point drying of the PA1/PA2 mixtures. Samples were aged for four days at pH 3, pH 6.45, and pH 6.9 in water. Arrows indicate locations where hierarchical bundling is visible.

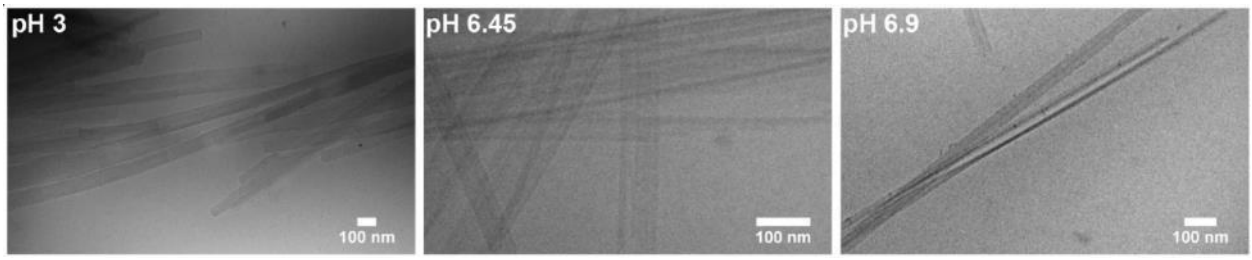


**Figure 2.7: Cryo-TEM images of the PA1/PA2 mixture aged 4 days.**

*Characterization of PA assemblies by x-ray scattering*

Next, *in situ* x-ray scattering of PA solutions was used to understand how intermolecular cohesion among molecules within primary assemblies drives the formation of hierarchical supramolecular superstructures. While TEM showed **PA1** formed wide structures at pH 3 and narrower ribbons at pH 6.45 (Figure 2.1c), the scattering patterns at pH 6.45 were dominated by the same set of diffraction peaks observed at pH 3 (Figure 2.9).

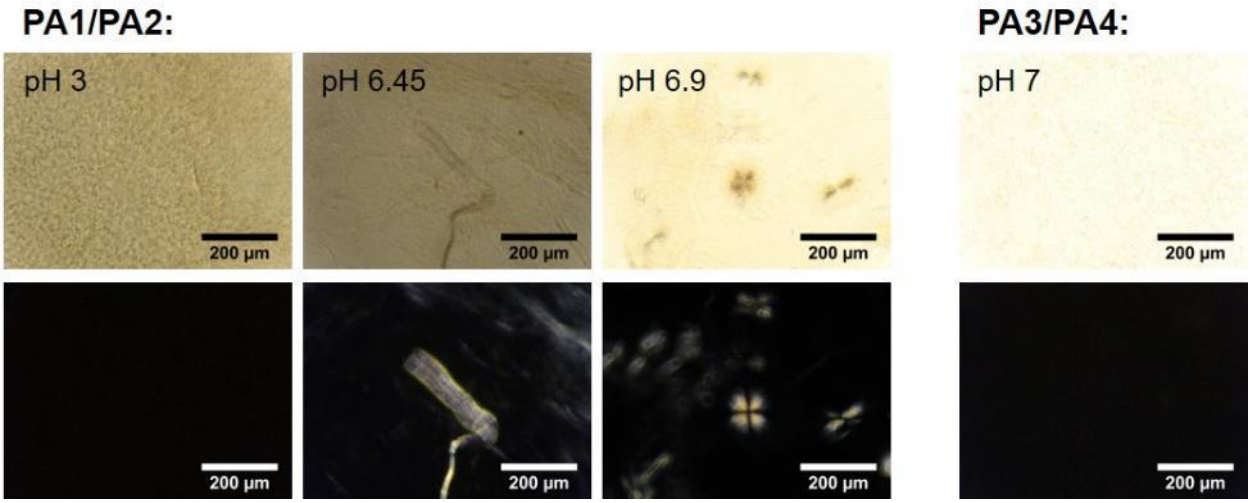


**Figure 2.8: Polarized optical microscopy of PA superstructures**
Optical microscopy of the **PA1**/**PA2** mixtures (pH 3, 6.45 and 6.9) and the **PA3**/**PA4** mixture (pH 7) under parallel polarizers (top row) and cross polarizers (bottom row).

**Table 2.1: WAXS and electron diffraction peaks for short PA assemblies**

| **PA1** | | | **PA1+PA2, 1 day** | | | **PA1+PA2, 4 days** | | |
|---|---|---|---|---|---|---|---|---|
| q ($nm^{-1}$) | d (nm) | Index | q ($nm^{-1}$) | d (nm) | Index | q ($nm^{-1}$) | d (nm) | Index |
| 1.4 | 4.36 | (001) | 1.8 | 3.49 | (001) | 12.9 | 0.49 | (100) |
| 2.9 | 2.19 | (002) | 5.3 | 1.19 | (003) | 15.1 | 0.41 | (110) |
| 4.3 | 1.46 | (003) | 10.3 | 0.61 | (010) | | | |
| 7.7 | 0.81 | (010) | 13.0 | 0.48 | (100) | | | |
| 8.2 | 0.77 | | 13.4 | 0.47 | | | | |
| 13.6 | 0.46 | (100) | 15.7 | 0.40 | (110) | | | |
| 14.7 | 0.43 | | 25.8 | 0.24 | (200) | | | |
| 15.5 | 0.41 | (020) | | | | | | |
| 15.8 | 0.40 | | | | | | | |
| 16.7 | 0.38 | | | | | | | |
| 17.3 | 0.36 | (110) | | | | | | |

A strong peak observed in the small angle region indicated a d-spacing of 4.36 nm. This is larger than the thickness expected for two extended **PA1** molecules stacked end-to-end, 3.58 nm, suggesting a roughly 0.8 nm spacing between each layer (Figure 2.11a; Table 2.1). To determine the packing of the PA molecules within these layers, selected area electron diffraction (SAED) of individual structures was used, which yielded diffraction spots consistent with the peaks observed

in the MAXS and WAXS regions, which in turn allowed us to index peaks (Figure 2.11b). This scattering pattern is consistent with hydrogen bonding **PA1** molecules aligned in strands parallel with the long axis ($\vec{a}$) of the structures. Within the rows, **PA1** molecules were spaced 0.48 nm apart in the axial direction—consistent with β-strand formation—and molecules in adjacent strands were separated by 0.85 nm ($\vec{b}$) offset at an angle of 74° (Figure 2.11a, inset; Figure 2.11b). At pH 6.45, the **PA2** SAXS pattern was consistent with a core-shell spherical structure with a 5.6 nm diameter (Figure 2.10).

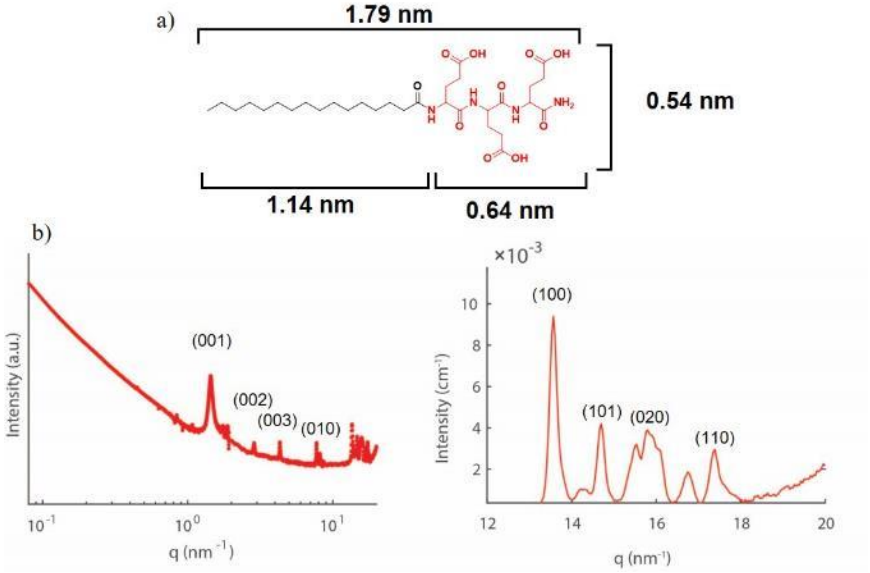


**Figure 2.9: X-ray scattering of short PA assemblies**
(a) Predicted molecular dimensions for **PA1** and (b) peak assignments for diffraction patterns produced by **PA1** at pH 3.

Immediately upon mixing **PA1** with **PA2** and readjusting the pH to 6.45, high-resolution TEM revealed a mixture of both ribbon-shaped structures and spherical micelles (Figure 2.5), presumably consisting of **PA1** and **PA2**, respectively. After aging for one day, superstructures of

bundled fibers emerged and observed a new x-ray scattering pattern appeared, distinct from either PA alone (Figure 2.11; Table 2.1).

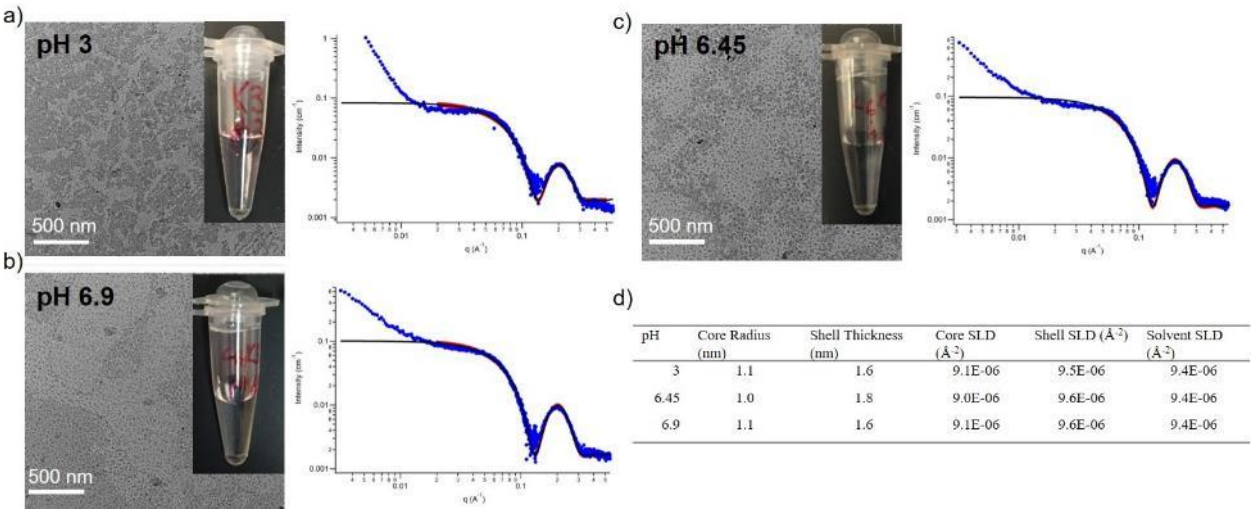


| pH | Core Radius (nm) | Shell Thickness (nm) | Core SLD (Å$^{-2}$) | Shell SLD (Å$^{-2}$) | Solvent SLD (Å$^{-2}$) |
|---|---|---|---|---|---|
| 3 | 1.1 | 1.6 | 9.1E-06 | 9.5E-06 | 9.4E-06 |
| 6.45 | 1.0 | 1.8 | 9.0E-06 | 9.6E-06 | 9.4E-06 |
| 6.9 | 1.1 | 1.6 | 9.1E-06 | 9.6E-06 | 9.4E-06 |

**Figure 2.10: Characterization of cationic short PA**
TEM, macroscopic appearance, and SAXS patterns for **PA2** at pH 3, 6.45, 6.9. Patterns were fit to a core shell sphere model giving micelle diameters of 5.4 nm, 5.6 nm, and 5.4 nm respectively.

Peaks in the SAXS and MAXS region broadened and shifted, corresponding to the thickness of PA molecule layers decreasing from 4.37 nm to 3.49 nm. The spacing between molecules in the axial direction ($\overrightarrow{\boldsymbol{a'}}$) increased slightly to 0.49 nm while the spacing between molecules in adjacent strands decreased to 0.61 nm ($\overrightarrow{\boldsymbol{b'}}$), indicating a significant change in molecular organization likely caused by redistribution of **PA2** monomers into the pre-existing **PA1** assemblies. TEM revealed increased PA fiber bundling after 4 days of aging (Figure 2.6a), while the scattering pattern of the mixtures continued to evolve as the structure of mixed supramolecular assemblies changed over four days. In the low-q region of the SAXS pattern, the slope increased as the PA assemblies continued to bundle, while the initial peak broadened and shifted toward the pre-mixing position.

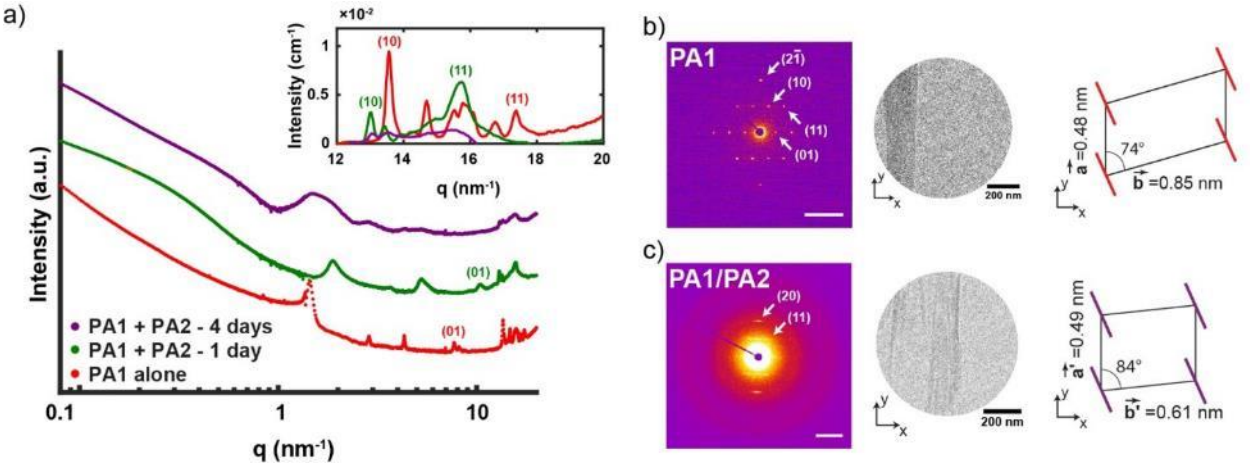


**Figure 2.11: X-ray scattering and electron diffraction characterization of PA superstructures**

(a) SAXS/MAXS/WAXS patterns for PA1 at t=4 days, PA1/PA2 mixture aged for 1 day, and PA1/PA2 mixture aged for 4 days at pH 6.45 in water, the inset figure expands the WAXS region; SAED scattering intensities of (b) **PA1** bilayers alone and of (c) **PA1**/**PA2** mixtures following aging for 4 days with TEM images of area used to acquire scattering pattern and a schematic showing spacing of molecules within the structures derived from the WAXS and SAED patterns. (SAED scale: q = 20 $nm^{-1}$)

In the WAXS region, peak positions remained unchanged but broadened significantly, suggesting the internal structure of the assemblies became more disordered. While SAED of thin nanofibers is technically challenging, the bundles that formed were wide enough to obtain diffraction patterns produced by aligned fibers within the hierarchical assembly. SAED showed the 0.49 nm d-spacing associated with hydrogen bonds among neighboring peptide backbones remained in the axial direction of the bundled fibers ($\vec{a'}$), while the angle between molecules in adjacent strands increased to 84° (Figure 2.11b). Continued changes in the supramolecular morphology between day 1 and day 4 suggest a two-step process where initial penetration of **PA2** into **PA1** assemblies is followed by narrowing of ribbon assemblies into fibers that form bundled superstructures. To determine the distribution of each PA component in the mixed fiber structures, we prepared mixed solutions at different molar ratios of the two PA molecules and aged them for

four days at pH 6.45. The dominant structure transitions from wide assemblies to ribbons with the addition of 20 mol% PA2 molecules; however, bundles formed only when the molar ratio fractions of **PA1** and **PA2** were near equal (40% to 60% of each PA). At lower **PA1** fractions, only disperse fibers and micelles remained (Figure 2.12). This may be because when a small number of **PA2** molecules were available in the system, penetration of these molecules into the **PA1** assemblies transitioned the structures from layers to ribbons. Assemblies could bundle with one another only when **PA1** charge was neutralized by a similar concentration of **PA2** within the assemblies.

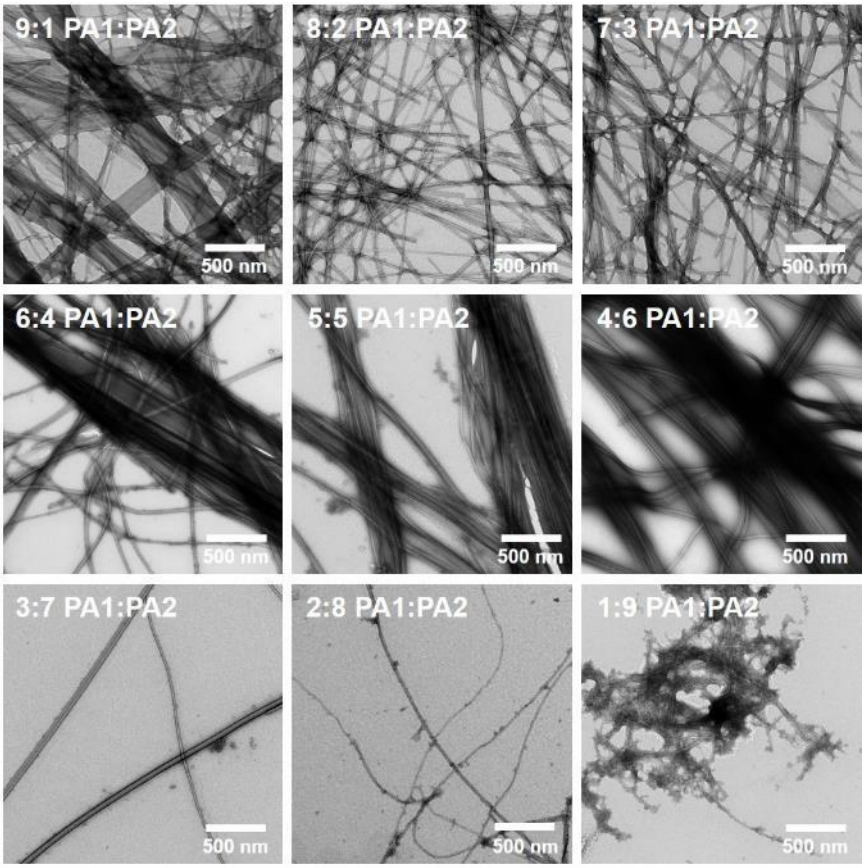


**Figure 2.12: Anionic and cationic short PAs mixed at varying ratios**
TEM micrographs of **PA1/PA2** mixtures prepared at the indicated molar ratios. pH was adjusted to 6.45 after mixing and samples were aged for 4 days prior to imaging.

*Controlling superstructure formation by tuning intermolecular cohesion*

To confirm that controlling intermolecular cohesion within the nanostructure is critical for hierarchical superstructure assembly, two additional PA pairs were synthesized: **PA3** and **PA4** (Figure 2.14a; Figure 2.23e-f) to increase cohesion by adding a β-sheet domain, and **PA5** and **PA6** (Figure 2.14b; Figure 2.23g-h) to decrease cohesion by increasing electrostatic repulsion among charged termini in PA molecules. Previous work suggests cohesion within supramolecular assemblies significantly affects monomer exchange kinetics. For example, cohesive β-sheet forming PA molecules were found to begin heterogeneous exchange of fiber domains over several hours, but the formation of homogenous mixed fibers did not occur within 48 hours of mixing.[96] On the other hand, more weakly cohesive supramolecular assemblies exchange quickly and can achieve completely homogeneous assemblies within hours of mixing.[156] Titration curves of the anionic PA molecules showed no buffering region for PA3 and a buffering region near pH 5.5 to 6.5 for **PA5**, slightly lower than that of **PA1** (Figure 2.13).

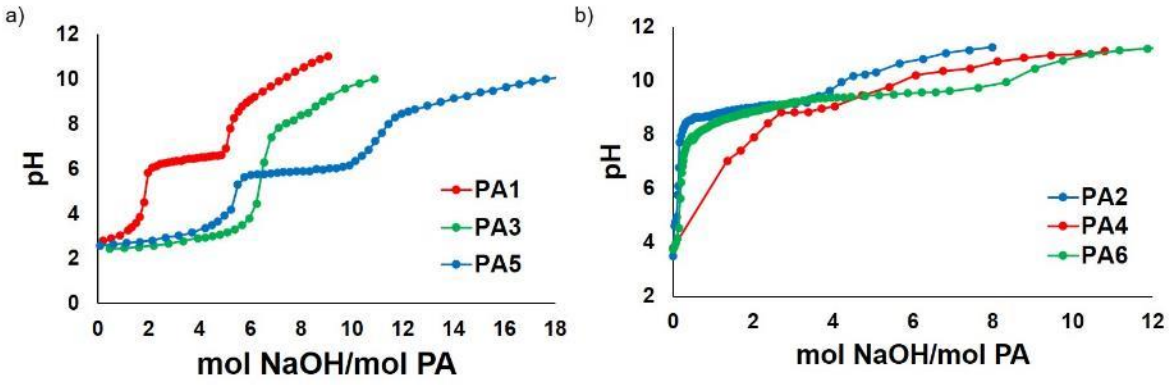


**Figure 2.13: PA titration curves**
(a) Titration curves of **PA3** and **PA5**, shown next to **PA1. (b)** Titration curves of **PA4** and **PA6**, shown next to **PA2.**

Stronger intermolecular cohesion yielded fibers in the pH range of 2.5 to 10 for **PA3**, while **PA5** formed flat structures that transitioned to cylindrical fibers at pH 5.9 and then no visible structures as pH was increased during buffering (Figure 2.13). The anionic samples were then mixed with their cationic counterparts, at neutral pH for **PA3** and at the middle of the buffering region (pH 5.9) for **PA5**. At the pH values tested, the positively charged **PA4** formed fibers and **PA6** did not form defined structures (Figure 2.13). After mixing and aging for 4 days, SEM showed no bundling in the PA mixtures with domains programmed to form β-sheets and the system remained a network of separated PA fibers (Figure 2.14c). With decreased intermolecular cohesion, **PA5** and **PA6** mixtures formed tightly packed fiber bundles, confirming dynamic monomer rearrangement is necessary for superstructures to form (Figure 2.14c).

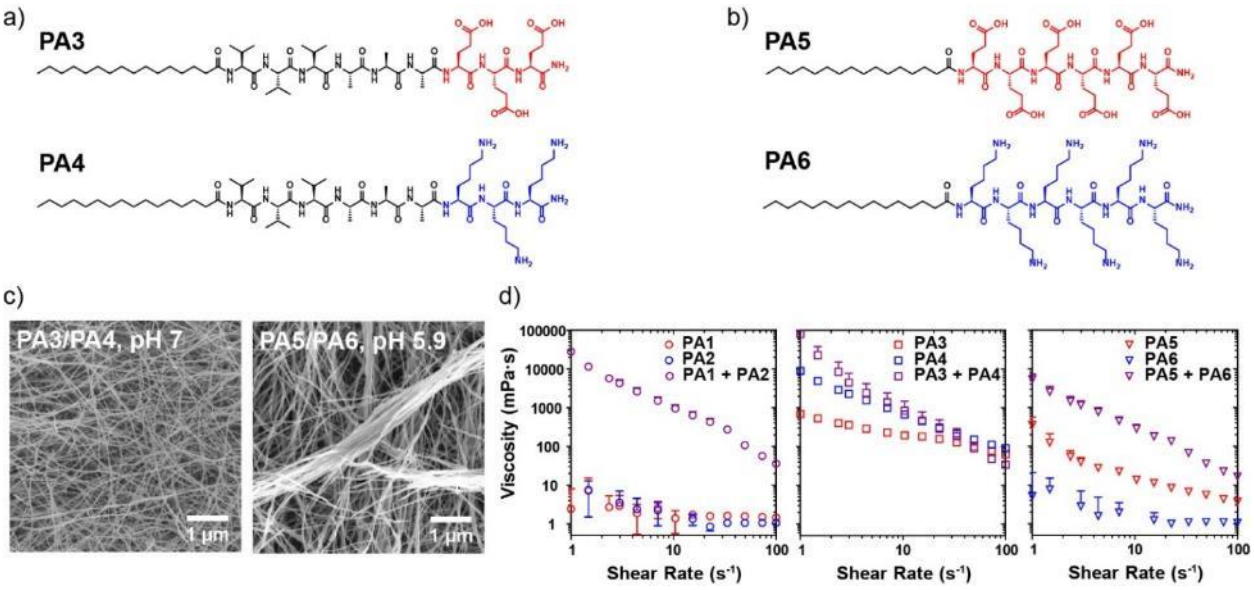


**Figure 2.14: PA mixtures with variable intermolecular cohesion**
(a) Molecular structures of **PA3** and **PA4** and of (b) **PA5** and **PA6**; (c) SEM of the **PA3**/**PA4** mixture at pH 7, and the **PA5**/**PA6** mixture at pH 5.9 dissolved in water, aged for 4 days, and cast on a polystyrene sponge for critical point drying and imaging; and (d) viscosity measurements of solutions of all six PA molecules tested and their mixtures with complementary charges.

In all three systems tested, mixing oppositely charged PA assemblies increased the viscosity of the supramolecular network (Figure 2.14d). Surprisingly, while PA molecules programmed to form β-sheets had much higher viscosities than any *N*-palmitoyl tripeptide or *N*-palmitoyl hexapeptide tested prior to mixing, mixing oppositely charged molecules yielded similarly viscous networks despite large differences in intermolecular cohesion (Figure 2.14d). This result suggests that superstructure formation increased solution viscosity as effectively as increasing intermolecular cohesion with the addition of a β-sheet peptide sequence.

X-ray scattering was then used to determine how intermolecular interactions affected superstructure formation. In highly cohesive fibers, molecular rearrangement was not observed. Prior to mixing, the SAXS patterns for **PA3** and **PA4** had low-q slopes of -1.1 and -1.4 respectively (Figure 2.15a). A strong WAXS peak at a 0.46 nm d-spacing showed both molecules formed assemblies with β-sheet domains. Mixing yielded an increase in slope in the low-q region to -2.1, while the peak position remained unchanged (Figure 2.15a). The position of the β-sheet peak was likewise unaffected by mixing (though intensity decreased as **PA3** concentration was decreased by half), suggesting the complete redistribution of molecules observed in **PA1**/**PA2** mixtures did not occur. On the other hand, molecules with more charged groups showed strong morphological changes within one day of mixing oppositely charged PA molecules. Prior to mixing, **PA5** molecules dissolved at pH 5.9 produced a peak in the SAXS region corresponding to an interlayer spacing of 6.74 nm and strong peaks in the MAXS and WAXS regions (Figure 2.15b). At this pH, **PA6** did not assemble and no x-ray scattering was observed. After mixing and readjusting pH to 5.9, the observed peaks in the SAXS region shifted to the right, corresponding to contraction of the spacing to 5.16 nm. In the WAXS region, all but one of the peaks disappeared after mixing and the remaining peak shifted from a d-spacing of 0.50 to 0.48 nm. This significant change in order

within the assemblies is consistent with large-scale redistribution of molecules following mixing as observed in **PA1**/**PA2** mixture.

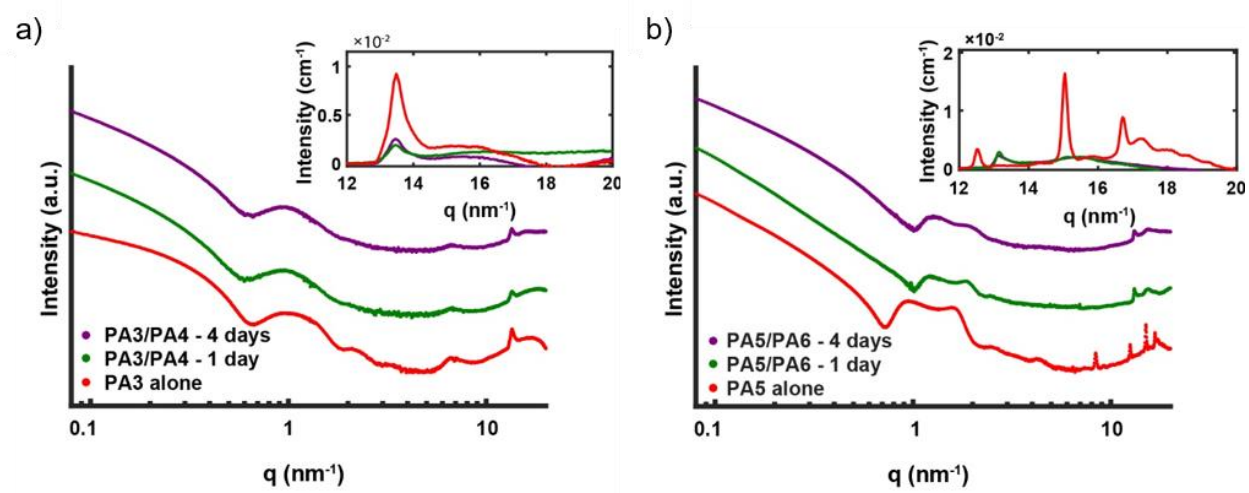


**Figure 2.15: X-ray scattering of PA mixtures with variable intermolecular cohesion**
(a) SAXS/MAXS and WAXS (inset) scans for **PA3** after 4 days, **PA3**/**PA4** mixture after 1 day, and **PA3**/**PA4** mixture after 4 days all at pH 7.0; (b) SAXS/MAXS and WAXS (inset) scans for **PA5** after 4 days, **PA5**/**PA6** mixture after 1 day, and **PA5**/**PA6** mixture after 4 days all at pH 5.9.

*Molecular redistribution leads to superstructure formation*

In order to demonstrate that molecular redistribution was necessary for hierarchical assembly, Fourier transform infrared spectroscopy (FTIR) absorbance spectra of mixed and aged PA solutions of assemblies with opposite charge and dissolved in deuterated water were obtained. While other spectroscopic techniques can indicate proximity of molecules to one another, monitoring deconvoluted peaks of FTIR spectra provides a label-free technique to track changes in intermolecular interactions that correlate with molecular redistribution into mixed assemblies.

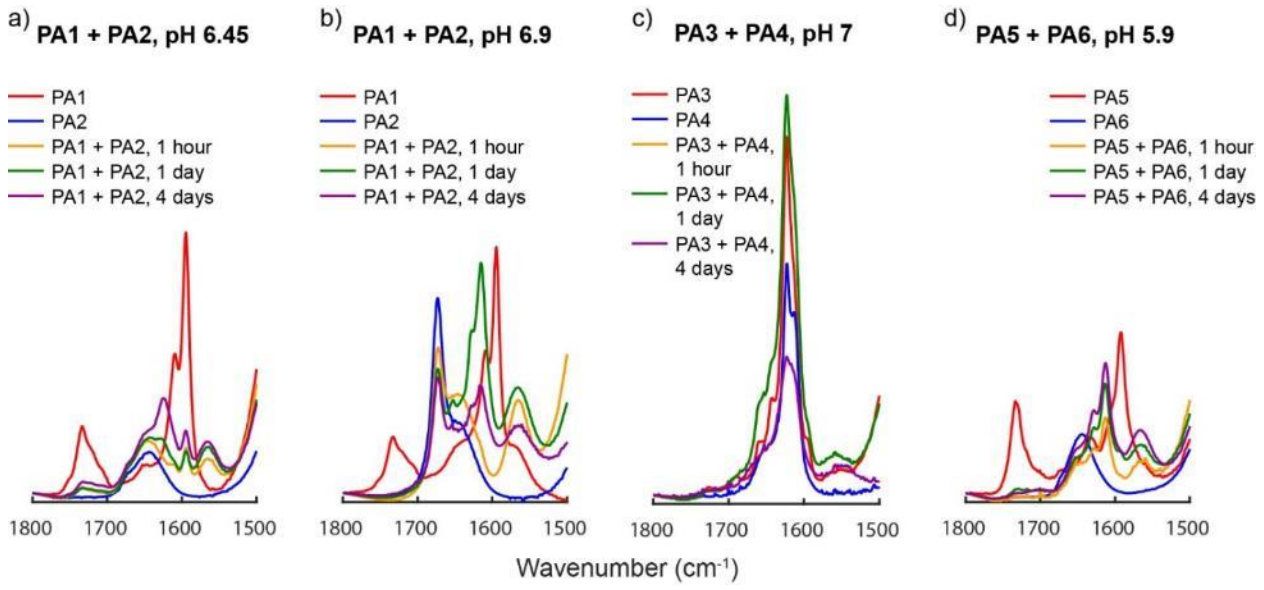


**Figure 2.16: Characterization of superstructure assembly by FTIR**
FTIR absorbance spectra for solutions of **PA1** and **PA2** after 4 days, **PA1**/**PA2** mixture after 1 hour, **PA1**/**PA2** mixture after 1 day, and **PA1**/**PA2** mixture after 4 days all at (a) pH 6.45 and (b) pH 6.9; (c) FTIR absorbance spectra for solutions of **PA3** and **PA4** after 4 days, **PA3**/**PA4** mixture after 1 hour, **PA3**/**PA4** mixture after 1 day, and **PA3**/**PA4** mixture after 4 days all at pH 7.0 ; (d) FTIR absorbance spectra for solutions of **PA5** and **PA6** after 4 days, **PA5**/**PA6** mixture after 1 hour, **PA5**/**PA6** mixture after 1 day, and **PA5**/**PA6** mixture after 4 days all at pH 5.9.

Prior to mixing, PA1 exhibited a strong peak at 1595 $cm^{-1}$, which is similar to the $COO^-$ band previously reported for poly(glutamic acid),[157] a smaller peak in the amide I′ band at 1612 $cm^{-1}$, and a complex band at 1735-1726 $cm^{-1}$ indicative of protonated acid groups. **PA2** exhibited a broader peak centered at 1642 $cm^{-1}$ as previously reported for poly(lysine)[157] with a sharp peak at 1668 $cm^{-1}$, which strengthened with increasing pH. When mixed at pH 3, no new bands appeared, suggesting molecules of opposite charge remained in separate assemblies (Figure 2.17). In contrast, 1 hour after mixing at pH 6.45, a new peak emerged at 1565 $cm^{-1}$ which is consistent with the formation of salt bridges between lysine and glutamic acid side chains,[158] indicating aggregation of the oppositely charged assemblies shortly after mixing. Peaks remained at 1732 $cm^{-1}$ and 1595 $cm^{-1}$ suggesting both protonated and deprotonated glutamic acid side chains

remained present. A peak in the amide I′ band at 1624 $cm^{-1}$appeared one day after mixing and was stronger after four days, indicating the formation of β-sheet-like domains due to redistribution of complementary PA molecules into combined assemblies (Figure 2.16a; Figure 2.18). The development of this peak over several days suggests monomer redistribution is a slow process, delaying the formation of superstructure bundles. When mixed at a higher pH of 6.9, peaks at 1734 $cm^{-1}$ and 1595 $cm^{-1}$ were replaced with a strong peak at 1564 $cm^{-1}$, suggesting the formation of salt bridges by the **PA1** side chains. The strong peak associated with **PA2** at 1673 $cm^{-1}$ remained after mixing, and though initially absent, the peak associated with **PA1** at 1612 $cm^{-1}$ returned after 1 day (Figure 2.16b; Figure 2.19). A small peak in the range of the amide I′ band at 1629 $cm^{-1}$ appeared after mixing, which may indicate redistribution of the highly charged monomers into mixed assemblies. Also after mixing, the COOH peak disappeared completely, suggesting all glutamic acid groups were deprotonated. Thus, the observation that bundles are not prone to form at pH 6.9, but do form robustly at pH 6.45, suggests that superstructure formation encounters mechanistic barriers when assemblies being mixed are highly charged. The nature of the barrier could be electrostatic “vitrification” among oppositely charged assemblies that prevents redistribution of molecules into a superstructure. This would happen even though the individual assemblies prior to mixing do have sufficiently low cohesion to exhibit significan supramolecular dynamics. In contrast, at pH 6.45, FTIR showed that protonated glutamic acid residues remained and in this case superstructures did form readily. At this value of pH, the barrier imposed by electrostatic interaction among oppositely charged assemblies would be lower, thus enabling redistribution of molecules into the thermodynamically favorable superstructures observed.

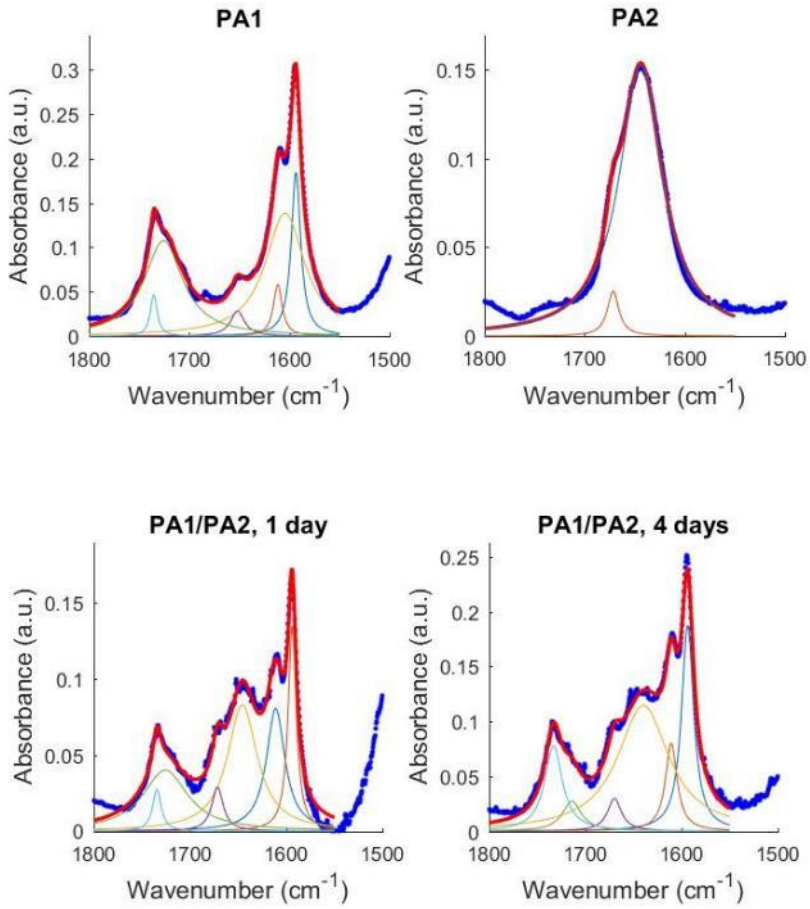


| | Position ($cm^{-1}$) | | | | | | Height (a.u.) | | | | | | Width ($cm^{-1}$) | | | | | |
|---|---|---|---|---|---|---|---|---|---|---|---|---|---|---|---|---|---|---|
| Peak | 1 | 2 | 3 | 4 | 5 | 6 | 1 | 2 | 3 | 4 | 5 | 6 | 1 | 2 | 3 | 4 | 5 | 6 |
| PA1 | 1735 | 1726 | 1652 | 1611 | 1604 | 1593 | 0.047 | 0.108 | 0.028 | 0.058 | 0.139 | 0.184 | 8.1 | 46.7 | 16.8 | 10.7 | 47.9 | 11.4 |
| PA2 | | | 1672 | 1644 | | | | | 0.025 | 0.152 | | | | | 14.0 | 52.3 | | |
| PA1/PA2, 1d | 1734 | 1726 | 1671 | 1646 | 1611 | 1594 | 0.028 | 0.040 | 0.029 | 0.083 | 0.081 | 0.135 | 10.6 | 56.9 | 14.5 | 37.9 | 23.4 | 10.2 |
| PA1/ PA2, 4d | 1733 | 1714 | 1670 | 1640 | 1611 | 1594 | 0.078 | 0.027 | 0.030 | 0.115 | 0.080 | 0.187 | 22.3 | 23.9 | 17.5 | 64.6 | 14.7 | 15.3 |

**Figure 2.17: FTIR spectra for PA mixtures at pH 3**
Deconvolution of FTIR spectra collected for **PA1**, **PA2** and

their mixtures at pH 3. Plots show collected data shown (blue), fit to data (red), and individual deconvoluted peaks. Table below shows relative peak positions, heights and areas for each plotted peak.

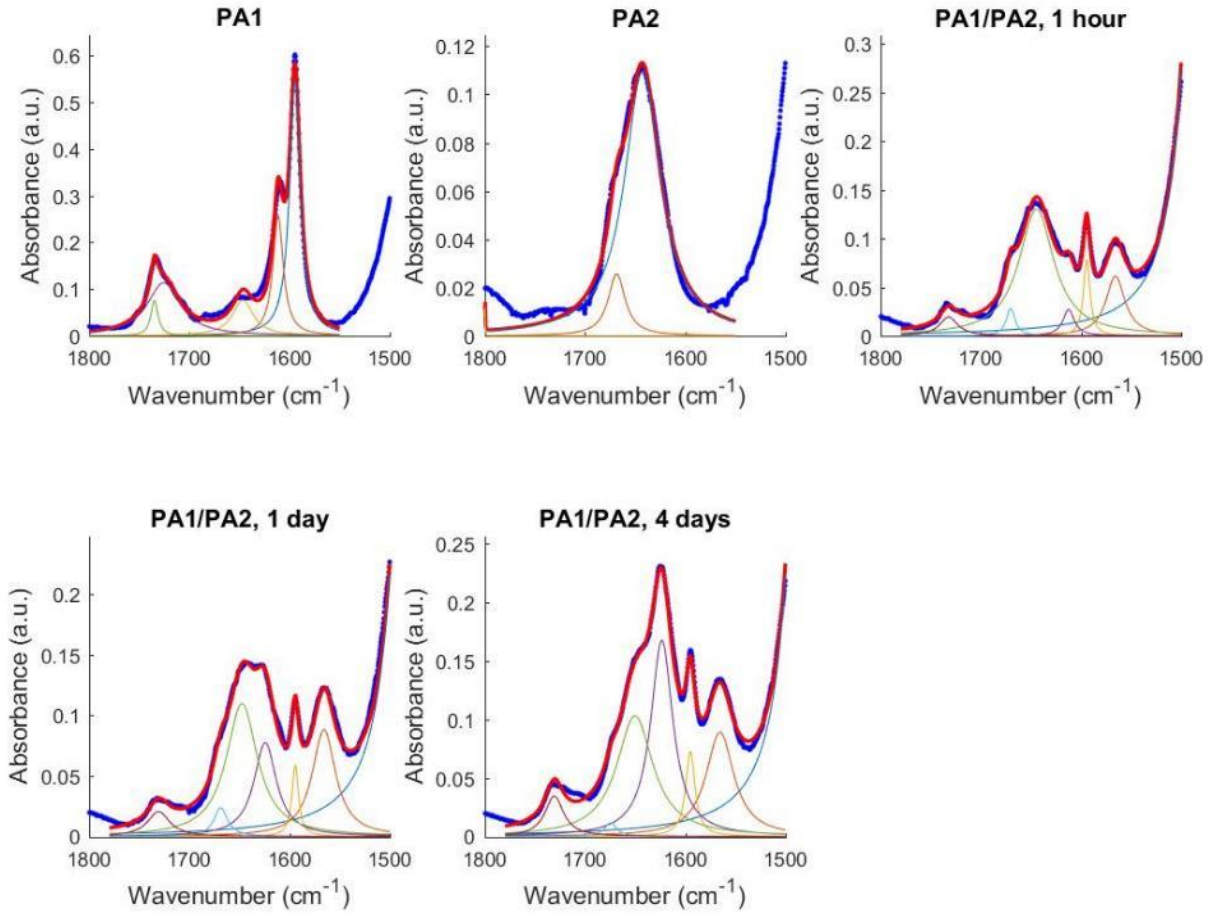


| | Position ($cm^{-1}$) | | | | | | Height (a.u.) | | | | | | Width (cm-1) | | | | | |
|---|---|---|---|---|---|---|---|---|---|---|---|---|---|---|---|---|---|---|
| Peak | 1 | 2 | 3 | 4 | 5 | 6 | 1 | 2 | 3 | 4 | 5 | 6 | 1 | 2 | 3 | 4 | 5 | 6 |
| PA1 | 1735 | 1726 | 1647 | 1611 | 1595 | | 0.075 | 0.114 | 0.076 | 0.257 | 0.547 | | 8.6 | 40.0 | 25.2 | 12.6 | 13.0 | |
| PA2 | 1800 | 1668 | 1643 | | | | 0.017 | 0.026 | 0.110 | | | | 0.5 | 20.5 | 43.9 | | | |
| PA1/PA2, 1h | 1732 | 1670 | 1644 | 1612 | 1594 | 1566 | 0.019 | 0.028 | 0.130 | 0.027 | 0.078 | 0.061 | 21.9 | 10.6 | 42.4 | 13.6 | 7.9 | 22.9 |
| PA1/PA2, 1d | 1731 | 1669 | 1648 | 1624 | 1594 | 1566 | 0.021 | 0.024 | 0.110 | 0.078 | 0.059 | 0.088 | 26.8 | 16.4 | 37.9 | 27.4 | 7.9 | 28.5 |
| PA1/ PA2, 4d | 1731 | 1674 | 1650 | 1623 | 1595 | 1565 | 0.035 | 0.012 | 0.103 | 0.168 | 0.073 | 0.089 | 22.4 | 14.6 | 44.2 | 27.0 | 11.3 | 33.8 |

**Figure 2.18: FTIR spectra for PA mixtures at pH 6.45**

Deconvolution of FTIR spectra collected for **PA1**, **PA2** and their mixtures at pH 6.45. Plots show collected data shown (blue), fit to data (red), and individual deconvoluted peaks. Table below shows relative peak positions, heights and areas for each plotted peak.

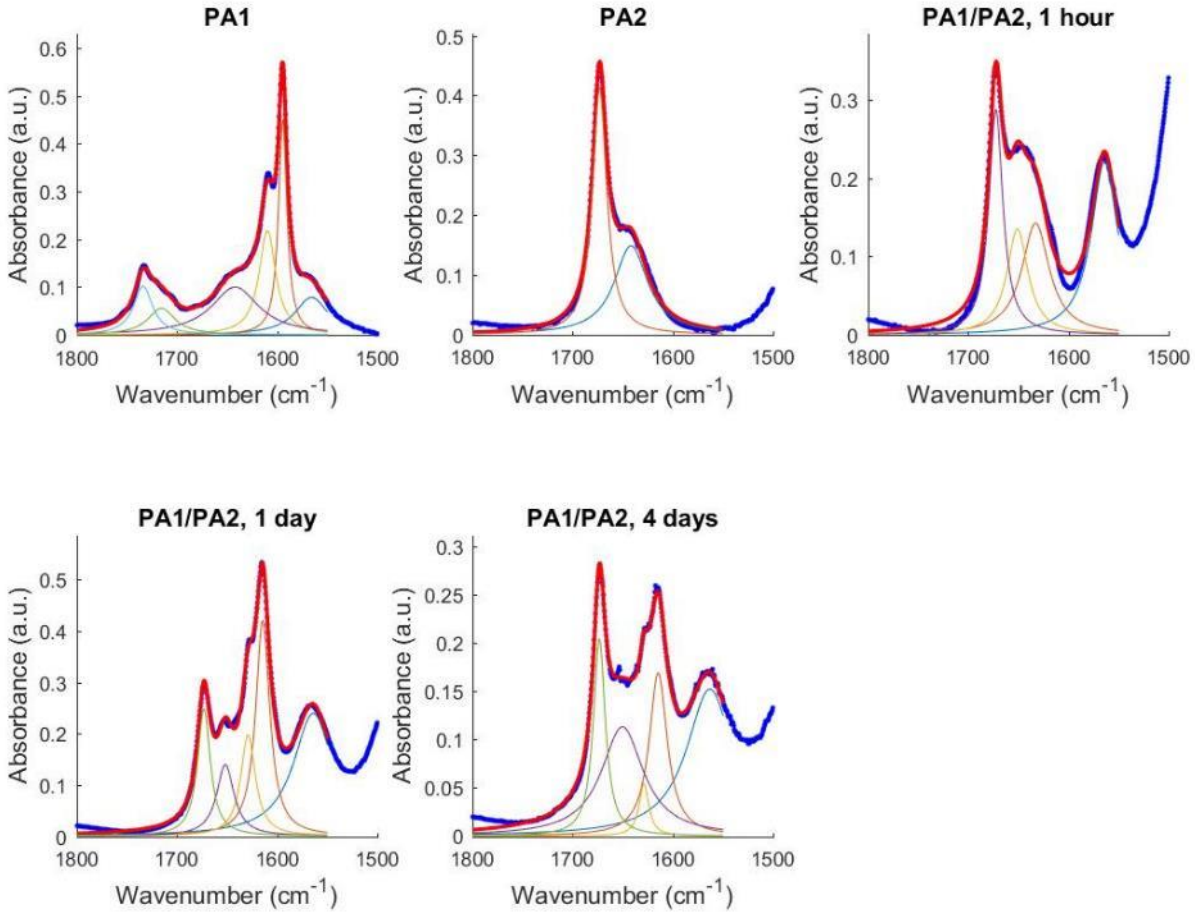


| | Position ($cm^{-1}$) | | | | | | Height (a.u.) | | | | | | Width ($cm^{-1}$) | | | | | |
|---|---|---|---|---|---|---|---|---|---|---|---|---|---|---|---|---|---|---|
| Peak | 1 | 2 | 3 | 4 | 5 | 6 | 1 | 2 | 3 | 4 | 5 | 6 | 1 | 2 | 3 | 4 | 5 | 6 |
| PA1 | 1734 | 1716 | 1642 | 1610 | 1594 | 1610 | 0.102 | 0.056 | 0.100 | 0.218 | 0.451 | 0.218 | 22.9 | 32.8 | 58.0 | 20.2 | 10.1 | 20.2 |
| PA2 | | 1673 | 1642 | | | | | 0.413 | 0.149 | | | | 0.0 | 17.3 | 40.8 | | | |
| PA1/PA2, 1h | | 1672 | 1651 | 1633 | | 1564 | | 0.287 | 0.135 | 0.142 | | 0.222 | 0.0 | 17.0 | 25.6 | 33.4 | | 32.5 |
| PA1/PA2, 1d | | 1673 | 1652 | 1629 | 1614 | 1564 | | 0.248 | 0.139 | 0.197 | 0.420 | 0.240 | 0.0 | 15.5 | 21.1 | 17.8 | 17.1 | 48.0 |
| PA1/ PA2, 4d | | 1673 | 1650 | 1629 | 1615 | 1563 | | 0.205 | 0.113 | 0.054 | 0.169 | 0.152 | 0.0 | 14.5 | 51.1 | 11.8 | 21.9 | 56.5 |

**Figure 2.19: FTIR spectra for PA mixtures at pH 6.9**

Deconvolution of FTIR spectra collected for **PA1**, **PA2** and their mixtures at pH 6.9. Plots show collected data shown (blue), fit to data (red), and individual deconvoluted peaks. Table below shows relative peak positions, heights and areas for each plotted peak.

We compared the time dependent behavior of the **PA1**/**PA2** system at pH 6.45 to the strongly cohesive **PA3**/**PA4** and the weakly cohesive **PA5**/**PA6**. **PA3** and **PA4** molecules with

programmed β-sheet sequences both displayed strong amide I′ peaks at 1613 cm-1, 1623 $cm^{-1}$, and 1647 $cm^{-1}$, but new bands were not observed four days after mixing, indicating the continued presence of strongly cohesive β-sheet hydrogen bonds (Figure 2.16c; Figure 2.20). Prior to mixing, **PA5** and **PA6** absorbed at similar bands as the *N*-palmitoyl tripeptides described here. A strong salt-bridge peak emerged at 1562 $cm^{-1}$ within one hour of mixing the solutions, while a weak COOH band remained near 1730 $cm^{-1}$. Also within one hour, a small amide I′ peak emerged at 1630 $cm^{-1}$, which grew considerably stronger after one day and maintained its intensity through day 4. The faster emergence of the β-sheet associated peak in **PA5**/**PA6** assemblies relative to **PA1**/**PA2** assemblies may be correlated with faster redistribution of the monomers into mixed fibers that form robust superstructures (Figure 2.16d; Figure 2.21).

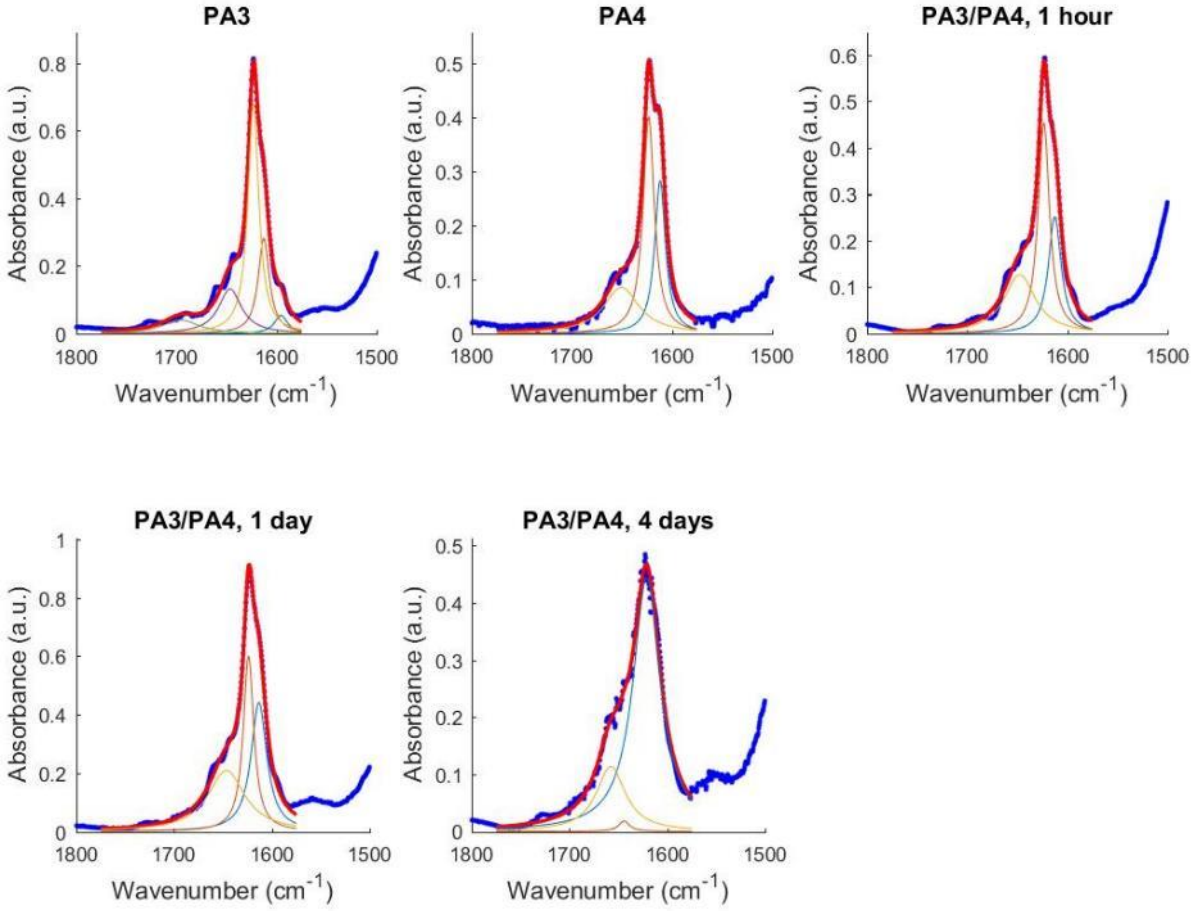


| | Position ($cm^{-1}$) | | | | | Height (a.u.) | | | | | Width ($cm^{-1}$) | | | | |
|---|---|---|---|---|---|---|---|---|---|---|---|---|---|---|---|
| Peak | 1 | 2 | 3 | 4 | 5 | 1 | 2 | 3 | 4 | 5 | 1 | 2 | 3 | 4 | 5 |
| PA3 | 1696 | 1646 | 1623 | 1613 | 1595 | 0.040 | 0.132 | 0.680 | 0.281 | 0.054 | 44.5 | 27.9 | 13.2 | 13.5 | 16.1 |
| PA4 | | 1650 | 1623 | 1612 | | | 0.086 | 0.400 | 0.282 | | | 43.0 | 13.6 | 13.0 | |
| PA3/PA4, 1h | | 1647 | 1623 | 1613 | | | 0.127 | 0.454 | 0.252 | | | 38.0 | 13.8 | 15.4 | |
| PA3/PA4, 1d | | 1647 | 1624 | 1613 | | | 0.209 | 0.600 | 0.441 | | | 45.9 | 13.0 | 19.6 | |
| PA3/PA4, 4d | | 1656 | 1623 | 1609 | | | 0.125 | 0.411 | 0.082 | | | 40.2 | 32.1 | 12.1 | |

**Figure 2.20: FTIR spectra of strongly cohesive PA assemblies**

Deconvolution of FTIR spectra collected for **PA3**, **PA4** and their mixtures at pH 7. Plots show collected data shown (blue), fit to data (red), and individual deconvoluted peaks. Table below shows relative peak positions, heights and areas for each plotted peak.

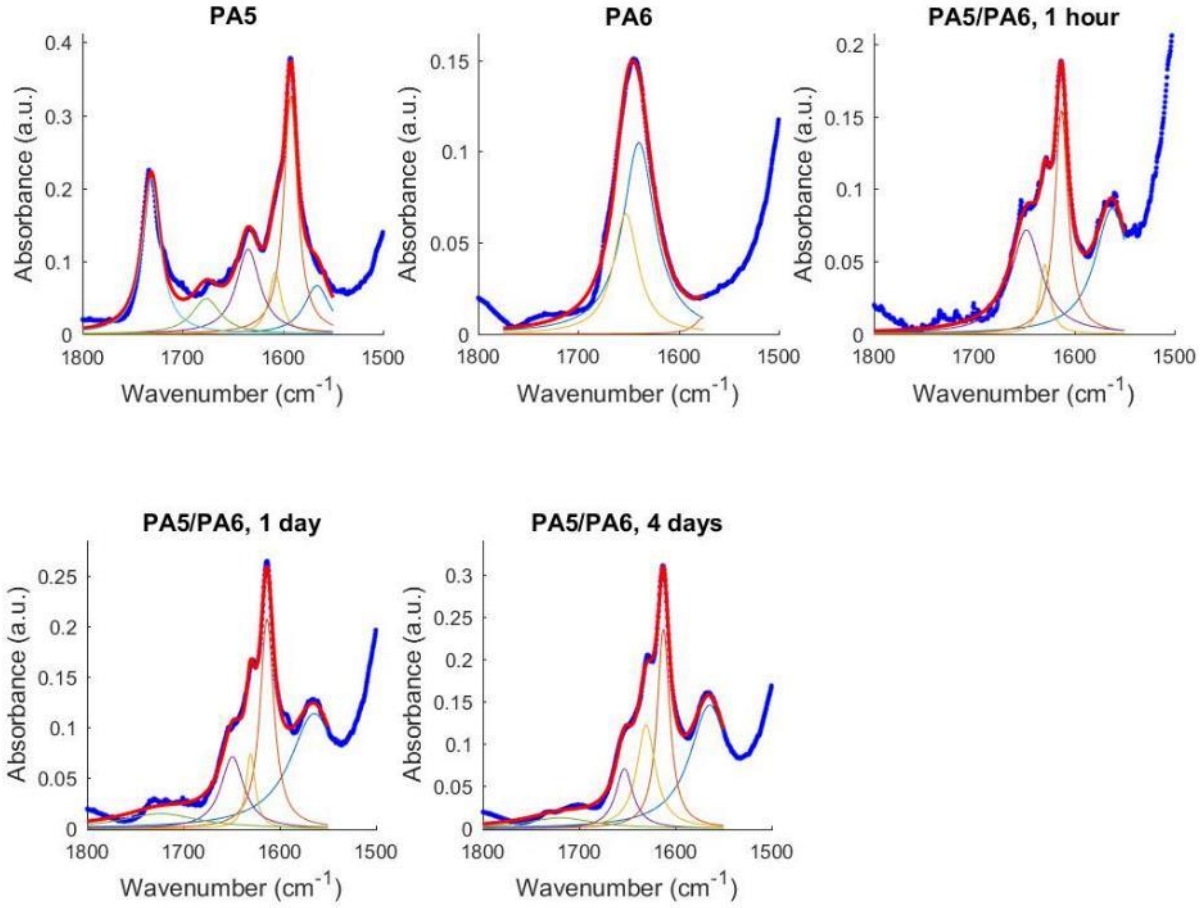


| | Position ($cm^{-1}$) | | | | | | Height (a.u.) | | | | | | Width ($cm^{-1}$) | | | | | |
|---|---|---|---|---|---|---|---|---|---|---|---|---|---|---|---|---|---|---|
| Peak | 1 | 2 | 3 | 4 | 5 | 6 | 1 | 2 | 3 | 4 | 5 | 6 | 1 | 2 | 3 | 4 | 5 | 6 |
| PA1 | 1731 | 1676 | 1635 | 1608 | 1592 | 1566 | 0.214 | 0.049 | 0.116 | 0.084 | 0.327 | 0.066 | 21.5 | 34.0 | 28.7 | 15.1 | 16.6 | 30.6 |
| PA2 | | 1659 | 1643 | 1539 | | | | 0.030 | 0.143 | 0.033 | | | | 12.1 | 15.8 | 42.0 | | |
| PA1/PA2, 1h | | 1648 | 1629 | 1613 | | 1562 | | 0.072 | 0.048 | 0.154 | | 0.087 | | 37.1 | 12.1 | 15.8 | | 42.0 |
| PA1/PA2, 1d | 1724 | 1649 | 1630 | 1613 | | 1564 | 0.071 | 0.074 | 0.207 | 0.114 | | 0.114 | 98.3 | 28.9 | 11.5 | 17.4 | | 61.7 |
| PA1/ PA2, 4d | 1720 | 1653 | 1630 | 1612 | | 1564 | 0.070 | 0.122 | 0.235 | 0.146 | | 0.146 | 84.5 | 21.9 | 23.5 | 15.8 | | 50.2 |

**Figure 2.21: FTIR spectra of weakly cohesive PA assemblies**

Deconvolution of FTIR spectra collected for **PA5**, **PA6** and their mixtures at pH 5.9. Plots show collected data shown (blue), fit to data (red), and individual deconvoluted peaks. Table below shows relative peak positions, heights and areas for each plotted peak.

These results indicate that redistribution of molecules by exchange among supramolecular assemblies into mixed charge structures with more cohesive primary interactions was necessary

for superstructure formation. Only **PA1**/**PA2** and **PA5**/**PA6** assembled into hierarchical structures at an intermediate ionization state because their molecules were not trapped in highly cohesive structures and were therefore able to redistribute into even more cohesive assemblies. We hypothesize that oppositely charged PA assemblies were first attracted to one another electrostatically (Figure 2.22a). Because the cohesive interactions among the molecules were weak, molecules exchanged among the assemblies, decreasing electrostatic repulsion among the molecules within the structures (Figure 2.22b). As the molecules redistributed the surface charge of the assemblies decreased and bundled superstructures formed (Figure 2.22c).

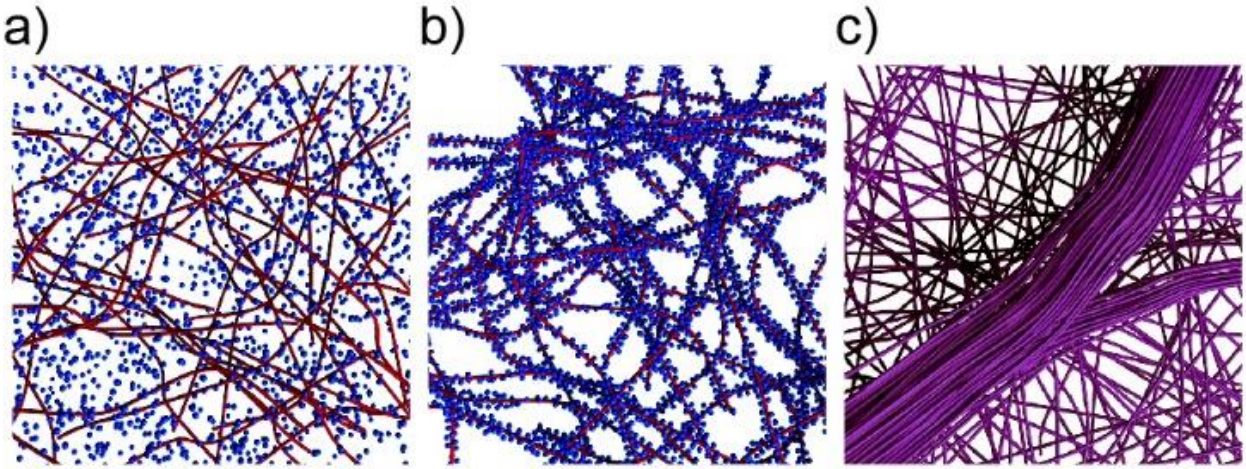


**Figure 2.22: Schematic of superstructure formation**
Representation of proposed superstructure formation where (a) high-aspect-ratio **PA1** assemblies (red) and **PA2** micelles (blue) are mixed and (b) the oppositely charged assemblies are attracted to one another. Over four days, the molecules redistribute forming (c) mixed fibers containing both **PA1** and **PA2** (purple) which form hierarchical bundles.

In contrast, strong cohesive interactions among molecules within PA1 assemblies at pH 3 or within PA3 assemblies at neutral pH limited molecular redistribution between the structures, so mixed assemblies did not form and bundling did not occur. Finally, while mixed structures formed from **PA1**/**PA2** at pH 6.9, intermolecular cohesion among these assemblies was weaker than at pH

6.45, which limited the formation of high-aspect ratio structures that could bundle with one another to form large superstructures. These results demonstrate that in short peptide model systems, ionization state and hydrogen bonding can determine superstructure formation by controlling molecular redistribution among supramolecular assemblies.

## 2.4. Conclusions

This work shows that the ability of molecules in large assemblies to redistribute in space is mechanistically important to create highly cohesive superstructures. By focusing on pairs of assemblies with molecules of opposite charge, the study deomonstrates that fibrillar superstructures form only in those systems in which molecular exchange dynamics yields heterogeneous assemblies with positively and negatively charged components. This mechanism to build superstructures from supramolecular assemblies offers a strategy to control physical properties of soft matter, and in this study significant changes in viscosity were observed which are important in processing of supramolecular materials to create 3D structures. This led to the conclusion that such hierarchical structures are formed by self-optimization of electrostatic structure among oppositely charged molecules “within” and also “between” the assemblies. Finally, these results show that limited cohesion is a necessary but not sufficient condition to readily form superstructures through redistribution since systems may encounter kinetic barriers as a result of high initial charge densities.

## 2.5. Materials and Methods

*PA synthesis and purification:* All PA molecules were synthesized using standard Fmoc synthesis and purified by reverse phase high performance liquid chromatography (HPLC) as previously reported.[128] The purity of the peptides was confirmed by liquid chromatography - electrospray ionization mass spectrometry in positive mode (ESI-MS, Agilent 6510 Q-TOF).

*Titrations and sample preparation:* Titrations were performed in aqueous solutions at concentrations of 0.05 wt%. Samples were adjusted with 1 M hydrochloric acid (HCl) to pH 2 and then 0.1M sodium hydroxide (NaOH) was titrated into the solutions. The pH was measured using a Mettler Toledo FiveEasy Plus FEP20 pH meter, which was calibrated with buffer solutions at pH values of 4, 7 and 10 prior to each titration. For characterization, PA molecules were in aqueous solutions as pH was adjusted using the above titration procedure, followed by the addition of a 1 M NaCl solution to obtain a 75 mM NaCl sample solution. For mixtures, samples were pH adjusted separately in water and then mixed at equal volumes. pH was readjusted to the desired value if necessary, followed by the addition of NaCl as above. Mixtures were aged at room temperature.

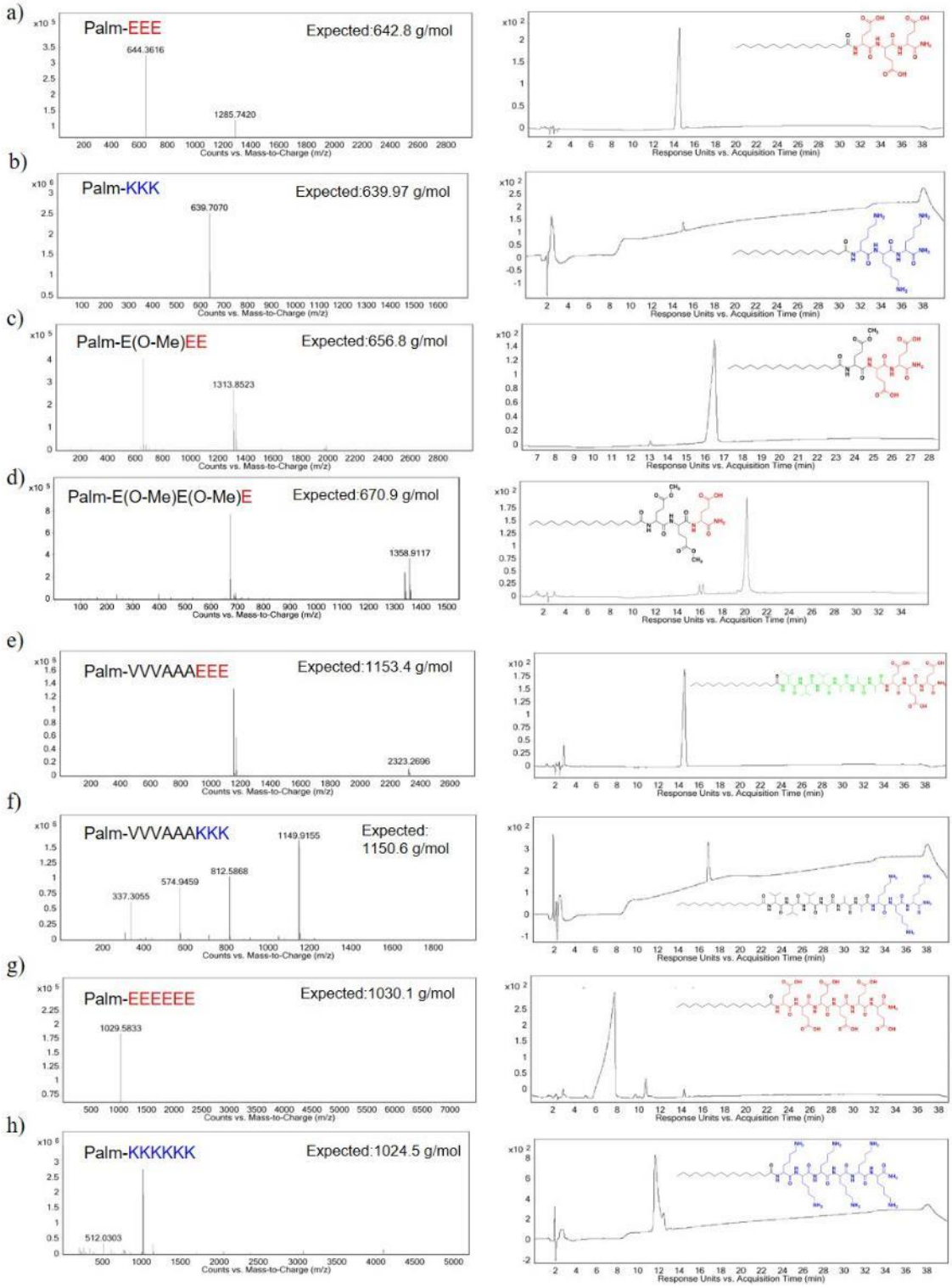


**Figure 2.23: Chemical characterization of PA molecules used in study**

MS and LC-MS purity check of (a) **PA1**, (b) **PA2**, (c) single methylated PA, (d) double methylated PA, (e) **PA3,** (f) **PA4,** (g) **PA5,** and (h) **PA6**.

*Transmission electron microscopy and electron diffraction***:** For conventional TEM, 10 µl of a 0.5 wt% PA solution were placed on copper mesh TEM grids (Electron Microscopy Science) for 3 minutes, rinsed twice with water, stained twice with 2 wt% uranyl acetate and dried for 10 minutes. Samples were imaged using a FEI Spirit G2 TEM. The width of PA1 at pH 3 and pH 6.45 was approximated by averaging the width of 20 structures of the 4-day aged conventional TEM samples. Cryo-TEM imaging was performed on a JEOL 1230 microscope and was operated at 100 kV. After placing 6.5 µl of solution on a lacey carbon copper grid (Electron Microscopy Science), the grid was held by tweezers and mounted on a Vitrobot Mark IV equipped with a set temperature of 24°C and 90% humidity. The sample was blotted and plunged into a liquid ethane reservoir which was cooled by liquid nitrogen. The vitrified samples were then transferred to a Gatan 626 cryo-holder using a cryo-transfer stage that was cooled by liquid nitrogen and kept below -180°C during imaging. For SAED, samples were prepared in similar methods to conventional TEM but without staining. SAED patterns were obtained on a JEOL ARM300F cold field emission gun TEM operated at 300 kV acceleration voltage with a camera length of 60 to 80cm, equipped with a Gatan OneView IS CMOS camera. The images were acquired using the *in situ* mode of the OneView IS camera at a frame rate of 4-15 fps to avoid smearing of the diffraction patterns from electron beam-induced sample degradation. Following the acquisition of the diffraction patterns, bright field images of the same area was obtained to correlate the alignment between real space morphological features and the diffraction patterns.

*Scanning Electron Microscopy:* Following sample preparation at 0.5 wt%, a small piece of a polystyrene sponge was placed in the sample solution for 1 hour. The sponge was transferred to absolute ethanol for 15 minutes followed by drying at the critical point of $CO_2$ on a critical point dryer (Tousimis Samdri-795). Dried samples were coated with 15 nm of osmium using an osmium

plasma coater (Filgen, OPC-60A) and imaged using a LEO Gemini 1525 field emission scanning electron microscope at 20 kV accelerating voltage.

*X-ray scattering***:** Samples were prepared using a concentration of 2 wt% and scattering patterns collected at beamline 5ID-D at the Dupont-Northwestern-Dow Collaborative Access Team Synchrotron Research Center in the Advanced Photon Source of Argonne National Laboratory. Sample solutions were flowed through a 1.5 mm diameter quartz capillary tube flow-cell at 1 mm/sec to limit x-ray induced damage. Samples were then exposed to 17 keV monochromatic x-rays five times for 0.5 seconds (SAXS patterns) and five times for 5 seconds (WAXS patterns) and intensities were recorded on a CCD detector placed 245 cm behind the sample. The collected two-dimensional scattering images were averaged by azimuthal integration using the data reduction program FIT2D, plotted against the wave vector $q = (4\pi)\sin(\theta/2)$ where $d = 2\pi/q$, and subtracted by buffer only controls. SAXS patterns were plotted on a log-log scale and WAXS patterns on a linear scale. Fitting to a core-shell cylinder or a core-shell sphere model was performed as reported using the NCNR analysis macro for Igor.[159]

*Rheology***:** 2 wt % PA samples were prepared and mixed as indicated four days before testing. Measurements were performed on an Anton Paar MCR 302 rheometer with a 25 mM diameter 2° angle cone-plate geometry. 150 μl samples were placed between the cone and plate and temperature was maintained at 25°C during the duration of the test. Viscosity was measured as rotational rate was increased from 1 to 100 radians per second.

*Fourier transform infrared spectroscopy:* PA samples were dissolved in $D_2O$ at concentrations of 2 wt% and then acidified with 1 M deuterium chloride followed by pH adjustment with 1 M sodium deuteroxide. 1 M NaCl dissolved in $D_2O$ was added to a final concentration of 75 mM NaCl. After appropriate aging, samples were sandwiched between two calcium fluoride windows separated by

a 50 μm spacer. Transmittance was measured on a Bruker Tensor 27 spectrometer and solvent background was subtracted from the obtained sample spectra. Peaks were deconvoluted to a Lorentzian line shape using a MATLAB peak fitting tool.

# CHAPTER 3

# 3. Self-Assembly of Nonionic Peptide Amphiphiles

## 3.1. Objectives and Significance

Supramolecular peptide assemblies generally rely on ionic groups for solubility in aqueous media. Yet ionic charge can affect the adhesion, biodistribution, and signaling properties of these systems. To control charge, this study reports on a filament-forming nonionic PA molecule containing a decaethylene glycol group. Unlike charged PA sequences, these molecules self-assemble to form high-aspect ratio filaments with β-sheet hydrogen bonding at acidic, neutral, and basic pH. Co-assembling the nonionic PA with charged PA produced filaments with tunable surface charge density and thereby demonstrate that a small number of charged molecules within the assemblies produced supramolecular structures similar to the completely charged filaments. Nonionic filaments were cell compatible and increased differentiation of stem cells in osteogenic media conditions relative to anionic PA filaments, demonstrating that ionic charge can affect the biological properties of PA systems.

## 3.2. Background

Electrostatic charge plays a key role in determining the biological performance of nanostructured materials. Because of their high interfacial energy, the charged surfaces of nanomaterials adsorb biomolecules, with the sign and magnitude of the charge determining the content and kinetics of surface adhesion.[160,161] In addition to the surface charge of the nanomaterial itself, the biomolecular corona determines its biodistribution and its ability to be taken up by

specific tissues or cells.[162-164] Electrostatic charge also plays an important role in cellular adhesion, proliferation, and toxicity.[165-167] PEG is often used to decrease the surface energy of a nanomaterial by surrounding the structure with a hydrated, uncharged polymer shell that limits accumulation of biomolecules and prolongs bioretention.[168-170] This strategy has been applied to self-assembling peptide nanomaterials, where the addition of PEG chains can help solubilize hydrophobic peptide domains and increase order within the assemblies.[171] In these systems, appending PEG chains to other self-assembling peptides can strengthen secondary interactions among the molecules,[172] but can also increase critical micelle concentration due to increased steric repulsion among the PEG chains.[173] These systems, however, require conjugation of long PEG chains to each peptide within the assembly, making it difficult to probe how controlling electrostatic charge can modulate self-assembly and the biological interactions by these nanomaterials.

PA molecules developed by Stupp and co-workers—comprising a peptide region conjugated to an alkyl tail—are a promising platform for biomedical applications because of their highly tunable self-assembly into dynamic nanostructures with programmed morphologies in aqueous media.[90,91,97,113,114,174-176] These molecules generally contain charged amino acid residues for solubility, constituting the hydrophilic domain of the amphiphile. These can include acidic residues, which are deprotonated at neutral pH or basic residues protonated at neutral pH.[92,175] In addition to charged amino acids, a widely used subclass of PA molecules includes a peptide sequence designed to promote intermolecular hydrogen bonding, which programs self-assembly of high-aspect-ratio, one-dimensional nanostructures. Self-assembly of these molecules produces nanostructures with a high density of surface charge, and limiting electrostatic repulsion via screening of these charges by ions in the media controls the morphology of the assemblies that form.[92,97,177,178] The charged groups in these assemblies determine many properties of the

nanostructures including peptide bioactivity,[106] cytocompatibility,[175] biodistribution,[179] and gel formation.[98,99] Although previous studies report that oppositely charged molecules cooperatively co-assemble into the same structure to neutralize net charge,[151,152,180,181] electrostatic interactions still determine how the molecules assemble and how the interact with the environments, especially in these dynamic systems where domains of a single charge can form. In previous reports, nonionic self-assembling PA structures were achieved through chemical functionalization of the peptide side-chains, producing hydrogels at low concentration.[182,183] How the effect of tuning or eliminating completely ionic charge within PA systems affects intermolecular interactions and the resultant biological response of cells to the assembly these assemblies remains unknown. Here, an uncharged PA molecule is used to demonstrate how eliminating ionic charge in some or all of the PA molecules within assemblies controls self-assembly and bioactivity of PA filaments.

## 3.3. Results and Discussion

*Self-assembly of nonionic PA filaments*

To produce PA filaments with no ionic charge, a short PEG chain was substituted for the ionizable amino acids typically included in PA molecules to maintain solubility of the PA in an aqueous environment. Previously reported filament forming PA molecules have included oligoethylene glycol as spacers between peptide domains for self-assembly and for bioactivity[113,128,184] or long PEG chains to decrease degradation of PA assemblies,[185] though each of these also included ionizable peptide domains. To form an uncharged PA filament, the sequence *N*-palmitoyl-VVAA was chosen as the aliphatic tail and hydrogen bonding peptide domains, which we previously reported to form filaments with β-sheet when the molecules contain ionic residues

at the C-terminus.[176] As the hydrophilic domain, a decaethylene glycol amino acid was selected, which previous work indicated would be short enough to limit steric repulsion among assembled molecules,[186] but we expected was ould be long enough to ensure solubility (**PA1**, Figure 3.1a, Figure 3.11a). The PA was synthesized by coupling the PEG amino acid to a rink-amide resin and completing the peptide using standard Fmoc solid phase peptide synthesis, leaving an uncharged amide group upon cleavage from the resin. Following synthesis and purification, the PA was readily resuspended in water, giving a cloudy solution without a noticeably higher viscosity. Two PA molecules in which the PEG domain was replaced with either two anionic glutamic acid residues (**PA2**, Figure 3.1a, Figure 3.11b), or two cationic lysine residues (**PA3**, Figure 3.1a, Figure 3.11c) were also prepared.

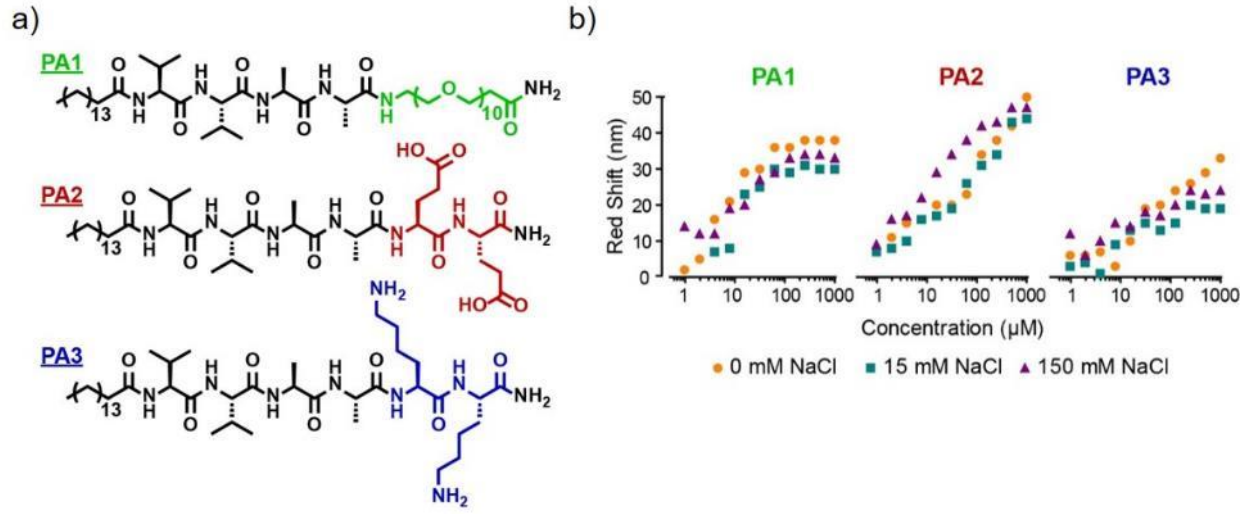


**Figure 3.1. Structure and assembly of nonionic and ionic PAs**
(a) Structures of the uncharged **PA1**, the anionic **PA2**, and the cationic **PA3**. (b) Redshift of peak Nile red fluorescence as a function of **PA1**, **PA2**, or **PA3** concentration at in buffers of 0 mM NaCl, 15 mM NaCl, and 150 mM NaCl.

The first experiments assessed how the elimination of charge via PEGylation affected the ability of the PA molecules to self-assemble. Because **PA1** lacks ionic residues, its self-assembly was hypothesized to be less dependent on buffer salinity than its charged counterparts, as screening by ionic solutes determines the length scale of electrostatic interactions. Self-assembly of the molecules was monitored using the Nile red assay where a redshift in the dye's fluorescence emission is correlated with the emergence of hydrophobic pockets as amphiphiles assemble.[187] Assembly of **PA1—**as indicated by the redshift in Nile red fluorescence—occurred independently of ionic strength, while assembly of **PA2** depended on the ionic strength of the buffer, with smaller shifts recorded in 0 mM and 15 mM NaCl than in 150 mM NaCl. Like **PA1,** the self-assembly of **PA3** was less dependent on ionic strength than **PA2**, though at higher concentrations the redshift in Nile red emission was about half that of **PA1** or **PA2**, suggesting less dye may have intercalated in the assemblies (Figure 3.1b). In contrast, CD spectroscopy showed assemblies of both **PA1** and **PA2** formed β-sheet without the addition of NaCl to the buffer, while **PA3** formed β-sheet only when salt was present in the buffer (Figure 3.2). Glutamic acid and lysine were chosen as charged groups due to their similar size and the similar magnitude of their opposite charges, yet these results indicate the two residues have disparate effects on self-assembly. Importantly though, **PA1** formed robust assemblies at low concentration and formed β-sheet in low screening conditions.

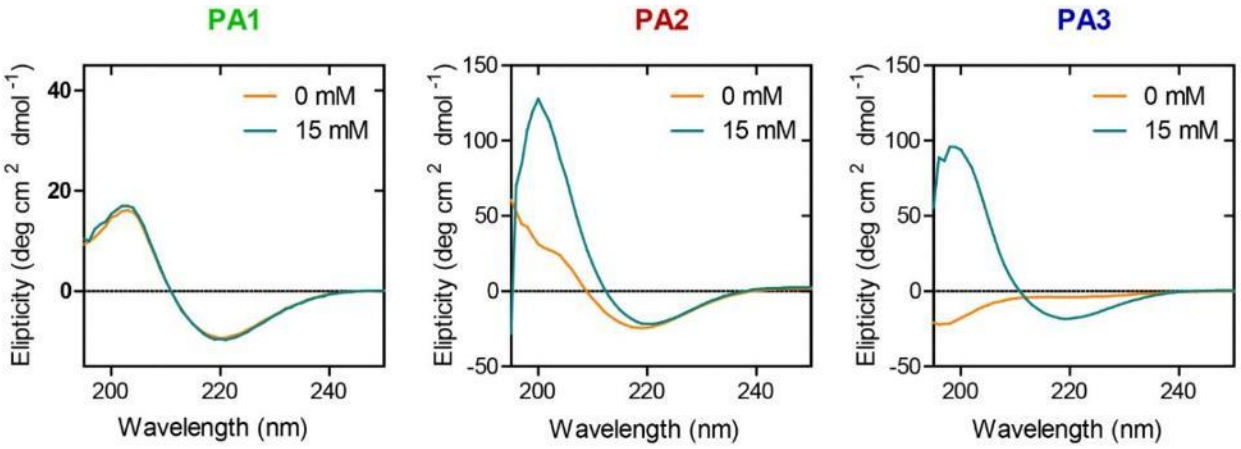


**Figure 3.2 CD spectra of nonionic and ionic PAs**
Circular dichroism of PA solutions plotted as a function of wavelength in 0 mM NaCl buffer and in 15 mM NaCl buffer.

*pH dependence of PA filament assembly*

The nonionizable headgroup of **PA1** was expected make its assembly much less pH dependent than **PA2** and **PA3**, which contain groups that are easily deprotonated or protonated. Indeed, zeta-potential measurements confirmed that the surface charge of **PA1** was approximately 0 mV from pH 2 to 12, whereas the surface charges of **PA2** and **PA3** decreased at low and high pH, respectively (Figure 3.3a). Cryo-TEM of samples preserved in vitreous ice showed that **PA1** uniformly formed narrow ribbon structures at all pHs tested, while the morphologies observed for **PA2** and **PA3** were pH-dependent. At low pH, **PA2** formed wide, short ribbons that bundled with each other, but at and above neutral pH **PA2** formed longer, narrow fibers. Similarly, **PA3** formed wide, short, bundled structures at high pH, but formed narrow, longer filaments when charged at neutral pH and below (Figure 3.3b).

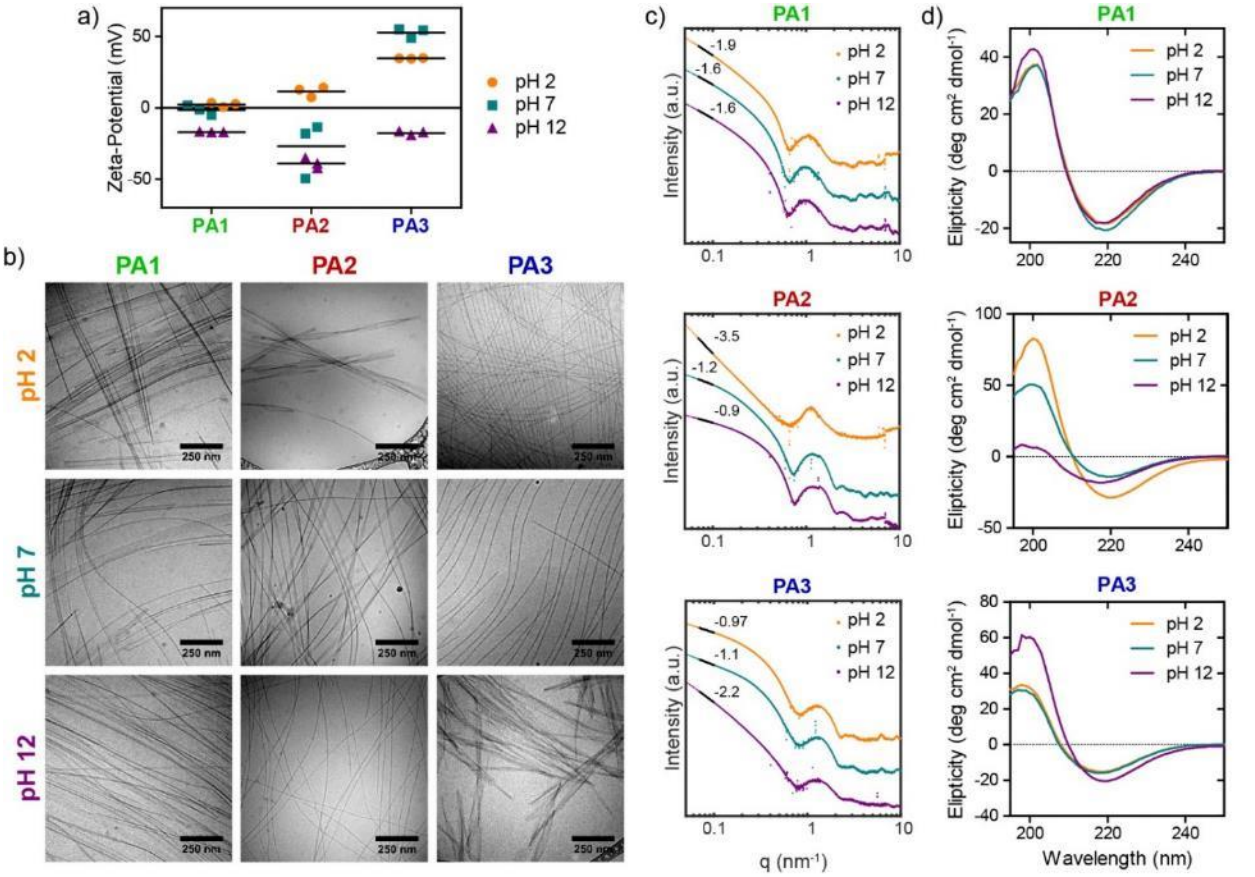


**Figure 3.3 pH dependence of self-assembly for nonionic and ionic PA**
(a) Zeta-potential measurements for **PA1**, **PA2**, and **PA3** solutions at pH2, pH 7, and pH 12. (b) Cryo-TEM images of **PA1**, **PA2**, and **PA3** each prepared at pH 2, 7, and 12 and preserved in vitreous ice. (c) Small-angle x-ray scattering intensity as a function of the wave vector for **PA1**, **PA2**, and **PA3** solutions at pH2, pH 7, and pH 12. (d) CD as a function of wavelength for **PA1**, **PA2**, and **PA3** solutions at pH2, pH 7, and pH 12.

These observations are supported by SAXS scattering data which showed little difference in the ribbon-like scattering pattern produced by **PA1** in acidic, neutral, or basic conditions, but showed a significant decrease in slope when ionic charge was increased for **PA2** and **PA3**, consistent with a transition from planar structures to cylindrical filaments (Figure 3.3c). Next, CD spectroscopy was used to determine how pH affected the secondary structure of PA molecules within the assemblies. **PA1** formed β-sheet in acidic, neutral, and basic conditions, with similar

patterns observed at all three pH values. In **PA2,** β-sheet character decreased with increased pH as acidic groups were deprotonated and repelled one another. CD spectra for **PA3** were not significantly pH dependent, which could be attributed to less ionization of its sidechain in the assembled state relative to glutamic acid (Figure 3.3d). This trend is consistent with reported pKa values for the non-assembled side chains, which differ more from neutral for lysine (10.4) than for glutamic acid (4.3).[188]

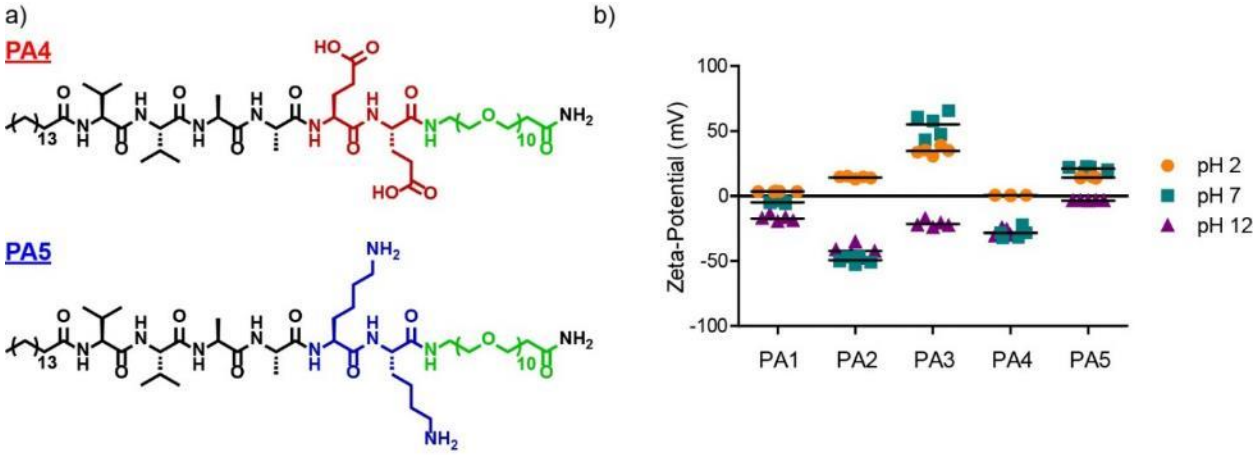


**Figure 3.4 Structure of ionic PEGylated PA**
(a) Structures of anionic, PEG-appended **PA4** and cationic, PEG-appended **PA5**. (b) Zeta-potential measurements for all PA molecules tested.

To determine if the observed pH-independent behavior was a result of PEGylation alone and not the nonionic design of **PA1**, two control molecules were synthesized, extending **PA2** and **PA3** with the 10-mer PEG amino acid to make *N*-palmitoyl-VVAAEE-$PEG_{10}$ (**PA4**; Figure 3.4a, Figure 3.11d) and *N*-palmitoyl-VVAAKK-$PEG_{10}$ (**PA5**; Figure 3.4a, Figure 3.11e). Zeta-potential measurements showed that PEGylation decreased but did not eliminate the surface charge of these molecules at neutral pH relative to their non-PEGylated counterparts, while zeta-potential was close to 0 mV when ionic charge was limited at pH 2 for **PA4** and pH 12 for **PA5** (Figure 3.4b).

SAXS showed that self-assembly of these molecules was pH dependent like the charged, non-PEGylated PA molecules tested, with low-q slope dependent on surface charge (Figure 3.5a). CD further confirmed that β-sheet formation by **PA4** and **PA5** was also pH dependent, with CD spectra showing β-sheet formed only when charge was minimal (pH 2 for **PA4** and pH 12 for **PA5**; Figure 3.5b). Despite its short length, the addition of the PEG chain may have increased steric repulsion among molecules in these dense assemblies, decreasing β-sheet content. Thus, pH-independent self-assembly by these PA molecules was achieved only by the removal of readily ionized groups, not merely extending the hydrophilic region of the molecule with PEG moieties.

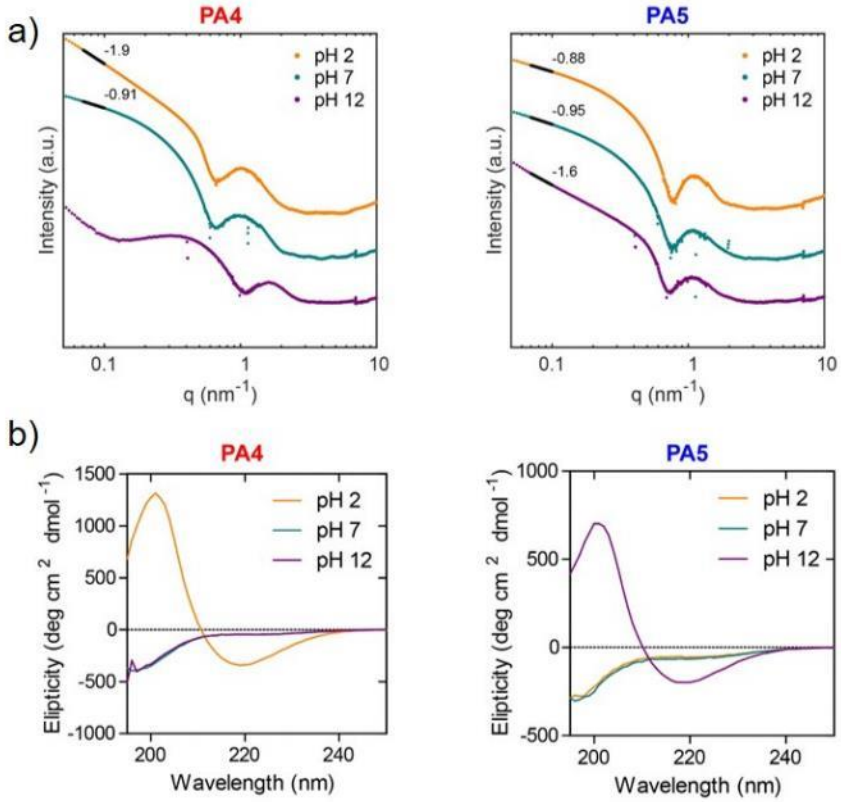


**Figure 3.5: Self-assembly of ionic PEGyalted PAs**
(a) Small-angle x-ray scattering intensity as a function of the wave vector for **PA4** and **PA5** solutions at pH2, pH 7, and pH 12. (b) Circular dichroism as a function of wavelength for **PA4** and **PA5** solutions at pH2, pH 7, and pH 12 in 30 mM NaCl.

*Co-assembly of nonionic and ionic PAs*

To see if the surface charge of the PA filaments could be tuned, co-assembled solutions of nonionic **PA1** with anionic **PA2** were prepared by mixing solutions of the individual PA molecules in a 30 mM NaCl buffer and sonicating prior to heat treatment. In a previous report, self-assembled morphology of ionic PA molecules co-assembled with nonionic, non-peptide surfactants depended on the relative concentration of the two components, which was attributed to the non-peptide surfactant disrupting hydrogen bonding among the peptide molecules.[189] In the system reported here, both the nonionic and ionic surfactant components are peptides, allowing us to study how changing the ratio of nonionic and ionic components affects interactions among the hydrogen-bonding peptide domains. Cryo-TEM of the co-assemblies showed that following the addition of 5 mol% **PA2** to **PA1**, assemblies formed similar narrow ribbons to those observed in **PA1** alone. With the addition of 25 mol% **PA2** or more, the resulting filaments appeared more similar to the broader, twisted ribbons formed by assemblies comprising entirely **PA2** (Figure 3.6a). This indicates that the charged system morphology can be achieved even with a fraction of the containing molecules charged headgroups. Consistent with this trend, SAXS showed significant changes in low-q slope with the addition of 25 mol% **PA2** to the uncharged **PA1** filaments, indicating a transition from ribbon-like to cylinder-like assemblies. Similarly, the first minimum in the pattern shifted to the right as uncharged **PA1** molecules were replaced with the charged **PA2** with the most significant change occurring with 25 mol% or less **PA2** added to the assemblies (Figure 3.6b). For co-assemblies of **PA1** and the cationic **PA3**, low-q slope changed more gradually with the addition of charged groups (Figure 3.7a), which supports the notion that electrostatic repulsion among lysine residues in neighboring β-strands affected assembled morphology less than repulsion among glutamic acid residues. Importantly, the transition of the

scattering patterns from a **PA1** like morphology to a **PA2** like morphology with the addition of only a minority of **PA2** groups suggests even when a small fraction of the PA molecules within the assemblies are charged, repulsion among these charged groups is sufficient to produce charged-like assemblies.

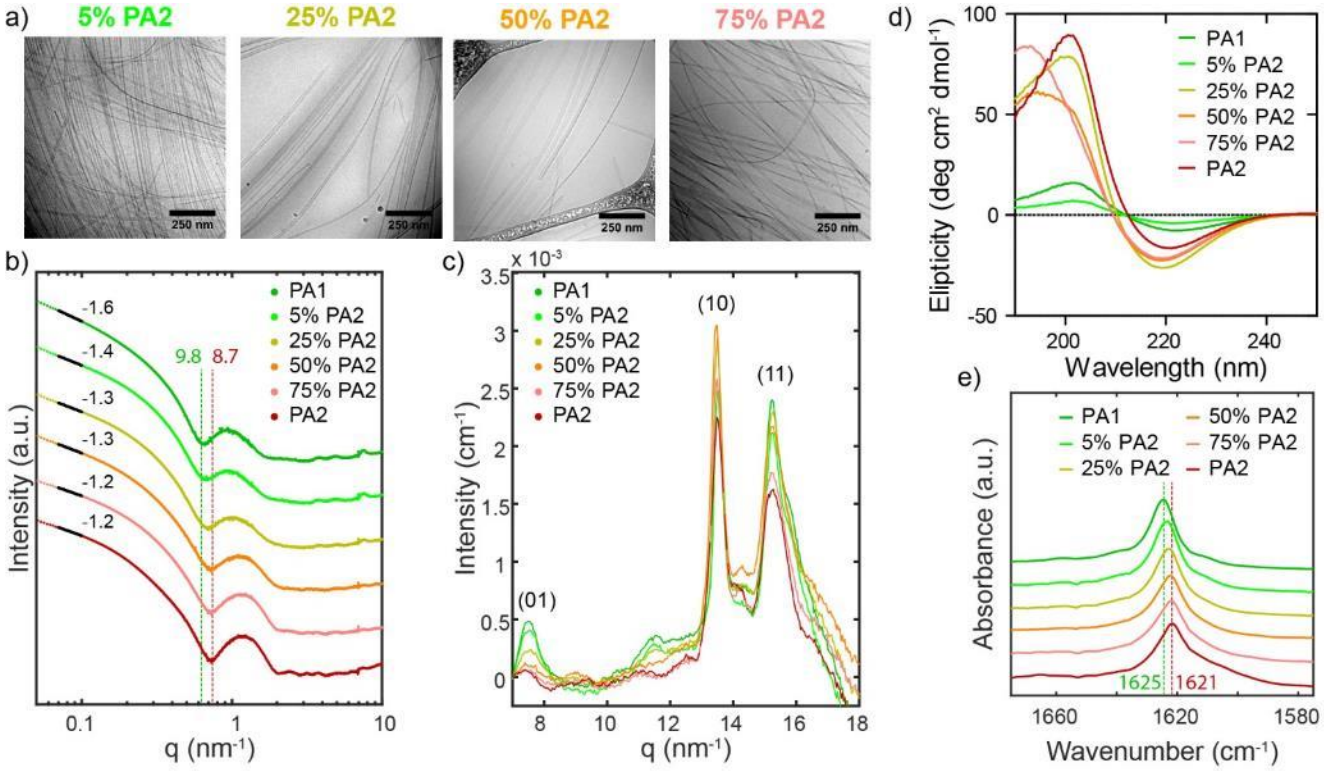


**Figure 3.6: Co-assemblies of nonionic and anionic PAs**

(a) Cryo-TEM micrographs of co-assemblies of nonionic **PA1** and anionic **PA2** preserved in vitreous ice with the molar fraction of **PA2** in the co-assemblies indicated. (b) Scattering intensities of the co-assembled PA systems as a function of the wave vector with vertical lines showing the first minimum of the **PA1** and **PA2** patterns and associated d-spacing given in nm. (c) WAXS intensity as a function of the wave vector for the co-assembled PA systems. (d) CD spectra as a function of wavelength for the co-assembled PA systems. (e) FTIR absorbance spectra as a function of wavenumber for the co-assembled PA systems with vertical line showing the peak absorbance in the amide I′ band for **PA1** and **PA2.**

Next, how changing the total charge affects intermolecular order among molecules within the assemblies was explored. WAXS showed three peaks, the first at a d-spacing of 0.84 nm is a

result of the (01) spacing between the β-strands, the second peak with a d-spacing of 0.47 nm results from the (10) β-sheet spacing, and the third peak corresponding to a d-spacing of 0.41 nm results from a (11) reflection. The intensity of the (01) and (11) peaks are stronger in the fully nonionic system than in the fully anionic assemblies. Because the length scale of electrostatics is greater than that of local steric interactions, repulsion among ionic charges on neighboring strands affected inter-strand spacing. Meanwhile, steric repulsion among PEG chains was more likely to affect interactions with the nearest neighbor only. Surprisingly, the strongest (10) peak occurred when **PA1** and **PA2** were mixed in an equimolar ratio, suggesting that the arrangement of molecules within the co-assemblies minimized repulsion among the molecules (Figure 3.6c). Thus, while the change in assembly morphology with increasing charge was monotonic, hydrogen bonding character among molecules within β-strands first increased and then decreased with increasing **PA2** content. For co-assemblies of **PA1** and the cationic **PA3**, the intensity of all three peaks decreased with increasing charged PA content (Figure 3.7b). While the lysine sidechains affected assembled morphology less than glutamic acid residues, interactions among lysine groups in the same β-strand may have had a stronger effect on hydrogen bonding along the filament axis.

The strong (10) WAXS peak observed when **PA1** and **PA2** were co-assembled was hypothesized to be a result of molecules within the assemblies arranging to minimize repulsive interactions with their neighbors—both by limiting steric interactions among neighboring PEG chains and by limiting electrostatic interactions among nearby charged groups. CD spectroscopy was used to further probe the effects of co-assembly on interactions among the molecules within filaments. CD showed weaker overall β-sheet signal for **PA1** alone and co-assemblies containing 5 mol% **PA2** and the greatest intensities occurring in systems containing 25-75 mol% **PA2** (Figure 3.6d), further supporting the result that co-assembling **PA1** and **PA2** increased β-sheet content

relative to either PA alone. To further probe the environment of the hydrogen bonding PA region, FTIR was performed to monitor the amide I′ peak, which is sensitive to β-sheet formed by peptides. The spectra showed a shift in the peak to lower wavenumbers for **PA2** relative to the nonionic **PA1**. In co-assembled systems, this shift could be seen with as little as 25 mol% **PA2** (Figure 3.6e). Previous reports of alanine-rich peptides indicate that this shift is correlated with hydration of the peptides, suggesting increasing charge leads to increased solvation of the hydrogen-bonding region.[190] Together, these results point to the complementary ways in which combining charged and non-charged groups can strengthen hydrogen bonding interactions within the assemblies. Adding even a minority of charged **PA1** to **PA2** increased separation between the strands leading to more cylindrical, better solvated assemblies. Better solvation of polymer chains like the PEG group on **PA1** resulted in decreased repulsion among the chains, which can in turn increase β-sheet character. On the other hand, co-assembling nonionic **PA1** with PA2 can separate **PA2** molecules from one another within the strand, decreasing longer range repulsive interactions among glutamic acid groups and yielding increased β-sheet content. Therefore, co-assembling PA molecules with different hydrophilic groups is a potential strategy to limit the repulsive interactions present in homogeneous assemblies.

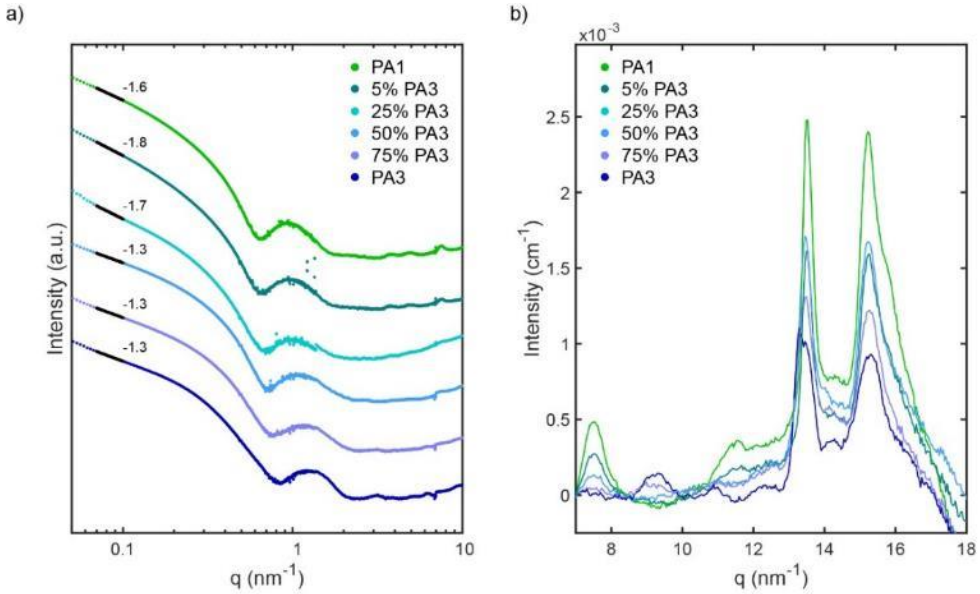


**Figure 3.7: Co-assemblies of nonionic and cationic PAs**
(a) SAXS intensities of co-assembled systems of **PA1** and **PA3** as a function of the wave vector. (b) WAXS intensities of the co-assembled systems of **PA1** and **PA3** as a function of the wave vector.

*Effect of surface charge on PA bioactivity*

Surface charge of PA structures is well known to affect cell survival, and cationic PA assemblies have been found to induce cell death due to electrostatic interactions with cell membranes.[97,175] To test the cytocompatibility of the nonionic **PA1**, normal human lung fibroblast (nHLF) cultures were treated with PA solutions of various concentrations. Both **PA1** and **PA2** were non-cytotoxic, with over 85% of cells staining positive for calcein at up to 100 μM PA, whereas **PA3** was highly cytotoxic ($EC_{50} = 25 \pm 4$ μM). Thus, **PA1** is a cytocompatible alternative to **PA3** for applications where negatively charged surfaces are undesirable (Figure 3.8, Figure 3.9a). Because only **PA1** and **PA2** were non-toxic to the cell cultures, these molecules were used to compare how they affect cell fate in additional experiments.

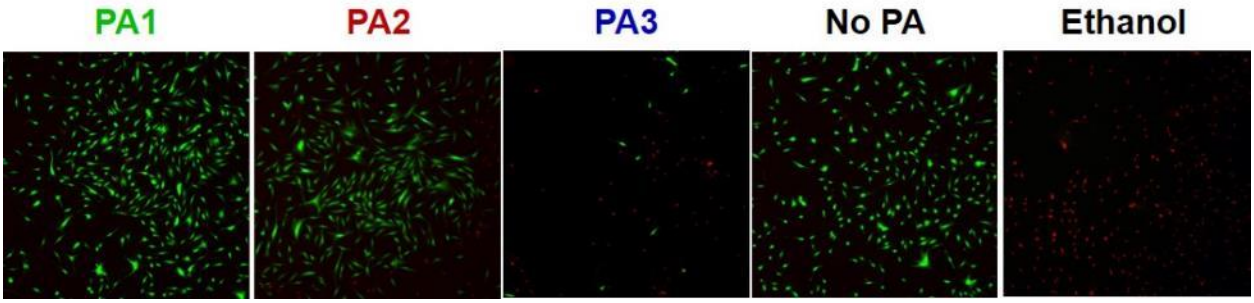


**Figure 3.8: Live/dead assay of nonionic and ionic PAs**
Fluorescence imaging of live cells stained with calcein (green) and dead cells stained with ethidium homodimer (red) after 36 hour treatment with 100 μM **PA1**, **PA2**, or **PA3** compared to cells with no PA treatment and cells with no PA treatment treated with 20% ethanol 30 minutes prior to staining.

Nonionic or anionic surface modifications are known to control progenitor cell differentiation with amine or hydroxyl groups inducing osteogenesis, carboxylic acid groups inducing chondrogenesis, and methyl groups inducing quiescence.[191] Osteogenic differentiation of MSCs is similarly reduced by carboxylic acid functionalization relative to amine group or hydroxyl group functionalization of gold nanoparticles[192] or titanium nanorods,[193] due to upregulation of proliferative signals like transforming growth factor β (TGFβ) by acidic groups. To determine how the presence of charged functional groups affected osteogenic differentiation, human MSCs were cultured in either growth media or osteogenic media with **PA1** or **PA2** at various concentrations for one week. In growth media, osteogenic differentiation—as indicated by alkaline phosphatase (ALP) activity—increased with increasing **PA2** concentration, but was not affected by supplementation with **PA1**. This is likely due to the previously reported ability of anionic PA filaments to enhance growth factor signaling *in vitro*.[108] However, in osteogenic media supplemented with dexamethasone and β-glycerophosphate, the nonionic **PA1** increased ALP activity with the largest increase when 10 μM PA was supplemented in the media, while **PA2** did

not affect differentiation (Figure 3.9b, Figure 3.10). This result is consistent with previous reports of negatively charged nanomaterials limiting osteogenic differentiation relative to nonionic hydrophilic groups.[192,193]

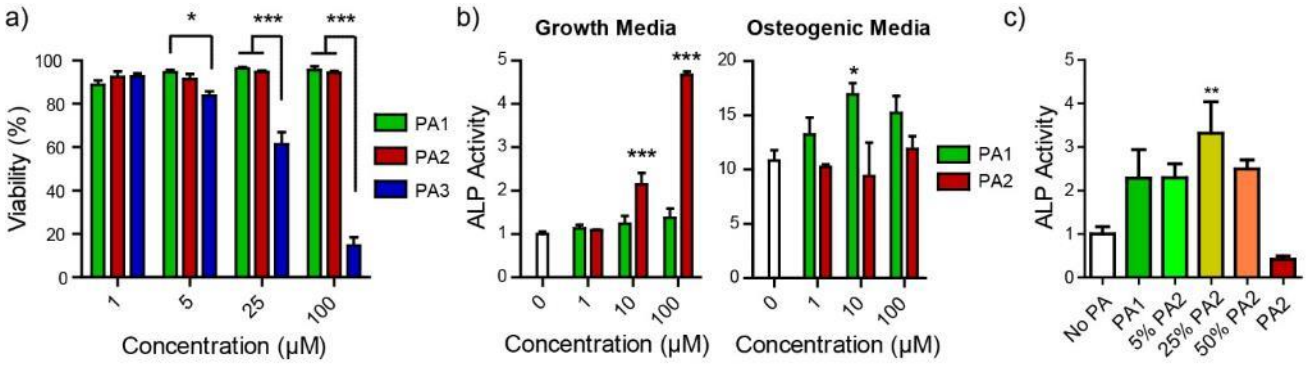


**Figure 3.9 Cytotoxicity and ALP activity of nonionic and anionic PA and co-assemblies**
(a) Percent viable cells as a function of PA concentration for nHLF cultures treated with **PA1**, **PA2**, or **PA3**; significance calculated relative to other PA solutions at the same concentration (n=3). (b) ALP activity normalized to DNA content as a function of PA concentration for human MSCs cultured in growth media and in osteogenic media for 7 days; significance calculated relative to no PA control in growth media (n=3). (c) ALP activity normalized to DNA content for **PA1** and **PA2** co-assemblies cultured in osteogenic media for 14 days; significance calculated relative to no PA control (n=4). (*, $p < 0.05$; **, $p < 0.01$; ***, $p < 0.001$)

To determine how co-assembling ionic and nonionic PAs affected MSC differentiation, human MSCs were cultured in the presence of **PA1** and **PA2** co-assemblies in osteogenic media. After 2 weeks, the greatest overall increase in osteogenesis was induced by a co-assembly of 25 mol% **PA2** with 75 mol% **PA1** (Figure 3.9c). Based on characterization studies at this co-assembly ratio, the PA molecules formed more hydrated, ionic-like assemblies, while maintaining a high surface density of PEGylated groups. The increased spacing between PEG moieties in these co-assemblies may have increased their ability to interact with cell surfaces and induce osteogenesis. Thus, both the overall charge of PA functional groups and the spatial orientation of those groups contribute to controlling osteogenic differentiation in response to the assemblies.

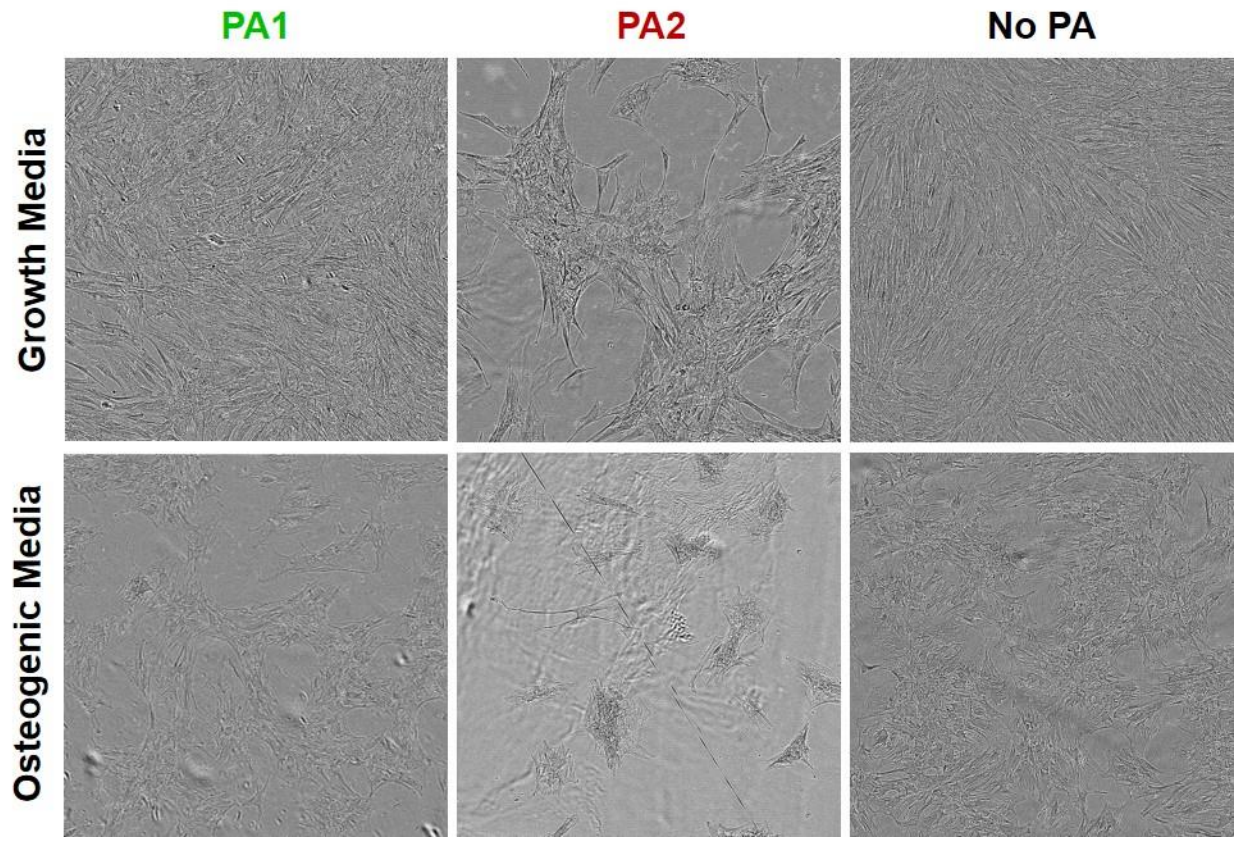


**Figure 3.10 Phase-contrast imaging of PA treated MSCs**
Phase-contrast microscopy images of hMSCs cultured for seven days in growth media or in osteogenic media supplemented with 100 μM **PA1**, 100 μM **PA2**, and without PA added.

### 3.4. Conclusions

this study, reports on a nonionic PEGylated PA that can self-assemble into similar nanofilaments at acidic, neutral, and basic pH with limited sensitivity to buffer ionic strength. Co-assembling these nonionic PA molecules with their charged counterparts produced a PA system with a tunable surface charge and demonstrated that only a minority of charged groups within an assembly are necessary to direct the morphology of the final assembly. Finally, controlling charge was shown to affect cell viability and osteogenic differentiation in response to the filaments. These nonionic, filament forming PA molecules are a useful tool in future PA applications where it is

important to control electrostatic surface interactions or biodistribution of supramolecular PA structures.

### 3.5. Materials and Methods

*PA synthesis and purification:* All PA molecules were synthesized using standard Fmoc synthesis on a Rink amide resin as previously reported.[128] For standard couplings, four equivalents of the amino acid was added in dimethyl formamide (DMF) with six equivalents of diisopropylethylamine (DIEA) and 3.95 equivalents 2-(1H-Benzotriazole-1-yl)-1,1,3,3-tetramethyluronium hexafluorophosphate (HBTU). For the PEG-10 amino acid (ChemPEP, Wellington, FL, USA), 1.5 equivalents were added in DMF with an equal concentration of (Benzotriazol-1-yloxy)tripyrrolidinophosphonium hexafluorophosphate (PyBOP) and 2 equivalents of DIEA overnight. Following coupling of the palmitic acid tail, peptides were cleaved from the resin in a 95:2.5:2.5 trifluoroacetic acid (TFA)/triisopropylsilane (TIS)/water mixture for 3 hours and precipitated in cold diethyl ether. The crude peptide was dissolved in 0.1% TFA (**PA1**, **PA3**, and **PA5**) or 0.1% ammonium hydroxide (**PA2** and **PA4**) and purified by high-performance liquid chromatography (HPLC). **PA1** was purified against a 5% to 95% gradient of water to a mixture of 75% acetonitrile and 25% tetrahydrofuran (THF), while all other PA molecules were purified over a 5 to 95% gradient of water to acetonitrile. All PA molecules were lyophilized following purification. For **PA1**, the dehydrated peptide was rehydrated and then lyophilized twice to remove any excess THF. The purity of the PA molecules was confirmed to be above 95% by liquid chromatography - electrospray ionization mass spectrometry using an Agilent 6520

quadrupole time-of-flight (Q-TOF) ESI-MS instrument over a 5% to 95% water to acetonitrile gradient.

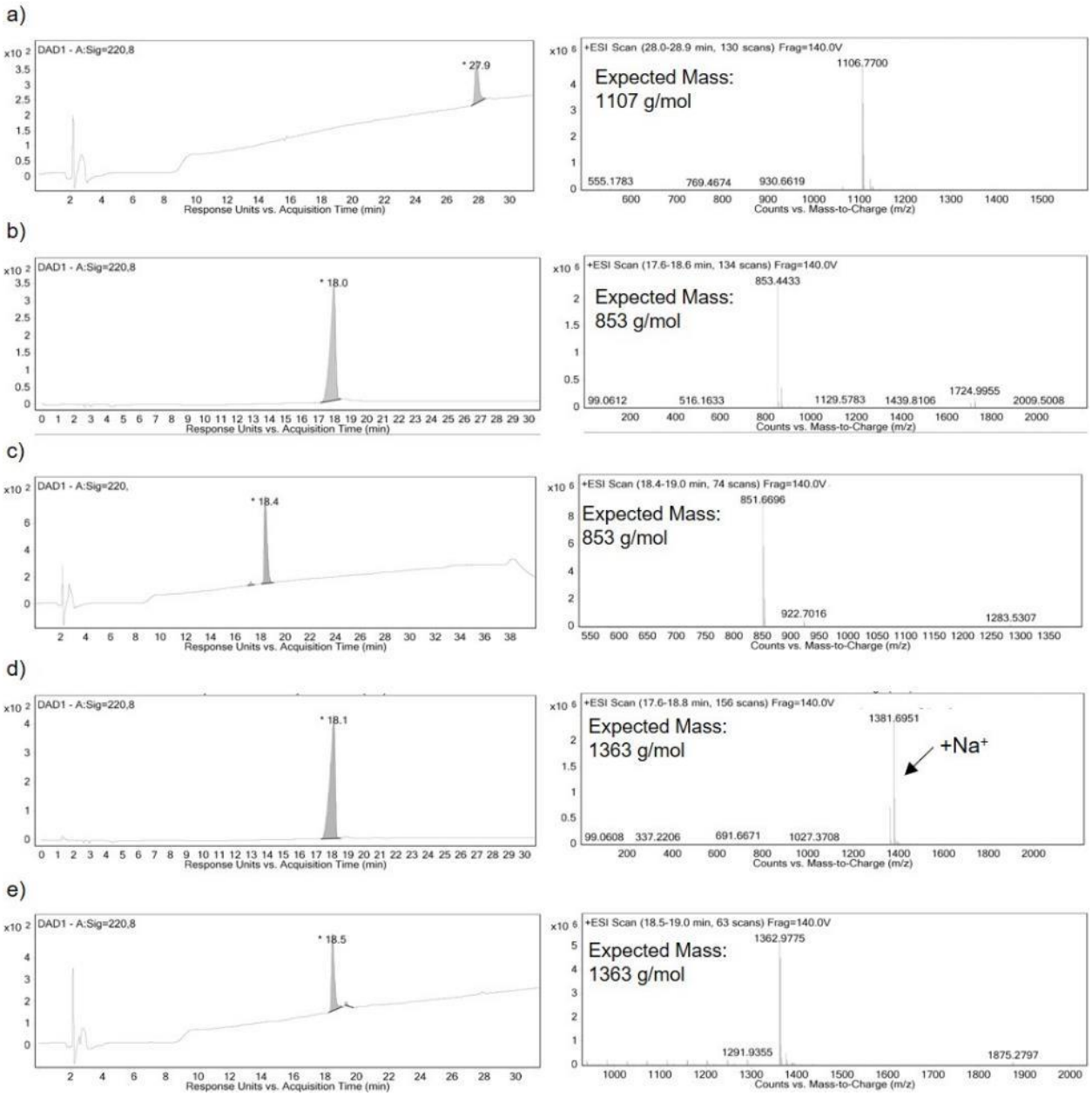


**Figure 3.11: Chemical characterization of nonionic and ionic PA molecules**

LC-MS and MS of highlighted peak to confirm purity of (a) **PA1**, (b) **PA2**, (c) **PA3**, (d) **PA4**, and (e) **PA5**.

*Solubilization and heat treatment:* PA powders were resuspended to 10 mM in water for experiments at pH 7, in 10 mM hydrochloric acid for pH 2 and 10 mM sodium hydroxide for pH 12. After resuspension, 1 M sodium hydroxide or 1 M hydrogen chloride were added to achieve the desired pH. To co-assemble PA molecules, PA solutions were mixed volumetrically, bath sonicated for 1 hour and then left on the bench to age for at least 2 hours. A solution of 150 mM NaCl was added to all samples to achieve a final NaCl concentration of 30 mM. All samples were heat treated at 80°C for 30 minutes followed by gradual cooling by 1°C per minute to 25°C.

*Nile red assay:* Following heat treatment, PA solutions were serially diluted in water (0 mM NaCl), or a buffer of 15 mM NaCl, or 150 mM NaCl. A solution of 100 μM Nile red was added to the PA solutions to one thousandth the total volume and incubated for 1 hour. The fluorescence spectrum was read from 600 nm to 700 nm using a BioTek Cytation 3 microplate reader using 560 nm excitation and the fluorescence shift was determined by subtracting the maximum excitation wavelength for each sample from that of the dye solution diluted in each buffer alone.

*X-ray scattering:* SAXS and WAXS measurements were obtained simultaneously at the Dupont-Northwestern-Dow Collaborative Access Team Synchrotron Research Center at the Advanced Photon Source at Argonne National Lab using beamline 5ID-D. Heat treated PA samples were flowed through a 1.5 mm glass capillary at 1 mm/sec during x-ray exposure for consistent background subtraction with buffer only samples. Five exposures of 10 seconds were obtained using 17 keV monochromatic x-rays using a CCD detector which was 245 cm behind the sample. The collected two-dimensional scattering images were averaged by azimuthal integration using FIT2D software. Intensities were plotted background subtracted and plotted against the wave vector $q = (4\pi)\sin(\theta/2)$ where $d = 2\pi/q$.

*Circular dichroism:* For ionic strength experiments, heat treated PA solutions were diluted 200 times in water, 15 mM NaCl, or 150 mM NaCl prior to measurement. For all other experiments, PA solutions were diluted in a buffer of either 10 mM HCl and 10 mM NaCl, 10 mM NaCl, or 10 mM NaOH and 10 mM NaCl for measurements at pH 2, pH 7, and pH 12 respectively. CD spectra were acquired on a J-815 CD spectrophotometer (Jasco Analytic Instruments, Easton, MD) in a 2 mm quartz cuvette. The average of 3 measurements over 250 nm to 190 nm was recorded.

*Zeta-potential:* Heat-treated PA solutions were diluted 20 times in 30 mM NaCl with 10 mM HCl, 30 mM NaCl, or 30 mM NaCl with 10 mM NaOH for pH 2, pH 7, and pH 12 respectively. For each PA, three separate samples were prepared at each pH. Samples were loaded in a disposable folded capillary cell and zeta-potential was measured at 25°C using a Zetasizer Nano ZS (Malvern Instruments, Malvern, UK). The average of the three measurements for each sample was plotted.

*Transmission electron microscopy:* TEM was performed on PA solutions preserved in vitreous ice on a JEOL 1230 TEM with a Gatan 831 CCD camera using an accelerating voltage of 100 kV. Samples were diluted with milli-Q water to 1 mM immediately prior to blotting. Copper mesh TEM grids with lacey carbon support (Electron Microscopy Sciences) were treated with glow discharge and then 7 µl of sample was pipetted onto the grid. Samples were blotted twice and plunged into liquid ethane using a Vitrobot Mark IV instrument (FEI) with 95-100% humidity in the chamber at 20°C. Samples were then transferred to a Gatan 626 cryo-holder under liquid nitrogen for imaging.

*Fourier transform infrared spectroscopy:* Following heat treatment, PA solutions were lyophilized and then reconstituted in $D_2O$ after which samples were heat treated a second time. For measurement, PA solutions were placed between two $CaF_2$ windows spaced 50 µm apart and a

Bruker Tensor 27 spectrometer was used to measure transmittance. Solvent background was subtracted from the obtained spectrum and plotted against the wavenumber.

*Cytotoxicity:* nHLFs were obtained from Lonza and maintained in growth medium consisting of DMEM with 10% fetal bovine serum (FBS) and 1% penicillin/streptomycin. Cells (passage 5) were tryspinized and resuspended in media containing 2% FBS and 150 μl of the cell suspension was added to each well of a 96 well microplate for a total of 2,500 cells per well. After 2 hours attachment, 50 μl PA solutions diluted in phosphate buffered saline (PBS) to 4 μM, 20 μM, 100 μM, or 400 μM were added to each well. After 36 hours culture, the media was removed and replaced with a solution of 2 μM calcein and 4 μM ethidium homodimer in PBS. After 30 minutes, cells were imaged using a Cytation 3 microplate reader. Live and Dead cells were counted using the MATLAB Image Processing Toolbox to determine viability.

*Alkaline phosphatase activity:* hMSCs were obtained from Lonza and maintained in Mesenchymal Stem Cell Growth Media (Lonza). Cells were used for experiments prior to passage 6. Cells were trypsinized and resuspended in growth media containing high glucose DMEM supplemented with 10% FBS and 1% penicillin/streptomycin and 50 mg/L sodium ascorbate. 500 μl of the cell suspension was placed in each well of a 24 well plate and incubated for 24 hours. Media was removed and replaced with 540 μl of growth media or osteogenic media containing low glucose DMEM supplemented with 10% FBS, 50 mg/L sodium ascorbate 10 mM β-glycerophosphate, and 100 nM dexamethasone. 60 μl of a 10 times concentrated PA solution in PBS was then added to each well. Every 3-4 days, media was replaced by removing 300 μl media and adding 270 μl growth media or osteogenic media and 30 μl of the 10 times concentrated PA solution in PBS. ALP activity was determined using the SensoLyte pNPP ALP Assay Kit (Anaspec, Fremont, CA) according to the manufacturer's instructions. Briefly, cells were washed once with the assay buffer

and the 200 µl of the assay buffer supplemented with Triton-X was added to each well. The plate was incubated for 1 hour at 4°C under mild agitation, cells were scraped with a pipette tip and collected, and the suspension was centrifuged for 10 minutes at 5,000 g. The supernatant was mixed with the assay's detection buffer in a microplate and the optical absorbance was read after a four-hour incubation using a Cytation 3 microplate reader. The supernatant was also used to determine DNA concentration using a Quant-iT PicoGreen dsDNA kit (Molecular Probes, Eugene, OR). ALP concentration was normalized to DNA concentration for each sample.

# CHAPTER 4

# 4. Transforming Growth Factor β-1 Binding by Peptide Amphiphile Hydrogels

## 4.1. Objectives and Significance

Supramolecular biomaterials are promising systems to bind or deliver therapeutic growth factors given their great structural versatility and tunability of properties by simply mixing molecules. In this work, this approach is investigated for the growth factor cytokine TGFβ-1, which is potentially important in the regeneration of damaged cartilage or in the prevention of fibrinogenesis of organs and the progression of tumors. Previous work by Stupp and colleagues identified a peptide sequence capable of binding TGFβ-1 and supramolecular PA nanofiber hydrogels that displayed the sequence were found to enhance regeneration of cartilage in a rabbit model. Here, we have synthesized novel PA molecules motivated by the tendency of the original bioactive peptide to undergo deamidation during purification procedures, thus interfering with synthesis of molecularly well-defined structures. Here, novel PA nanofibers that can be purified without deamidation are reported to establish if the chemical reaction affects chondrogenesis. Interestingly, gels formed from nanofibers displaying a fully deamidated sequence by introducing an asparagine to aspartic acid mutation retain 25% more growth factor relative to those displaying the original bioactive peptide even though the individual peptides have similar affinity for the cytokine. This difference in growth factor retention may be attributed to bundling of nanofibers displaying the original asparagine-containing sequence, thus masking the growth factor-binding structure. Improved retention of the growth factor resulted in chondrogenesis of cells encapsulated

in the gels as indicated by a more than 50% increase in Sox 9 expressing cells at three days and a 100% increase in glycosaminoglycan production at 21 days. Therefore, this design is a more effective bioactive supramolecular biomaterial to bind TGFβ-1. These experiments also demonstrated how bioactive peptide sequences in supramolecular biomaterials can have impact on their structure at larger length scales that change their biological functions.

## 4.2. Introduction

Regeneration of damaged articular cartilage is an important biomedical challenge with current clinical strategies failing to regrow healthy hyaline tissue.[53] Yet morbidity due to cartilage degeneration is widespread, affecting 15% of adults over 60[194] with an associated economic burden estimated at 2.5% of gross domestic product of developed countries.[35] Cartilage is avascular and comprises primarily ECM maintained by a small population of native chondrocytes.[30] In healthy tissue, maintenance of the ECM is regulated by a number of growth factors and cytokines; however, with no blood profusion and a small native cell population, regenerating adult cartilage lacks a source of bioactive signals needed to promote the production of new ECM.[36,195] Therefore, therapies that can deliver or sequester morphogenic signals are expected to induce improved regeneration of cartilage lesions.[45]

Regulation of the cytokine TGFβ-1 is critical in controlling skeletal development,[196] tissue fibrosis,[197] immune response,[198] and tumor progression.[199] The growth factor's role in chondrogenesis has been utilized to promote cartilage regeneration in scaffolds by promoting matrix synthesis and inducing chondrogenic differentiation of encapsulated cells.[59,200] However, maintaining the appropriate therapeutic concentration of TGFβ-1 is challenging since the signaling pathway activated is concentration dependent. Low physiological concentrations

promote maintenance of healthy cartilage while high physiological concentrations initiate inflammation and are toxic to the surrounding healthy cartilage, synovium, and subchondral bone.[48,201,202] In addition, low doses of the growth factor are quickly depleted due to TGFβ-1's short half-life (2-3 minutes in its active form).[203] Therefore, biomaterials that protect the retained growth factor from degradation while slowly releasing a therapeutic dose are expected to promote the regeneration of healthy tissue.[204] Previously reported techniques to prolong release of TGFβ-1 include covalent conjugation of the growth factor to a hydrogel scaffold such as PEG or chitosan,[205-207] non-specific encapsulation of the growth factor in a biopolymer matrix like fibrin or alginate,[208,209] and specific binding of the growth factor by synthetic peptides conjugated to a scaffold.[60,210,211] To achieve specific binding, the authors' laboratory reported previously on a scaffold formed by self-assembling peptide PA nanofibers that incorporated a peptide sequence evolved by phage-display (HSNGLPL) to specifically bind TGFβ-1.[60] These scaffolds promoted substantial repair of healthy hyaline cartilage in a rabbit model both through retention of exogenous growth factor and sequestration of endogenous growth factor following implantation in a cartilage lesion.

Self-assembling PA molecules are a promising platform for regenerative medicine because they can be programmed by their chemical structure to form high-aspect-ratio bioactive nanofibers that mimic ECM filamentous structures, thus serving as a temporary scaffold to support tissue repair.[60,103,105,107,112,114,115,150] Consisting of a peptide conjugated to a hydrophobic aliphatic tail,[90] PA molecules can degrade as the tissue regenerates, producing amino acids and lipids that are easily cleared from the lesion site.[82] The peptide sequence generally includes a hydrophilic domain of charged amino acids for solubility in aqueous conditions, while hydrogen bonding among specific peptide domains, particularly those with high tendency to form β-sheet secondary

structures, drives long range order and nanofiber formation.[212] These fibers form hydrogel networks when screened by physiological electrolytes,[99] and charge screening of acidic PA molecules by ionic calcium produces a robust, cell supporting hydrogel that can be formed *in situ.*[213] Bioactive signaling epitopes can be added to the peptide sequence and presented at a high density on the surface of the nanofiber.[150] In addition, PA molecules displaying bioactive sequences can be mixed with diluent PA molecules lacking the sequence to form co-assembled fibers where only a fraction of the molecules contain the bioactive epitope.[104,214] This controls the density of these signals and can initiate robust formation of nanofibers;[108] for instance, in the previously reported TGFβ-1 binding PA nanofibers, 10% of the PA molecules in each fiber contained the growth factor binding peptide epitope.[60]

Due to the promising ability of supramolecular PA systems to initiate cartilage repair by prolonging TGFβ-1 release, the initial hypothesized was that increasing the scaffold's ability to retain the growth factor would yield further improvements in cartilage regeneration. One approach to extend the growth factor's release profile is to improve the chemical stability of the peptide sequence used to bind the growth factor. The TGFβ-1 binding peptide used in the previous PA system contained an asparagine residue followed by a glycine residue, which is known to spontaneously deamidate under basic conditions. The lone pair on the amide nitrogen of the glycine residue can attack the carbonyl on the asparagine sidechain, forming an asymmetric cyclic imide, which opens to either aspartic acid or the β-amino acid (isoaspartic acid).[215] Subsequent analysis of the PA molecules used in previous *in vivo* rabbit study showed nearly complete deamidation of the PA sequence, which presumably occurred during purification of the molecule by reverse-phase HPLC under basic conditions. Yet despite deamidation of the phage display-evolved sequence, *in vitro* work had confirmed the PA system's ability to bind the growth factor

and promote chondrogenesis. This work explores whether preventing deamidation and therefore preserving the phage display sequence can improve the ability of the PA to bind TGFβ-1 and promote chondrogenesis, which required developing novel molecules in which deamidation is fully suppressed.

## 4.3. Results and Discussion

*Preparation of non-deamidating TGFβ-1 binding PA*

The initial goal was to prepare self-assembled PA filaments that displayed on their surfaces the TGFβ-1 binding peptide sequence discovered earlier by phage display. This required PA molecules displaying the sequence that could be purified in acidic rather than basic conditions to avoid deamidation. This also required co-assembling the TGFβ-1 binding PA with a filament-forming diluent PA since the former does not self-assemble into high-aspect-ratio nanofibers. The same diluent PA used in the previously reported system was chosen, which included three glutamic acid residues for solubility (**PA1**; Figure 4.1a, Figure 4.17).[60] Although a PA system including cationic residues like lysine instead of glutamic acid residues could be purified in acidic conditions, PA fibers with a high density of cationic groups are known to disrupt cell membranes under certain conditions.[97,175] Additionally, PA filaments displaying a high-density of acidic residues form robust gels with the addition of ionic calcium,[98] which is useful for sustained delivery of the growth factor.[60] The selection of an anionic diluent PA precluded co-assembly with a cationic PA displaying the binding epitope, since replacing the glutamic acid residues in the binding PA with lysine residues and co-assembling with **PA1** was previously shown to limit the structural integrity of the resulting nanofibers.[180] Therefore, a new growth factor binding PA that is soluble over a wide pH range was prepared by incorporating a 10-unit PEG chain. This PEG molecular segment

replaced a seven amino sequence of the previously reported TGFβ-1 binding PA, including the hydrophilic glutamic acid domain which made nanofibers soluble in water and the glycine linker domain which separated the binding epitope from the nanofiber surface (**PA2**; Figure 4.1a, Figure 4.17).

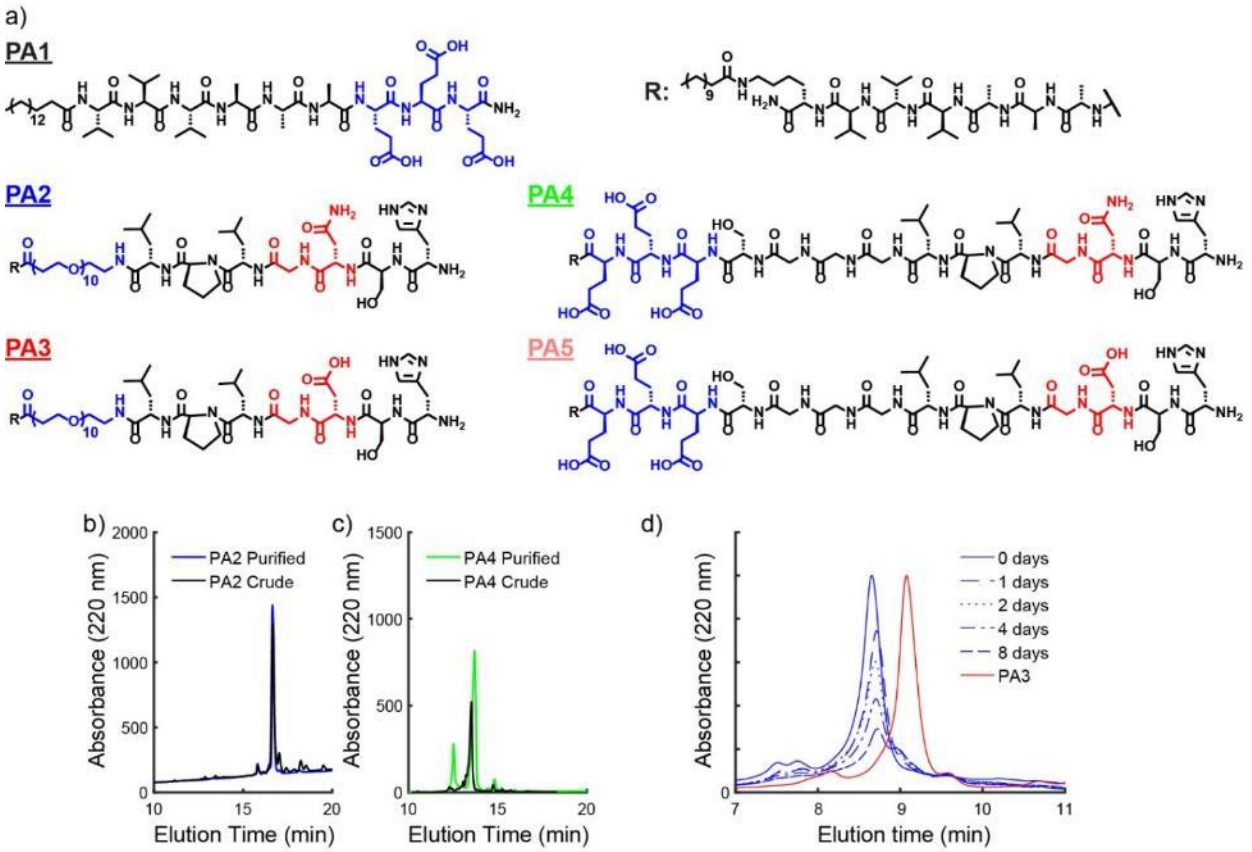


**Figure 4.1: Structure and chemical stability of TGFβ-1 binding PA system**
(a) Chemical structures of diluent and binding PA molecules. Hydrophilic domains for solubility are indicated in blue and the sites where deamidation occurs are indicated in red. (b) LC-MS trace following purification of **PA2** in acidic conditions and (c) **PA4** in basic conditions. (d) Analytical HPLC trace of **PA2** samples collected over 8 days compared to fresh PA molecules synthesized with an aspartic acid (**PA3**) substitution.

In order to understand the functional role of a deamidated sequence, the same PA molecule was synthesized with aspartic acid rather than asparagine in the growth factor binding domain (**PA3**; Figure 4.1a, Figure 4.17). After purification, mass spectroscopy showed a difference of one

atomic mass unit between **PA2** and **PA3**, indicating the asparagine residue was preserved in **PA2** (Figure 4.2).

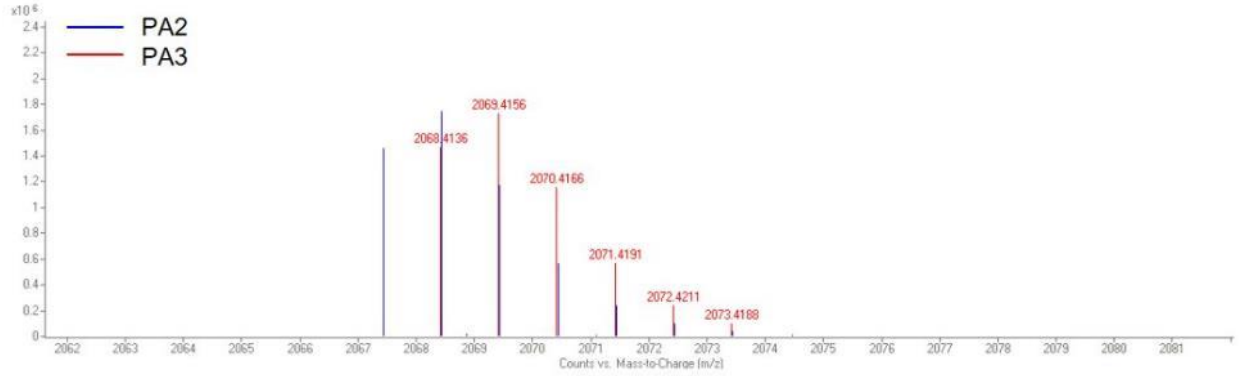


**Figure 4.2: MS of binding and deamidated PA sequences**
Mass-spectroscopy data showing that the purified asparagine-containing **PA2** differs in mass from the aspartic acid bearing **PA3**, confirming deamidation did not occur during synthesis and purification.

Additionally, liquid chromatography-mass spectroscopy (LC-MS) showed no elution peak of the deamidated product when the asparagine-containing sequence was used (Figure 4.1b). We also prepared a PA with an asparagine-to-isoaspartic acid substitution, but failed to purify more than a very small quantity due to the formation of a side product that largely coeluted with the expected product (Figure 4.3). For comparison, the previously reported TGFβ-1 binding PA (**PA4**, Figure 4.1a, Figure 4.17) and its aspartic acid mutated counterpart were synthesized (**PA5**; Figure 4.1a, Figure 4.17) and purified them under basic conditions. The chromatogram of **PA4** showed elution of the deamidated product despite immediate acidification in order to limit the hydrolysis reaction once the product was purified (Figure 4.1c).

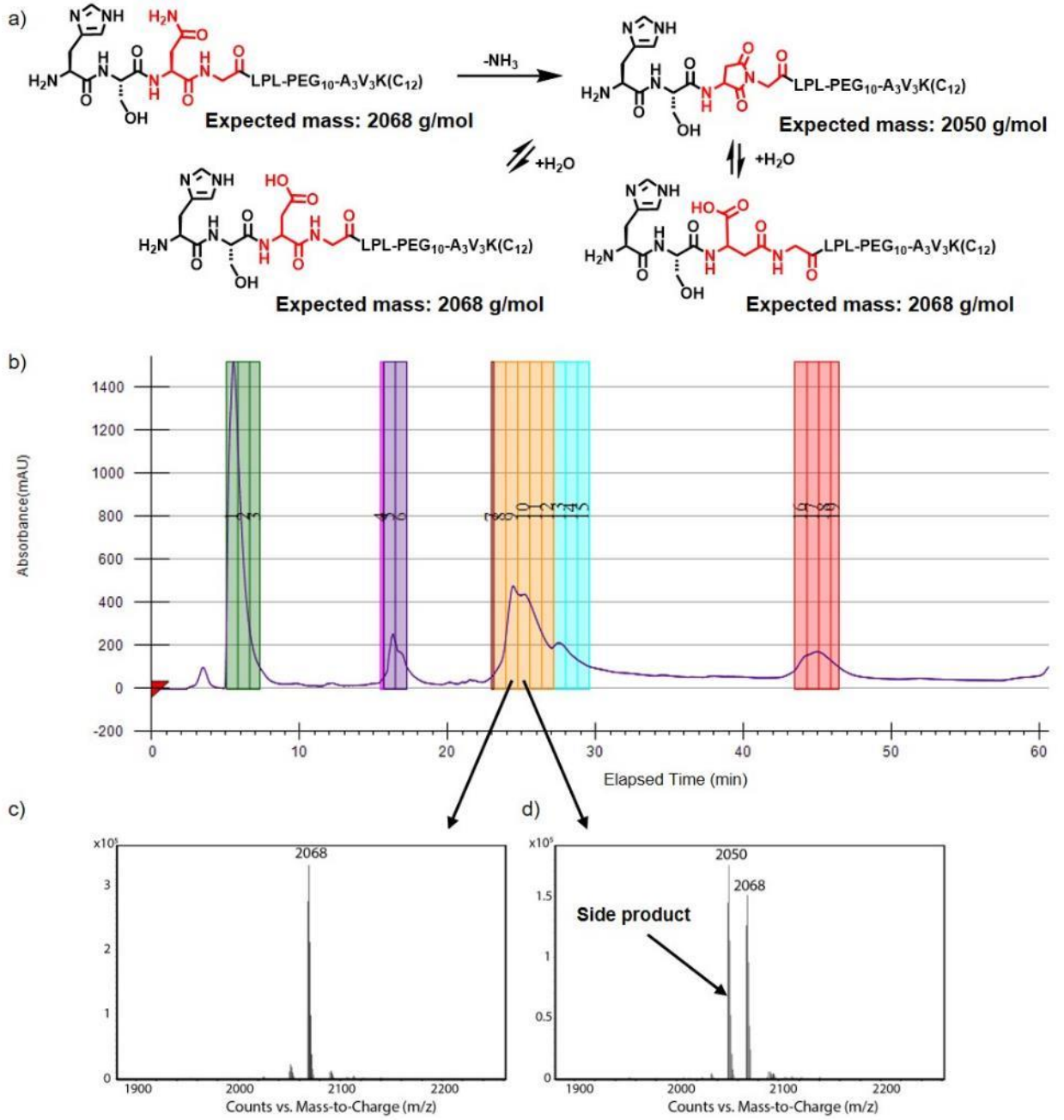


**Figure 4.3: Synthesis and purification of isaspartic acid mutant binding PA**

(a) Schematic showing deamidation of **PA2** to its asparagine-to-aspartic acid mutant, or its asparagine-to-isoaspartic acid mutant via a succinimide intermediate. (b) Preparatory HPLC trace obtained during purification of the directly prepared isoaspartic acid mutant sequence; product eluted during fractions 8-12. MS of purified collected fractions (c) 9 and (d) 10 showing expected product mass for fraction 9 and a -18 g/mol side-product co-eluting in fraction 10. Spontaneous conversion of the directly synthesized isoaspartic acid PA limited the product yield and suggest possible interconversion between deamidated sequences via the succinimide intermediate.

To track deamidation of **PA2** following solubilization, the molecule was dissolved in Tris-buffered Saline (TBS) and incubated the solution over 8 days at 37 °C, removing aliquots throughout the experiment for analysis by analytical HPLC (Figure 4.1d). As peptides, asparagine-, aspartic acid-, and isoaspartic acid- containing sequences can be differentiated from one another by analytical HPLC.[216] Comparing the elution times of **PA2**, **PA3**, and the asparagine-to-isoaspartic acid mutated acid PA showed that **PA3** eluted later than **PA2** allowing the two to be differentiated, but **PA3** eluted at a similar retention time to the isoaspartic acid-containing PA, which is unsurprising given the chemical similarity (Figure 4.4). Comparing analytical HPLC traces of the aliquots to those of the asparagine-to-aspartic acid mutated showed preservation of the expected elution peak over the first 6 days. A second peak more closely matching the elution peaks of the mutated sequences emerged only after 8 days, indicating the intended peptide sequence was largely preserved for up to one week. This strategy of using a PEGylated hydrophilic domain to produce PA molecules soluble over a wide pH range that can later be co-assembled with an anionic diluent PA may be useful in a number of other applications. These include incorporation of the NGR peptide motif used in delivery of cancer therapeutics[217] or the presentation of nitrosylated groups used to prevent restenosis.[218]

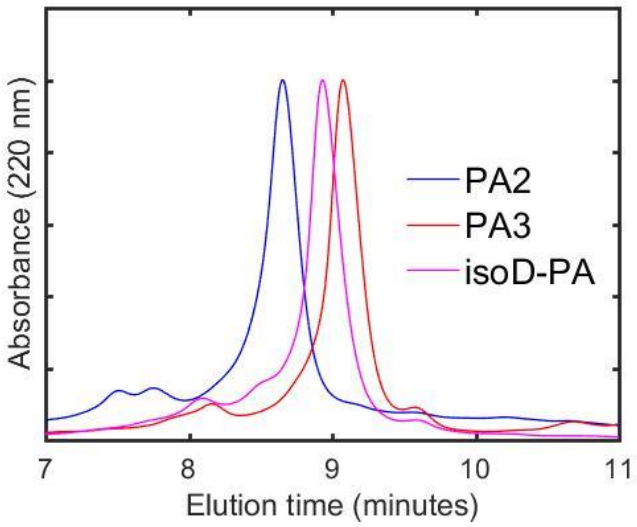


**Figure 4.4: Elution times of TGBβ-1 binding PA molecules by analytical HPLC**
Analytical HPLC traces showing elution of the asparagine containing **PA2**, the asparagine-to-aspartic acid mutated **PA3** and asparagine-to-isoaspartic acid mutated PA. The small difference in elution time prevented quantification of the relative ratio of the two products following **PA2** deamidation.

*Effect of deamidation on TGFβ-1 binding*

Since the previously reported TGFβ-1 binding PA was significantly deamidated during purification, whether deamidation affected the binding affinity of the bioactive epitope to the growth factor was next investigated. TEM and SAXS showed these molecules assembled into short filaments, and CD showed peptides had random coil secondary structure (Figure 4.5).

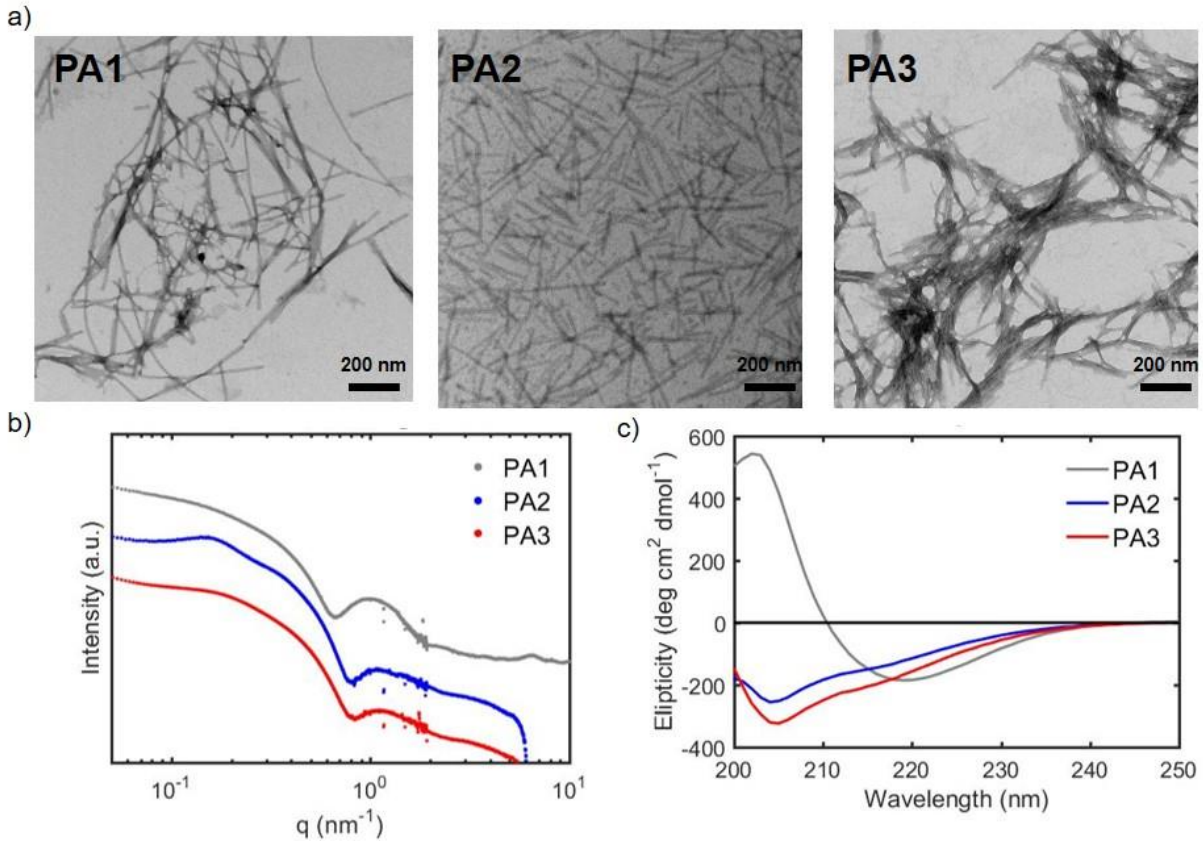


**Figure 4.5: Self-assembly of TGFβ-1 binding PAs without co-assembly**
(a) Conventional TEM images of solubilized **PA1**, **PA2**, and **PA3** without heat treatment. (b) SAXS patterns of **PA2** and **PA3** had a lower low-q slope and a higher-q minimum than **PA1**, indicating a more micelle like morphology with a smaller radius than the **PA1** fibers. (c) CD showed that while **PA1** formed β-sheet, the **PA2** and **PA3** structures had a random coil secondary structure prior to co-assembly.

Binding of **PA2** and **PA3** molecules to TGFβ-1 was assessed using Biolayer Interferometry, a label-free technique for measuring bimolecular interactions,[219] by measuring association of the epitope bearing PA molecules to a growth factor coated sensor. **PA2**, which displays the asparagine sequence derived from phage-display, bound the coated probe with a $K_D$ of 39 ± 12 μM (Figure 4.6a). **PA3** had a similar binding affinity ($K_D$ = 36 ± 14 μM) to the coated

probe, indicating the deamidation substitution to aspartic acid on its own did not significantly diminish growth factor binding (Figure 4.6b).

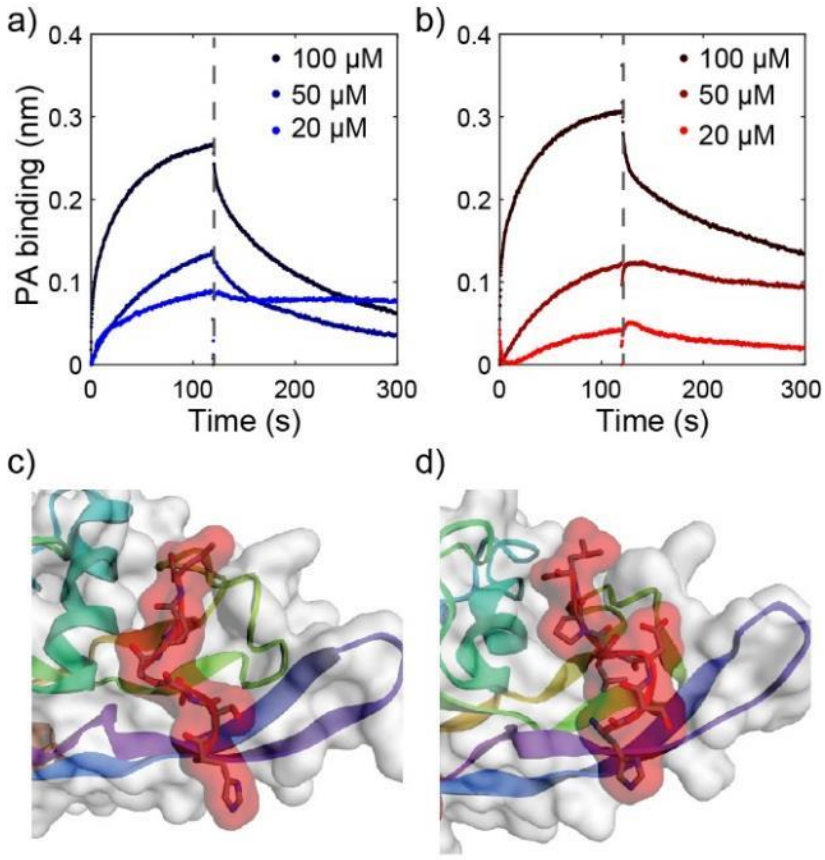


**Figure 4.6: Epitope binding to TGFβ-1**
Biolayer interferometry binding curves of **PA2** (a) and **PA3** (b) association (120 s) and dissociation (180 s) to TGFβ-1 coated probes obtained at several PA concentrations. Molecular graphics of the most likely conformation of the asparagine epitope (c) and the aspartic acid epitope (d) to TGFβ-1 simulated by CABS-Dock.

Because the change in binding affinity due to deamidation was minimal, both peptides were expected to be able to bind the growth factor at the same binding pocket. To validate this hypothesis, blind Monte Carlo simulations of peptide binding were implemented using the CABS-dock software package,[220] which produced the 10 most likely binding conformations by mathematically clustering the locations of the peptide at the end of 1000 independent model

runs. Root mean square deviation (RMSD) and cluster density for these conformations are given in Table 4.1. In the predicted conformations, both peptides bound the growth factor at the same pocket deep between the two monomers that comprise the TGFβ-1 dimer (Figure 4.6c,d). Interestingly, this binding motif mimics the binding of TGFβ-1 to latency associated peptide (LAP), which is bound to TGFβ-1 following biosynthesis and is cleaved in order to activate the cytokine.[221] The leucine- and isoleucine-rich α1 helix in LAP is known to interact with tryptophan residues on the growth factor,[222] and CABS-dock model showed that these same tryptophan residues are in close proximity to the leucine residues on the bound peptides (Figure 4.7).

**Table 4.1: RMSD and cluster density values over three independent CABS-dock simulations**

| | *Model #* | *Density* | *Avg RMSD* | *Max RMSD* | *# of Elements* |
|---|---|---|---|---|---|
| **HSNGLPL** | 1 | 62.6 | 2.2 | 8.6 | 139 |
| | 2 | 34.9 | 2.0 | 5.5 | 70 |
| | 3 | 33.2 | 2.9 | 7.6 | 97 |
| | 4 | 33.0 | 2.3 | 7.2 | 79 |
| | 5 | 25.2 | 1.7 | 5.1 | 44 |
| | 6 | 51.7 | 1.6 | 7.1 | 83 |

| | *Model #* | *Density* | *Avg RMSD* | *Max RMSD* | *# of Elements* |
|---|---|---|---|---|---|
| **HSDGLPL** | 1 | 63.8 | 2.8 | 9.6 | 179 |
| | 2 | 52.1 | 2.7 | 13.0 | 142 |

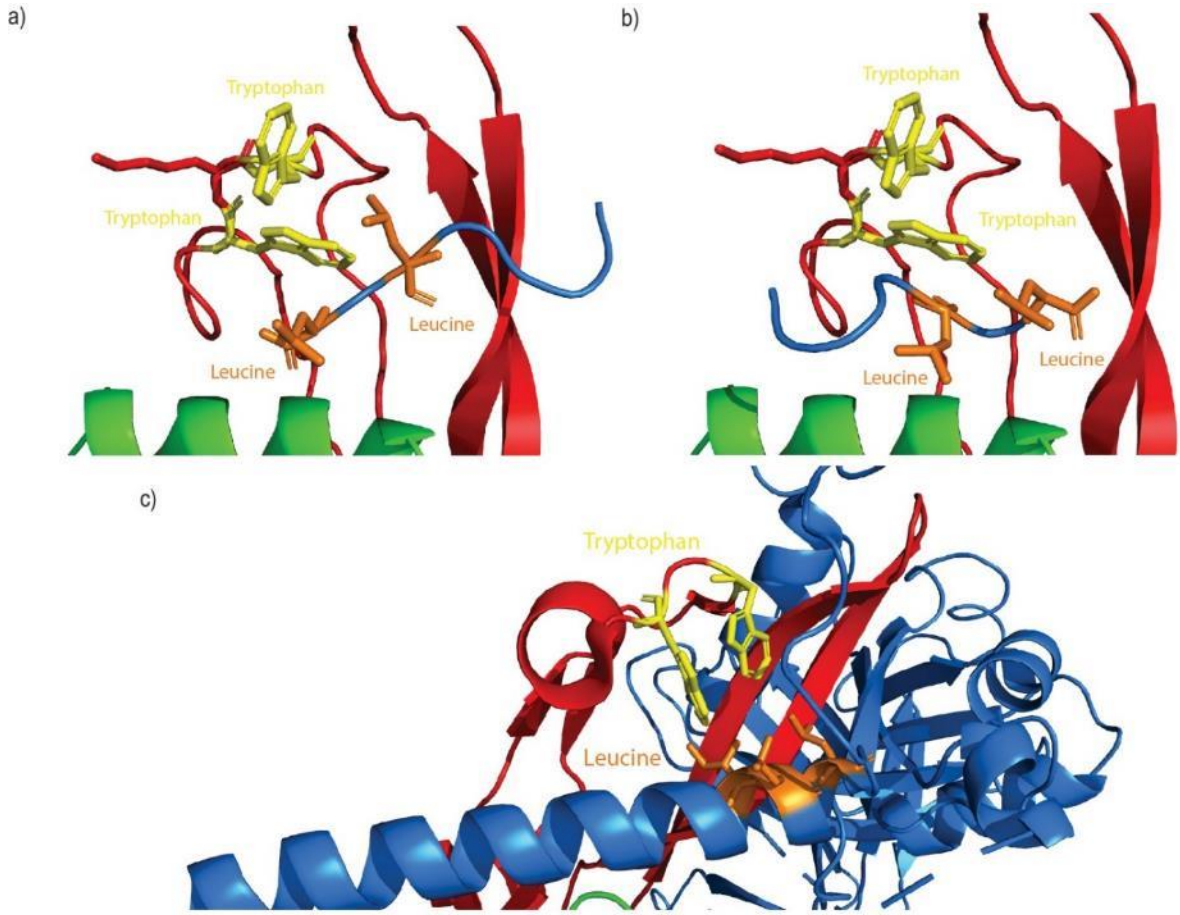


**Figure 4.7: Binding simulations of peptide epitopes to TGFβ-1**
CABS-dock simulated binding conformations of (a) HSNGLPL peptide sequence and (b) HSDGLPL peptide sequence to TGFβ-1, and (c) previously reported binding conformation of LAP to TGFβ-1.[222] Tryptophan residues on TGFβ-1 are marked in yellow and leucine residues on the binding peptides or leucine and isoleucine residues on LAP are marked in orange.

The binding energy of the peptides to the growth factor at the predicted site were estimated using the molecular modeling software Autodock Vina,[223] which gave a binding energy for the asparagine epitope of -6.0 ± 0.3 kcal/mol ($K_D$ = 40 ± 26 μM), compared to -5.6 ± 0.3 kcal/mol ($K_D$ = 78 ± 51 μM) for the aspartic acid sequence (Table 4.2). These data indicate that deamidation does not strongly affect the binding affinity of the peptide to TGFβ-1, which led us to investigate

next if the ability of the PA nanofiber gels to prolong growth factor release and induce chondrogenesis is significantly affected by the conversion.

**Table 4.2: Highest frequency trajectories for each peptide from 4 independent model**

| HSNGLPL | *Model Run #* | | | |
|---|---|---|---|---|
| | *1* | *2* | *3* | *4* |
| *1* | -6.2 | -6.6 | -6.1 | -6.6 |
| *2* | -6.2 | -6.4 | -5.9 | -6.5 |
| *3* | -6.1 | -6.4 | -5.8 | -6.3 |
| *4* | -6 | -6.3 | -5.8 | -6.3 |
| *5* | -6 | -6.1 | -5.8 | -6.2 |
| *6* | -5.9 | -6.1 | -5.7 | -6.2 |
| *7* | -5.9 | -6 | -5.5 | -6.1 |
| *8* | -5.9 | -6 | -5.4 | -6 |
| *9* | -5.8 | -5.9 | -5.4 | -6 |
| Avg [kcal/mol] | -6.0 | -6.2 | -5.7 | -6.2 |
| St Dev | 0.1 | 0.2 | 0.2 | 0.2 |

| | [kcal/mol] | [μM] |
|---|---|---|
| Overall Avg | -6.0 | 37.2 |
| Overall St Dev | 0.3 | |

| HSDGLPL | *Model Run #* | | | |
|---|---|---|---|---|
| | *1* | *2* | *3* | *4* |
| *1* | -6 | -6.1 | -5.5 | -6.4 |
| *2* | -6 | -6 | -5.4 | -6 |
| *3* | -6 | -5.9 | -5.3 | -6 |
| *4* | -6 | -5.8 | -5.2 | -6 |
| *5* | -6 | -5.6 | -5.2 | -5.9 |
| *6* | -6 | -5.6 | -5.2 | -5.8 |
| *7* | -6 | -5.6 | -5.1 | -5.8 |
| *8* | -6 | -5.5 | -5 | -5.7 |
| *9* | -6 | -5.5 | -5 | -5.7 |
| Avg Avg [kcal/mol] | -6.0 | -5.7 | -5.2 | -5.9 |
| St Dev | -6.0 | 0.2 | 0.2 | 0.2 |

| | [kcal/mol] | [μM] |
|---|---|---|
| Overall Avg | -5.7 | 64.1 |
| Overall St Dev | 0.4 | |

*Growth factor release by TGFβ-1 binding PA hydrogels*

In order to investigate prolonged release of TGFβ-1, **PA2** or **PA3** were co-assembled with the diluent **PA1**, forming binding epitope displaying filaments that gelled upon addition of calcium. To produce co-assembled structures, each PA was dissolved separately to the same molar concentration and then mixed the solutions volumetrically to achieve the desired ratio. After mixing, the solutions were bath sonicated for 1 hour, heated to 80°C, and cooled to room temperature. Using cryo-TEM imaging of samples preserved in vitreous ice showed that co-assembly of 90 mol% **PA1** with 10 mol% of either **PA2** or **PA3** did not disrupt the one-dimensional

fiber morphology observed in **PA1** alone. The micrographs showed more ribbon-like filaments for **PA2/PA1** co-assemblies and aggregation of the filaments that was not present in solutions of **PA1** alone, while less filament aggregation occurred in **PA3/PA1** mixtures (Figure 4.8a).

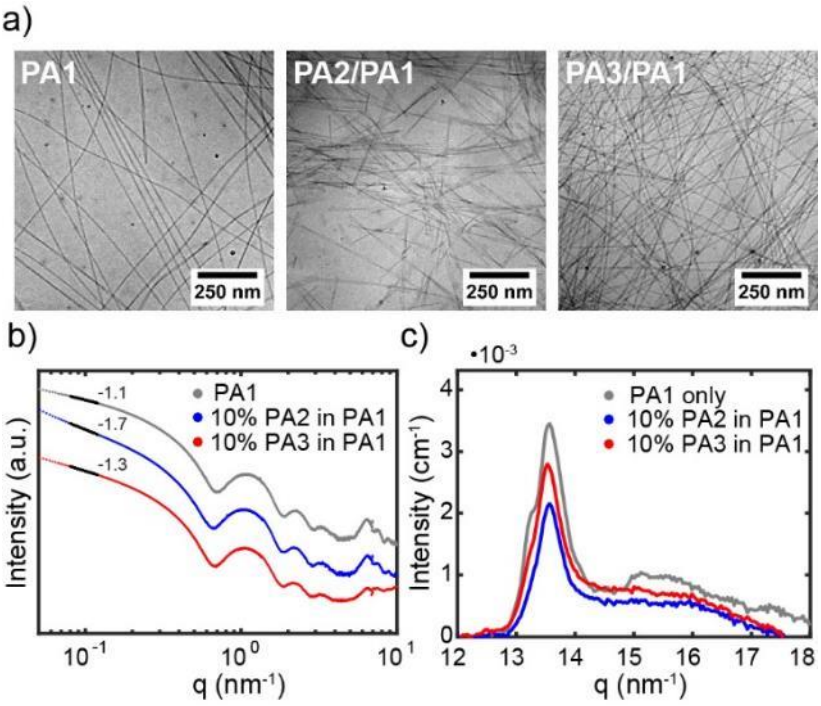


**Figure 4.8: Self-assembly of TGFβ-1 binding PA filaments**
(a) Cryo-TEM images of PA filaments preserved in vitreous ice. SAXS (b) and WAXS (c) patterns of 8 mM PA solutions of **PA1** alone and **PA1** co-assembled with 10 mol% **PA2** or **PA3**.

TEM imaging of PA nanofibers negative stained with uranyl acetate for high contrast showed similarly bundled and aligned fibers in the co-assembly of **PA2** and **PA1**, but not for **PA1** alone or in the co-assembly of **PA1** and **PA3** (Figure 4.9a). SAXS scans for **PA1** confirmed the nanofiber morphology observed by TEM with a low-q slope of -1.1. When co-assembled with **PA2**, the observed slope increased to -1.7, consistent with fiber aggregation. However, when co-assembled with **PA3** the slope increased slightly to -1.3, suggesting less aggregation of the filaments as indicated also by electron microscopy (Figure 4.8b). Apart from this change in slope,

scattering patterns for all three systems were similar, indicating co-assembly did not significantly change fiber morphology. To confirm the binding PA molecules co-assembled with the diluent PA, changes in intermolecular interactions among the PA molecules were investigated. **PA2** and **PA3** have a shorter alkyl hydrophobic segment conjugated to the ε-amino group in a lysine residue side chain at the C-terminus rather than a longer alkyl chain conjugated to the N-terminus of the peptide in **PA1**.

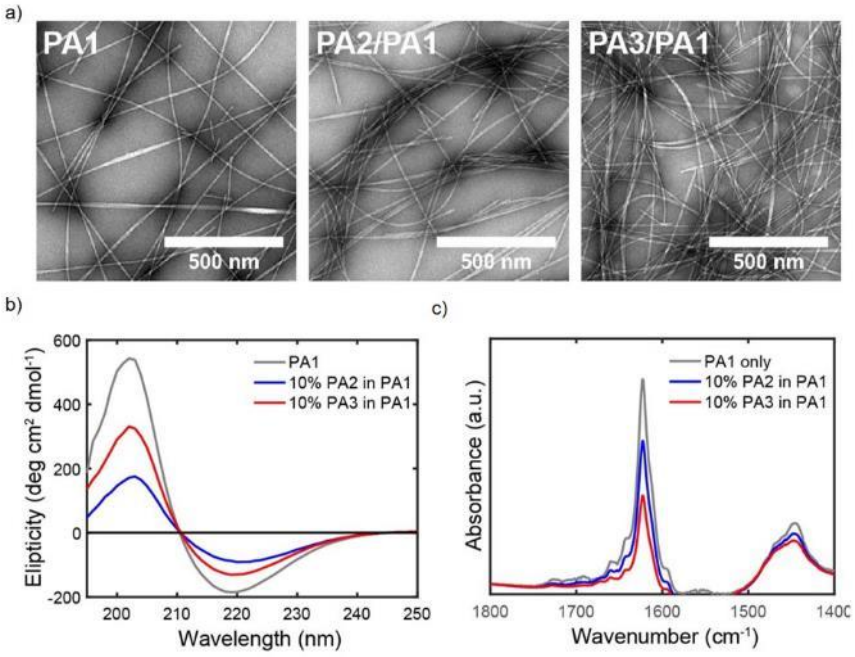


**Figure 4.9 Co-assembly of TGFβ-1 binding PA molecules and diluent PA**
(a) Negative stained TEM images of PA solutions. **PA1** shows separate. 10% **PA2** in **PA1** shows parallel fibers arranged in a bundle, and **PA3** in **PA1** shows largely separate fibers. (b) CD and (c) FTIR spectra indicate a decrease in β-sheet character following addition of **PA2** or **PA3** supporting co-assembly into diluent PA fibers.

This difference may disrupt supramolecular packing of PA molecules within the nanofiber and thus weaken intermolecular bonds. Indeed, WAXS of **PA1** reveals a strong peak corresponding to a d-spacing of 4.65 Å, indicating supramolecular ordering within these

assemblies consistent with the expected separation of β-sheet-forming strands.[224] Upon addition of **PA2** or **PA3**, the intensity of this Bragg peak decreased, suggesting that insertion of the binding PA in the co-assemblies led to some disruption of intermolecular packing order (Figure 4.8c). CD likewise showed a decrease in β-sheet signal with the addition of the binding PA molecules (Figure 4.9b), FTIR also revealed a decrease in the amide I′ peak at 1624 $cm^{-1}$ associated with β-sheet ordering within the assemblies (Figure 4.9c). These results support self-assembly of both molecules with a decrease in internal order relative to nanofibers formed by the diluent PA molecules.

After confirming that **PA2** and **PA3** co-assembled with **PA1** to form binding epitope-displaying PA nanofibers, the next experiments comparted how mutation of the bioactive sequence affected the ability of gels to prolong TGFβ-1 release. A TGFβ-1 solution was mixed with a solution of PA filaments, formed a hydrogel by adding a calcium chloride solution,[99] and added TBS on top of the gels to measure the rate of growth factor release into the TBS solution. Surprisingly, **PA2/PA1** co-assemblies containing the asparagine binding epitope selected by phage-display released over 25% more TGFβ-1 over 3 weeks than **PA3/PA1** co-assemblies containing the mutated aspartic acid epitope that mimics the deamidated product. However, both co-assemblies revealed the capacity to limit the release of growth factor relative to gels composed of **PA1** alone (Figure 4.10a). Fitting the data to a two-phase exponential indicated that differences in binding PA co-assemblies vs. diluent PA assemblies were due primarily to greater growth factor release in the burst phase compared to the subsequent sustained release phase. **PA2/PA1** and **PA3/PA1** co-assemblies released a similar amount of growth factor during the burst release phase, but during the sustained release phase the rate constant of **PA2/PA1** ($0.0100 \pm 0.0048$ $days^{-1}$) exceeded that of **PA3/PA1** ($0.0033 \pm 0.0019$ $days^{-1}$), leading to significantly greater total release

by day 7. This indicates that while more growth factor was retained by **PA2/PA1** gels relative to those formed by **PA1** alone at early times, weaker association of TGFβ-1 by **PA2/PA1** gels led to greater sustained release than gels formed by **PA3/PA1** supramolecular co-assemblies over the 21 day experiment (Table 4.3).

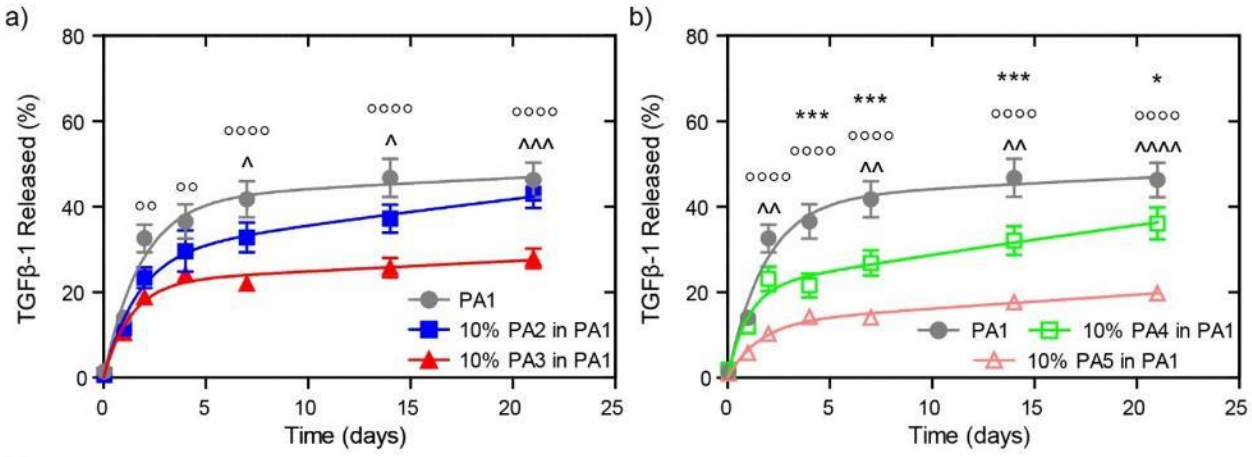


**Figure 4.10: TGFβ-1 retention by PA hydrogels**
(a) Plot of percent cumulative TGFβ-1 released as a function of time from gels comprising only the diluent **PA1**, **PA1** co-assembled with 10 mol% of the asparagine containing **PA2**, and **PA1** co-assembled with 10 mol% of the aspartic acid-containing **PA3** (*, **PA1** vs. **PA2/PA1**; °, **PA1** vs. **PA3/PA1**; ^, **PA2/PA1** vs**. PA3/PA1**); and (b) from gels where glutamic acid residues and not PEG were used in the hydrophilic domain comprising only the diluent **PA1**, **PA1** co-assembled with 10 mol% of the asparagine containing **PA4**, and **PA1** co-assembled with 10 mol% of the aspartic acid-containing **PA5** (*, **PA1** vs. **PA4/PA1**; °, **PA1** vs. **PA5/PA1**; ^, **PA4/PA1** vs**. PA5/PA1**). Curves were fit to a two-phase exponential release model. (*/^, $p < 0.05$; °°/^^, $p < 0.01$; ***/^^^, $p < 0.001$; °°°°/^^^^, $p < 0.0001$)

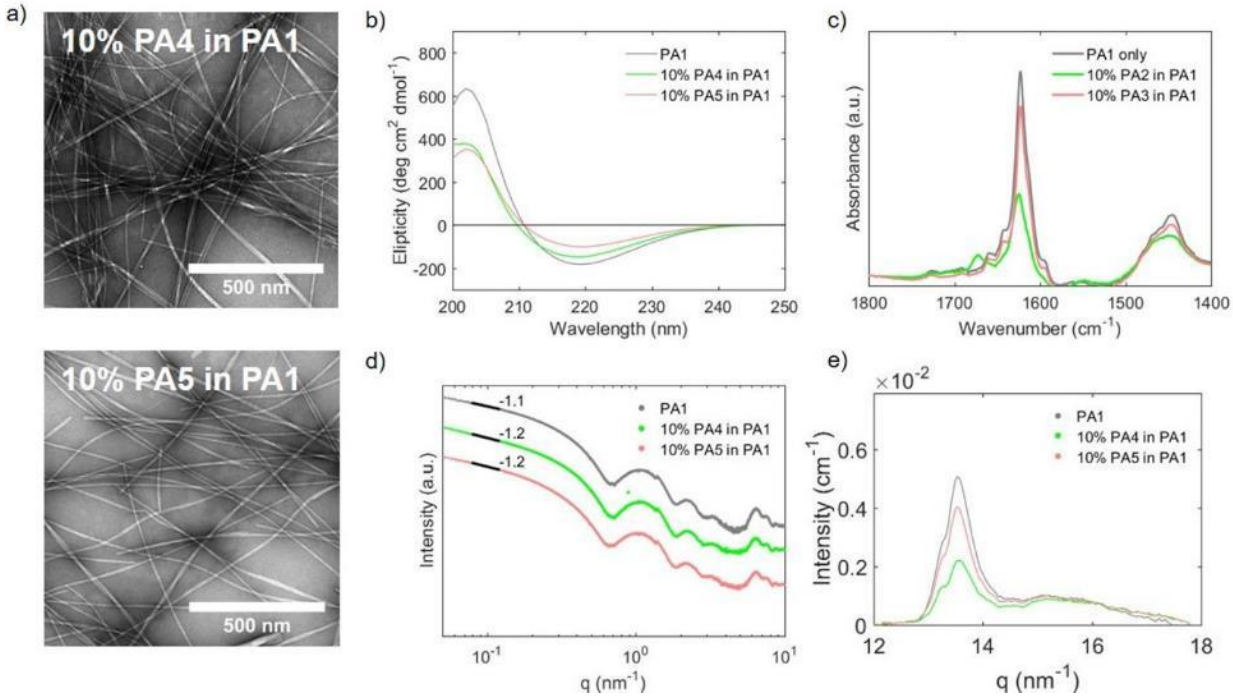


**Figure 4.11: Self-assembly of anionic backbone TGFβ-1 binding PA filaments**
(a) Negative Stained TEM imaging of 10% **PA4** in **PA1** and 10% **PA5** in **PA1** revealed fiber morphologies with some bundling in both samples. (b) CD and (c) FTIR showed a decrease in β-sheet character following co-assembly of either PA. (d) SAXS scattering confirmed fiber-like morphologies for the co-assemblies and (e) WAXS confirmed a decrease in β-sheet character following co-assembly.

To confirm that the difference in growth factor retention was not a result of the PEG chain, **PA1** was co-assembled with 10 mol% of **PA4**, the original PA design containing a glutamic acid hydrophilic region and a partially deamidated binding sequence, or with 10 mol% **PA5**, its aspartic acid mutant counterpart (see Figure 4.1a). These systems formed co-assembled nanofibers (Figure 4.11) and allowed for quantification of growth factor release from gels prepared with these supramolecular nanofibers. TGFβ-1 release studies followed the trend observed in the PA systems with a PEG linker in the binding PA. Specifically, **PA5/PA1** co-assemblies displaying the aspartic acid sequence retained more growth factor than **PA4/PA1** co-assemblies displaying primarily the asparagine sequence, which in turn retained more growth factor than **PA1** alone (Figure 4.10b).

Interestingly, both the asparagine sequence and the aspartic acid sequence co-assemblies had similar rate constants during the sustained release phase to their PEG-linker counterparts, suggesting that the binding sequence and not PEGylation determines the sustained release kinetics (Table 4.3). Contrary to the initial hypothesis that deamidation limited TGFβ-1 binding, conversion of the previously reported PA likely prolonged growth factor retention by the co-assembled PA fiber systems and may have improved its biological efficacy.

**Table 4.3: Fit-parameters for release kinetics of TGFβ-1 from PA hydrogels**

| Two-phase Association | **PA1** | **PA2/PA1** | **PA3/PA1** | **PA4/PA1** | **PA5/PA1** |
|---|---|---|---|---|---|
| Plateau (%) | 100 | 100 | 100 | 100 | 100 |
| Y0 (%) | 0 | 0 | 0 | 0 | 0 |
| Percent Fast | 41.8 | 28.9 | 22.4 | 21.0 | 12.8 |
| $K_{Fast}$ ($days^{-1}$) | 0.54 | 0.60 | 0.75 | 1.00 | 0.66 |
| $K_{Slow}$ ($days^{-1}$) | 0.0045 | 0.0100 | 0.0033 | 0.0103 | 0.0040 |
| Fast Half-Life (days) | 1.27 | 1.15 | 0.92 | 0.69 | 1.05 |
| Slow Half-Life (days) | 155.4 | 69.15 | 211.9 | 67.56 | 175.2 |

| Standard Error | **PA1** | **PA2/PA1** | **PA3/PA1** | **PA4/PA1** | **PA5/PA1** |
|---|---|---|---|---|---|
| Percent Fast | 6.0 | 4.9 | 2.1 | 3.2 | 1.2 |
| $K_{Fast}$ ($days^{-1}$) | 0.15 | 0.21 | 0.17 | 0.43 | 0.13 |
| $K_{Slow}$ ($days^{-1}$) | 0.0067 | 0.0048 | 0.0019 | 0.0032 | 0.0009 |

| Goodness of Fit | **PA1** | **PA2/PA1** | **PA3/PA1** | **PA4/PA1** | **PA5/PA1** |
|---|---|---|---|---|---|
| Degrees of Freedom | 32 | 32 | 32 | 32 | 32 |
| R square | 0.83 | 0.83 | 0.87 | 0.78 | 0.93 |

*Superstructure formation by growth factor binding PA filaments*

Next, the supramolecular structure of the TGFβ-1 binding nanofiber system was explored to determine why conversion from asparagine to aspartic acid prolongs growth factor release, despite not improving the binding affinity of the peptide alone. SEM showed that nanostructures containing co-assemblies of **PA1** and **PA2** and gelled with 25 mM $CaCl_2$ formed bundles of filaments. However, only limited bundling occurred in co-assemblies with **PA3** and none at all in

gels formed by **PA1** nanofibers alone (Figure 4.12a). Dynamic light scattering (DLS) of solutions of sonicated assemblies showed that **PA2/PA1** co-assemblies formed larger particles relative to **PA3/PA1** co-assemblies or **PA1** fibers alone, further confirming the observations of bundling by SEM (Figure 4.12b). Stupp and colleagues previously reported that extending a fraction of the PA molecules in a negatively charged nanofiber containing glutamic acid residues with a peptide domain containing multiple lysine residues resulted in PA nanofiber superstructures (bundled filaments).[128] Because **PA2** has a more positive net charge than **PA3**, the observed bundling suggested fibers displaying the asparagine-containing epitopes had a greater propensity to form fiber bundles by the same mechanism. In a previous study, bundling among neighboring PA nanofibers that display signals to cells on their surfaces was reported to lower their bioactivity due to masking of the peptide epitopes within the aggregates.[106] Because the TGFβ-1 binding epitopes on **PA2** and **PA3** are positively charged while the diluent **PA1** is negatively charged, surface charge was expected to correlate with availability of the binding sequence. When zeta potential (ζ-potential) of the supramolecular nanofibers was used to quantify their surface charge, **PA2/PA1** co-assemblies were more negatively charged than **PA1** alone, despite an expected epitope net charge of +2. This may reflect changes in ionization of carboxyl groups on the surfaces of **PA2/PA1** assemblies. In contrast, **PA3/PA1** co-assemblies were slightly less negatively charged than **PA1** alone, as expected for the epitope with a net charge of +1 (Figure 4.12c).

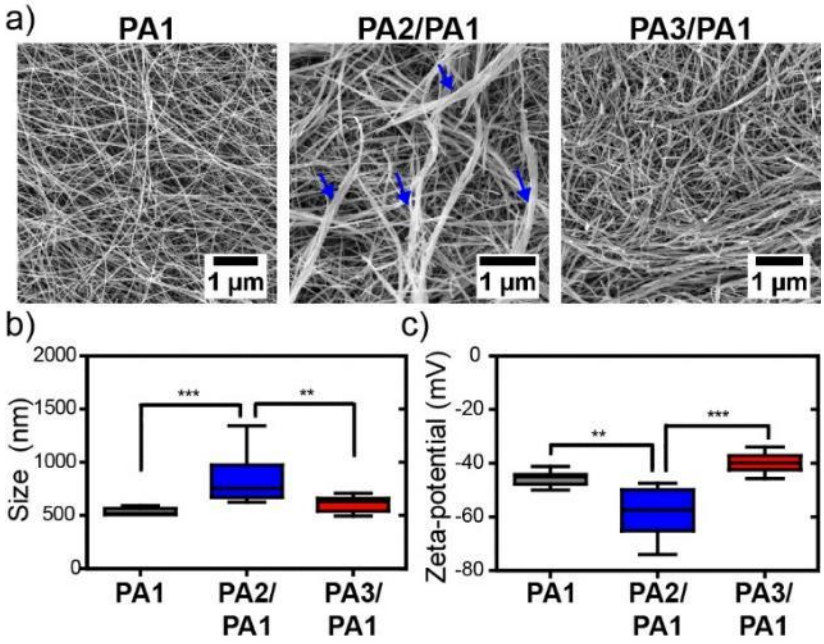


**Figure 4.12: Superstrucutre formation by TGFβ-1 binding PA filaments**
(a) SEM images of PA gels formed by the addition of aqueous calcium with arrows pointing to filament bundles. (b) DLS measurements of diluted PA nanofiber solutions sonicated before measurement, and (c) zeta potential measurements of the same PA samples to measure surface charge. (**, $p < 0.01$; ***, $p < 0.001$)

These results suggested that bundling of **PA2/PA1** nanofibers buried the growth factor binding epitope within the structures, leaving only negatively charged diluent PA molecules exposed to the surface. In **PA3/PA1** co-assemblies, the lower net charge of the epitope limited bundle formation, so binding sequences were available on the surface of the structures, increasing surface charge. To confirm changes in growth factor release rates were not caused by changes in the mechanical properties of the gels, rheological measurements showed that **PA2/PA1** and **PA3/PA1** had similar storage moduli (Figure 4.13). These data suggest that in supramolecular biomaterials, the ability to bind bioactive signals depends not only on the chemistry designed specifically to do so but also on the ability of the bioactive components to alter the structure of

assemblies in ways that mask display of the signals to cells. The superstructures observed here in **PA2/PA1** assemblies is a good example of this principle.

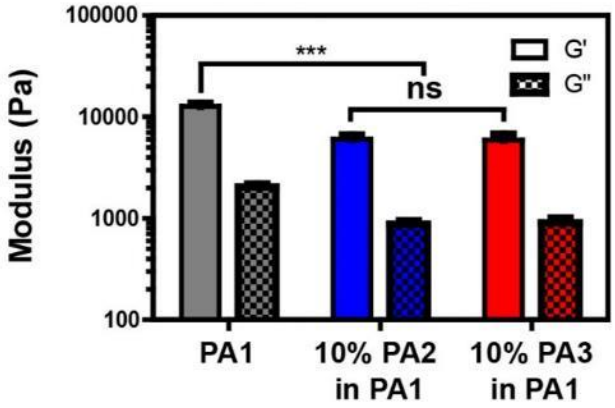


**Figure 4.13: Mechanical properties of TGFβ-1 binding PA hydrogels**
Rheological measurements of calcium gelled solutions of PA solutions obtained at 0.1% strain and a 10 rad/s frequency showed **PA1** alone had a higher storage modulus than **PA2/PA1** or **PA3/PA1** co-assemblies. The storage moduli of co-assembled fibers were similar to each other.

*Chondrogenesis by cells encapsulated in TGFβ-1 binding PA gels*

Having determined that the PA co-assemblies including the aspartic acid binding sequence prolong TGFβ-1 release compared to those containing asparagine-containing binding sequences, further experiments tested whether these gels could improve chondrogenesis in response to the growth factor, using the ATDC5 cell line known to model skeletal development *in vitro*.[225] Cytotoxicity assays confirmed cells could be encapsulated in gels of all the PA compositions tested without adversely affecting cell survival (Figure 4.14).

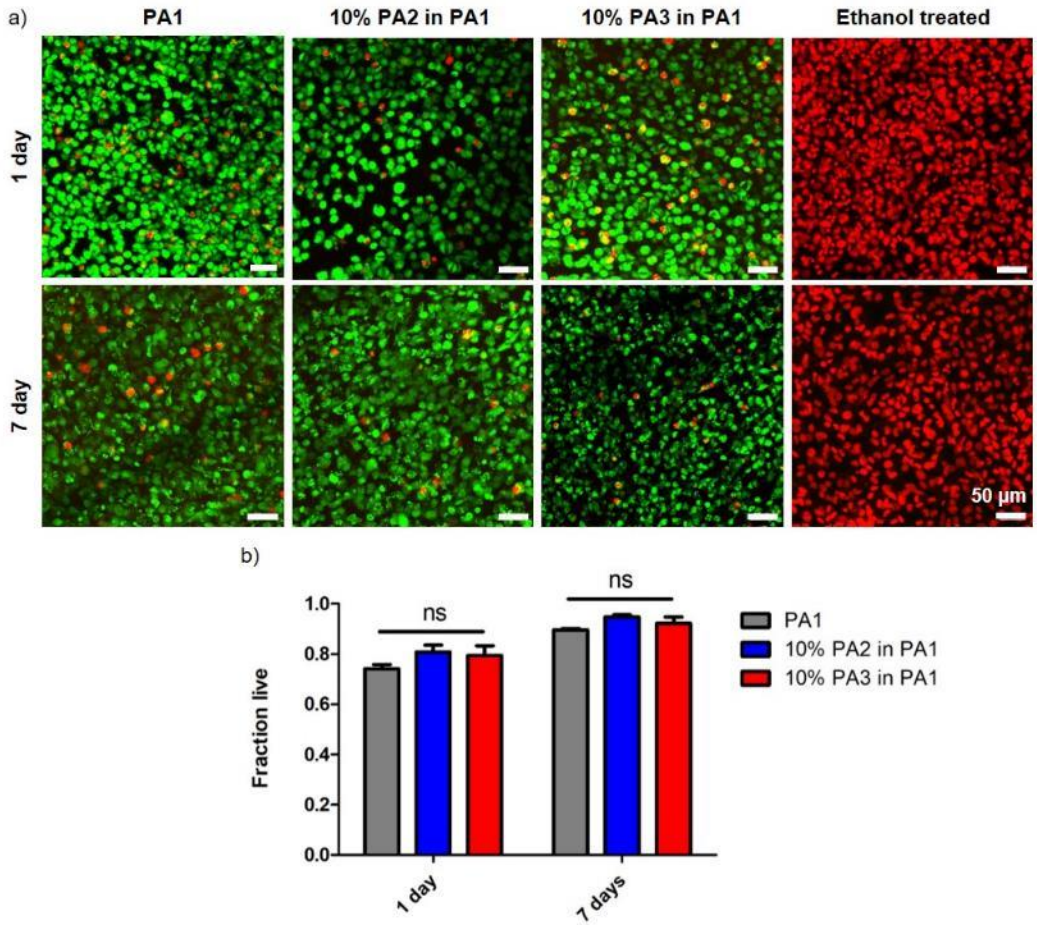


**Figure 4.14: Cell-compatibility of TGFβ-1 binding PA hydrogels**
(a) Live-dead staining of ATDC5 cells encapsulated in PA gels after 1 day and after 7 days of culture. Live cells are stained with calcein in green and dead cells with propidium iodide in red. (b) Quantification of fraction of cells stained with calcein.

To determine the effect of encapsulated TGFβ-1 on early chondrogenic differentiation, cells were encapsulated in PA gels, some of which were pre-loaded with either 10 ng/ml TGFβ-1 or 100 ng/ml TGFβ-1. After three days in culture, confocal imaging showed that cells encapsulated in **PA1** gels appeared more condensed within the gels, while in the **PA3/PA1** co-assemblies cells were round and well distributed (Figure 4.15a). The fraction of cells cultured in **PA2/PA1** co-assemblies that expressed Sox 9, an early marker of chondrogenesis, did not increase relative to

cells cultured in **PA1** alone regardless of the amount of TGFβ-1 pre-loaded in the gels. However, significantly more cells cultured in **PA3/PA1** gels expressed the marker when 10 ng/ml TGFβ-1 was pre-loaded in the gels (Figure 4.15b). To evaluate chondrogenic differentiation of the cells at later times, sulfated glycosaminoglycan (sGAG) production was quantified after three weeks in culture using the dimethylmethylene blue (DMMB) assay.[226] Cells cultured in both **PA2/PA1** co-assemblies and **PA3/PA1** co-assemblies produced more sGAG than cells cultured in **PA1** alone with 10 ng/ml TGFβ-1 pre-loaded in the gels (Figure 4.15c).

While better retention of the growth factor led to more chondrogenesis at the lowest tested TGFβ-1 loading concentration, these results suggest that when a large amount of the growth factor was pre-loaded in the gels there was enough available to induce chondrogenic differentiation regardless of binding affinity. Because **PA1/PA2** co-assemblies were less able to retain the growth factor, the PA system may not have improved expression of Sox 9 at early times. However, analytical HPLC showed deamidation occurred more rapidly in culture media than in TBS alone (Figure 4.16). Thus, during most of the three-week culture period, **PA2** can be assumed to have been deamidated, prolonging TGFβ-1 release and enhancing sGAG production. Therefore, improved retention of TGFβ-1 by the aspartic acid-containing sequence correlated with improved chondrogenesis at both early and late times. The implications of these findings to *in vivo* performance of these systems is beyond the scope of this work. However, it is clear that systems in which growth factor binding sequences lead to superstructure formation are likely to have diminished levels of bioactivity due to their inability to fully expose their “active” surfaces. At the same time, the aspartic acid-containing binding sequences should be more reproducibly bioactive by eliminating the uncertainty of degree of deamidation *in vivo*.

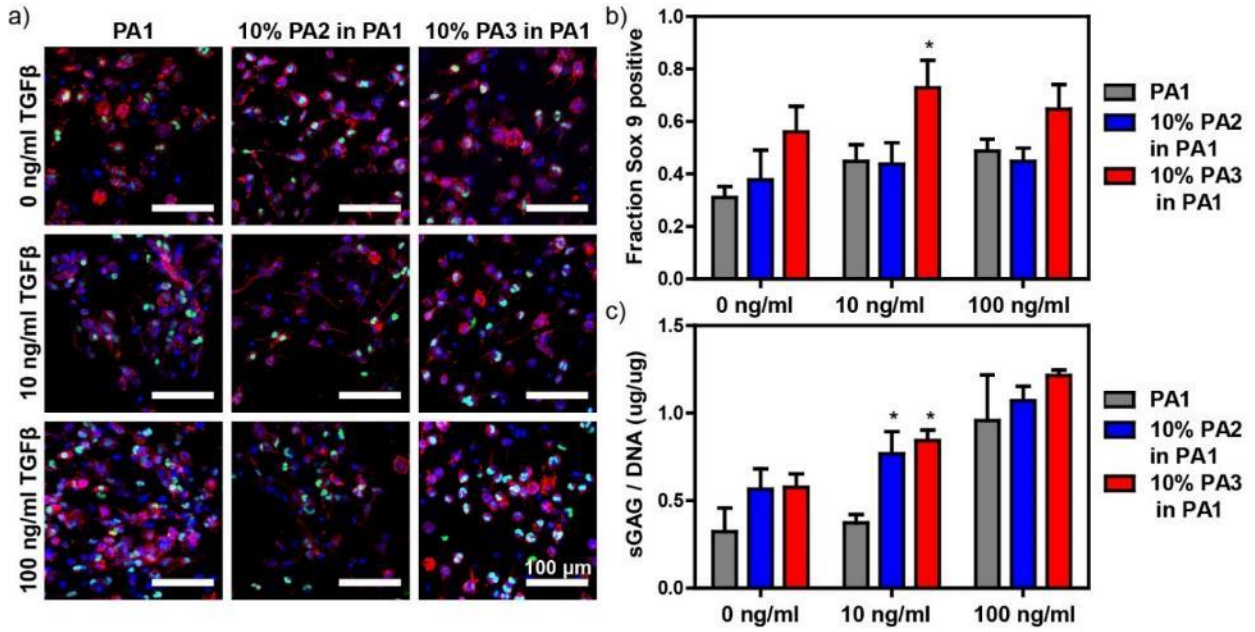


**Figure 4.15: chondrogenesis induced by TGFβ-1 releasing PA hydrogels**

(a) Cells cultured in PA gels with immunocytochemistry with nuclei stained with Hoechst 33258 in blue, Sox 9 stained with an anti-Sox 9 primary antibody in green, and actin stained with phalloidin in red. (b) Quantification of Sox 9 positive cells after 3 days of culture by counting fraction of cells nuclei stained positive for Sox 9 and (c) quantification of sGAG production after 3 weeks in culture using a colorimetric DMMB assay. (*, $p < 0.05$; relative to **PA1**)

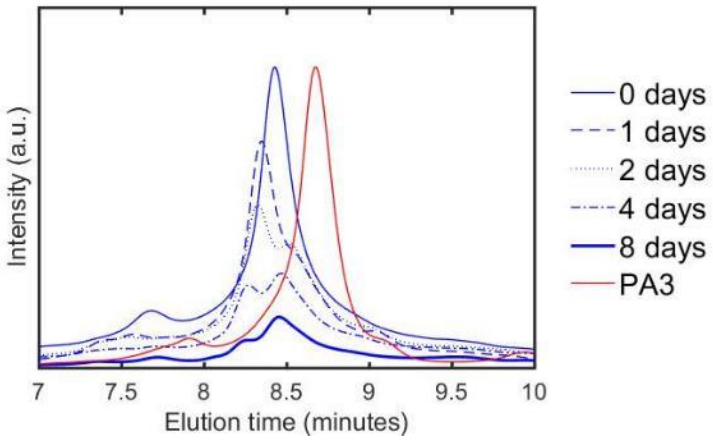


**Figure 4.16: Deamidation in cell culture conditions**

Analytical HPLC traces of **PA2** in the media used for ATDC5 culture from samples take over 8 days. The majority of the remaining PA deamidated after 4 days, and eluted at a later time at like **PA3**.

## 4.4. Conclusions

The synthesis and purification of two TGFβ-1 binding PA molecules were reported to determine if eliminating the deamidation of an asparagine side chain affected the ability of PA nanoscale filaments to retain this important growth factor. Filaments displaying an aspartic acid-containing sequence formed PA gels that were better able to prolong TGFβ-1 release relative to filaments displaying the asparagine-containing sequence evolved by phage-display. Furthermore, this work showed that superstructures in supramolecular biomaterials, such as the bundling of filaments, can interfere with bioactivity based on chemical segments selected by methodologies independent of the material's design.

## 4.5. Materials and Methods

*Synthesis and purification*: PA molecules were synthesized by solid-phase peptide synthesis using 9-fluorenyl methoxycarbonyl chemistry on a Rink amide resin (EMD Millipore, Billerica, MA, USA). Couplings of standard amino acids and the palmitic acid tail was performed at 4 equivalents in DMF with 3.95 equivalents of HBTU and 6 equivalents of DIEA. The PEG-10 amino acid (ChemPEP, Wellington, FL, USA) was coupled at 1.5 equivalents with 1.4 equivalents of benzotriazol-1-yl-oxytripyrrolidinophosphonium hexafluorophosphate as the coupling agent, and 2 equivalents of DIEA overnight. Following synthesis, PA molecules were cleaved from the resin in a 95:2.5:2.5 TFA/TIS/water mixture for 2-3 hours and precipitated in cold diethyl ether. Following cleavage, the crude peptide was dissolved in 0.1% ammonium hydroxide for basic HPLC or dissolved in 0.1% TFA for acidic HPLC as indicated. Purity of crude and purified samples was assessed by an Agilent 6520 Q-TOF ESI-MS instrument, using a Phenomenex Jupiter C18 analytical column (acidic conditions) or a Phenomenex Gemini C18 analytical column (basic

conditions). LC-MS was run over a 5% to 95% acetonitrile gradient with 0.1% formic acid for acidic conditions and 0.1% ammonium hydroxide for basic conditions. A total ion chromatogram was obtained in MS mode and integrated using Mass Hunter Agilent software. Purified material was stored dry at -20°C and periodic LC-MS prior further experiments confirmed no deamidation occurred during storage.

*Deamidation characterization by analytical HPLC:* PA solutions were dissolved at 0.1 wt% in TBS or cell culture media (1:1 DMEM:Ham's, 5% fetal bovine serum, 1% penicillin streptomycin), and incubated at 37°C in sterile conditions. Samples were removed and stored at -20°C immediately following dissolution and at several time points over 8 days. Deamidation was assessed by analytical reverse phase HPLC over a 5% to 50% acetonitrile gradient in 0.1% TFA to prevent further deamidation during the test.

*Solubilization and heat treatment:* Samples were prepared by dilution in water and pH adjusted with 1 M NaOH to pH 7. Care was taken to avoid reaching a pH higher than 7 for any sample. For co-assembled samples, PA solutions at the same molar concentration were mixed volumetrically and bath sonicated for 1 hour, followed by resting for 2 hours. Samples were heating to 80°C for 30 minutes followed by gradual cooling by 1°C / minute.

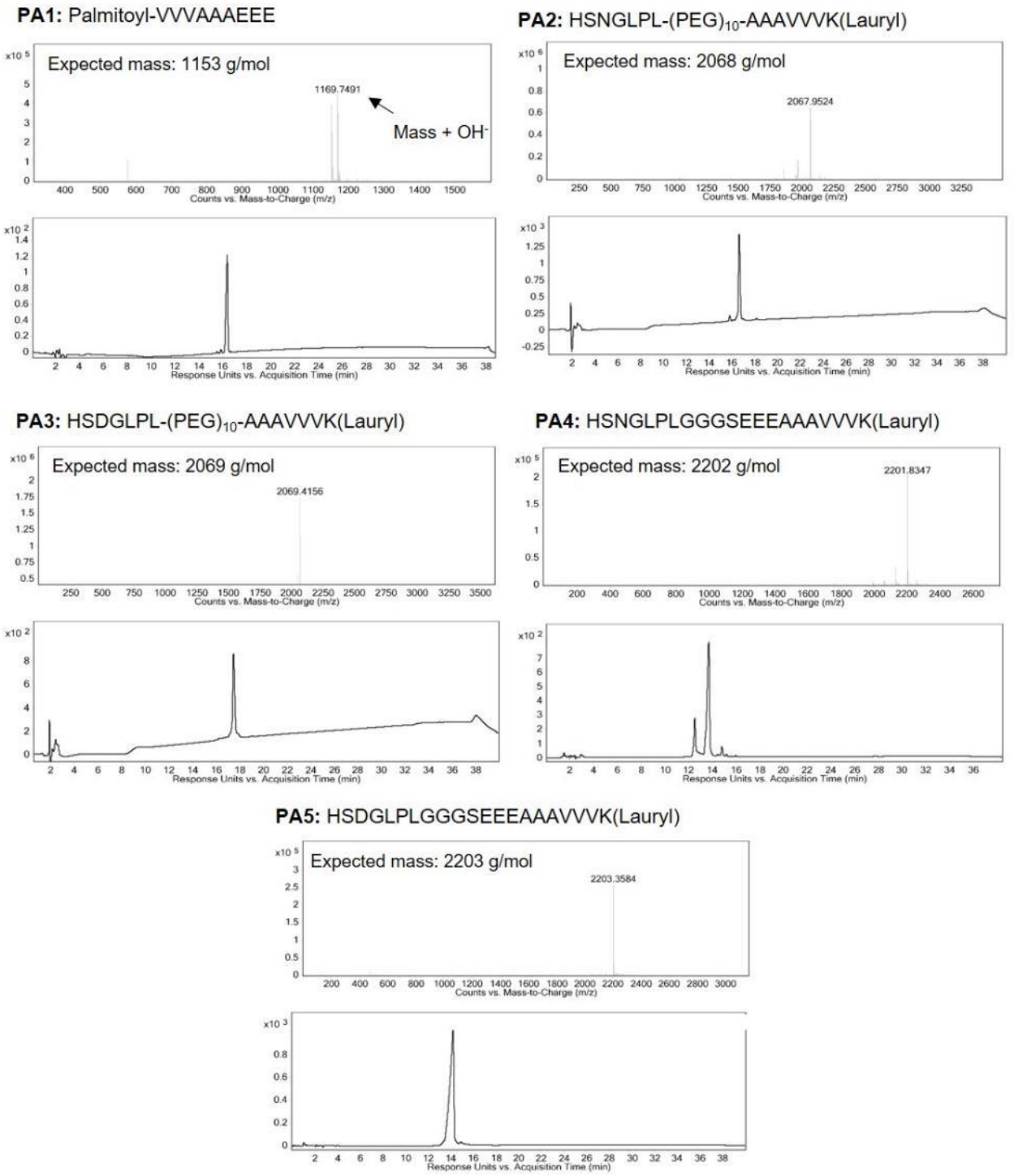


**Figure 4.17: Chemical characterization of TGFβ-1 binding PAs and diluent PA**

Chemical structures of each PA investigated. MS confirmed expected mass following synthesis and purification and LC-MS confirmed at least 95% purity for each PA (except for **PA4** which deamidated during purification).

*Biolayer interferometry*: Experiments were performed on a BLItz interferometer (ForteBio, Freomnt, CA) using anti-penta-His tag probes. Probes were functionalized by treatment with a 20 μl/ml recombinant histidine-tagged TGFβ-1 (Abcam, Cambridge, UK) in water for three minutes. Prior to experiment, PA solutions were bath sonicated for 1 hour. Functionalized probes were exposed to PA solutions at several concentrations for two minutes of association, followed by three minutes of dissociation in water. Association-dissociation curves for three separate tests were averaged and the global $K_D$ was computed for all replicates at all concentrations tested using the BLItz software.

*Peptide docking simulation*: Simulations were performed using the CABS-dock server, with TGFβ-1 pdb structure acquired from the online Protein Data Bank (1KLA, RCSB.org) and generated via multinuclear NMR spectroscopy measurements. Binding epitopes were each evaluated as an independent molecule from PA structures to monitor any differences arising purely from the exchange of asparagine and aspartic acid residues. Briefly, random peptide structures were created by the software, followed by Replica Exchange Monte Carlo dynamic simulations. Subsequent filtering of models based on calculated energy minima of bound states. K-medoid clusters were generated from filtered models (1000 models total) to result in a final representation of 10 consensus models. Lastly, coarse-grained C-alpha traces were translated to all-atom representations for visualization and analysis. For docking prediction comparisons, Model #1 generated by the simulation was selected due to its ranking as the highest occurring trajectory, or most probable docking result. Contact map data was subsequently evaluated for Model #1 with a contact cutoff of 4.5 Å. Cluster densities were calculated by dividing the number of elements within the cluster by the average RMSD of all elements within the cluster. Simulated binding affinities between peptides and target protein were generated using the open-source program

AutoDock Vina (Scripps Research Institute). Affinities were calculated across four separate simulations, with each simulation containing 9 trajectories.

*Transmission electron microscopy*: PA solutions were annealed at 10 mM and then a 150 mM NaCl solution was added to a final NaCl concentration of 30 mM. Samples were diluted 5 times and 10 uL drops of each sample were cast on carbon coated copper grids (Electron Microscopy Sciences, Hatfield, PA) for 5 minutes, washed twice with water, stained twice with 4% uranyl acetate for 20 seconds, and dried. TEM maging was performed on an FEI Spirit instrument (Hillsboro, OR) at 100 kV accelerating voltage. CryoTEM was performed on a JEOL 1230 TEM at an accelerating voltage of 100KV equipped with a Gatan 831 CCD camera. PA solutions were diluted with milli-Q $H_2O$ from 8mM stocks to 1mM immediately prior to blotting. Samples were pipetted (7.0 μL) onto 300-mesh copper grids with lacey carbon support (Electron Microscopy Sciences) that were treated with glow discharge for 30 seconds prior to use. Samples were blotted twice at one second per blot before plunging into liquid ethane using a Vitrobot Mark IV (FEI) vitrification robot operating at 20$^{o}$C and 95-100% humidity. After vitrification, the samples were transferred under liquid nitrogen to a Gatan 626 cryo-holder for imaging.

*X-ray scattering:* SAXS and WAXS measurements were recorded simultaneously at beamline 5ID-D in the Dupont-Northwestern-Dow Collaborative Access Team Synchrotron Research Center at the Advanced Photon Source at Argonne National Lab. Following annealing, 10 mM PA solutions were adjusted to 30 mM NaCl with a 150 mM NaCl solution. During measurements, samples were flowed through a 1.5 mm glass capillary at 1 mm/sec for consistent background subtraction. Five exposures to 17 keV monochromatic x-rays 10 seconds in duration were collected using a CCD detector placed 245 cm behind the sample. The collected two-dimensional scattering

images were averaged by azimuthal integration using the data reduction program FIT2D and plotted against the wave vector $q = (4\pi)\sin(\theta/2)$ where $d = 2\pi/q$.

*Circular dichroism spectroscopy:* PA molecules were dissolved at 10 mM and heat treated as described. The samples were diluted 200 times in 10 mM NaCl and measurements were performed on a J-815 CD spectrophotometer (Jasco Analytic Instruments, Easton, MD) in a 2 mm quartz cuvette. The average of three spectra from 250 nm to 190 nm normalized to the number of amino acid residues in each PA is reported. For co-assemblies, the number of residues was taken as the average of the components weighted by molar fraction.

*Fourier transform infrared spectroscopy:* PA solutions were prepared at 10 mM, followed by adjustment to 30 mM NaCl with 150 mM NaCl after annealing. Next, solutions were lyophilized to remove all water and then reconstituted in $D_2O$ followed by heat treatment for a second time. Sample solutions were placed between two $CaF_2$ windows spaced 50 μm apart and transmittance was measured on a Bruker Tensor 27 FTIR spectrometer. Solvent background was subtracted from the obtained spectrum and intensities were normalized.

*Protein release kinetics:* Recombinant human TGFβ-1 (eBioscience, San Diego, CA) was dissolved in a 0.1% BSA to 10 μg/ml. 360 μl of a 8.67 mM PA solution was mixed with 40 μl of the protein solution and allowed to stand on ice with periodic mixing for 2 hours. Five PA hydrogels were prepared for each condition tested by mixing 80 μl PA solution containing TGFβ-1 and 80 μl gelling solution comprising TBS supplemented with 25 mM $CaCl_2$ and 0.1% BSA and allowed to gel at 37°C. After 2 hours, 440 μl release buffer containing TBS supplemented with 10 mM $CaCl_2$ and 0.1% BSA was added to each gel. Samples were incubated at 37°C, and at each timepoint 200 μl of the supernatant was removed and stored at -30°C. The supernatant was

replaced each time after the sample was taken. After the final timepoint, 100 mM phosphate buffer was added to each gel and the gels were broken apart by vortexing. The resulting solution was stored for quantification. Total TGFβ-1 was measured using a Ready-Set-Go Human/Mouse TGFβ-1 ELISA kit (eBioscience) according to the manufacture instructions. Measured TGFβ-1 was normalized to a protein sample incubated in release buffer for an equivalent time to the samples measured. For each gel, the protein released was normalized to the total protein recovered from the sample.

*Scanning electron microscopy:* A gelling solution of 150 mM NaCl, 25 mM $CaCl_2$, and 3 mM KCl was added to the PA an 8.67 mM PA solution to form a hydrogel. The resulting gels were dehydrated through a series of ethanol water gradients to 100% ethanol. Following dehydration, samples were dried at the critical point of $CO_2$ using Samdri-795 Critical Point Dryer (Tousimis, Rockville, MD). Samples were coated with 20-30 nm of $OsO_4$ (OCP-60A, Filgen, Nagoya, JP) and imaged using a LEO Gemini 1525 SEM at an accelerating voltage of 3.0 kV.

*Rheology*: Measurements were taken using an Anton Paar MCR302 rheometer with a 25 mm cone-plate fixture. 100 ul of 8.67 mM PA solution was placed on the sample stage and 100 ul of gelling solution was placed on the cone fixture. The fixture was lowered in place for measurement and gelation was followed for 30 minutes at 10 rad/s and 0.1% strain. Next, a strain sweep was performed at 10 rad/s from 0.1% to 100% strain.

*Dynamic light scattering and zeta-potential measurements:* PA solutions were prepared at 10 mM, annealed, and then diluted 10 times in water. Samples were then bath sonicated for one hour and then further diluted with a NaCl solution to a final concentration of 250 μM PA and 30 mM NaCl. DLS and zeta-potential measurements were recorded in triplicate for three separate solutions of

each sample at 25°C using a Zetasizer Nano ZS (Malvern Instruments, Malvern, UK) with samples loaded in a disposable folded capillary zeta cell.

*Cell culture and encapsulation:* ATDC5 cells were obtained from Sigma-Aldrich and maintained in 1:1 DMEM/Ham's buffer with 2 mM glutamine, 5% fetal bovine serum and 1% Penicillin/Streptomycin. All cells were used before passage 10. Cells were trypsinized for 5 minutes with 0.25% trypsin/EDTA, counted and resuspended in PBS at 40 million cells/ml. PA solutions were mixed with recombinant human TGFβ-1 (R&D Systems, Minneapolis, MN) diluted in water to achieve the reported concentrations. The cell suspension was mixed with an equal volume of heat-treated 17.3 mM PA solution. 10 ul of the PA and cell suspension were placed in a 24 well plate for sGAG quantification or in a 15-well microscope slide (Ibidi, Martinsried, Germany) and allowed to attach. After 10 minutes, 10 ul of gelling solution containing 150 mM NaCl, 25 mM $CaCl_2$, and 3 mM KCl was added to each mass to gel the PA. After 3 hours attachment, 500 µl of maintenance media was added to 24 well plates and 50 ul was added to the 15 well slides. Cells were maintained at 37°C with 5% $CO_2$ and the media was changed every 2-3 days without growth factor supplementation.

*Cytotoxicity assay:* Cells were cultured in 15 well microscope slides in triplicate for each condition. In 3 wells for each timepoint, 20% ethanol was added for 30 minutes as a negative control. All cells were rinsed once with 150 mM NaCl and stained with a solution of 3 µg/ml calcein (Thermo-Fisher, Waltham, MA) and 5 µg/ml propidium iodide in 150 mM NaCl for 30 minutes. Cells were rinsed twice with 150 mM NaCl and imaged using a Nikon A1R confocal microscope. Live and dead cells were counted using the MATLAB Image Processing Toolbox.

*Immunocytochemical staining:* After 3 days of culture in 15-well microscope slides, cell masses were fixed with 4% paraformaldehyde in 150 mM NaCl for 30 minutes, followed by three washes in 150 mM NaCl. Following fixation, cells were permeabilized in blocking buffer containing 150 mM NaCl, 2% goat serum and 0.2% Triton X-100 for 2 hours. After blocking, the primary antibody against Sox 9 (Novus Biologicals, Littleton, CO) at 250 times dilution with phalloidin-AlexaFluor-488 (250 times dilution) and Hoechst 33258 (250 times dilution) in the blocking buffer were added and incubated overnight. The cells were washed three times for 10 minutes with blocking buffer and the Alexa-Fluor-647 conjugated secondary antibody (250 times dilution, Invitrogen, Carlsbad, CA) was added in blocking buffer for 3 hours. The cells were washed three times with blocking buffer for 10 minutes and then three times in 150 mM NaCl. Cells from two regions of three separate gels were imaged using a Nikon W1 Dual Cam Spinning Disk Confocal Microscope. Cells were counted using the MATLAB Image Processing Toolbox.

*DMMB blue assay*: Cells were encapsulated in 24 well plates in triplicate for each condition and cultured for three weeks. The media was removed cell masses were washed once with PBS. 200 ul of digestion buffer was added to each well containing 0.2 mg/ml papain (Sigma-Aldrich), 10 mM L-cysteine, 60 mM $NaH_2PO_4$, and 40 mM $NA_2HPO_4$. Cell masses were broken up by agitation, transferred with the digestion buffer to Eppendorf tubes, and incubated at 65°C overnight. After digestion, the tubes were spun down at 5000 rcf for 5 minutes. 20 ul of the supernatant was added to 180 ul of DMMB solution reported by Farndale et al.[59] containing 1.6 mg/ml NaCl, 3 mg/ml glycine, 10 mM acetic acid, and 16 μg/ml DMMB, pH 1. A standard curve was prepared using CS from bovine trachea (Sigma-Aldrich). Absorbance was read at 525 nm using a Cytation 3 microplate reader (BioTek, Winooski, VT). DNA content was measured using a Quant-iT PicoGreen assay kit (Invitrogen, Carlsbad, CA) using the manufacturer protocols.

*Statistical analysis:* Means were compared using Analysis of Variance in Graphpad Prism. Tukey's Range test was used for post-hoc determination of significance.

# CHAPTER 5

# 5. A Supramolecular-Covalent Hybrid Material for Cartilage Repair in a Sheep Model

## 5.1. Objectives and Significance

Hybrid materials comprising self-assembling and covalent polymer components are a promising strategy to design injectable materials with suitable physical and bioactive properties for bioregenerative applications. This study reports a composite material combining PA filaments designed to bind the chondrogenic cytokine TGFβ-1 and cross-linked hyaluronic acid microgels to produce a mechanically resilient scaffold able to support hyaline cartilage repair in large-animal joints. Combining the supramolecular and covalent components produced a porous network of bundled PA fibers, which supported chondrogenic differentiation of encapsulated stem cells in response to sustained delivery of TGFβ-1. Four weeks following implantation in shallow osteochondral defects in sheep stifle joints, the scaffold improved macroscopic scoring of defect fill and integration in both the medial femoral condyle and the trochlear groove. After twelve weeks, histological staining revealed that the hybrid scaffold supported regeneration of hyaline-like tissue. These results demonstrate the potential of supramolecular-covalent hybrid scaffolds to produce scaffolds that can support cartilage repair in a clinically relevant large-animal model.

## 5.2. Background

Therapies for the repair of articular cartilage defects are of critical clinical need due to the inability of hyaline cartilage to heal on its own.[36,195] Without effective treatments to regenerate damaged tissue, over 700,000 total knee replacements are performed annually in the USA, with the procedure increasingly performed on younger patients expected to outlive the lifespan of the implant.[227] For male patients under 60, the risk of requiring implant revision is as high as 35%,[228] and the overall cost of implant failures is expected to expected to exceed $13 billion annually by 2030.[229] Alternative techniques to replace cartilage or osteochondral defects include autografts and allografts, though these procedures suffer from poor integration of the implant to the defect site and limited implant availability due to donor site morbidity or scarcity of cadaveric tissue.[230] Thus, microfracture—a procedure where damaged cartilage is removed and small fractures in the underlying bone are made to induce filling of the defect with a marrow blood clot[49]—remains the gold-standard surgical technique to induce cartilage repair.[231] However, microfracture often results in mechanically inferior fibrocartilage rather than hyaline tissue,[232] resulting in significant deterioration of regenerated tissue by 18 months following intervention.[233] More recently, clinical techniques such as ACI[234] or MACI[235] have been developed to deliver hyaline cartilage producing chondrocytes to cartilage defect sites.[236] While promising, these strategies require an initial surgery to harvest the cells followed by extensive *ex vivo* cellular manipulation, making their widespread implementation expensive and impractical.[53] Cell based therapies using other cell sources such as MSCs have been proposed, but to date these have failed to succeed in clinical trials.[237]

Cell-free biomaterials implants are a promising alternative to support cartilage repair following infiltration native cells.[238] Hydrogel scaffolds can mimic the highly hydrated

environment of native cartilage,[239] and can be produced from natural polymers like the GAGs HA[240,241] and CS,[242] or synthetic polymers such as PEG[55] or polyesters.[243,244] Ideally, these materials should be injectable to allow application via arthroscopy and biodegrade without toxicity so they are cleared following healing.[239,245,246] Often, bioactive signals such the TGFβ family of cytokines are incorporated in these materials in order to direct differentiation of infiltrating cells.[59,208,241] Yet while many of the strategies induce chondrogenic differentiation *in vitro* or in small-animal models, few have succeeded in regenerating cartilage in large-animal models that better model human joints.[195] Possible strategies to improve outcomes in large animals include (1) improving mechanical resilience of the material to withstand higher mechanical loads,[247] (2) modulating the dose and delivery of bioactive signals to prevent the damaging effect of high local cytokine concentrations,[48] and (3) better recapitulating the architecture of hyaline cartilage to induce regeneration of healthy tissue.[195,230,248]

We reported earlier on a self-assembling PA capable of binding the growth factor TGFβ-1 and promoting the regeneration of healthy cartilage in a rabbit model.[60] Generally comprising a charged, hydrophilic peptide conjugated to an hydrophobic alkyl tail, PA molecules are a promising platform for use in bioregenerative applications due to their ability to form high-aspect ratio filaments that mimic the morphology of the nature ECM.[90,91,113-115,150] PA filament networks can be injected through a syringe and induced to form hydrogels in response to screening by counterions in their environment,[99,249] which are cleared via proteolytic degradation producing only natural amino acids and fatty acids.[101] While successfully implemented for regenerating a variety of tissue types, PA scaffolds may have a limited ability to withstand the high strains expected to occur in a large animal joint,[98] which previously necessitated use of a non-injectable collagen scaffold in some musculoskeletal regeneration applications.[107,114]

To improve the mechanical performance of PA-based scaffolds, this study reports on a hybrid material combining supramolecular PA filaments and crosslinked HA particles. In recent work, Stupp and co-workers have developed a versatile class of covalent-supramolecular polymer hybrids combining covalent polymer chains with self-assembling PA materials where self-assembly can control covalent polymerization[250] and covalent components can control thermal responsiveness[126] and hierarchical assembly of PA filaments.[128] Increasingly, hybrid materials combining the bioactivity of cartilage ECM components with the mechanical integrity of polymer networks like polycaprolactone[251] or silk-fibroin[73] have been employed in cartilage engineering applications.[252] For example, combining HA with elastin-like protein hydrogel improved cartilage-like development of encapsulated chondrocytes with increasing HA dose.[253] Here, by combining growth factor binding PA filaments with HA particles, the aim is to produce mechanically resilient scaffolds with the bioactive potential of both constituent components.

## 5.3. Results and Discussion

*Preparation and characterization of PA/HA hybrid gels*

The design of the supramolecular component of the hybrid system was based on TGFβ-1 binding filaments previously reported by Stupp and co-workers, which include a bioactive PA displaying a TGFβ-1 binding sequence and a diluent PA without a bioactive sequence (Figure 5.1a, Figure 5.17a,b).[60] The binding sequence contained an asparagine-to-aspartic acid mutation based resulted described in the previous chapter.[254] This molecule was co-assembled at a 1:9 ratio with an anionic diluent PA known to form gels following charge screening by divalent cations.[99] Transmission electron microscopy confirmed the co-assemblies formed filaments following heat treatment at 80°C (Figure 5.2). HA was chosen as the covalent component of the hybrid material

due its ubiquity in cartilage tissue and its known chondrogenic effect, especially when used in conjunction with TGFβ-1.[255] In previous work, crosslinked hydrogel microparticles produced porous, injectable materials with voids between the particles facilitating cell infiltration.[256] Therefore, the HA component was crosslinked to improve its mechanical and topological properties. To crosslink the material, dissolved HA was combined with an L-lysine methyl ester crosslinker and N-(3-Dimethylaminopropyl)-N′-ethylcarbodiimide hydrochloride (EDC) as the coupling agent. The mixture was spread across a flat dish at 1 ml/cm$^2$ and allowed to dry to concentrate the solution during crosslinking. The resulting film was rehydrated, thoroughly washed to remove excess crosslinker, and shredded in a blender to produce particles that were lyophilized prior to future use (Figure 5.1b, Figure 5.3). To confirm crosslinking of the material, the change in the elemental composition of the gels was used to determine the amount of the crosslinker incorporated and compared that to the number of primary amine groups remaining due to incomplete crosslinking as calculated using a colorimetric ninhydrin assay. This analysis showed a 21 ± 3% degree of crosslinking, with an additional 17 ± 2% incomplete crosslinks (Table 5.1). This concentration is higher than the initial ratio of crosslinker added to the reaction, implying non-reacted HA chains were washed away during washing steps.

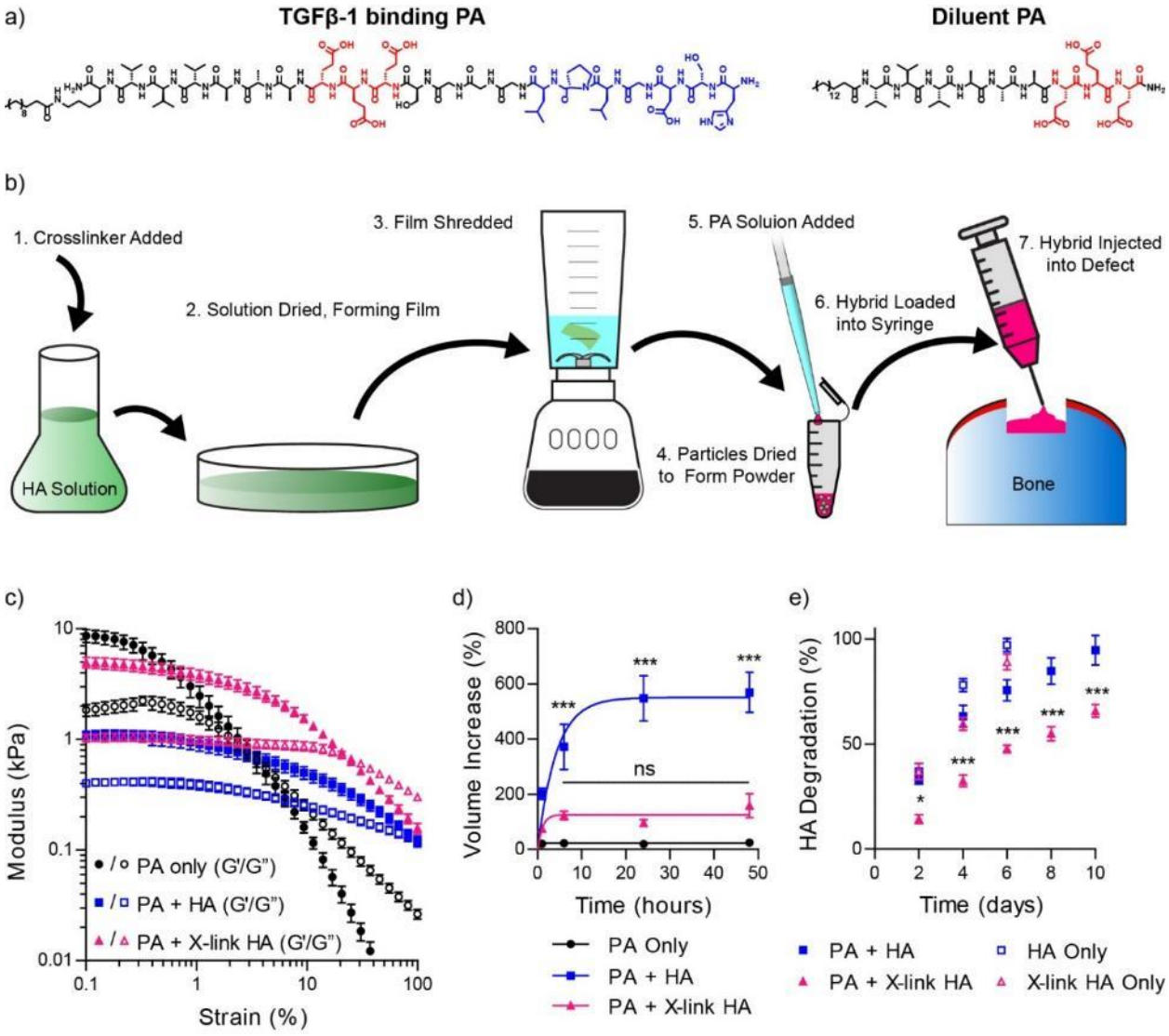


**Figure 5.1: Preparation and physical performance of PA/HA hybrid gel**

(a) Chemical structure of PA molecules used. (b) Schematic showing preparation of crosslinked HA and PA/HA hybrid. (c) Storage and loss modulus as a function of strain for gels comprising PA only, PA added to 4% unmodified HA, and PA added to 4% crosslinked HA particles (n=3). (d) Volume increase as a function of incubation time for PA only gels and PA/HA gels with unmodified or crosslinked HA; significance calculated relative to PA only gels (n=5). (e) Hyaluronidase catalyzed degradation of HA as a function of time quantified by carbazole assay for HA only or PA/HA gels for both unmodified and crosslinked HA; significance calculated for crosslinked HA relative to unmodified HA (n=4). (*, $p < 0.05$; ***, $p < 0.001$)

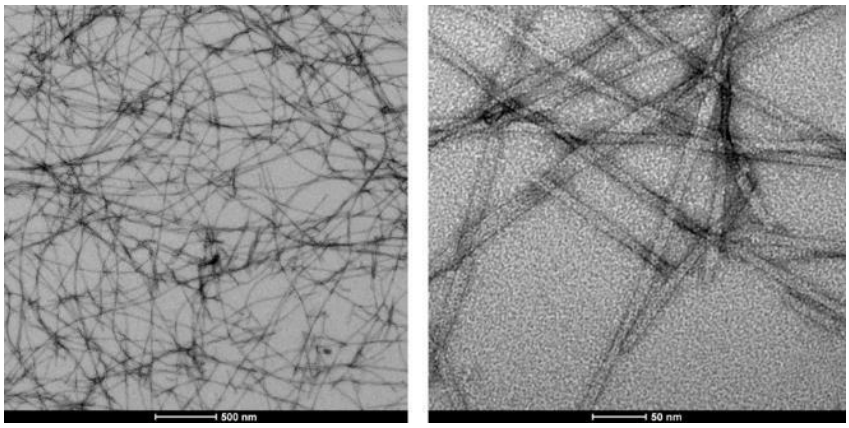


**Figure 5.2: TEM micrographs of PA filemnts used in hybrid gel formulations**
Conventional TEM imaging of heat treated PA filaments used to prepare PA/HA hybrid material used in surgery.

**Table 5.1**: **Chemical characterization of crosslinked HA**
Nitrogen content of unmodified and crosslinked HA determined by elemental analysis with the amount of incorporated crosslinker necessary for the given increase in nitrogen; and primary amine content of unmodified and crosslinked HA as determined by ninhydrin assay with fraction of amine modified HA monomers. Crosslinking extent calculated by subtracting fraction of free amine modified from total incorporated crosslinker molecules to give total crosslinker with both amine groups binding HA polymer chains.

| | Unmodified HA | Crosslinked HA | Fold Increase | Crosslinker/HA (%) |
|---|---|---|---|---|
| %Nitrogen | 3.13 | 4.89 | 1.57 | 36 |
| | 3.09 | 5.04 | 1.62 | 39 |
| | 3.11 | 4.95 | 1.59 | 37 |
| Mean | 3.11 | 4.96 | 1.59 | 38 ± 2 |

Molecular weight of crosslinked HA = 477.2 mg/mmol HA monomer

| | **Unmodified HA** | **Crosslinked HA** | |
|---|---|---|---|
| | Primary Amines (μmol/mg) | | Primary Amine/HA (%) |
| | 0.03 | 0.37 | 18 |
| | 0.03 | 0.33 | 16 |
| | 0.02 | 0.35 | 17 |
| | 0.04 | 0.34 | 16 |
| | 0.02 | 0.43 | 20 |
| Average | 0.03 | 0.36 | 17 |
| St Dev | 0.01 | 0.04 | 2 |

Extent of crosslinking = 21 ± 3%

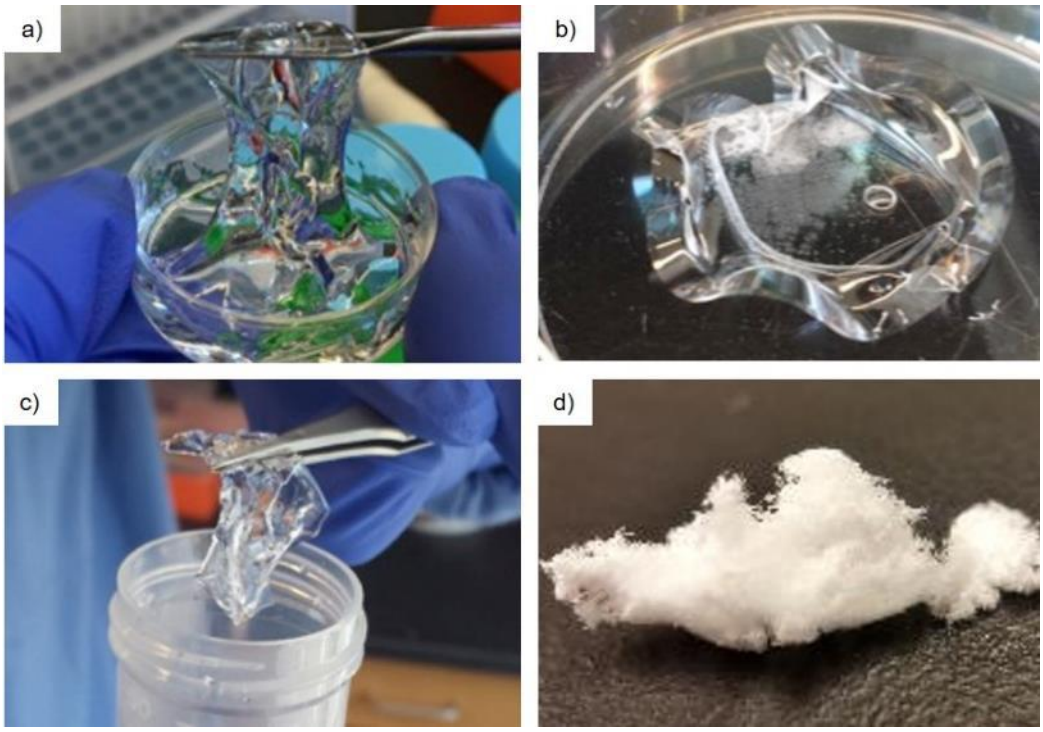


**Figure 5.3: Preparation of crosslinked HA microgels**
Preparation steps for crosslinked HA particles. (a) Viscous HA solution is mixed with crosslinker solution and poured into a flat dish to form (b) a film. (c) The film is rehydrated and washed to remove excess crosslinker and coupling agent and then shredded in a blender to form (d) a poweder following lyophilization.

To produce the hybrid material, the solution of PA filaments was combined with the lyophilized HA particles and stirred with a spatula. Initially, the two phases remained separate, but after one hour the phases combined to form a think putty that could be formed into a desired shape yet could still be ejected through a syringe. Qualitatively, combining PA solutions prepared at 2 wt% added to HA particles for a final concentration of 4% HA produced a gel with the best handling properties for use in surgery. To assess the change in performance of the material due to the addition of crosslinked HA, rheological strain sweeps on the material were performed with ionic $CaCl_2$ added to stiffen the PA component of the hybrid. The addition of HA significantly improved the flow strain of the material from 3.3 ± 1.5% for PA alone to 23 ± 6.3% for the

crosslinked PA/HA hybrid or 89 ± 4.9 % for the unmodified hybrid, suggesting the HA based material would be more resilient to shear strain *in vivo* (Figure 5.1c). While the flow strain was higher for PA combined with unmodified HA, PA/HA gels made with crosslinked particles were significantly stiffer than the soft gels made from unmodified HA (5.0 ± 1.0 kPA vs. 1.1 ± 0.2 kPa). For use as a surgical material, it was important to ensure the gels did not swell excessively, which could lead to ejection of the implant from the defect site. Tracking the volume increase of gels in water over time showed PA only gels had nominal volume change over 48 hours, while the volume of PA/HA gels produced from unmodified HA swelled to 5 times their initial volume. Crosslinking the HA particles significantly decreased swelling, suggesting it would be better maintained in cartilage defects than its unmodified HA counterpart (Figure 5.1d). It was likewise important to ensure that the HA component of the material would not be cleared too quickly from the defect site. HA without added PA—whether crosslinked or not—degraded completely within 6 days when incubated in a hyaluronidase solution. The addition of PA to HA slowed the degradation, and crosslinking the HA significantly decreased degradation relative to the PA/unmodified HA control (Figure 5.1e). To validate are choice to prepare the PA/HA hybrid with 4% crosslinked HA, rheological and swelling experiments were performed at several crosslinked HA concentrations. These experiments showed the 4% crosslinked HA composition had similar flow strain and swelling properties and a higher storage modulus at low strain compared to a 2% crosslinked HA compositions, while 10% crosslinked HA compositions swelled excessively, confirming 4% crosslinked HA compositions balanced desirable mechanical and swelling properties (Figure 5.4). Together, these data supported use of the PA/HA hybrid with cross-linked HA particles in large-animal studies based on their increased toughness, low swelling, and slow degradation properties.

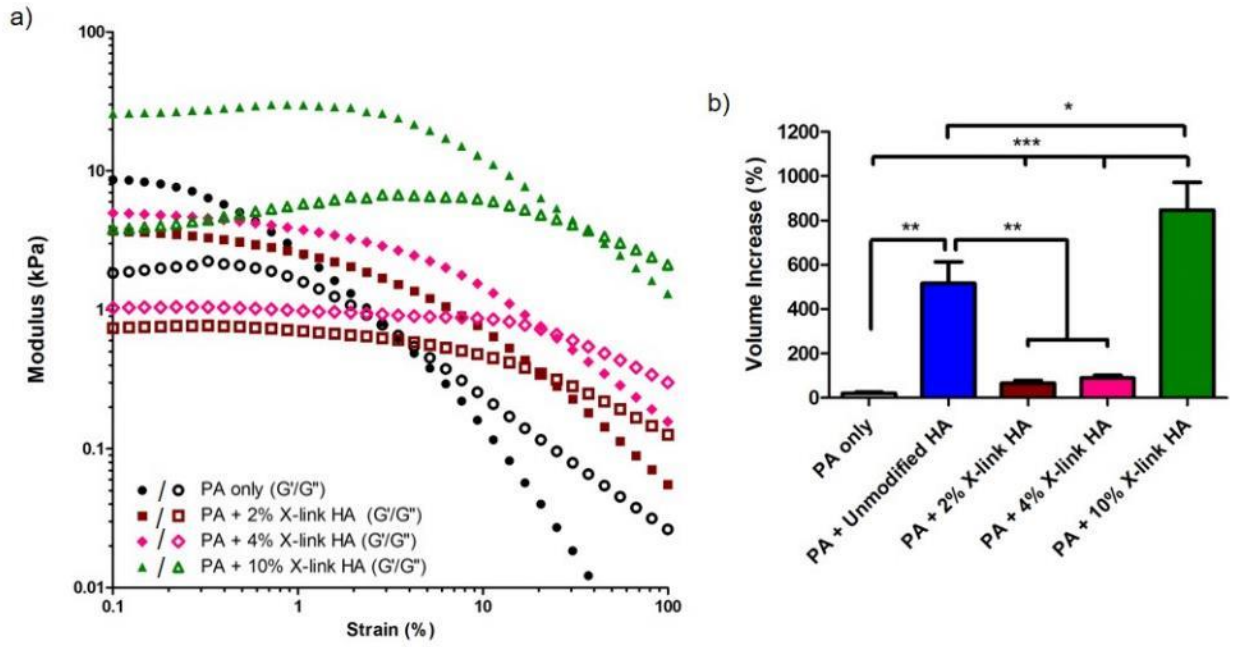


**Figure 5.4: Effect of HA concentration on hybrid gel performance**
(a) Storage modulus and loss modulus as a function of strain for 2 wt% PA only samples and PA/HA samples comprising 2% PA and 2%, 4%, or 10% crosslinked HA (n=3). (b) Volume increase after 24 hours in water for 2% PA only gels, 2% PA and 4% unmodified, 2% PA and 2% crosslinked HA, 2% PA and 4% crosslined HA, and 2% PA and 10% crosslinked HA (n=5).

*Self-assembly of PA/HA hybrid material*

Next, how combining the PA and HA components affected the self-assembly of the system was investigated. Surprisingly, SEM revealed that while PA alone forms a dense network of randomly oriented filaments, the PA/HA hybrid material comprised dense bundles of filaments with large pores between the bundles. These bundles were not comprised of HA particles alone, which appear as sphere-like particles when dehydrated for SEM (Figure 5.6a), Interestingly, bundles formed with the addition of 2-4% HA, but not with the addition of 10% HA to the PA solution (Figure 5.5a; Figure 5.6b). The morphology and molecular organization of these structures was characterized using a simultaneously collected SAXS, MAXS, and WAXS patterns. The SAXS scattering pattern produced PA solution alone fit a core-shell cylinder model with a fiber

diameter of 8 nm (Figure 5.7). In the WAXS region, Bragg peaks with associated d-spacings of 0.47 nm and 0.24 nm were consistent with β-sheet formation among the PA molecules. In the MAXS region, a peak corresponding to a d-spacing of 0.99 nm was observed which can be attributed to the spacing between β-strands withing the filaments. In the PA/HA hybrid material, a strong Bragg peak at a d-spacing of 15 nm appeared, which can be attributed to regular spacing of the filaments within the observed aggregates. This spacing was less than twice the diameter of each fiber, indicating that the filaments within the superstructures were packed close to one another. In these patterns, the characteristic form factor for cylindrical fibers remained and the position of the higher-q Bragg peaks was unchanged, suggesting the fiber structure did not change with bundling. The low-q Bragg peak was significantly weakened with 10% added HA, further indicating that the peak arose due to the aggregation of the fibers into the bundles observed by SEM (Figure 5.5b).

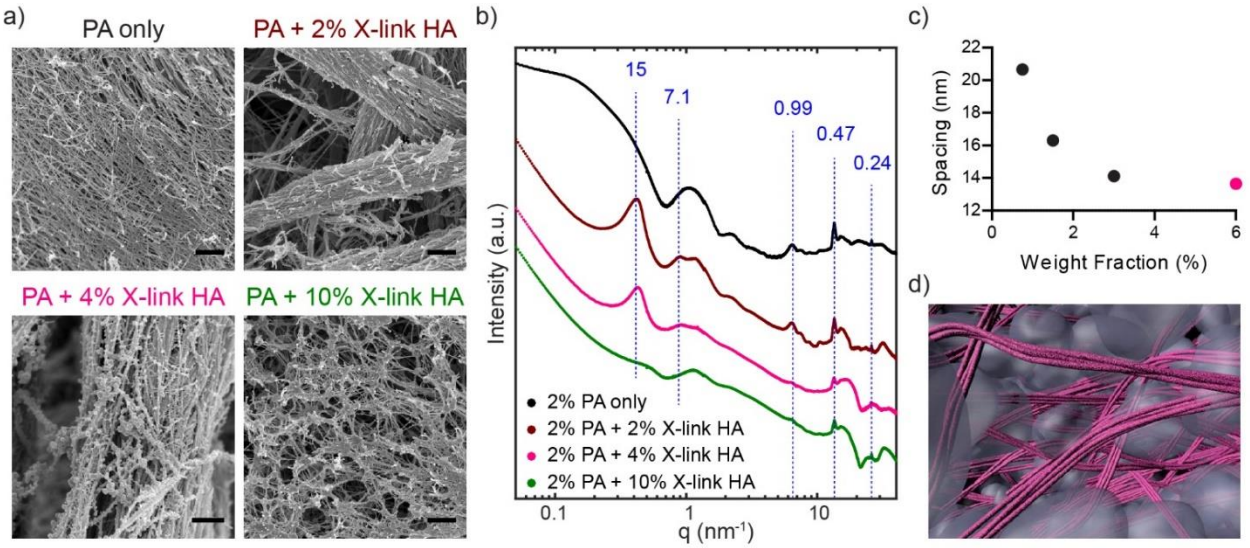


**Figure 5.5: Self-assembly of PA/HA hybrid gels**

(a) Scanning electron micrographs of gels formed by 2 wt% PA only, or the same concentration added to crosslinked HA for a final concentration of 2%, 4%, and 10%; scale = 1 μm. (b) SAXS/WAXS intensity as a function of the wave vector for PA only and PA/HA with d-spacings associated with observed peaks indicated. (c) D-spacing associated with the first observed Bragg peak produced by PA/HA gels produced by adding 2 wt% PA to 4% crosslinked HA (pink) and

then diluting the mixture to the given total weight fraction (black). (d) Schematic showing arrangement of PA fibers (pink) and swelling HA particles (gray).

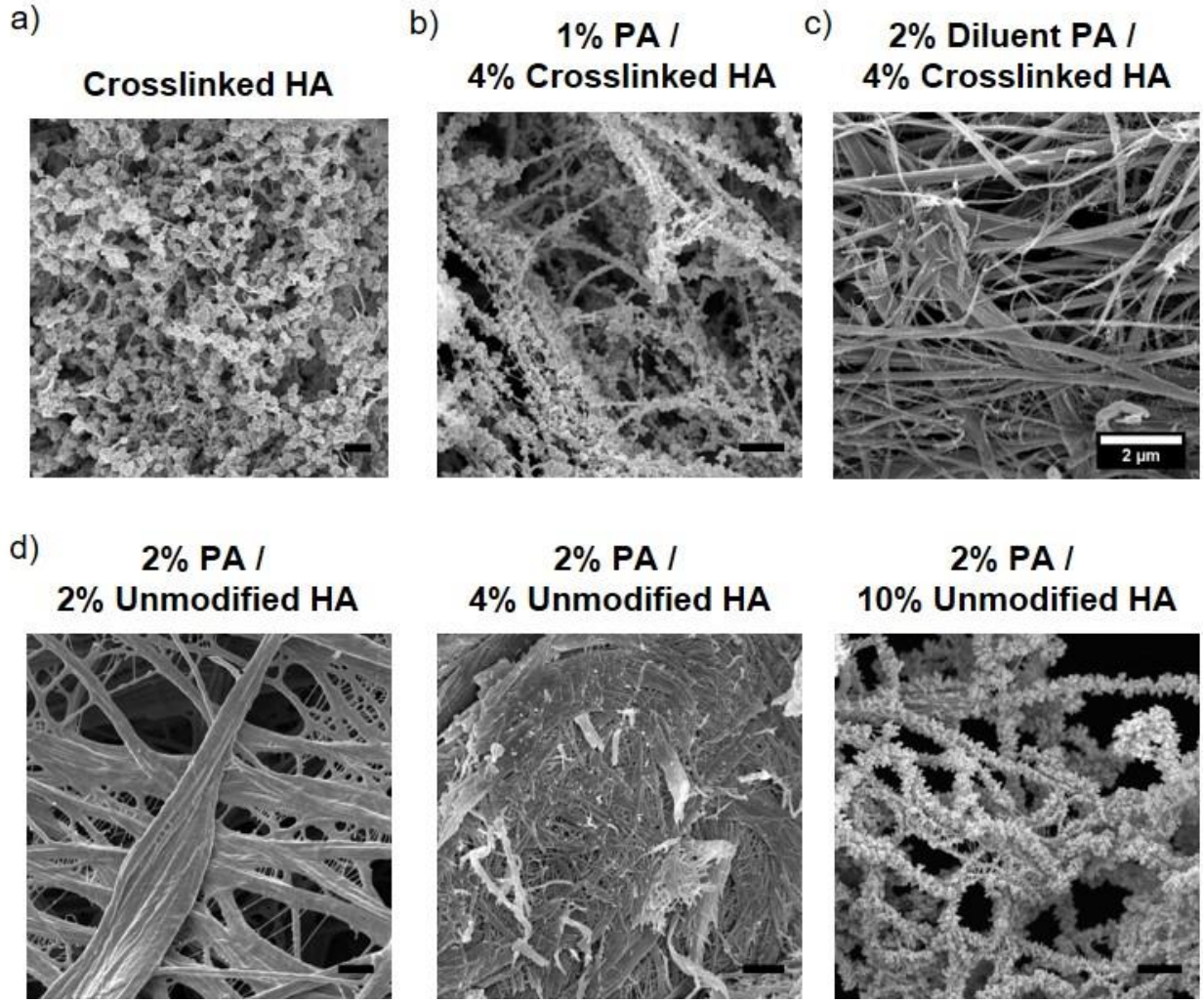


**Figure 5.6: SEM microscopy of PA/HA hybrids with varying composition**

SEM micrographs of (a) crosslinked HA particles alone, (b) 1% PA solution added to 4% crosslinked HA particles, (c) diluent PA only combined 4% crosslinked HA particles. (d) 2% PA solution added to 2% unmodified HA, (d) 2% PA added to 4% unmodified HA, and 2% PA added to 10% unmodified HA; Scale = 1 μm.

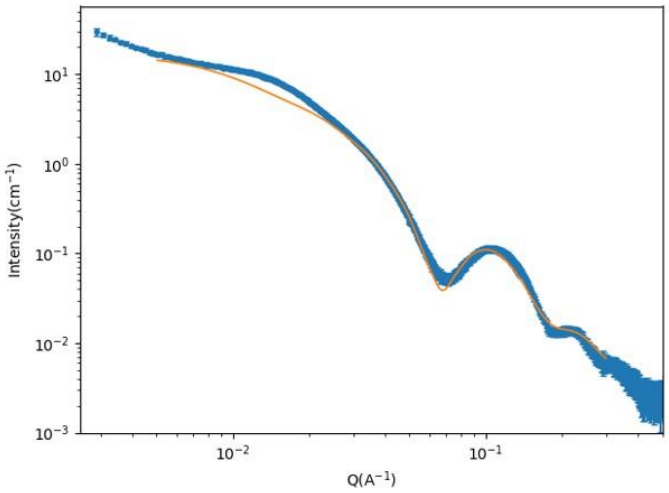


| | |
|---|---|
| scale | 0.30 |
| Background ($cm^{-1}$) | 0.0045 |
| SLD core ($nm^{-2}$) | 7.25e-4 |
| SLD shell ($nm^{-2}$) | 9.91e-4 |
| SLD solvent ($nm^{-2}$) | 9.42e-4 |
| Radius (nm) | 0.90 |
| Thickness (nm) | 3.57 |
| Length (nm) | 40 |

**Figure 5.7: Fitting of PA filament SAXS pattern**
SAXS pattern produced by a 2 wt% PA solution (blue) fit to a core-shell cylinder model using SASView software (orange), with fitting parameters used to produce the displayed model.

Next, the mechanism of bundle formation in the hybrid system was investigated. The observed bundling was not a result of HA crosslinking (or amine groups remaining from incomplete crosslinks) as SEM showed similar filament aggregates (Figure 5.6d) and SAXS showed a similar Bragg peak (Figure 5.8) for the PA/HA hybrid made with unmodified HA at the same concentrations. In addition, bundling was not due to interactions between the positively charged binding epitope and the negatively charged HA, as bundles were observed when diluent PA only filaments were added to HA particles (Figure 5.6c). These results led to the hypothesis that bundle formation was a result of the high hydrophilicity of HA. Stupp and co-workers previously reported that X-ray induced ionization of PA filaments causes fiber alignment to maximize the distance between the highly charged fibers.[92] In the hybrid system, HA has a higher propensity for osmotic swelling than the PA filaments. Therefore, the available water is primarily associated with swollen HA particles, confining the PA filaments to a limited volume. In this

confined space, fibers aligned to maximize distance between their negatively charged surfaces, suggesting that at a spacing of 15 nm the osmotic force produced by the swelling HA equaled the repulsive force between neighboring filaments. To test this hypothesis, PA and HA were cobined at the normal ratio and diluted with water by physical mixing to change the weight fraction of the material. Following dilution, inter-filament distance increased as a function of decreasing concentration, supporting the notion that the regular spacing of PA filaments was a result of volume confinement and not a result of attractive interactions among the assemblies (Figure 5.5c). Thus, the microstructure of the hybrid material consists of dense PA bundles made of peptides surrounded by a highly solvated glycosaminoglycan matrix (Figure 5.5d). This architecture mimics the organization of hyaline cartilage were fibrous collagen is surrounded by a web of solvated glycosaminoglycans including HA and CS.[30]

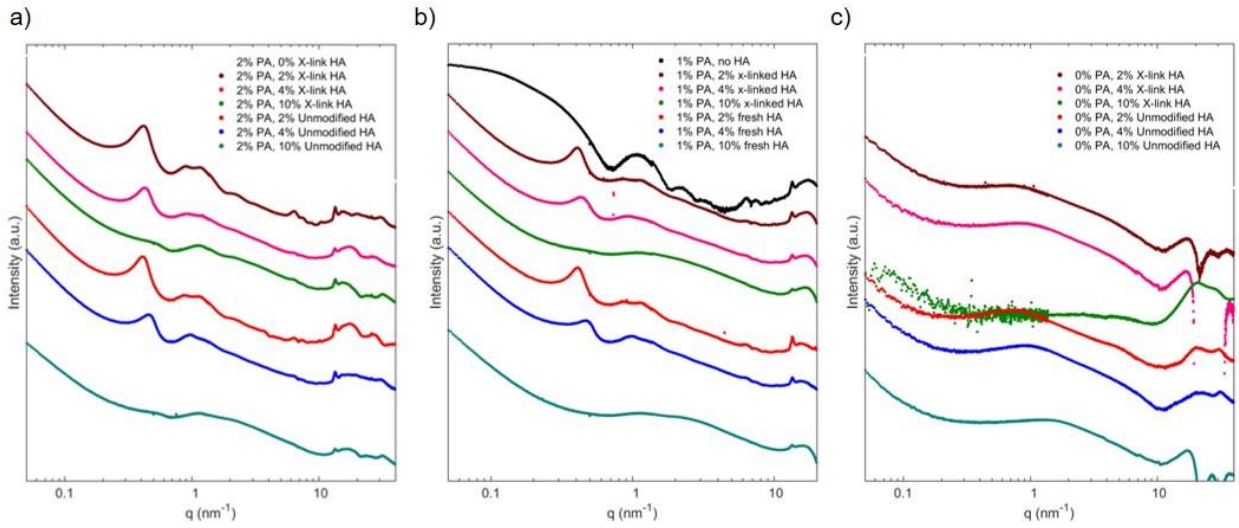


**Figure 5.8: SAXS patterns of PA/HA hybrid at variable compositions**
SAXS pattern for gels produced by adding (a) 2 wt% PA solutions, (b) 1 wt% PA solutions, or (c) water without PA to crosslinked HA or unmodified HA at concentration of 2%, 4%, and 10%.

*Chondrogenesis in PA/HA hybrid gels*

Next , the chondrogenic potential of cells encapsulated in the cartilage mimetic scaffolds was characterized to ensure that the addition of HA particles did not inhibit the bioactivity of the PA filaments. Initial experiments determined that PA nanofibers retained their bioactivity with the addition of HA by quantifying growth factor release from the hybrid material. Compared to hybrid gels made with diluent PA only, hybrid gels that included PA filaments presenting the TGFβ-1 binding epitope retained more growth factor over 3 weeks, although a significant majority of the growth factor remained in both formulations during the experiment (Figure 5.9a). The high retention by both gels is likely due to the tight bundling of PA nanofibers associated with the growth factor, limiting diffusion out of the bundles. In enzymatically active conditions *in vivo*, the improved ability of the binding epitope to retain the growth factor can help extend the molecule's release even as the hybrid gel is degraded. Next, cytotoxicity experiments ensured cells could survive encapsulation by mixing hMSCs in suspension with a solution of PA fibers before adding the combination to dried crosslinked HA particles and gelling with ionic calcium. A live/dead assay showed 89 ± 2% of cells were viable after 24 hours, which was statistically similar to survival following encapsulation in PA only gels (Figure 5.9b; Figure 5.10). The morphology of the encapsulated cells was characterized by SEM and confocal microscopy. SEM showed cells in cavities between the bundles, with cell extensions binding to filament bundles (Figure 5.9c). Cells encapsulated in PA without HA added could not be located through the dense network of PA filaments, highlighting the increased gel porosity due to HA addition. Confocal fluorescent microscopy showed rounded cells dispersed within both PA only gels and hybrid gels, where PA filaments were visualized with a carboxytetramethyrhodamine (TAMRA)-tagged PA (Figure 5.9d,e; Figure 5.17d).

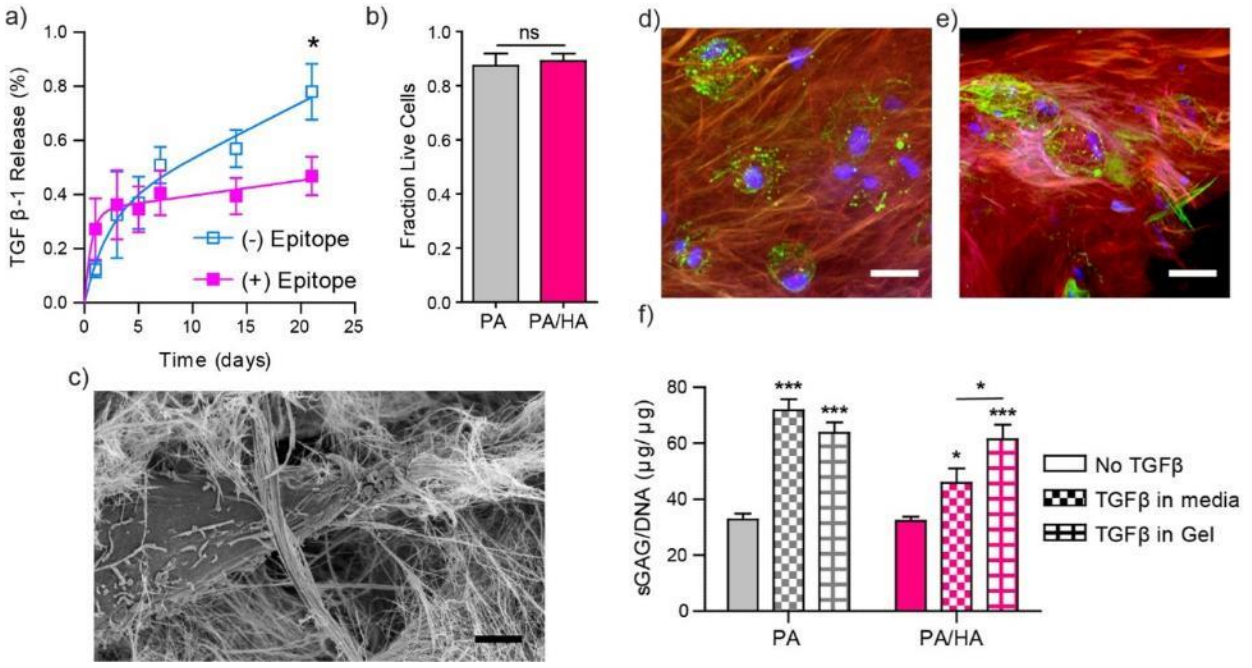


**Figure 5.9: Biological performance of PA/HA hybrid *in vitro***

(a) TGFβ-1 release from PA/HA gels as a function of time where gels were made either from filaments containing only the diluent PA or filaments containing the diluent and 10 mol% of the bioactive PA displaying the TGFβ-1 binding epitope (n = 4). (b) Cell survival 24 hours following encapsulation for hMSCs in PA only or PA/HA gels (n = 3). (c) SEM micrograph an hMSC encapsulating PA/HA; scale = 2 μm. Immunocytochemistry confocal microscopy images showing an hMSC encapsulating (d) PA only gel and (e) PA/HA gel; nuclei stained with Hoechst (blue), actin stained with phalloidin (green), and PA tagged with TAMRA (red); scale = 25 μm. (f) sGAG content normalized to DNA concentration 4 weeks following encapsulation in PA only and PA/HA gels where gels were cultured without TGFβ-1, with TGFβ-1 supplemented media, or with TGFβ-1 added to the PA solution prior to cell encapsulation; significance relative to no TGFβ-1 control for each gel (n = 5). (*, $p < 0.05$; ***, $p < 0.001$)

After 4 weeks of culture, the chondrogenic potential of the gels was quantified by measuring production of sGAG for both PA only and PA/HA gels in serum free chondrogenic media without added growth factor, with 10 ng/ml TGFβ-1 supplemented media, and with TGFβ-1 encapsulated in the gels. The experiment was designed so that over 4 weeks the total amount of TGFβ-1 added in the media supplemented group from aliquots freshly thawed at each media change equaled the total amount of TGFβ-1 encapsulated in the gels at the start of the experiment.

For both PA only and PA/HA gels, the addition of TGFβ-1 either in the media throughout the experiment or in the gels at the start improved sGAG production (Figure 5.9f). For PA only gels, there was no statistical difference between gel encapsulation or media supplementation, but in hybrid gels encapsulation induced significantly more normalized sGAG production than media supplementation of TGFβ-1. This result suggests that TGFβ-1 encapsulated in the hybrid gels retained activity throughout the experiment, inducing chondrogenesis at least as well as periodic addition of freshly thawed growth factor. Importantly, there was no statistically significant difference in normalized sGAG production for TGFβ-1 encapsulating PA gels relative to PA/HA hybrid gels, indicating the improvements in physical performance do not come at the expense of the material's bioactivity. These experiments verified the chondrogenic potential for the hybrid gel, recommending their use for cartilage regeneration *in vivo*.

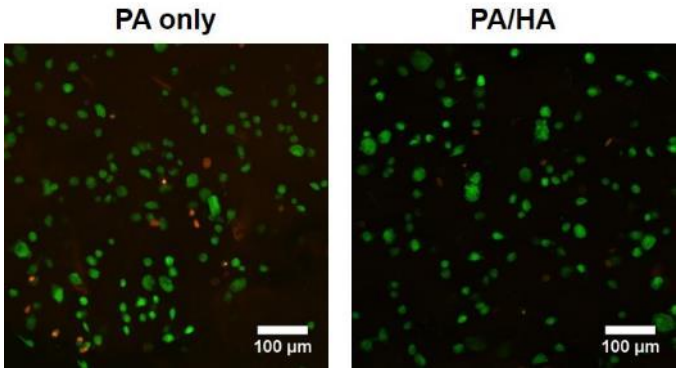


**Figure 5.10: Cell viability following gel encapsulation**
Live/dead staining for cells encapsulated in PA gels or PA/HA gels cultured for 24 hours. Live cells stained with calcein (green) and dead cells stained with propidium iodide (red).

*PA/HA hybrid implantation and retention*

An ovine model was selected to assess the efficacy of the hybrid material to induce cartilage healing *in vivo* due to the similarities in weight bearing and in anatomy of sheep hind-stifles and to human knees.[257,258] Osteochondral defects were made in both the medial femoral

condyle—a weight bearing surface—and in the femoral trochlear groove—a surface of the joint that bears less weight—to determine how mechanical shear stress affects the materials performance. At each location, the defects were critically sized at 7 mm wide[259] and were 3 mm deep (Figure 5.11a,c). Although human knee cartilage can exceed 3 mm in thickness,[260] the cartilage in ovine stifles is around 0.5 mm thick,[261] meaning the defects extended into the subchondral bone and induced bleeding. Defects were filled by ejecting the PA/HA hybrid from a syringe fitted with an 18-guage needle and packing the material to fill the defect space (Figure 5.11b,d). The ability to form the implant into the shape of the defect was crucial, as even custom fabricated implants often fail to integrate when fabricated prior to implantation.[262] A calcium chloride solution was then dripped on the defect in order to induce gelation of the PA filaments, stiffening the implant surface.

To ensure the material was well retained within the defects, a pilot experiment evaluated defect filling after 7 days *in vivo*. Defects in both stifles were filled with a hybrid gel containing TAMRA-tagged PA filaments, and one hindlimb was placed in a sling following surgery while the other was loadbearing. After 7 days, H&E staining showed good filling of both condyle defects and trochlea defects in both the sling and non-sling stifles. Fluorescent imaging to unstained sections showed the fluorophore remained throughout the defects, confirming material filling the defect retained the bioactive PA filaments (Figure 5.11e,f). Retention of the bioactive component of the implant material for 7 days, especially in the non-slung condyle, indicated the material could withstand the mechanical shear stress present in large-animal joints and influence healing in longer term experiments. In addition, retention of the material without the use of a sling allowed for treating one limb with the hybrid material, while the other limb could be used as a contralateral control in subsequent experiments.

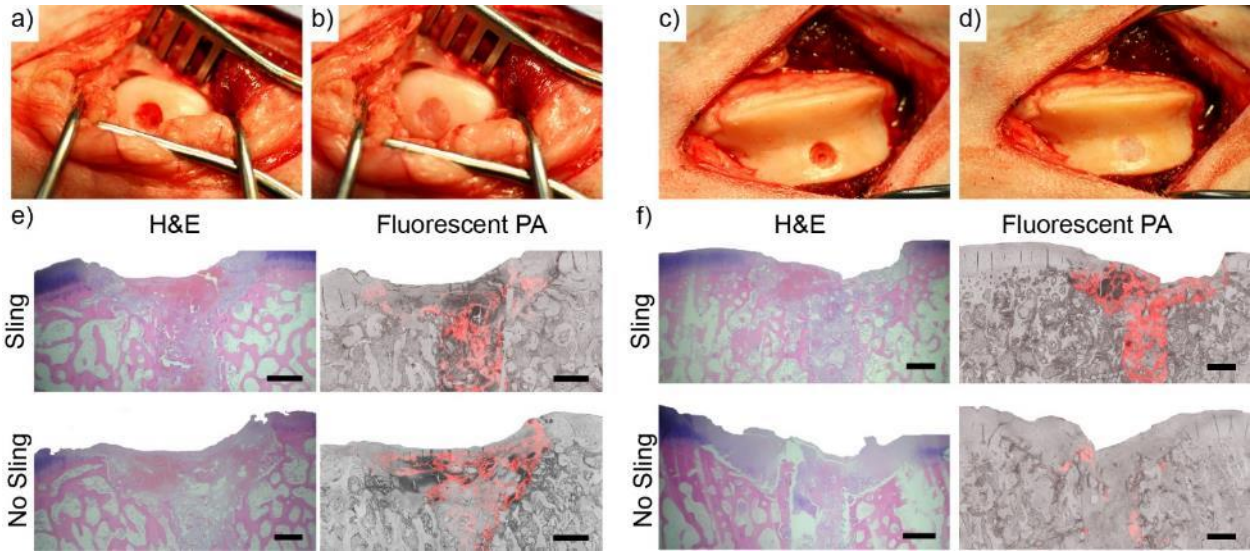


**Figure 5.11: Defect filling by PA/HA hybrid material**
Photographs of (a) a 3 mm deep, 7 mm diameter shallow osteochondral defect made by drilling into the medial condyle of a sheep stifle, and (b) the defect with the PA/HA hybrid. Photographs of (c) a 3 mm deep, 7 mm diameter shallow osteochondral defect made by drilling into femoral trochlear groobe of a sheep stifle, and (d) the defect with the PA/HA hybrid. H&E histological staining and fluorescence imaging produced by TAMRA-tagged PA filaments (red) in the PA/HA hybrid overlaying unstained sections for slung and contralateral non-slung stifles prepared from sections of the (e) medial condyle (f) femoral trochlear groove obtained 7 days following implantation. Scale = 1 mm.

*Defect filling and integration after four weeks*

To assess the ability of the mechanically improved PA/HA hybrid to influence cartilage healing, a four-week study evaluated defect filling and material integration with host cartilage. In previous work in a rabbit model, TGFβ-1 binding PA filaments improved cartilage healing both with and without the addition of TGFβ-1, presumably due to the ability of the material to bind endogenous growth factor.[60] To determine if exogenous growth factor was necessary in the large animal model, sheep were divided into two groups of six sheep. In the first group, (+) TGFβ, the hybrid was loaded with 1 μg/ml TGFβ-1 prior to implantation in a condyle defect and a trochlea defect in one stifle, while an equal concentration of the growth factor in saline was dripped into

control defects made in the contralateral stifle. While this dose was greater than the TGFβ-1 dose used in prior rabbit studies (100 ng/ml),[60] the dose used here is believed to be the lowest TGFβ dose reported in a material delivering the TGFβ-1 or TGFβ-3 to a full-thickness cartilage or osteochondral defect in a large animal model.[243,263-265] In the second group, (-) TGFβ, no TGFβ-1 was added to the material prior to implantation in a condyle defect and a trochlear defect in one stifle and only saline was added to the control defects in the contralateral stifle. Because of high variability in sheep age, size, and condition prior to surgery, the aim of this experiment design was to compare the PA/HA hybrid treated defects with control defects in the same animal population and thereby evaluate the efficacy of the hybrid material relative to no material controls in the same population.

Following surgery, animals were allowed to move freely and were sacrificed after four weeks. Macroscopic scoring by blinded experts of defect fill, surface, and integration showed a statistically significant ($p < 0.05$) improvement median score in PA/HA hybrid treated condyle defects and trochlear groove defects relative to controls treated with the growth factor alone (Figure 5a-c; Table 5.2; Table 5.3). Scoring of histological sections of the condyle defects showed a similar trend ($p < 0.1$) to macroscopic scoring with higher median scores for hybrid treated defects, but there was no difference for trochlear groove defects (Figure 5d; Table 5.3; Table 5.4). Because 4 weeks is an early timepoint in the cartilage regeneration process, macroscopic appearance was expected to be more indicative of material response than staining for markers of hyaline tissue which develop at later times. Still, Safranin O staining of sGAG and hematoxylin & eosin (H&E) staining in the PA/HA hybrid treated defects of the (+) TGFβ group showed instances of strong integration between the defect fill and native tissue, indicating strong compatibility of the implant material with surrounding tissue. There was no statistical difference in macroscopic

scores or in histological scores for defects treated with the material alone relative to defects filled with the saline vehicle only (Figure 5e-f; Table 5.3). While the average score of all treated and untreated condyle defects was higher for the (-) TGFβ group than for the (+) TGFβ group, this difference could be attributed to animal-to-animal variability between the small populations included in each group. Importantly though, improved healing due to TGFβ-1 loaded PA/HA hybrid implants indicates the supramolecular scaffold has the physical integrity needed to support improved filling and integration of cartilage defects, including in the mechanically active femoral condyle and in the trochlear groove.

**Table 5.2: ICRS macroscopic scoring system criteria**
Table adapted from ref.[266]

| Cartilage repair assessment | Points |
|---|---|
| *Degree of defect repair* | |
| In level with surrounding cartilage | 4 |
| 75% repair of defect depth | 3 |
| 50% repair of defect depth | 2 |
| 25% repair of defect depth | 1 |
| 0% repair of defect depth | 0 |
| *Integration to border zone* | |
| Complete integration with surrounding cartilage | 4 |
| Demarcating border<1 mm | 3 |
| 3/4th of graft integrated, 1/4th with a notable border>1 mm width | 2 |
| 1/2 of graft integrated with surrounding cartilage, 1/2 with a notable border>1 mm | 1 |
| From no contact to 1/4th of graft integrated with surrounding cartilage | 0 |
| *Macroscopic appearance* | |
| Intact smooth surface | 4 |
| Fibrillated surface | 3 |
| Small, scattered fissures or cracks | 2 |
| Several, small or few but large fissures | 1 |
| Total degeneration of grafted area | 0 |

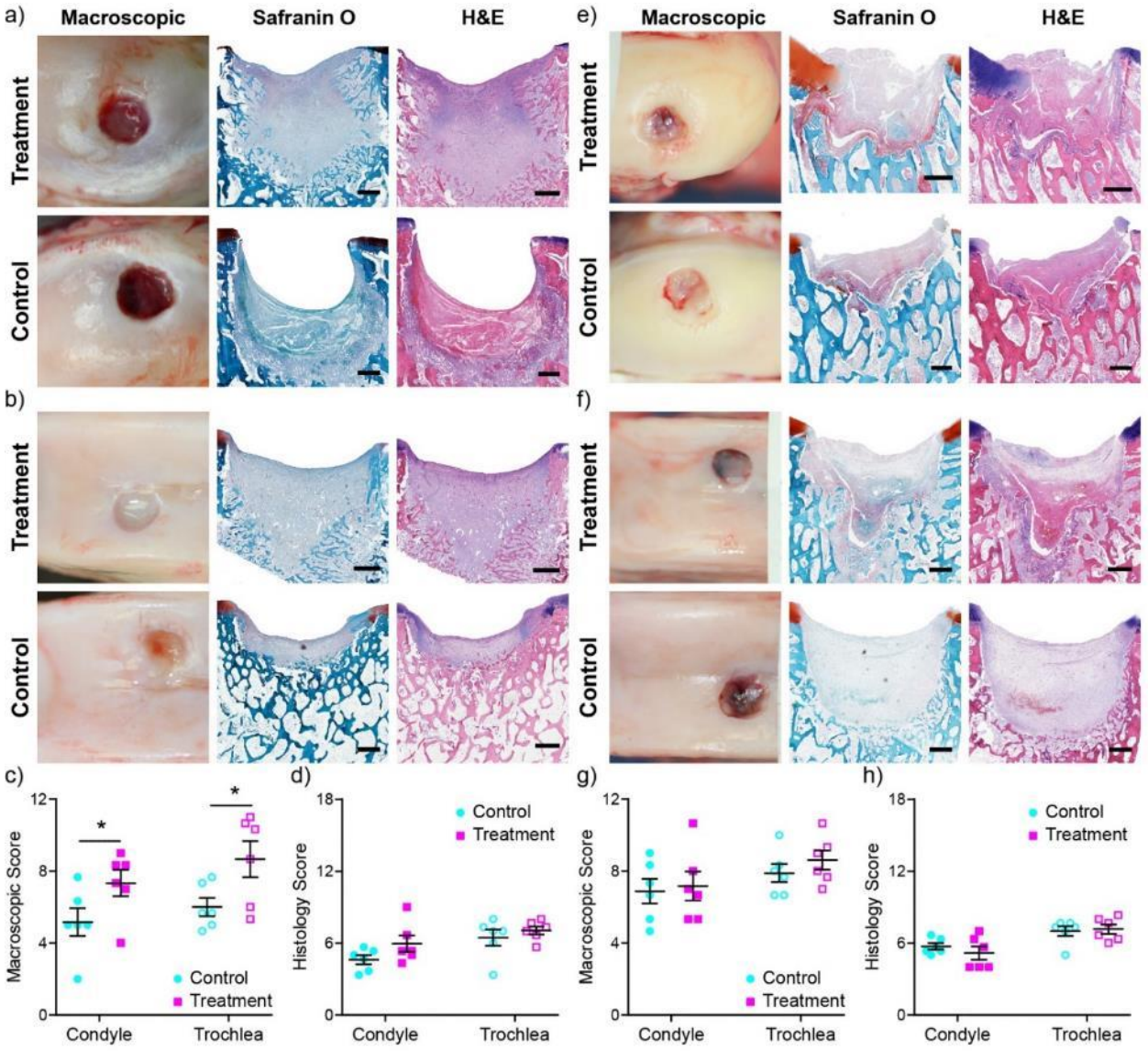


**Figure 5.12: Defect filling and integration four weeks post-surgery**

Representative macroscopic appearance, Safranin O stained sections, and H&E stained sections of (a) medial condyle defects and (b) trochlear groove defects treated with PA/HA hybrid material delivering TGFβ-1 and contralateral controls where TGFβ-1 was applied in saline solution four weeks following implantation along with blinded ICRS scoring of (c) macroscopic appearance and (d) histological sections for all samples (n = 6). Macroscopic imaging, Safranin O stained sections, and H&E stained sections of (e) medial condyle defects and (f) trochlear groove defects treated with PA/HA hybrid material without growth factor and contralateral controls where only the saline vehicle was applied four weeks following implantation along with blinded ICRS scoring of (g) macroscopic appearance and (h) histological sections for all samples (n = 6). Scale = 1 mm. (*, $p < 0.05$; Mann-Whitney Test)

**Table 5.3: Macroscopic and histological scoring of cartilage defect repair**
Comparison of median macroscopic scores and median histology scores of PA/HA treated and control defects in four-week and twelve-week sample groups with number of animals in each group and p-value calculated using a non-parametric Man-Whitney test. Histology scores for four weeks given on 18-point ICRS scale and scores for twelve weeks given on 24-point O'driscoll scale.

Macroscopic Scores

| | | Treated | Control | n | p | Treated | Control | n | p |
|---|---|---|---|---|---|---|---|---|---|
| Condyle | 4 weeks | 7.83 | 5 | 6 | 0.045 | 6.83 | 7 | 6 | 0.50 |
| | 12 weeks | 9.33 | 7 | 13 | 0.064 | 5.25 | 5.75 | 4 | 0.33 |
| Trochlea | 4 weeks | 9.5 | 5.7 | 6 | 0.033 | 8.5 | 7.8 | 6 | 0.19 |
| | 12 weeks | 10 | 10.33 | 13 | 0.41 | 6.5 | 11.25 | 4 | 0.055 |

Histology Scores

| | | Treated | Control | n | p | Treated | Control | n | p |
|---|---|---|---|---|---|---|---|---|---|
| Condyle | 4 weeks | 5.3 | 4.8 | 6 | 0.098 | 4.8 | 5.5 | 6 | 0.29 |
| | 12 weeks | 10.67 | 10 | 13 | 0.36 | 7.5 | 11 | 4 | 0.17 |
| Trochlea | 4 weeks | 7.2 | 7 | 6 | 0.34 | 7.2 | 7.3 | 6 | 0.40 |
| | 12 weeks | 13.3 | 11 | 13 | 0.042 | 12 | 13.33 | 4 | 0.23 |

*Effect of PA/HA hybrid on cartilage healing after twelve weeks*

Based on these short-term studies, (+) TGFβ scaffolds were selected to evaluate cartilage regeneration at twelve weeks. We chose twelve weeks expecting that this would be too early for hyaline-like tissue to develop without intervention, but long enough that cartilage repair could occur in response to the bioactive scaffold. In this experiment, samples of the joint fluid were drawn prior to surgery and at variable time points following implantation of the material. Fourteen sheep were initially included in this study, though evaluation of the synovial fluid drawn prior to surgery showed significantly elevated TNF-α in one of its joints, with the concentration relative to the contralateral joint over three standard deviations larger than the mean for across all animals tested prior to surgery. Because this cytokine is highly correlated with acute inflammation,[267] this sheep was determined to have had an underlying condition prior to surgery and excluded the

animal from further analysis. Evaluation of the macroscopic appearance of defects following resection showed a trend of improved scores for condyle defects treated with the hybrid material relative to control defects treated with the growth factor only (Figure 5.13a,b; Table 5.3). In the trochlea, both treated and control defects healed significantly, making it difficult to discern differences in macroscopic appearance between treated and control groups (Figure 5.13d,e; Table 5.3). Histological sections of condyle defects stained with Safranin O or H&E showed high variability in condyle defects with hyaline-like tissue observed in some treated defects, but poor healing in others, resulting in no significant difference in their score (Figure 5.13a,c; Table 5.3). In the trochlear groove, however, treatment with the hybrid material resulted in better repair of hyaline-like tissue overall as indicated by the development of a neocartilage layer rich in sGAG and collagen II (Figure 5.13d). This difference resulted in a statistically a statistically significant improvement in blinded scores of the histological sections (Figure 5.13f; Table 5.3). Treatment resulted in higher mean scores across all evaluation categories, with the most significant improvement in the development of hyaline-like cellular morphology (Figure 5.14; Table 5.4). The difference in response may be related to differences in healing time course for the two defect sites. In the more mechanically active condyle, slow cartilage healing may have resulted continued differences in defect fill between the treated and control groups, but limited the formation of hyaline-like tissue at twelve weeks regardless of treatment. On the other hand, faster healing in the trochlear groove may have led to high macroscopic scores regardless of treatment, but enhanced histological scoring only in response to hybrid material treatment. In addition, treated trochlear groove defects developed more regular surfaces than treated condyle defects, suggesting that further improvements in material toughness may be necessary for optimal healing of condyle defects. Importantly, improved regeneration of hyaline-like tissue due to the hybrid scaffold in

trochlear groove defects demonstrates the biological ability of the material to effect cartilage repair.

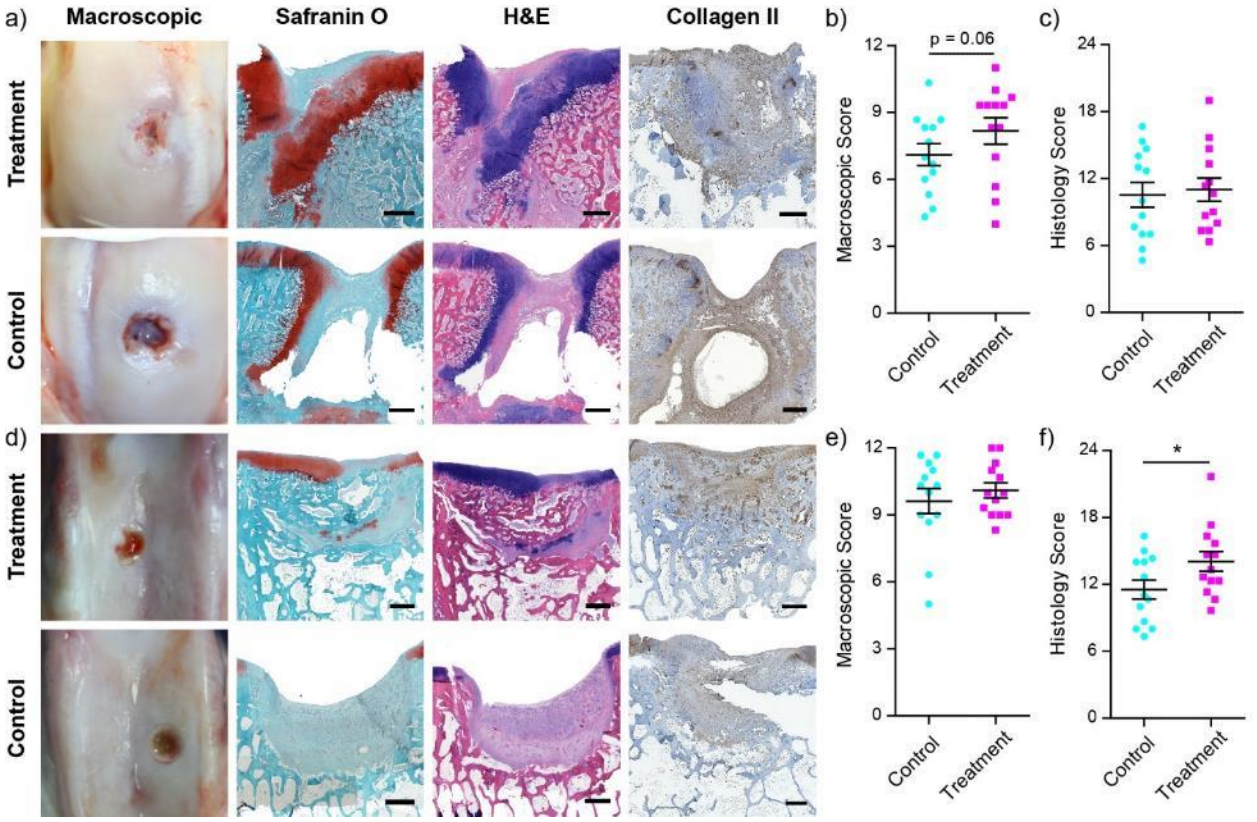


**Figure 5.13: Cartilage repair twelve weeks post-surgery**

(a) Representative macroscopic appearance, Safranin O stained sections, H&E stained sections, and immunohistology staining of collagen II for condyle defects twelve weeks following implantation with (b) ICRS scoring of the macroscopic appearance and (c) O'driscoll scoring of the histological sections (n = 13). (d) Representative macroscopic appearance, Safranin O stained sections, H&E stained sections, and immunohistology staining of collagen II for condyle defects twelve weeks following implantation with (e) ICRS scoring of the macroscopic appearance and (f) O'driscoll scoring of the histological sections (n = 13). Scale = 1 mm. (*, $p < 0.05$; Mann-Whitney Test)

**Table 5.4: O'driscoll histology scoring criteria**
Table adapted from ref.[268]

| Characteristics | Score |
|---|---|
| **Nature of predominant tissue** | |
| *Cellular morphology* | |
| Hyaline cartilage | 4 |
| Incomplete differentiated mesenchyme | 2 |
| Fibrous tissue or bone | 0 |
| *Safranin O staining of matrix* | |
| Normal | 3 |
| Moderate | 2 |
| Slight | 1 |
| None | 0 |
| **Structural characteristics** | |
| *Surface regularity* | |
| Smooth and intact | 3 |
| Superficial horizontal lamination | 2 |
| Fissures 25% - 100% of thickness | 1 |
| Severe disruption, fibrillation | 0 |
| *Structural integrity* | |
| Normal | 2 |
| Slight disruption, cysts | 1 |
| Severe disintegration | 0 |
| *Thickness* | |
| 100% of normal adjacent cartilage | 2 |
| 50% - 100% of normal cartilage | 1 |
| 0% - 50% of normal cartilage | 0 |
| **Freedom from cellular changes of degeneration** | |
| *Hypocellularity* | |
| Normal cellularity | 3 |
| Slight hypocellularity | 2 |
| Moderate hypocellularity | 1 |
| Severe hypocellularity | 0 |
| *Chondrocyte clustering* | |
| No clusters | 2 |
| < 25% of cells | 1 |
| 25% - 100% of cells | 0 |

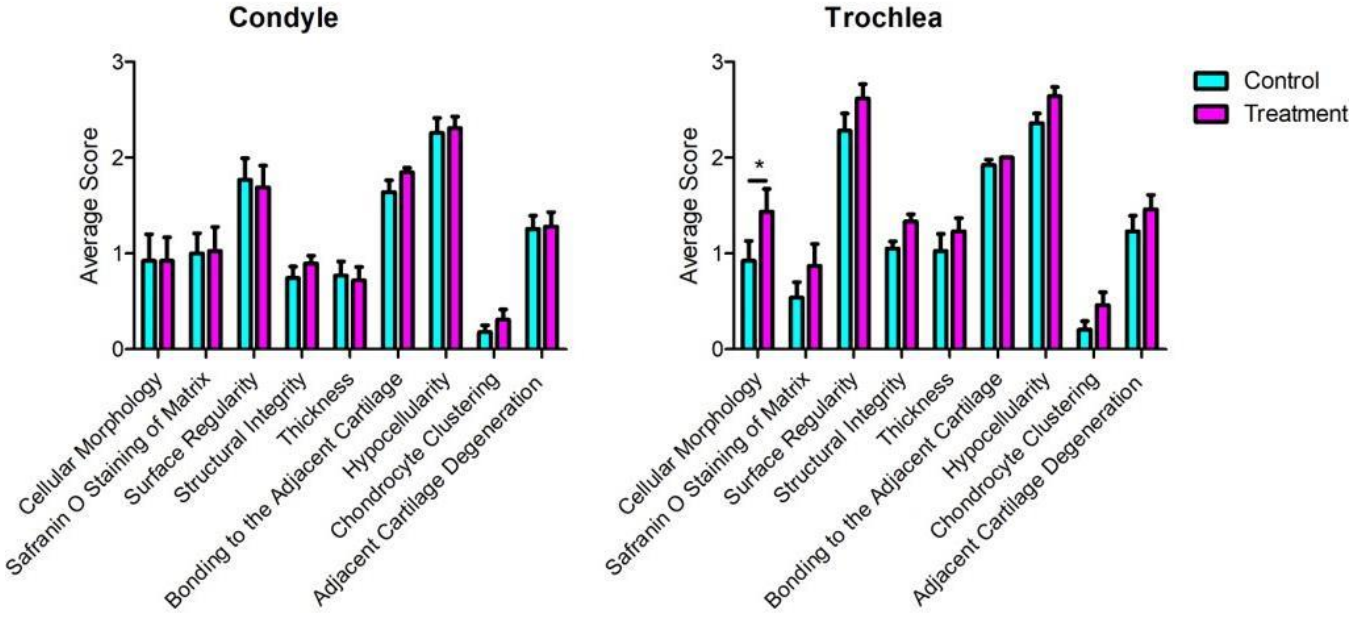


**Figure 5.14: Histological scoring by category twelve weeks post-surgery**
Mean histological scores by category for condyle and trochlea defects for the 12-week study in the (+) TGF group. n = 13. 2-way ANOVA treatment effect: condyle, ns; trochlea, **. (*, $p < 0.05$; **, $p < 0.01$)

To confirm that TGFβ-1 delivery was necessary for cartilage repair at twelve weeks a four-animal, twelve-week pilot study was implemented where treated defects were filled with the hybrid material only and control defects were treated with the growth factor vehicle only. Consistent with the four-week study, application of the material without the addition of the growth factor did not improve the macroscopic appearance or histological scores for defects in either the condyle or the trochlea (Figure 5.15; Table 5.3). The lack of score improvement in the PA/HA hybrid treated defects in the (-) TGFβ group at both four weeks and twelve weeks may be related to decreased physiological growth factor availability in large animals like sheep relative to smaller mammals like rabbits. Alternatively, the tight bundles of PA filaments that form following the addition of HA may limit the efficacy of the displayed binding epitope by inhibiting diffusion of endogenous

growth factor between PA filaments. Thus, while the hybrid material could influence cartilage repair in a sheep model with a low dose of delivered TGFβ-1, future work may be necessary to eliminate the need for exogenous growth factor entirely.

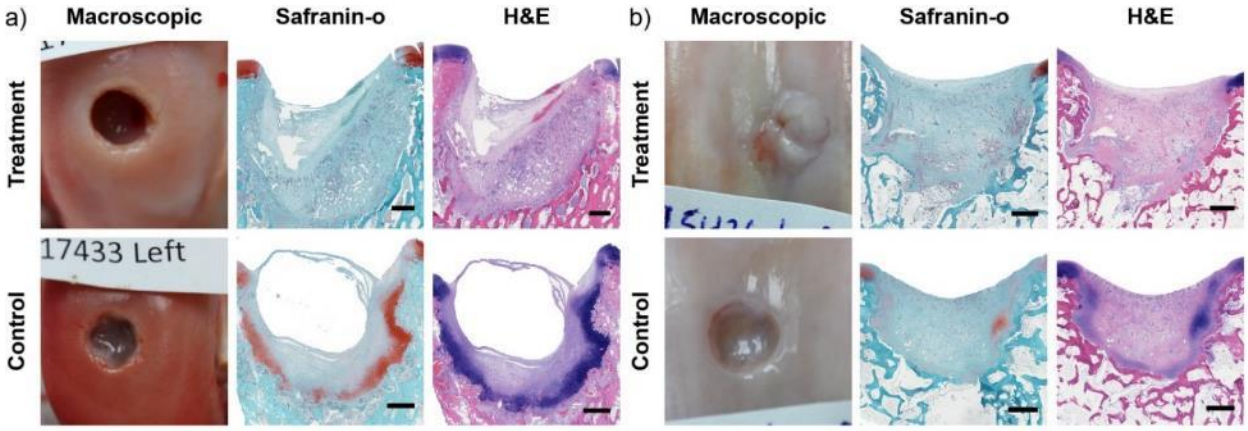


**Figure 5.15: Cartilage repair twelve weeks post-surgery without exogenous TGFβ**
Macroscopic appearance and histological staining of (a) medial condyle and (b) trochlear groove defects treated with PA/HA hybrid material without growth factor and contralateral controls where only the saline vehicle was applied. Scale = 1 mm.

Taken together, these *in vivo* studies show that when delivering TGFβ-1 the PA/HA hybrid material has both mechanical and biological properties necessary to enhance cartilage repair in a large animal. Improved defect filling at four weeks demonstrated the material is resilient enough to sustain TGFβ-1, even in highly sheared condyle defects. Improved hyaline-like tissue formation at twelve weeks revealed the hybrid implants effect a biological response that improves repair of the articular cartilage. Although this effect was evident only in trochlear groove defects, future experiments that investigate later time points are necessary to determine if more hyaline-like tissue would eventually form in treated condyle defects. In addition, while treated trochlear groove defects showed strong remodeling of underlying bone at twelve weeks, new bone was not evident

in treated condyle defects. Combining the cartilage regenerating material with an underlying osteoinductive material may hasten regeneration of underlying bone and localize cartilage regeneration at the joint surface.

In addition to the selection of sacrifice time, several other experimental factors may have affected the study. For instance, the high variability in scores observed at both four weeks and twelve weeks was likely a result of the sheep population used in this study. Sheep were acquired from local farms and had a wide range of ages and weights at the time of surgery. In addition, synovial fluid analysis showed there was further variability in inflammatory state of the joints prior to surgery. Creating bilateral defects and treating only one side helped mitigating this problem by ensuring treatment and control defects were from the same sheep population in each study group, but could not reduce the wide range of scores across animals. In addition, differences between joints may develop within the same animal due to inflammation or anatomical changes that can occur with age. Still, studies at both four weeks and twelve weeks resulted in statistically significant differences in macroscopic and histological scores, respectively, suggesting a strong effect that could be measured despite these confounding factors. The behavior of the sheep following surgery may also have affected how the hybrid material performed. Although the pilot study showed little difference in defect fill between the slung limb and contralateral unslung limb, placing one limb in a sling likely decreased the sheep's movement following surgery. It was observed that when no limbs were placed in slings for the four-week and twelve-week studies, sheep were more active in the days following surgery, which may have resulted in higher mechanical shear on the defect relative to the non-slung limb in the pilot study. Because clinical patients would be expected to be sedentary for some time following cartilage repair treatments, the animal model may be improved by restricting sheep movement in the days following material

implantation. This effect may have contributed to the more irregular surface morphology observed in histological sections of treated condyle defects relative to treated trochlear groove defects.

*Cytokine biomarkers in the ovine joint space during cartilage healing*

To better understand the physiology of the joint during the healing process, the concentration of several inflammatory cytokines was quantified using a multiplex assay. In addition, the inflammatory response to the formation of the defect and to the hybrid material, TGFβ-1 has significant inflammatory modulating properties that may also affect the immune response during cartilage repair.[198] For several cytokines, joint fluid concentrations increased significantly following surgery and then tapered in the following weeks. For example, upregulation of IL-6 is a known response to cartilage damage.[269] Despite very low concentrations prior to surgery, levels of the cytokine increased to ng/ml concentrations one week following surgery, but decreased threefold by the next week (Figure 5.16a). Other markers associated with acute inflammation such as interleukin-8 (IL-8 or CXCL-8), macrophage inflammatory protein-1α (MIP-1α), interferon gamma-induced protein-10 (IP-10), monocyte chemoattractant protein-1 (MCP-1 or CCL-2)[267] showed similar trends. These factors were likely secreted in response to elevated IL-6[270] and in the case of MCP-1 may be involved in initiating cartilage repair (Figure 5.16b-e).[271] The angiogenic VEGF also increased to its highest level one week following surgery, possibly due to early vascularization during the development of new subchondral bone (Figure 5.16f). Importantly, both treated and control samples in the (+) TGFβ group and in the (-) TGFβ group had similar concentrations of these cytokines in the weeks following surgery, suggesting the hybrid gel did not change the acute immune response to the formation for the osteochondral defect. For several other factors, concentration increased following surgery and the elevated levels were sustained throughout the twelve-week study. These included the pro-inflammatory factors IL-1α

and TNF-α as well as the anti-inflammatory signals interleukin-10 (IL-10) and interleukin-36 receptor antagonist (IL-36RA; Figure 5.16g-j). The continued presence of these factors suggests their involvement in continued inflammatory modulation in the joint space during joint healing following the acute response.[272] Though mean levels of these factors were somewhat lower in the (-) TGFβ group than in the (+) TGFβ group, the similar concentrations in the treatment and control group many weeks after the initial TGFβ-1 injection suggests this difference is due to inter-animal variability between he small sample groups and not a response to the delivered growth factor.

## 5.4. Conclusions

This study described the development of an injectable bioactive cell-free scaffold capable of inducing cartilage regeneration in a large-animal sheep model. Combining a bioactive-self assembling component with HA microgels produced a resilient material with the mechanical properties necessary to improve osteochondral defect fill over short times and the biological properties necessary to induce chondrogenesis in response to sustained delivery of a low TGFβ-1 dose at longer times. Characterization of the material revealed a previously unknown phenomenon whereby combining the supramolecular PA and covalent HA components produced bundled, porous scaffolds. These biocompatible gels supported chondrogenesis of embedded progenitor cells and may be useful in other regenerative applications where scaffold topology is important in cellular response. Due to the chemical versatility of the supramolecular PA fibers, the system described here can be adapted to deliver additional growth factor binding or signaling peptides. Based on this work the PA/HA hybrid is envisioned as a materials platform that can be delivered arthroscopically, withstand the mechanical stresses of large-animal joints, and display programmed bioactive signals tailored to any number of bioregenerative applications.

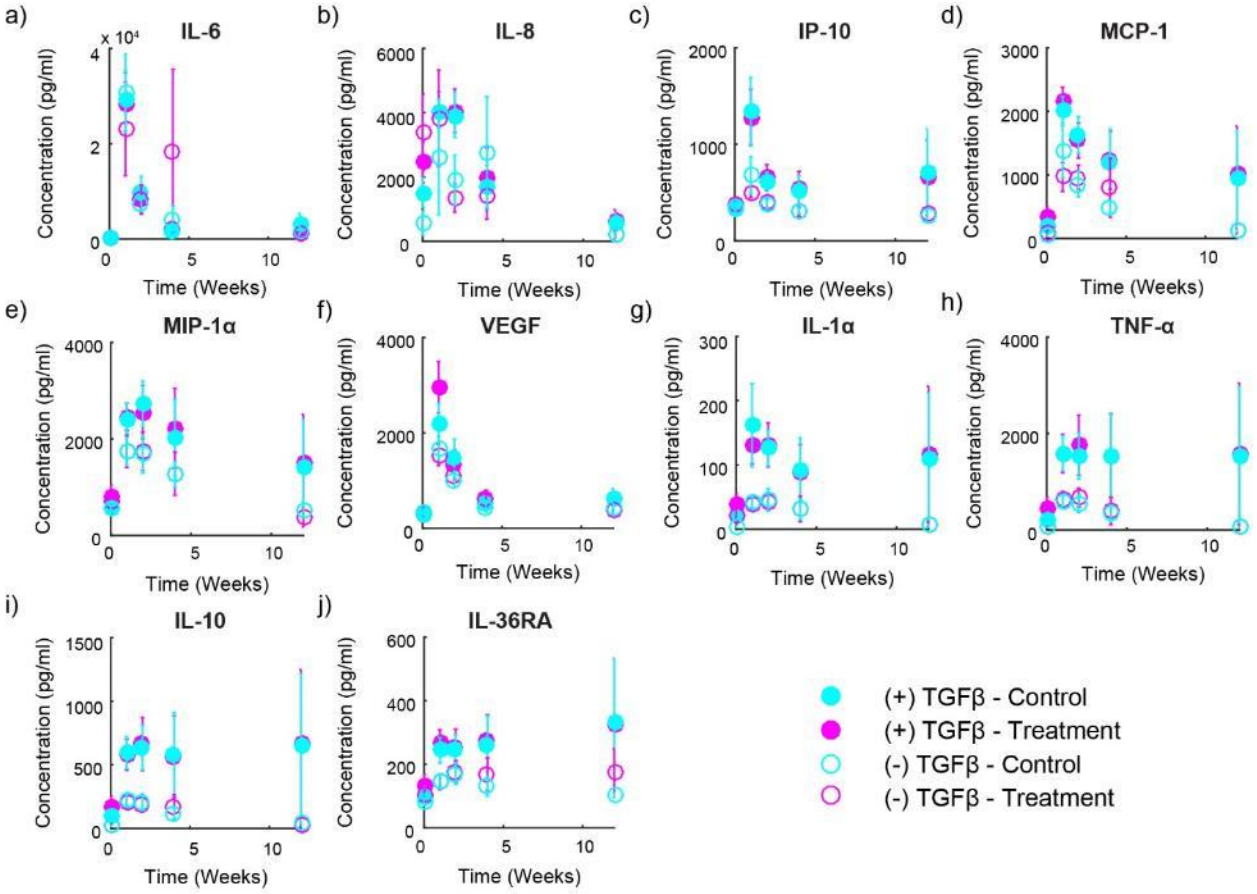


**Figure 5.16: Inflammatory biomarkers in the synovial fluid during defect healing**
Synovial fluid concentration of (a) IL-6, (b) IL-8, (c) IP-10, (d) MCP-1 (e) MIP-1α, (f) VEGF, (g) IL-1α, (h) TNF-α, (i) IL-10, and (j) IL-36RA as a function of time after defect formation where 0 week samples were drawn prior to surgery. (For (+) TGFβ group: 0 week, n = 13; 1 week, n = 13; 2 weeks, n = 11; 4 weeks, n = 6; 12 weeks, n = 5. For (-) TGFβ group: all weeks, n = 4.)

## 5.5. Materials and Methods

*Peptide amphiphile synthesis:* Peptides synthesis was performed at the Peptide Synthesis Core at the Simpson Querrey Institute via standard Fmoc solid-phase peptide synthesis chemistry on a Rink MBHA resin using a CEM Liberty microwave-assisted synthesizer. For dye-labelled PA, a methtrityl protecting group was first removed from the lysine using 1:5:94 solution of TFA: TIS:

DCM. For carboxytetramethyrhodamine (TAMRA)-PA, after washing with DCM, the TAMRA was coupled using 1.2 equivalents of TAMRA,1.2 equivalents of PyBOP and 8 equivalents of N,N-diisopropylethylamine overnight. For fluorescein isothiocyanate (FITC)-labeled PA, the dye was added in the same manner, but without the addition of PyBop. Peptides were cleaved from the resin using a 95:2.5:2.5 solution of TFA:TIS:DCM for three hours followed by concentration and precipitation dropwise into cold diethyl ether. The precipitate was resuspended in 0.1% ammonium hydroxide in water and passed through a 0.2 μm syringe filter prior to purification. Peptides were purified by standard reverse phase HPLC on a Waters Prep150 instrument (Milford, MA, USA) against a water/acetonitrile gradient with 0.1% ammonium hydroxide. Eluted fractions were collected and assessed using Agilent 6520 QTOF liquid chromatograph-mass spectrometer (LC-MS; Santa Clara, CA, USA). Confirmed fractions were pooled, acetonitrile was removed by rotary evaporation, and solutions were frozen and dried via lyophilization Purity of the product was confirmed by LCMS using a Phenomenex Gemini C18 column over a 5% to 95% water to acetonitrile gradient with 0.1% ammonium hydroxide.

*HA particle synthesis:* HA sodium salt from *Streptococcus equi* with a 1.5-1.8 MDa molecular weight (Sigma-Aldrich) was obtained and autoclaved for sterilization. In a biological safety cabinet, sterile water was added to the powder to 1.25 wt% and the solution was agitated overnight to dissolve the material. A solution was prepared in sterile water of 3 mg/ml EDC (Sigma-Aldrich) and 3.5 mg/ml L-lysine methyl ester dihydrochloride (Sigma-Aldrich) and sterile filtered and added to the HA solution to 20% of the total volume. The mixed solution was agitated for 30 minutes and then poured into cell culture flasks to cover their surface at 1 ml/cm$^2$. The solution was allowed to dry in the biological safety cabinet over 72 hours. The resulting film was rehydrated with sterile water and washed by in an excess of water under agitation for at least 24 hours with 3

changes of water to remove excess crosslinker. The gel was transferred to a Magic Bullet blender and blended for a total of 5 minutes. The resulting suspension was frozen and lyophilized.

*Ninhydrin assay*: 1 mg HA was dissolved in 1 ml of water for 1 hour to which was added 500 µl ninhydrin reagent (Sigma-Aldrich). Samples were placed in boiling water for 10 minutes and transferred to a microplate. Absorbance at 570 nm was read using a Cytation 3 microplate reader. Absorbance was compared to a standard curve of L-lysine methyl ester dissolved at known concentrations to calculate primary amine content.

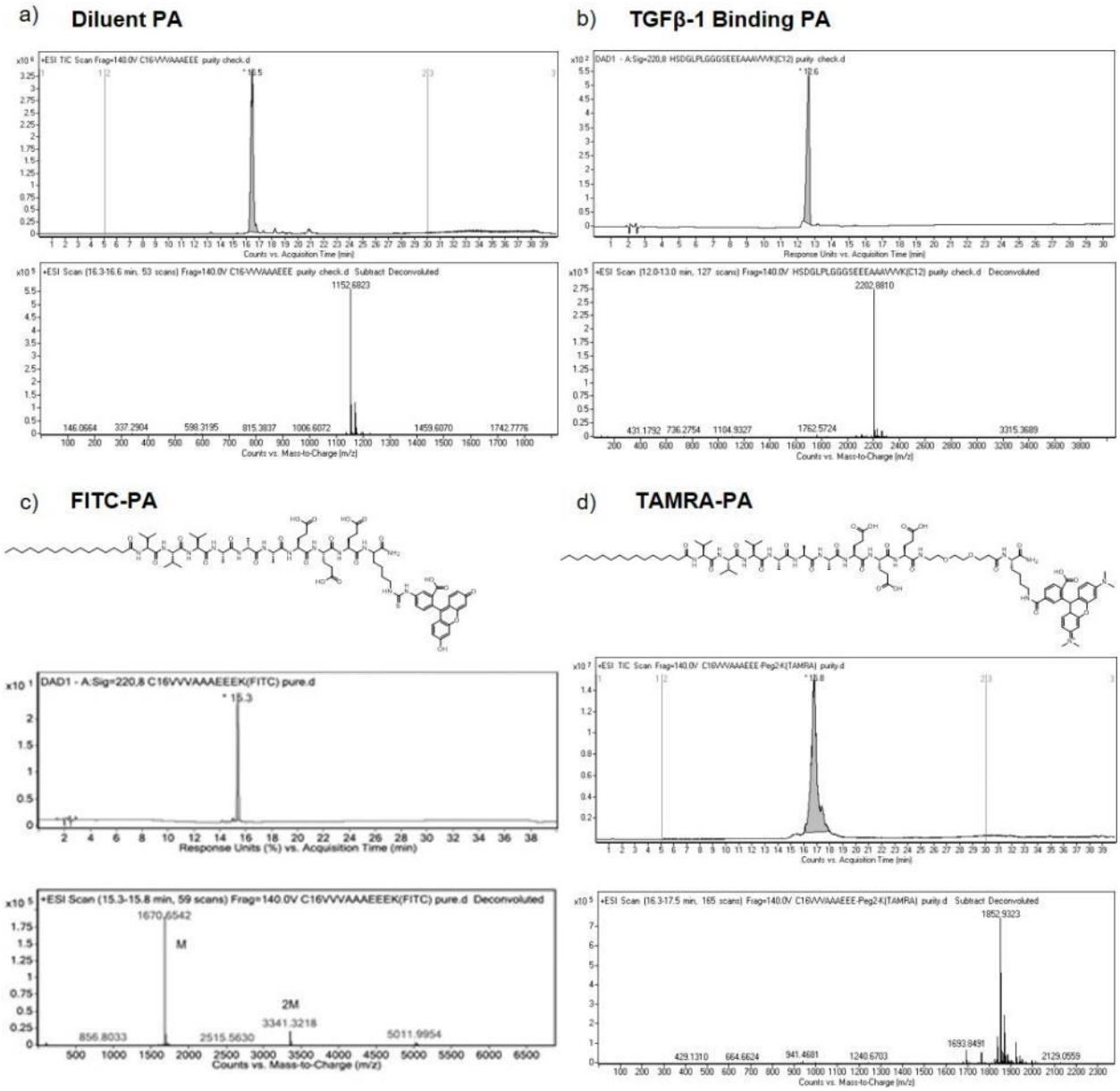


**Figure 5.17: Chemical characterization of PA moelcules reported**
LC-MS confirming purity and MS for (a) Diluent PA, (b) TGFβ-1 Binding PA, (c) FITC tagged PA, and (d) TAMRA tagged PA.

*Gel preparation:* The diluent PA molecule and TGFβ-1 binding PA molecule were each suspended in sterile water to19 mM for materials characterization or *in vivo* experiments and to 38 mM for *in vitro* biological experiments and the pH of the solution was adjusted to 7 using a sterile filtered

solution of 1 M sodium hydroxide. For experiments where a fluorescently tagged PA was used, the fluorescently tagged PA was dissolved to its stated final concentration and then the diluent PA or binding PA powders were resuspended in the fluorescent PA solution. Solutions of the diluent PA and binding PA were mixed at a 9:1 ratio, sealed in a sterile tube, and bath sonicated for 1 hour. The solutions were heated in a water bath to 80°C for 1 hour and allowed to cool in the bath overnight. Immediately prior to further use, PA solutions were diluted by 10% with either sterile water or a solution of recombinant human TGFβ-1 to achieve the stated protein concentration and a molar PA concentration equivalent to 2 wt% diluent PA. To produce the composite gel, the PA solution was added to HA for to a final HA concentration to the indicated concentration (4 wt% for all biological experiments). The resulting slurry was mixed with a spatula and spun down with a microcentrifuge several times to initiate hydration. Samples were allowed to hydrate on ice for 1 hour prior to use.

*Rheology:* Measurements were performed on an Anton Paar MCR302 rheometer with 25 mm parallel-plate fixture. 90 μl of the PA solution or the PA/HA hybrid slurry was placed on the measurement stage and 30 μl of a 50 mM $CaCl_2$/75 mM NaCl gelling solution was placed on the upper fixture. The fixture was lowered to a 0.5 mm gap for 5 minutes and then lowered further to 0.25 mm for another 5 minutes during which time a 0.1% oscillatory strain was applied with a 10 rad/s angular frequency. A strain sweep was then performed at the same angular frequency from 0.1% to 100% strain.

*HA degradation assay:* HA only samples were prepared by dissolving the HA powder as received or following crosslinking to 4 wt% in 100 μl sterile water. PA/HA hybrid samples were prepared to 100 μl using HA as received or following crosslinking to 4 wt%. 5 replicates were prepared of each sample were prepared in conical microcentrifuge tubes. To each sample, 50 μl of a 25 mM

$CaCl_2$ and 0.1% BSA in TBS gelling solution was added for 1 hour. Then, 850 µl of a 100 U/ml solution of hyaluronidase Type I-S (Bovine source; Sigma-Aldrich) in 10 mM $CaCl_2$ and 0.1% BSA supplemented TBS was added to each sample and incubated at 37°C. Every 2 days, the tubes were inverted twice and 200 µl of the supernatant was removed and flash frozen. After 10 days, 500 µl PBS was added to each tube and the remaining material was titrated and agitated for 1 hour to break apart the remaining gel. The degradation of HA was quantified by measuring the concentration of uronic acid functional groups in the supernatant or in remaining gel as previously described.[273] Briefly, samples were thawed and batch sonicated for 1 hour. A standard curve was prepared by serially diluting a 1 mg/ml glucuronic acid glucuronic acid γ-lactone in water. 25 µl of sample or standard was placed in a 96 well plate in triplicate and solutions were diluted 1:1 in saturated benzoic acid. To each well was added 100 µl fuming sulfuric acid supplemented with 25 mM sodium tetraborate. Samples were heated to 100°C in a sand bath for 10 minutes and then allowed to cool to ambient temperature. To each well was added 25 µl 0.125% carbazole in absolute ethanol and samples were heated again to 100°C for 10 minutes and cooled to ambient temperature. Optical absorbance of each well was read at 550 nm using a Biotek Cytation 3 microplate reader and uronic acid concentration was determined based on the glucuronic acid γ-lactone standard curve. Total degradation was normalized to the fraction of uronic acid groups released at each timepoint relative to the sum of the total detected during the degradation timepoints and total remaining in the gel after 10 days.

*Swelling assay:* 50 µl PA solution or PA/HA hybrid was added to a conical microcentrifuge tube and 50 µl of a 50 mM $CaCl_2$/75 mM NaCl gelling solution was added to each tube. After one hour, excess gelling solution was removed and 950 µl water was added to each tube. At each timepoint, five gels of each sample were removed from their tube and transferred to a pre-weighed

microcentrifuge tube. The weight was recorded and then the gels were frozen with liquid nitrogen, lyophilized, and weighed again to determine the volumetric swelling ratio. The final ratio was compared to the ratio of water to material as prepared to determine the volume increase at each timepoint.

*Scanning electron microscopy:* Cell-free samples were prepared by gelling PA solution or the PA/HA hybrid using a 50 mM $CaCl_2$/75 mM NaCl gelling solution for 1 hour. For cell-encapsulating gels, the media was removed and samples were fixed for 30 minutes with 2% paraformaldehyde/2.5% glutaraldehyde in 150 mM NaCl followed by 3 washes with 150 mM NaCl. Gels were transferred to a stainless-steel cage and dehydrated through a series of water-ethanol solutions to absolute ethanol. The samples were then dried at the critical point of $CO_2$ using Samdri-795 Critical Point Dryer (Tousimis). Prior to imaging, samples were coated with 25 mm osmium using Filgen OPC-60A plasma coater. Imaging was performed using a Gemini 1525 SEM at an accelerating voltage of 3.0 kV for cell-free samples or a Hitachi SU8030 SEM at an accelerating voltage of 2.0 kV for cell-encapsulating samples.

*X-ray scattering:* SAXS and WAXS measurements were performed simultaneously using beamline 5ID-D in the Dupont-Northwestern-Dow Collaborative Access Team Synchrotron Research Center at the Advanced Photon Source at Argonne National Lab. To prepare the samples, an adhesive silicone spacer was placed on a piece of Kapton tape and the PA solution or the PA/HA hybrid was placed within the spacer. A second piece of tape was the flattened above the tape to seal the sample between two Kapton windows. The sample was exposed to 17 keV x-rays five times for 1 second and two-dimensional scattering patterns were recorded with using three Rayonix CCD detectors. The patterns were converted to one-dimensional intensity profiles by

azimuthal integration using the data reduction program FIT2D and plotted against the wave vector $q = (4\pi)\sin(\theta/2)$ where $d = 2\pi/q$.

*Protein release:* Solutions of 100% diluent PA or 90% diluent PA and 10% binding PA were heat treated at 17 mM and combined 9:1 with a solution of 10 μg/ml recombinant human TGFβ-1 (eBioscience) and 0.1% BSA and allowed to mix for 1 hour on ice. As a control, the TGFβ-1 solution was diluted 10 times in water. 100 of each μl PA was combined with HA to 4 wt% and allowed to hydrate for 1 hour on ice in a conical microcentrifuge tube. To each PA/HA hybrid or control sample was added 50 μl of a 25 mM $CaCl_2$ and 0.1% BSA in TBS gelling solution and samples were incubated at 37°C for 1 hour. After gelling, each tube was filled with 400 μl 10 mM $CaCl_2$ and 0.1% BSA supplemented TBS and incubated at 37°C. At each timepoint, 200 μl of the buffer solution was removed and replaced and samples were stored at -80°C. After 21 days, samples were removed, 400 μl PBS was added to each tube followed by triteration and agitation for 1 hour to remove the remaining growth factor from the gels. The TGFβ-1 concentration of each sample was quantified using a Ready-Set-Go Human/Mouse TGFβ-1 ELISA kit (Invitrogen) according to the manufacturers instruction and normalized to the gel-free control sample. At each timepoint, the protein released was normalized to the sum of the total protein released and protein remaining within each gel.

*Cellular encapsulation:* Human MSCs were obtained from Lonza and maintained in MSC growth media (Lonza). Cells were used for experiments prior to passage 6. Cells were trypsinized and resuspended in growth media for counting followed by centrifugation and resuspension to 4 million cells/ml in DMEM. Cells were mixed 1:1 volumetrically with PA solutions heat treated at 38 mM and diluted 10% with water or a 20 μg/ml solution of recombinant human TGFβ-1 (R&D Systems) as indicated and incubated together for one hour on ice. 50 μl PA/cell solutions were

added to a conical centrifuge tube containing a 2 mg HA, mixed with a spatula, and incubated for 1 hour at 37°C. To each sample was added 50 µl sterile gelling solution (50 mM $CaCl_2$/75 mM NaCl) and excess gelling solution was removed after 30-minute incubation at 37°C. Each tube was filled with 770 µl chondrogenic media containing DMEM supplemented with 4.5 g/L glucose, 1% penicillin/streptomycin, 1% insulin/human transferrin/selenous acid premix, 0.1 mM l-ascorbic acid 2-phosphate sesquimagnesium salt hydrate, and 100 nM dexamethasone. Media was supplemented with freshly thawed aliquots of TGFβ-1 to 10 ng/ml for soluble TGFβ-1 experimental groups. Half the media was removed and replaced three times a week during the culture period.

*Cytotoxicity assay:* Cells were cultured encapsulated in PA only gels or PA/HA hybrid gels for 24 hours in TGFβ-1 free media. Media was removed and replaced with 2 µg/ml calcein and 5 µg/ml propidium iodide in TBS. Samples were incubated at 37°C for 1 hour and then washed 3 times with TBS. Gels were removed and placed on a coverglass immediately prior to imaging. Three regions of each of three gels per experimental group were imaged Nikon W1 Dual Cam Spinning Disk Confocal Microscope and cells were counted using the MATLAB Image Processing Toolbox.

*Immunohistochemistry:* Gels were fixed with 4% paraformaldehyde in 150 mM NaCl for 20 minutes and washed 3 times 150 mM NaCl. Gels were then snap frozen in liquid nitrogen and cut into sections with a razor blade. Sections were laid flat on a microscope coverglass and cells were permeabilized for one hour with a blocking buffer containing 150 mM NaCl, 2% goat serum and 0.2% Triton X-100. Sections were stained overnight with a solution containing a rabbit derived anti-Sox 9 primary antibody at 400x dilution (Novus), rhodamine-phalloidin at 100x dilution, and Hoechst 33258 at 100x dilution in blocking buffer. Samples were rinsed three times and stained with a goat-anti-rabbit Alexa 647 conjugated primary antibody (250x dilution) for 2 hours in

blocking buffer. Samples were rinsed, coverslipped, and imaged using a Nikon A1R laser confocal microscope.

*Sulfated glycosaminoglycan quantification assay:* Cells were encapsulated in either PA only gels or PA/HA hybrid gels. For each material, 5 sample replicates were prepared and maintained in each of three conditions. These were (1) gels cultured without TGFβ-1 supplementation, (2) gels cultured in TGFβ-1 supplemented media, and (3) gels prepared containing 1 μg/ml TGFβ-1 and cultured without further TGFβ-1 supplementation. After 4 weeks of culture, the total TGFβ-1 added via media supplementation in the soluble TGFβ-1 group equaled the total TGFβ-1 encapsulated in the gels in the growth factor encapsulation group (50 ng). At 4 weeks, the media was removed and to each tube was added 250 μl digestion buffer containing 0.2 mg/ml papain (Sigma-Aldrich), 10 mM L-cysteine, 60 mM $NaH_2PO_4$, and 40 mM $NA_2HPO_4$. Gels were broken apart via trituration, transferred to screw-top conical microcentrifuge tubes, and incubated for 18 hours at 60°C. A standard curve was prepared by serially diluting a 250 μg/ml solution of CS from bovine trachea in the digestion buffer. After digestion, 25 μl of each sample or standard solution was added in triplicate to a 96 well plate and diluted 1:1 in the digestion buffer. To each well was added 250 μl of a detection solution reported containing mg/ml NaCl, 3 mg/ml glycine, 10 mM acetic acid, and 16 μg/ml DMMB, pH 1 as previously reported.[226] Optical absorbance for each well at 525 nm was recorded using a Cytation 3 microplate reader (BioTek, Winooski, VT). Total DNA concentration for each sample was measured using a Quant-iT PicoGreen assay kit (Invitrogen, Carlsbad, CA) according to the manufacturer's protocol and total sGAG content was normalized to DNA content for each sample.

*Preparation of material for surgical implant:* Heat treated PA solutions prepared at 19 mM were combined with a 10 μg/ml TGFβ-1 solution (R&D Systems) dissolved in a 0.1% BSA, 4 mM HCl

buffer or with the buffer alone at a 9:1 ratio. The combination was mixed by pipetting and kept on ice for 1 hour. 900 µl of the mixed solution was added to 36 mg of crosslinked HA particles prepared under sterile conditions and allowed to hydrate for 1 hour. The hybrid material was packed into a 1 ml syringe with a 19-gauge needle attached and kept on ice until use during surgery.

*Animal study design:* Animal work was performed at the University of Wisconsin, School of Veterinary Medicine, and all procedures were approved by the Institutional Animal Use and Care Committee. Thirty-five mature female sheep ranging in age from 2-7 (mean = 3.7 ± 1.7) years weighing between 60 and 100 (mean = 74 ± 8.3) kg were used in this study. Animals were divided into 6 groups: (1) 1 pilot sheep sacrificed at 1 week to assess material retention, (2) 6 sheep sacrificed at 4 weeks treated with PA and TGFβ-1, with one sheep sacrificed prior to 4 weeks due to patellar luxation and excluded from the analysis, (3) 6 sheep sacrificed at 4 weeks with PA, but without TGFβ-1 treatment, (4) 14 sheep sacrificed at 12 weeks with PA and TGFβ-1 treatment, with 4 sheep sacrificed prior to 12 weeks due to patellar luxation and excluded from analysis, (5) 6 sheep sacrificed at 12 weeks with PA but without TGFβ-1 treatment, with 2 sacrificed prior to 12 weeks due to patellar luxation and excluded from analysis, and (6) two sheep sacrificed at 24 weeks with PA and TGFβ-1 treatment.

*Surgical technique:* Prior to surgery the sheep were fasted for 24 hours, and withheld water for 12 hours. Sheep were administered a dose of Xylazine (0.1-0.22mg/kg IM) in their pen to sedate them for transport to the surgical suite as well as a pre-operative dose of buprenorphine (0.0006-0.01 mg/kgIM) for analgesia. Sheep were then induced with ketamine/midazolam (2-10mg/kg/0.1-0.3mg/kg) IM and immediately intubated. Once intubated the sheep were maintained on isoflurane (0-4%) in 100% O2. At this time, a dose of Procaine Penicillin-G (10,000-20,000 IU/kg) IM was

administered. Using aseptic techniques, a medial stifle arthrotomy was performed on both limbs of each sheep. In each stifle, one osteochondral defect was made in the medial femoral condyle and a second was made in the femoral trochlear groove using a Stryker EHD variable speed surgical drill and a canuulated drill bit. For the 24-week group, defects were made in the condyle only and not the trochlear groove. Defects were 3 mm deep and 7 mm in diameter which is previously reported to be critical sized for sheep osteochondral. For the one-week pilot group, all defects were filled with the PA/HA material, which included TAMRA-tagged PA filaments. For TGFβ-1 treated groups, each defect on one side was filled with the TGFβ-1 supplemented PA/HA material which was ejected from the syringe and packed into the defect space, while each defect on the control side was filled with 1 μg/ml TGFβ-1 in saline solution. For the no growth factor experimental groups, the PA/HA material without added TGFβ-1 was used to fill the defects on one side in the same manner while defects on the opposite side were filled with saline solution only. After defect filling with PA/HA or saline solution, approximately 30 μl of a sterile 50 mM $CaCl_2$, 75 mM NaCl gelling solution was added dropwise on top of each defect. Arthrotomies were closed in a routine manner after thoroughly lavaging the joint with physiological saline Immediately after surgery, all sheep were individually housed in a small pen that allowed for limited movement for the first 3 weeks post-surgery. After this the sheep were moved to group housing and allowed to move freely. In the 1-week group, one hindlimb was kept in a sling, but all other animals were allowed to walk freely on both hindlimbs.

*Synovial fluid sample collection:* For the twelve-week survival group, joint fluid was collected via a joint tap prior to arthrotomy using a 3 ml syringe with an 18-gauge needle under an aseptic condition. Additional joint fluid samples were collected via a sterile joint tap at 1 week, 2 weeks, and 4 weeks post-surgery, and immediately following sacrifice. Samples were stored at -80°C and

thawed prior to evaluation. Cytokine concentration was determined using a MILLIPLEX Bovine Cytokine/Chemokine 15 plex panel (Millipore-Sigma) using a Luminex instrument according to the manufacturer's instructions. The analytes IL-1α, IL-6, IL-8, IL-10, MIP-1α, IL-36RA, IP-10, MCP-1, TNF-α, and VEGF were reliably detected and their concentrations are reported. The analytes interleukin-1β, interleukin-4, interleukin-17A, interferon-γ, and macrophage inflammatory protein-β were not detected in the samples.

*Sample collection*: After euthanasia, operative joints were harvested and the gross appearance was documented with digital photographs. The gross appearance of both condylar and trochlear defect areas was assessed subjectively using the ICRS macroscopic scoring system (Table 5.2)[266] by 3 experienced evaluators blinded to treatment group (L.Y, J. B. and B.M). Mean scores between the PA/HA treated and limbs control limbs for the 4-week and 12-week survival groups were compared using a Mann-Whitney test. The operated medial condyles and trochleae in each group then were cut using a band saw into small bone blocks, which included the defect and its associated underlying subchondral bone.

*Histological staining and evaluation:* The bone blocks were fixed in 10% neutral buffered formalin, and subsequently decalcified using an EDTA/Sucrose decalcifying solution (20% EDTA in 5% Sucrose, Newcomer Supply, Middleton WI). After decalcification, the blocks were cut in half through the center of the defect using a razor blade and both pieces were embedded in the same block of paraffin. Successive five-micron thick sections were prepared and stained with H&E to evaluate general morphology of the grafted site, and Safranin O to evaluate the proteoglycans of the extracellular matrix. All sections were scored by the same 3 investigators who performed the macroscopic scoring. Scorers were blinded to group assignment and used a modified O' Driscoll scoring system (Table 5.4).[268] Mean scores for treated and control limbs for the four-

week and twelve-week survival groups were compared using a Mann-Whitney test. Following scoring, stained sections were imaged using a TissueGnostics microscope. Unstained sections from the pilot study where TAMRA-tagged PA filaments were used were imaged using a Nikon Ti2 Widefield microscope.

# CHAPTER 6

# 6. Discussion and Future Direction

Together, these projects highlight the importance of rational design in the formation of superstructures in supramolecular systems. Efforts to produce biomimetic materials scaffolds must account for the hierarchical nature of the nature assemblies that underly and support tissue development and homeostasis. But superstructure formation can significantly alter the characteristics and performance of these materials. The proceeding chapters explore how peptide superstructures form and ways in which they affect their ability to influence biology. In the future, these lessons can be extended to design more effective complex systems to advance supramolecular chemistry and regenerative engineering.

## 6.1. Tuning Intermolecular Cohesion to Control Hierarchical Assembly

The work in Chapter 2 builds upon a model of superstructure formation by peptide assemblies via molecular redistribution reported in previous work using PA-nucleic acid conjugates. While the previously reported system used strong interactions among assemblies to overcome strong cohesive interactions among PA molecules, these new results demonstrate an alternative approach—weakening intermolecular cohesion to promote superstructure formation without strong inter-assembly crosslinking. By confirming and advancing the design rules needed to build PA structures, the results support further exploration of superstructure formation by PA systems. Applying these rules to new designs can tailor the thermodynamics and architecture of these assemblies for regenerative engineering applications.

An important next step in the development of these systems will be the design of superstructure forming PAs with intermediate cohesive interactions. Building weak β-sheet into these systems may template more robust superstructures that form even longer assemblies. Alternatively, mutating the peptide sequence may produce assemblies with different morphologies such as belts and sheets.[274] Superstructure formation by these altered assemblies may produce new hierarchical structures such as lamellar stacks of PA layers. Increased cohesion could be overcome by adding enough charged residues to strengthen hierarchical attraction among the assemblies. A second important step in advancing these systems is exploring how processing affects their assembly. In the work here, oppositely charged PA assemblies were mixed and allowed to age over time. Heat treatment and varying ionic concentrations may profoundly impact how superstructures form. A detailed study of these effects is underway to better understanding of the thermodynamics of these reactions and thereby develop more robust superstructures.

Another area of future work is the use of superstructure forming PA systems as biomaterials. While these structures may mimic biological topographies, how that will affect cellular behavior is unknown. The tunable mechanical and topographical properties of these systems make them ideal candidates as cell substrates or cell encapsulating gels. By rational design of these very simple building blocks, this work will likely provide straightforward tools to manipulate cell adhesion, migration, and fate.

### 6.2. Nonionic PA Systems for Biomedical Applications

Chapter 3 reports nonionic PA systems that can be used to produce uncharged PA assemblies or assemblies with tunable charge. The work focuses on how charged groups affect the ways PA molecules assemble and explores how PA charge can affect cell behavior in a model for

osteogenesis. The development of this system lays the groundwork for controlling PA charge in a variety of biomedical applications where assembly charge is important.

Assembly of nonionic PA filaments are expected to be a useful tool in determining how charged groups affect the binding of PA assemblies to other biomolecules. In the near term, experiments to determine how ions in solution interact with these nonionic PA filaments will be useful in explaining how nonionic filaments form. In addition, decreasing charge may decrease non-specific binding by eliminating electrostatic interactions between the assemblies and charged biomolecules. Charge may also affect the specific binding of targeted ligands by peptide or DNA epitopes. Displaying these epitopes on nonionic on nonionic PA backbones co-assembled with nonionic diluent PA produces PA filaments where the only charge is in the epitope. Using this design strategy will be useful in determining if charge in the PA backbone affects the ability of these bioactive peptides to bind their targets. Several effects may be important including the balance of on-target specific and electrostatic non-specific effects on binding, off-target non-specific binding masking epitope moieties and decreasing specific binding, or interactions between charged epitopes and charged filament surfaces. In addition, these nonionic systems may be useful in limiting the types of counterproductive superstructure formation discussed in Chapter 4.

Because these PEGylated PA molecules are expected to be non-adhesive, they are strong candidates for systemic administration. Following injection, nonionic or weakly charged PA assemblies will not form gels and will not have the cytotoxic effects reported for anionic and cationic PA assemblies, respectively. Controlling charge can be used to tune biodistribution of the assemblies while binding motifs may be useful in directing these molecules to specific tissue targets. Alternatively, charge is important in determining the immune response to nanomaterials. This effect may work synergistically with the ability to tune the morphology of PA systems, as

nano-scale topography is also known to influence immune interactions. Uncharged PA systems are an easy to prepare and assembly platform to examine the relationship between charge and shape in determining immune response.

### 6.3. Hierarchical Assembly and Epitope Presentation

Chapter 4 reports the use of nonionic PA backbones to display a TGFβ-1 binding epitope. Using this system, the PA could be purified in acidic conditions to avoid a deamidation reaction that occurred during basic purification. Characterization of filaments presenting the epitope showed that deamidation had improved retention of the growth factor by PA hydrogels and suggested that superstructure formation by filaments displaying the non-deamidated sequence may have contributed to inferior performance. These outcomes have implications for both expanding the epitope library that can be presented by PA assemblies and for improving the efficacy of displayed biological signals.

The reported method to prevent deamidation may be applied in a number of PA chemistries where exposure to base is to be avoided. This is obviously important for other peptides sequences with asparagine residues followed by a non-bulky residue where deamidation may occur. In addition, this approach can be extended to other purification sensitive chemistries such as S-nitrosylation. PA with S-nitrosylated cysteine residues are known to deliver therapeutic nitrous oxide (NO), preventing restenosis of vascular implants.[218] However, purification in basic conditions leads to disulfide linkages that can prevent S-nitrosylation,[275] preventing displaying the group on biocompatible acidic backbones. Furthermore, nearby charged groups may catalyze premature NO release,[276] making display on a nonionic PA preferable.

A second major implication of this work is the role superstructure formation can play in epitope activity. The observed effect is expected to be general and displaying cationic epitopes on anionic filaments or vice-versa can limit the activity of many epitope displaying systems. The major implication is that PA systems should be designed to account for these interactions when possible. Possible techniques include the use of nonionic filaments as described in Chapter 3 or the limitation of net charge by adding oppositely charged residues or acetylation of terminal amines. Ideally, computational modeling techniques may be able to better predict when bioactivity limiting salt bridges may occur, and these techniques should be considered prior to the synthesis of new PA systems.

Importantly, the research in Chapter 4 helped overcome a longstanding problem with the design of chondrogenic PA assemblies—the instability of the binding epitope. Using the system described gave chemically pure products as needed for clinical translation. Moreover, the techniques used identified a PA design that was better able to bind the growth factor. This design was applied to pre-clinical work in a large animal in Chapter 5, laying the groundwork for developing a potentially clinically useful therapy for cartilage regeneration.

### 6.4. Next Steps in Cartilage Regenerating Supramolecular Materials

The study described in Chapter 5 is an important step toward the clinical application of supramolecular PA materials for cartilage repair. Currently, pilot studies are in progress to determine the ability of the material to influence the repair of hyaline-like tissue at 6 months. These studies will help establish if there are differences in the healing rate between the condyle and the trochlea, while indicating if biological improvement due to the material treatment is still apparent after a longer period. In future studies, several aspects of the system could be further studies and

improved to produce a translational regenerative therapy. These may include expanded studies of the material's nanoscopic architecture, improvements in the materials mechanical performance, and expansion of the system's bioactivity.

Further studies may help explain of how and when hydrophilic polymers drive the formation of hierarchical assembly of PA filaments. These experiments could include changes to both the covalent and the supramolecular components of the system. For example, substituting the HA used for HA of different molecular weight of for polymers with variable hydrophilicity can help explain the relationship between PA packing and polymer swelling. Alternatively, studying the system at different pH values to determine how repulsion among PA filaments determines the assemblies that form will likewise help explain the intermolecular interactions that drive hierarchal assembly. Finally, because the superstructures evolve over time, manipulating cohesive interactions among PA molecules may change the bundled assemblies that form, highlighting the role PA dynamics plays in the hierarchical self-assembly.

A second area for further development is the physical performance of the material. While the hybrid described here significantly improved the mechanical behavior of the material, further development may be necessary to produce a therapy that is consistently resilient enough for clinical use. In addition, the stiffness of the hybrid material is still lower than the reported stiffness of articular cartilage, which can have a Young's modulus in the MPa range.[277] One possible approach may be the addition of covalent crosslinks between the PA and covalent polymer components of the system. Chemical crosslinks between the two components will likely increase the material's stiffness, while further decreasing swelling which may help the material's retention in the defect. Further work may also focus on varying the materials properties throughout the implant so the deep portion better matches bone while the surface better matches articular cartilage.

Finally, this work can serve as the basis for future materials with more advanced bioactive properties. For example, TGFβ-1 bind can be augmented with binding or mimicking other chondrogenic factors such as IGF. Alternatively, PA filaments could display bioactive sequences that are important in stem cell infiltration and adhesion.[73,240] Increasingly, cartilage engineering is understood as a metabolic and inflammatory conditions,[41] so designing materials to modulate these factors would further improve material performance. For example, free fatty acids such as palmitic acid have recently been showed limit chondrogenesis by directing cells toward angiogenic lineages.[46,278] Because PA molecules contain fatty acid moieties, studying how these chemical groups affect chondrogenesis when incorporated in PA systems will be important in establishing the materials efficacy for cartilage repair. Another area of growing research is biomaterials scaffolds that can modulate inflammatory signaling to improve regeneration.[279,280] Importantly, this work explores the time dependent profile of important inflammatory cytokines in the time following cartilage injury in an ovine model. This data may be paired with previous work on inflammatory modulating PA systems in order to improve the pro-chondrogenic niche.[281] Ultimately, the hybrid scaffold reported here is envisioned as a the foundation of a multifunctional platform that can control multiple mediators of cartilage biology.

# REFERENCES


1. Elemans, J. A. A. W.; Rowan, A. E.; Nolte, R. J. M. Mastering molecular matter. Supramolecular architectures by hierarchical self-assembly. *Journal of Materials Chemistry* **2003,** *13*, (11), 2661-2670. DOI: 10.1039/b304972h.
2. Mendes, A. C.; Baran, E. T.; Reis, R. L.; Azevedo, H. S. Self-assembly in nature: using the principles of nature to create complex nanobiomaterials. *Wiley Interdisciplinary Reviews: Nanomedicine and Nanobiotechnology* **2013,** *5*, (6), 582-612. DOI: 10.1002/wnan.1238.
3. Whitesides, G. M.; Grzybowski, B. Self-assembly at all scales. *Science* **2002,** *295*, (5564), 2418-21. DOI: 10.1126/science.1070821.
4. Cademartiri, L.; Bishop, K. J. Programmable self-assembly. *Nature Materials* **2015,** *14*, (1), 2-9. DOI: 10.1038/nmat4184.
5. Philp, D.; Stoddart, J. F. Self-Assembly in Natural and Unnatural Systems. *Angewandte Chemie International Edition in English* **1996,** *35*, (11), 1154-1196. DOI: 10.1002/anie.199611541.
6. Lehn, J. M. Perspectives in chemistry--steps towards complex matter. *Angewandte Chemie International Edition in English* **2013,** *52*, (10), 2836-50. DOI: 10.1002/anie.201208397.
7. Pollard, T. D.; Borisy, G. G. Cellular Motility Driven by Assembly and Disassembly of Actin Filaments. *Cell* **2003,** *112*, (4), 453-465. DOI: 10.1016/s0092-8674(03)00120-x.
8. Sivan, S. S.; Wachtel, E.; Tsitron, E.; Sakkee, N.; van der Ham, F.; Degroot, J.; Roberts, S.; Maroudas, A. Collagen turnover in normal and degenerate human intervertebral discs as determined by the racemization of aspartic acid. *Journal of Biological Chemistry* **2008,** *283*, (14), 8796-801. DOI: 10.1074/jbc.M709885200.
9. Qiang, W.; Yau, W. M.; Lu, J. X.; Collinge, J.; Tycko, R. Structural variation in amyloid-beta fibrils from Alzheimer's disease clinical subtypes. *Nature* **2017,** *541*, (7636), 217-221. DOI: 10.1038/nature20814.
10. Lim, E. W.; Aarsland, D.; Ffytche, D.; Taddei, R. N.; van Wamelen, D. J.; Wan, Y. M.; Tan, E. K.; Ray Chaudhuri, K.; Kings Parcog group, M. D. S. N. s. g. Amyloid-beta and Parkinson's disease. *Journal of Neurology* **2019,** *266*, (11), 2605-2619. DOI: 10.1007/s00415-018-9100-8.
11. Edbauer, D.; Haass, C. An amyloid-like cascade hypothesis for C9orf72 ALS/FTD. *Current Opinions in Neurobiology* **2016,** *36*, 99-106. DOI: 10.1016/j.conb.2015.10.009.
12. Wang, J.; Liu, K.; Xing, R.; Yan, X. Peptide self-assembly: thermodynamics and kinetics. *Chemical Society Reviews* **2016,** *45*, (20), 5589-5604. DOI: 10.1039/c6cs00176a.
13. Sippel, K. H.; Quiocho, F. A. Ion-dipole interactions and their functions in proteins. *Protein Science* **2015,** *24*, (7), 1040-6. DOI: 10.1002/pro.2685.
14. Pieters, B. J.; van Eldijk, M. B.; Nolte, R. J.; Mecinovic, J. Natural supramolecular protein assemblies. *Chemical Society Reviews* **2016,** *45*, (1), 24-39. DOI: 10.1039/c5cs00157a.
15. Frantz, C.; Stewart, K. M.; Weaver, V. M. The extracellular matrix at a glance. *Journal of Cell Science* **2010,** *123*, (Pt 24), 4195-200. DOI: 10.1242/jcs.023820.
16. Mwenifumbo, S.; Stevens, M. M. ECM interactions with cells from the macro-to nanoscale. *Biomedical nanostructures* **2007,** *1*, 225-260. DOI: 10.1002/9780470185834.ch9.

17. Ricard-Blum, S.; Ruggiero, F. The collagen superfamily: from the extracellular matrix to the cell membrane. *Pathologie Biologie (Paris)* **2005,** *53*, (7), 430-42. DOI: 10.1016/j.patbio.2004.12.024.
18. Hara, M.; Kobayakawa, K.; Ohkawa, Y.; Kumamaru, H.; Yokota, K.; Saito, T.; Kijima, K.; Yoshizaki, S.; Harimaya, K.; Nakashima, Y.; Okada, S. Interaction of reactive astrocytes with type I collagen induces astrocytic scar formation through the integrin-N-cadherin pathway after spinal cord injury. *Nature Medicine* **2017,** *23*, (7), 818-828. DOI: 10.1038/nm.4354.
19. Janson, I. A.; Putnam, A. J. Extracellular matrix elasticity and topography: material-based cues that affect cell function via conserved mechanisms. *Journal of Biomedical Materials Research A* **2015,** *103*, (3), 1246-58. DOI: 10.1002/jbm.a.35254.
20. Stevens, M. M.; George, J. H. Exploring and engineering the cell surface interface. *Science* **2005,** *310*, (5751), 1135-8. DOI: 10.1126/science.1106587.
21. Fratzl, P.; Weinkamer, R. Nature's hierarchical materials. *Progress in Materials Science* **2007,** *52*, (8), 1263-1334. DOI: 10.1016/j.pmatsci.2007.06.001.
22. Ling, S.; Kaplan, D. L.; Buehler, M. J. Nanofibrils in nature and materials engineering. *Nature Reviews Materials* **2018,** *3*, (4). DOI: 10.1038/natrevmats.2018.16.
23. Wang, Y.; Azais, T.; Robin, M.; Vallee, A.; Catania, C.; Legriel, P.; Pehau-Arnaudet, G.; Babonneau, F.; Giraud-Guille, M. M.; Nassif, N. The predominant role of collagen in the nucleation, growth, structure and orientation of bone apatite. *Nature Materials* **2012,** *11*, (8), 724-33. DOI: 10.1038/nmat3362.
24. Fratzl, P.; Misof, K.; Zizak, I.; Rapp, G.; Amenitsch, H.; Bernstorff, S. Fibrillar structure and mechanical properties of collagen. *Journal of Structural Biology* **1998,** *122*, (1-2), 119-22. DOI: 10.1006/jsbi.1998.3966.
25. Horkay, F.; Basser, P. J.; Hecht, A. M.; Geissler, E. Hierarchical organization of cartilage proteoglycans. *Macromolecular Symposia* **2011,** *306-307*, (1), 11-17. DOI: 10.1002/masy.201000115.
26. Place, E. S.; Evans, N. D.; Stevens, M. M. Complexity in biomaterials for tissue engineering. *Nature Materials* **2009,** *8*, (6), 457-70. DOI: 10.1038/nmat2441.
27. Wegst, U. G.; Bai, H.; Saiz, E.; Tomsia, A. P.; Ritchie, R. O. Bioinspired structural materials. *Nature Materials* **2015,** *14*, (1), 23-36. DOI: 10.1038/nmat4089.
28. Sophia Fox, A. J.; Bedi, A.; Rodeo, S. A. The basic science of articular cartilage: structure, composition, and function. *Sports Health* **2009,** *1*, (6), 461-8. DOI: 10.1177/1941738109350438.
29. Wang, Y.; Wei, L.; Zeng, L.; He, D.; Wei, X. Nutrition and degeneration of articular cartilage. *Knee Surgery, Sports Traumatology, Arthroscopy* **2013,** *21*, (8), 1751-62. DOI: 10.1007/s00167-012-1977-7.
30. Cohen, N. P.; Foster, R. J.; Mow, V. C. Composition and dynamics of articular cartilage: structure, function, and maintaining healthy state. *Journal of Orthopaedic & Sports Physical Therapy* **1998,** *28*, (4), 203-15. DOI: 10.2519/jospt.1998.28.4.203.
31. Mow, V. C.; Ratcliffe, A.; Robin Poole, A. Cartilage and diarthrodial joints as paradigms for hierarchical materials and structures. *Biomaterials* **1992,** *13*, (2), 67-97. DOI: 10.1016/0142-9612(92)90001-5.
32. Baumann, C. A.; Hinckel, B. B.; Bozynski, C. C.; Farr, J. Articular Cartilage: Structure and Restoration. *Joint Preservation of the Knee: A Clinical Casebook* **2019**, 1.

33. Goldring, S. R.; Goldring, M. B. Changes in the osteochondral unit during osteoarthritis: structure, function and cartilage-bone crosstalk. *Nature Reviews Rheumatology* **2016,** *12*, (11), 632-644. DOI: 10.1038/nrrheum.2016.148.
34. Lozano, R.; Naghavi, M.; Foreman, K.; Lim, S.; Shibuya, K.; Aboyans, V.; Abraham, J.; Adair, T.; Aggarwal, R.; Ahn, S. Y. Global and regional mortality from 235 causes of death for 20 age groups in 1990 and 2010: a systematic analysis for the Global Burden of Disease Study 2010. *The lancet* **2012,** *380*, (9859), 2095-2128. DOI: 10.1016/S0140-6736(12)61728-0.
35. Glyn-Jones, S.; Palmer, A. J.; Agricola, R.; Price, A. J.; Vincent, T. L.; Weinans, H.; Carr, A. J. Osteoarthritis. *The lancet* **2015,** *386*, (9991), 376-87. DOI: 10.1016/S0140-6736(14)60802-3.
36. Huey, D. J.; Hu, J. C.; Athanasiou, K. A. Unlike bone, cartilage regeneration remains elusive. *Science* **2012,** *338*, (6109), 917-21. DOI: 10.1126/science.1222454.
37. Khan, M.; Osman, K.; Green, G.; Haddad, F. S. The epidemiology of failure in total knee arthroplasty: avoiding your next revision. *The Bone & Joint Journal* **2016,** *98-B*, (1 Suppl A), 105-12. DOI: 10.1302/0301-620X.98B1.36293.
38. Pap, T.; Korb-Pap, A. Cartilage damage in osteoarthritis and rheumatoid arthritis--two unequal siblings. *Nature Reviews Rheumatology* **2015,** *11*, (10), 606-15. DOI: 10.1038/nrrheum.2015.95.
39. Heinegard, D.; Saxne, T. The role of the cartilage matrix in osteoarthritis. *Nature Reviews Rheumatology* **2011,** *7*, (1), 50-6. DOI: 10.1038/nrrheum.2010.198.
40. Martel-Pelletier, J.; Barr, A. J.; Cicuttini, F. M.; Conaghan, P. G.; Cooper, C.; Goldring, M. B.; Goldring, S. R.; Jones, G.; Teichtahl, A. J.; Pelletier, J. P. Osteoarthritis. *Nature Reviews Disease Primers* **2016,** *2*, 16072. DOI: 10.1038/nrdp.2016.72.
41. Mobasheri, A.; Rayman, M. P.; Gualillo, O.; Sellam, J.; van der Kraan, P.; Fearon, U. The role of metabolism in the pathogenesis of osteoarthritis. *Nature Reviews Rheumatology* **2017,** *13*, (5), 302-311. DOI: 10.1038/nrrheum.2017.50.
42. Mak, J.; Jablonski, C. L.; Leonard, C. A.; Dunn, J. F.; Raharjo, E.; Matyas, J. R.; Biernaskie, J.; Krawetz, R. J. Intra-articular injection of synovial mesenchymal stem cells improves cartilage repair in a mouse injury model. *Scientific Reports* **2016,** *6*, 23076. DOI: 10.1038/srep23076.
43. Jeon, O. H.; David, N.; Campisi, J.; Elisseeff, J. H. Senescent cells and osteoarthritis: a painful connection. *The Journal of clinical investigation* **2018,** *128*, (4), 1229-1237.
44. Jeon, O. H.; Kim, C.; Laberge, R.-M.; Demaria, M.; Rathod, S.; Vasserot, A. P.; Chung, J. W.; Kim, D. H.; Poon, Y.; David, N. Local clearance of senescent cells attenuates the development of post-traumatic osteoarthritis and creates a pro-regenerative environment. *Nature Medicine* **2017,** *23*, (6), 775. DOI: 10.1038/nm.4324.
45. Fortier, L. A.; Barker, J. U.; Strauss, E. J.; McCarrel, T. M.; Cole, B. J. The role of growth factors in cartilage repair. *Clinical Orthopaedics and Related Research* **2011,** *469*, (10), 2706-15. DOI: 10.1007/s11999-011-1857-3.
46. van Gastel, N.; Stegen, S.; Eelen, G.; Schoors, S.; Carlier, A.; Daniels, V. W.; Baryawno, N.; Przybylski, D.; Depypere, M.; Stiers, P. J.; Lambrechts, D.; Van Looveren, R.; Torrekens, S.; Sharda, A.; Agostinis, P.; Lambrechts, D.; Maes, F.; Swinnen, J. V.; Geris, L.; Van Oosterwyck, H.; Thienpont, B.; Carmeliet, P.; Scadden,

D. T.; Carmeliet, G. Lipid availability determines fate of skeletal progenitor cells via SOX9. *Nature* **2020,** *579*, (7797), 111-117. DOI: 10.1038/s41586-020-2050-1.

47. Loeser, R. F.; Collins, J. A.; Diekman, B. O. Ageing and the pathogenesis of osteoarthritis. *Nature Reviews Rheumatology* **2016,** *12*, (7), 412-20. DOI: 10.1038/nrrheum.2016.65.
48. van der Kraan, P. M. The changing role of TGFbeta in healthy, ageing and osteoarthritic joints. *Nature Reviews Rheumatology* **2017,** *13*, (3), 155-163. DOI: 10.1038/nrrheum.2016.219.
49. Steadman, J. R.; Briggs, K. K.; Rodrigo, J. J.; Kocher, M. S.; Gill, T. J.; Rodkey, W. G. Outcomes of microfracture for traumatic chondral defects of the knee: average 11-year follow-up. *Arthroscopy* **2003,** *19*, (5), 477-84. DOI: 10.1053/jars.2003.50112.
50. Mithoefer, K.; McAdams, T.; Williams, R. J.; Kreuz, P. C.; Mandelbaum, B. R. Clinical efficacy of the microfracture technique for articular cartilage repair in the knee: an evidence-based systematic analysis. *American Journal of Sports Medicine* **2009,** *37*, (10), 2053-63. DOI: 10.1177/0363546508328414.
51. Gillogly, S. D.; Voight, M.; Blackburn, T. Treatment of articular cartilage defects of the knee with autologous chondrocyte implantation. *Journal of Orthopaedic & Sports Physical Therapy* **1998,** *28*, (4), 241-51. DOI: 10.2519/jospt.1998.28.4.241.
52. Frenkel, S. R.; Toolan, B.; Menche, D.; Pitman, M. I.; Pachence, J. M. Chondrocyte transplantation using a collagen bilayer matrix for cartilage repair. *The Journal of Bone and Joint Surgery* **1997,** *79*, (5), 831-6. DOI: 10.1302/0301-620x.79b5.7278.
53. Makris, E. A.; Gomoll, A. H.; Malizos, K. N.; Hu, J. C.; Athanasiou, K. A. Repair and tissue engineering techniques for articular cartilage. *Nature Reviews Rheumatology* **2015,** *11*, (1), 21-34. DOI: 10.1038/nrrheum.2014.157.
54. Benthien, J. P.; Behrens, P. The treatment of chondral and osteochondral defects of the knee with autologous matrix-induced chondrogenesis (AMIC): method description and recent developments. *Knee Surg Sports Traumatol Arthrosc* **2011,** *19*, (8), 1316-9. DOI: 10.1007/s00167-010-1356-1.
55. Sharma, B.; Fermanian, S.; Gibson, M.; Unterman, S.; Herzka, D. A.; Cascio, B.; Coburn, J.; Hui, A. Y.; Marcus, N.; Gold, G. E.; Elisseeff, J. H. Human cartilage repair with a photoreactive adhesive-hydrogel composite. *Science Translational Medicine* **2013,** *5*, (167), 167ra6. DOI: 10.1126/scitranslmed.3004838.
56. Volz, M.; Schaumburger, J.; Frick, H.; Grifka, J.; Anders, S. A randomized controlled trial demonstrating sustained benefit of Autologous Matrix-Induced Chondrogenesis over microfracture at five years. *International Orthopaedics* **2017,** *41*, (4), 797-804. DOI: 10.1007/s00264-016-3391-0.
57. Teixeira, S. P. B.; Domingues, R. M. A.; Shevchuk, M.; Gomes, M. E.; Peppas, N. A.; Reis, R. L. Biomaterials for Sequestration of Growth Factors and Modulation of Cell Behavior. *Advanced Functional Materials* **2020**. DOI: 10.1002/adfm.201909011.
58. Yoo, J. U.; Barthel, T. S.; Nishimura, K.; Solchaga, L.; Caplan, A. I.; Goldberg, V. M.; Johnstone, B. The chondrogenic potential of human bone-marrow-derived mesenchymal progenitor cells. *The Journal of Bone and Joint Surgery* **1998,** *80*, (12), 1745-57. DOI: 10.2106/00004623-199812000-00004.
59. Madry, H.; Rey-Rico, A.; Venkatesan, J. K.; Johnstone, B.; Cucchiarini, M. Transforming growth factor Beta-releasing scaffolds for cartilage tissue engineering. *Tissue Engineering Part B: Reviews* **2014,** *20*, (2), 106-25. DOI: 10.1089/ten.TEB.2013.0271.

60. Shah, R. N.; Shah, N. A.; Del Rosario Lim, M. M.; Hsieh, C.; Nuber, G.; Stupp, S. I. Supramolecular design of self-assembling nanofibers for cartilage regeneration. *Proceedings of the National Academy of Sciences of the United States of America* **2010,** *107*, (8), 3293-8. DOI: 10.1073/pnas.0906501107.
61. Hemphill, D. D.; McIlwraith, C. W.; Slayden, R. A.; Samulski, R. J.; Goodrich, L. R. Adeno-associated virus gene therapy vector scAAVIGF-I for transduction of equine articular chondrocytes and RNA-seq analysis. *Osteoarthritis and Cartilage* **2016,** *24*, (5), 902-11. DOI: 10.1016/j.joca.2015.12.001.
62. Zhang, Z.; Li, L.; Yang, W.; Cao, Y.; Shi, Y.; Li, X.; Zhang, Q. The effects of different doses of IGF-1 on cartilage and subchondral bone during the repair of full-thickness articular cartilage defects in rabbits. *Osteoarthritis and Cartilage* **2017,** *25*, (2), 309-320. DOI: 10.1016/j.joca.2016.09.010.
63. Davies, L. C.; Blain, E. J.; Gilbert, S. J.; Caterson, B.; Duance, V. C. The potential of IGF-1 and TGFbeta1 for promoting "adult" articular cartilage repair: an in vitro study. *Tissue Engineering Part A* **2008,** *14*, (7), 1251-61. DOI: 10.1089/tea.2007.0211.
64. Sakata, R.; Reddi, A. H. Platelet-Rich Plasma Modulates Actions on Articular Cartilage Lubrication and Regeneration. *Tissue Engineering Part B: Reviews* **2016,** *22*, (5), 408-419. DOI: 10.1089/ten.TEB.2015.0534.
65. Yang, K. C.; Chen, I. H.; Yang, Y. T.; Hsiao, J. K.; Wang, C. C. Effects of scaffold geometry on chondrogenic differentiation of adipose-derived stem cells. *Materials Science & Engineering, C: Materials for Biological Applications* **2020,** *110*, 110733. DOI: 10.1016/j.msec.2020.110733.
66. Lee, H. P.; Gu, L.; Mooney, D. J.; Levenston, M. E.; Chaudhuri, O. Mechanical confinement regulates cartilage matrix formation by chondrocytes. *Nature Materials* **2017,** *16*, (12), 1243-1251. DOI: 10.1038/nmat4993.
67. Correia, C. R.; Reis, R. L.; Mano, J. F. Multiphasic, Multistructured and Hierarchical Strategies for Cartilage Regeneration. *Advanced Experimental Medical Biology* **2015,** *881*, 143-60. DOI: 10.1007/978-3-319-22345-2_9.
68. McCullen, S. D.; Autefage, H.; Callanan, A.; Gentleman, E.; Stevens, M. M. Anisotropic fibrous scaffolds for articular cartilage regeneration. *Tissue Engineering Part A* **2012,** *18*, (19-20), 2073-83. DOI: 10.1089/ten.TEA.2011.0606.
69. Shanmugasundaram, S.; Chaudhry, H.; Arinzeh, T. L. Microscale versus nanoscale scaffold architecture for mesenchymal stem cell chondrogenesis. *Tissue Engineering Part A* **2011,** *17*, (5-6), 831-40. DOI: 10.1089/ten.TEA.2010.0409.
70. Chow, L. W.; Armgarth, A.; St-Pierre, J. P.; Bertazzo, S.; Gentilini, C.; Aurisicchio, C.; McCullen, S. D.; Steele, J. A.; Stevens, M. M. Peptide-directed spatial organization of biomolecules in dynamic gradient scaffolds. *Advanced Healthcare Materials* **2014,** *3*, (9), 1381-6. DOI: 10.1002/adhm.201400032.
71. Moutos, F. T.; Freed, L. E.; Guilak, F. A biomimetic three-dimensional woven composite scaffold for functional tissue engineering of cartilage. *Nature Materials* **2007,** *6*, (2), 162-7. DOI: 10.1038/nmat1822.
72. Liao, I. C.; Moutos, F. T.; Estes, B. T.; Zhao, X.; Guilak, F. Composite three-dimensional woven scaffolds with interpenetrating network hydrogels to create functional synthetic articular cartilage. *Advanced Functional Materials* **2013,** *23*, (47), 5833-5839. DOI: 10.1002/adfm.201300483.

73. Shi, W.; Sun, M.; Hu, X.; Ren, B.; Cheng, J.; Li, C.; Duan, X.; Fu, X.; Zhang, J.; Chen, H.; Ao, Y. Structurally and Functionally Optimized Silk-Fibroin-Gelatin Scaffold Using 3D Printing to Repair Cartilage Injury In Vitro and In Vivo. *Advanced Materials* **2017,** *29*, (29). DOI: 10.1002/adma.201701089.
74. Liu, X.; Jin, X.; Ma, P. X. Nanofibrous hollow microspheres self-assembled from star-shaped polymers as injectable cell carriers for knee repair. *Nature Materials* **2011,** *10*, (5), 398-406. DOI: 10.1038/nmat2999.
75. Li, F.; Truong, V. X.; Fisch, P.; Levinson, C.; Glattauer, V.; Zenobi-Wong, M.; Thissen, H.; Forsythe, J. S.; Frith, J. E. Cartilage tissue formation through assembly of microgels containing mesenchymal stem cells. *Acta Biomater* **2018,** *77*, 48-62. DOI: 10.1016/j.actbio.2018.07.015.
76. Wade, R. J.; Burdick, J. A. Engineering ECM signals into biomaterials. *Materials Today* **2012,** *15*, (10), 454-459. DOI: 10.1016/s1369-7021(12)70197-9.
77. Lehn, J.-M. Toward self-organization and complex matter. *Science* **2002,** *295*, (5564), 2400-2403. DOI: 10.1126/science.1071063
78. Lutz, J.-F.; Lehn, J.-M.; Meijer, E. W.; Matyjaszewski, K. From precision polymers to complex materials and systems. *Nature Reviews Materials* **2016,** *1*, (5). DOI: 10.1038/natrevmats.2016.24.
79. Chivers, P. R. A.; Smith, D. K. Shaping and structuring supramolecular gels. *Nature Reviews Materials* **2019,** *4*, (7), 463-478. DOI: 10.1038/s41578-019-0111-6.
80. Zhang, F.; Yan, H. DNA self-assembly scaled up. *Nature* **2017,** *552*, (7683), 34-35. DOI: 10.1038/d41586-017-07690-y.
81. Matson, J. B.; Zha, R. H.; Stupp, S. I. Peptide Self-Assembly for Crafting Functional Biological Materials. *Current Opinions in Solid State Materials Science* **2011,** *15*, (6), 225-235. DOI: 10.1016/j.cossms.2011.08.001.
82. Stephanopoulos, N.; Ortony, J. H.; Stupp, S. I. Self-Assembly for the Synthesis of Functional Biomaterials. *Acta Materialia* **2013,** *61*, (3), 912-930. DOI: 10.1016/j.actamat.2012.10.046.
83. Zhang, S.; Holmes, T. C.; DiPersio, C. M.; Hynes, R. O.; Su, X.; Rich, A. Self-complementary oligopeptide matrices support mammalian cell. *Biomaterials* **1995,** *16*, (18), 1385-1393. DOI: 10.1016/0142-9612(95)96874-y.
84. Zhang, S. Emerging biological materials through molecular self-assembly. *Biotechnology Advances* **2002,** *20*, (5-6), 321-339. DOI: 10.1016/s0734-9750(02)00026-5.
85. Mahler, A.; Reches, M.; Rechter, M.; Cohen, S.; Gazit, E. Rigid, Self-Assembled Hydrogel Composed of a Modified Aromatic Dipeptide. *Advanced Materials* **2006,** *18*, (11), 1365-1370. DOI: 10.1002/adma.200501765.
86. Koutsopoulos, S.; Unsworth, L. D.; Nagai, Y.; Zhang, S. Controlled release of functional proteins through designer self-assembling peptide nanofiber hydrogel scaffold. *Proceedings of the National Academy of Sciences of the United States of America* **2009,** *106*, (12), 4623-8. DOI: 10.1073/pnas.0807506106.
87. Moore, A. N.; Hartgerink, J. D. Self-Assembling Multidomain Peptide Nanofibers for Delivery of Bioactive Molecules and Tissue Regeneration. *Accounts of Chemical Resarch* **2017,** *50*, (4), 714-722. DOI: 10.1021/acs.accounts.6b00553.

88. Pugliese, R.; Gelain, F. Peptidic Biomaterials: From Self-Assembling to Regenerative Medicine. *Trends Biotechnology* **2017,** *35*, (2), 145-158. DOI: 10.1016/j.tibtech.2016.09.004.
89. Doberdoli, D.; Bommer, C.; Begzati, A.; Haliti, F.; Heinzel-Gutenbrunner, M.; Juric, H. Randomized Clinical Trial investigating Self-Assembling Peptide P11-4 for Treatment of Early Occlusal Caries. *Scientific Reports* **2020,** *10*, (1), 4195. DOI: 10.1038/s41598-020-60815-8.
90. Hartgerink, J. D.; Beniash, E.; Stupp, S. I. Self-assembly and mineralization of peptide-amphiphile nanofibers. *Science* **2001,** *294*, (5547), 1684-8. DOI: 10.1126/science.1063187.
91. Hartgerink, J. D.; Beniash, E.; Stupp, S. I. Peptide-amphiphile nanofibers: a versatile scaffold for the preparation of self-assembling materials. *Proceedings of the National Academy of Sciences of the United States of America* **2002,** *99*, (8), 5133-8. DOI: 10.1073/pnas.072699999.
92. Cui, H.; Pashuck, E. T.; Velichko, Y. S.; Weigand, S. J.; Cheetham, A. G.; Newcomb, C. J.; Stupp, S. I. Spontaneous and x-ray-triggered crystallization at long range in self-assembling filament networks. *Science* **2010,** *327*, (5965), 555-9. DOI: 10.1126/science.1182340.
93. Hendricks, M. P.; Sato, K.; Palmer, L. C.; Stupp, S. I. Supramolecular assembly of peptide amphiphiles. *Accounts of Chemical Research* **2017,** *50*, (10), 2440-2448. DOI: 10.1021/acs.accounts.7b00297.
94. Lee, O. S.; Cho, V.; Schatz, G. C. Modeling the self-assembly of peptide amphiphiles into fibers using coarse-grained molecular dynamics. *Nano Letters* **2012,** *12*, (9), 4907-13. DOI: 10.1021/nl302487m.
95. Ortony, J. H.; Newcomb, C. J.; Matson, J. B.; Palmer, L. C.; Doan, P. E.; Hoffman, B. M.; Stupp, S. I. Internal dynamics of a supramolecular nanofibre. *Nature Materials* **2014,** *13*, (8), 812-816. DOI: 10.1038/nmat3979.
96. da Silva, R. M.; van der Zwaag, D.; Albertazzi, L.; Lee, S. S.; Meijer, E. W.; Stupp, S. I. Super-resolution microscopy reveals structural diversity in molecular exchange among peptide amphiphile nanofibres. *Nature Communications* **2016,** *7*, (1), 11561. DOI: 10.1038/ncomms11561.
97. Tantakitti, F.; Boekhoven, J.; Wang, X.; Kazantsev, R. V.; Yu, T.; Li, J.; Zhuang, E.; Zandi, R.; Ortony, J. H.; Newcomb, C. J.; Palmer, L. C.; Shekhawat, G. S.; de la Cruz, M. O.; Schatz, G. C.; Stupp, S. I. Energy landscapes and functions of supramolecular systems. *Nature Materials* **2016,** *15*, (4), 469-76. DOI: 10.1038/nmat4538.
98. Greenfield, M. A.; Hoffman, J. R.; de la Cruz, M. O.; Stupp, S. I. Tunable mechanics of peptide nanofiber gels. *Langmuir* **2010,** *26*, (5), 3641-7. DOI: 10.1021/la9030969.
99. Zhang, S.; Greenfield, M. A.; Mata, A.; Palmer, L. C.; Bitton, R.; Mantei, J. R.; Aparicio, C.; de la Cruz, M. O.; Stupp, S. I. A self-assembly pathway to aligned monodomain gels. *Nature Materials* **2010,** *9*, (7), 594-601. DOI: 10.1038/nmat2778.
100. Godbe, J. M.; Freeman, R.; Burbulla, L. F.; Lewis, J. A.; Krainc, D.; Stupp, S. I. Gelator Length Precisely Tunes Supramolecular Hydrogel Stiffness and Neuronal Phenotype in 3D Culture. *ACS Biomaterials Science & Engineering* **2020,** *6*, (2), 1196-1207. DOI: 10.1021/acsbiomaterials.9b01585.

101. Freeman, R.; Boekhoven, J.; Dickerson, M. B.; Naik, R. R.; Stupp, S. I. Biopolymers and supramolecular polymers as biomaterials for biomedical applications. *MRS Bulletin* **2015,** *40*, (12), 1089-1101. DOI: 10.1557/mrs.2015.270.
102. Prince, E.; Kumacheva, E. Design and applications of man-made biomimetic fibrillar hydrogels. *Nature Reviews Materials* **2019,** *4*, (2), 99-115. DOI: 10.1038/s41578-018-0077-9.
103. Sato, K.; Hendricks, M. P.; Palmer, L. C.; Stupp, S. I. Peptide supramolecular materials for therapeutics. *Chemical Society Reviews* **2018,** *47*, (20), 7539-7551. DOI: 10.1039/c7cs00735c.
104. Storrie, H.; Guler, M. O.; Abu-Amara, S. N.; Volberg, T.; Rao, M.; Geiger, B.; Stupp, S. I. Supramolecular crafting of cell adhesion. *Biomaterials* **2007,** *28*, (31), 4608-18. DOI: 10.1016/j.biomaterials.2007.06.026.
105. Tysseling-Mattiace, V. M.; Sahni, V.; Niece, K. L.; Birch, D.; Czeisler, C.; Fehlings, M. G.; Stupp, S. I.; Kessler, J. A. Self-assembling nanofibers inhibit glial scar formation and promote axon elongation after spinal cord injury. *Journal of Neuroscience Research* **2008,** *28*, (14), 3814-23. DOI: 10.1523/JNEUROSCI.0143-08.2008.
106. Goldberger, J. E.; Berns, E. J.; Bitton, R.; Newcomb, C. J.; Stupp, S. I. Electrostatic control of bioactivity. *Angewandte Chemie International Edition* **2011,** *50*, (28), 6292-5. DOI: 10.1002/anie.201100202.
107. Lee, S. S.; Huang, B. J.; Kaltz, S. R.; Sur, S.; Newcomb, C. J.; Stock, S. R.; Shah, R. N.; Stupp, S. I. Bone regeneration with low dose BMP-2 amplified by biomimetic supramolecular nanofibers within collagen scaffolds. *Biomaterials* **2013,** *34*, (2), 452-9. DOI: 10.1016/j.biomaterials.2012.10.005.
108. Lee, S. S.; Hsu, E. L.; Mendoza, M.; Ghodasra, J.; Nickoli, M. S.; Ashtekar, A.; Polavarapu, M.; Babu, J.; Riaz, R. M.; Nicolas, J. D.; Nelson, D.; Hashmi, S. Z.; Kaltz, S. R.; Earhart, J. S.; Merk, B. R.; McKee, J. S.; Bairstow, S. F.; Shah, R. N.; Hsu, W. K.; Stupp, S. I. Gel scaffolds of BMP-2-binding peptide amphiphile nanofibers for spinal arthrodesis. *Advanced Healthcare Materials* **2015,** *4*, (1), 131-141. DOI: 10.1002/adhm.201400129.
109. Serrano, C. M.; Freeman, R.; Godbe, J.; Lewis, J. A.; Stupp, S. I. DNA-Peptide Amphiphile Nanofibers Enhance Aptamer Function. *ACS Applied Bio Materials* **2019,** *2*, (7), 2955-2963. DOI: 10.1021/acsabm.9b00310.
110. Rajangam, K.; Behanna, H. A.; Hui, M. J.; Han, X.; Hulvat, J. F.; Lomasney, J. W.; Stupp, S. I. Heparin binding nanostructures to promote growth of blood vessels. *Nano Letters* **2006,** *6*, (9), 2086-90. DOI: 10.1021/nl0613555.
111. Rubert Pérez, C. M.; Álvarez, Z.; Chen, F.; Aytun, T.; Stupp, S. I. Mimicking the Bioactivity of Fibroblast Growth Factor-2 Using Supramolecular Nanoribbons. *ACS Biomaterials Science & Engineering* **2017,** *3*, (9), 2166-2175. DOI: 10.1021/acsbiomaterials.7b00347.
112. Webber, M. J.; Tongers, J.; Newcomb, C. J.; Marquardt, K. T.; Bauersachs, J.; Losordo, D. W.; Stupp, S. I. Supramolecular nanostructures that mimic VEGF as a strategy for ischemic tissue repair. *Proceedings of the National Academy of Sciences of the United States of America* **2011,** *108*, (33), 13438-43. DOI: 10.1073/pnas.1016546108.
113. Edelbrock, A. N.; Alvarez, Z.; Simkin, D.; Fyrner, T.; Chin, S. M.; Sato, K.; Kiskinis, E.; Stupp, S. I. Supramolecular Nanostructure Activates TrkB Receptor Signaling of

Neuronal Cells by Mimicking Brain-Derived Neurotrophic Factor. *Nano Letters* **2018,** *18*, (10), 6237-6247. DOI: 10.1021/acs.nanolett.8b02317.

114. Lee, S. S.; Fyrner, T.; Chen, F.; Alvarez, Z.; Sleep, E.; Chun, D. S.; Weiner, J. A.; Cook, R. W.; Freshman, R. D.; Schallmo, M. S.; Katchko, K. M.; Schneider, A. D.; Smith, J. T.; Yun, C.; Singh, G.; Hashmi, S. Z.; McClendon, M. T.; Yu, Z.; Stock, S. R.; Hsu, W. K.; Hsu, E. L.; Stupp, S. I. Sulfated glycopeptide nanostructures for multipotent protein activation. *Nature Nanotechnology* **2017,** *12*, (8), 821-829. DOI: 10.1038/nnano.2017.109.
115. Sleep, E.; Cosgrove, B. D.; McClendon, M. T.; Preslar, A. T.; Chen, C. H.; Sangji, M. H.; Perez, C. M. R.; Haynes, R. D.; Meade, T. J.; Blau, H. M.; Stupp, S. I. Injectable biomimetic liquid crystalline scaffolds enhance muscle stem cell transplantation. *Proceedings of the National Academy of Sciences of the United States of America* **2017,** *114*, (38), E7919-E7928. DOI: 10.1073/pnas.1708142114.
116. So, M. M.; Mansukhani, N. A.; Peters, E. B.; Albaghdadi, M. S.; Wang, Z.; Perez, C. M. R.; Kibbe, M. R.; Stupp, S. I. Peptide Amphiphile Nanostructures for Targeting of Atherosclerotic Plaque and Drug Delivery. *Advanced Biosystems* **2018,** *2*, (3). DOI: 10.1002/adbi.201700123.
117. Yuan, C.; Ji, W.; Xing, R.; Li, J.; Gazit, E.; Yan, X. Hierarchically oriented organization in supramolecular peptide crystals. *Nature Reviews Chemistry* **2019,** *3*, (10), 567-588. DOI: 10.1038/s41570-019-0129-8.
118. Jin, H. E.; Jang, J.; Chung, J.; Lee, H. J.; Wang, E.; Lee, S. W.; Chung, W. J. Biomimetic Self-Templated Hierarchical Structures of Collagen-Like Peptide Amphiphiles. *Nano Letters* **2015,** *15*, (10), 7138-45. DOI: 10.1021/acs.nanolett.5b03313.
119. Lampel, A. Biology-Inspired Supramolecular Peptide Systems. *Chem* **2020**. DOI: 10.1016/j.chempr.2020.03.005.
120. Bera, S.; Mondal, S.; Xue, B.; Shimon, L. J. W.; Cao, Y.; Gazit, E. Rigid helical-like assemblies from a self-aggregating tripeptide. *Nature Materials* **2019,** *18*, (5), 503-509. DOI: 10.1038/s41563-019-0343-2.
121. Roberts, S.; Harmon, T. S.; Schaal, J. L.; Miao, V.; Li, K. J.; Hunt, A.; Wen, Y.; Oas, T. G.; Collier, J. H.; Pappu, R. V.; Chilkoti, A. Injectable tissue integrating networks from recombinant polypeptides with tunable order. *Nature Materials* **2018,** *17*, (12), 1154-1163. DOI: 10.1038/s41563-018-0182-6.
122. Lampel, A.; McPhee, S. A.; Park, H. A.; Scott, G. G.; Humagain, S.; Hekstra, D. R.; Yoo, B.; Frederix, P.; Li, T. D.; Abzalimov, R. R.; Greenbaum, S. G.; Tuttle, T.; Hu, C.; Bettinger, C. J.; Ulijn, R. V. Polymeric peptide pigments with sequence-encoded properties. *Science* **2017,** *356*, (6342), 1064-1068. DOI: 10.1126/science.aal5005.
123. Zhou, M.; Smith, A. M.; Das, A. K.; Hodson, N. W.; Collins, R. F.; Ulijn, R. V.; Gough, J. E. Self-assembled peptide-based hydrogels as scaffolds for anchorage-dependent cells. *Biomaterials* **2009,** *30*, (13), 2523-30. DOI: 10.1016/j.biomaterials.2009.01.010.
124. Knowles, T. P.; Oppenheim, T. W.; Buell, A. K.; Chirgadze, D. Y.; Welland, M. E. Nanostructured films from hierarchical self-assembly of amyloidogenic proteins. *Nature Nanotechnology* **2010,** *5*, (3), 204-7. DOI: 10.1038/nnano.2010.26.
125. Capito, R. M.; Azevedo, H. S.; Velichko, Y. S.; Mata, A.; Stupp, S. I. Self-assembly of large and small molecules into hierarchically ordered sacs and membranes. *Science* **2008,** *319*, (5871), 1812-6. DOI: 10.1126/science.1154586.

126. Chin, S. M.; Synatschke, C. V.; Liu, S.; Nap, R. J.; Sather, N. A.; Wang, Q.; Alvarez, Z.; Edelbrock, A. N.; Fyrner, T.; Palmer, L. C.; Szleifer, I.; Olvera de la Cruz, M.; Stupp, S. I. Covalent-supramolecular hybrid polymers as muscle-inspired anisotropic actuators. *Nature Communications* **2018,** *9*, (1), 2395. DOI: 10.1038/s41467-018-04800-w.
127. Chen, Y.; Gan, H. X.; Tong, Y. W. pH-Controlled Hierarchical Self-Assembly of Peptide Amphiphile. *Macromolecules* **2015,** *48*, (8), 2647-2653. DOI: 10.1021/ma502572w.
128. Freeman, R.; Han, M.; Alvarez, Z.; Lewis, J. A.; Wester, J. R.; Stephanopoulos, N.; McClendon, M. T.; Lynsky, C.; Godbe, J. M.; Sangji, H.; Luijten, E.; Stupp, S. I. Reversible self-assembly of superstructured networks. *Science* **2018,** *362*, (6416), 808-813. DOI: 10.1126/science.aat6141.
129. Wong, G. C.; Tang, J. X.; Lin, A.; Li, Y.; Janmey, P. A.; Safinya, C. R. Hierarchical self-assembly of F-actin and cationic lipid complexes: stacked three-layer tubule networks. *Science* **2000,** *288*, (5473), 2035-9. DOI: 10.1126/science.288.5473.2035.
130. Dominguez, R.; Holmes, K. C. Actin structure and function. *Annual Review of Biophysics* **2011**, (1), 169-86. DOI: 10.1146/annurev-biophys-042910-155359.
131. Prockop, D. J.; Fertala, A. The collagen fibril: the almost crystalline structure. *Journal of Structural Biology* **1998,** *122*, (1-2), 111-8. DOI: 10.1006/jsbi.1998.3976.
132. Takahashi, Y.; Gehoh, M.; Yuzuriha, K. Structure refinement and diffuse streak scattering of silk (Bombyx mori). *International Journal of Biological Macromolecules* **1999,** *24*, (2-3), 127-38. DOI: 10.1016/s0141-8130(98)00080-4.
133. Li, G.; Zhou, P.; Shao, Z.; Xie, X.; Chen, X.; Wang, H.; Chunyu, L.; Yu, T. The natural silk spinning process. A nucleation-dependent aggregation mechanism? *European Journal of Biochemistry* **2001,** *268*, (24), 6600-6. DOI: 10.1046/j.0014-2956.2001.02614.x.
134. LaFerla, F. M.; Green, K. N.; Oddo, S. Intracellular amyloid-beta in Alzheimer's disease. *Nature Reviews Neuroscience* **2007,** *8*, (7), 499-509. DOI: 10.1038/nrn2168.
135. Jakob-Roetne, R.; Jacobsen, H. Alzheimer's disease: from pathology to therapeutic approaches. *Angewandte Chemie International Edition* **2009,** *48*, (17), 3030-59. DOI: 10.1002/anie.200802808.
136. Conway, K. A.; Harper, J. D.; Lansbury, P. T. Accelerated in vitro fibril formation by a mutant alpha-synuclein linked to early-onset Parkinson disease. *Nature Medicine* **1998,** *4*, (11), 1318-20. DOI: 10.1038/3311.
137. Narhi, L.; Wood, S. J.; Steavenson, S.; Jiang, Y.; Wu, G. M.; Anafi, D.; Kaufman, S. A.; Martin, F.; Sitney, K.; Denis, P.; Louis, J. C.; Wypych, J.; Biere, A. L.; Citron, M. Both familial Parkinson's disease mutations accelerate alpha-synuclein aggregation. *Journal of Biological Chemistry* **1999,** *274*, (14), 9843-6. DOI: 10.1074/jbc.274.14.9843.
138. DiDonato, M.; Craig, L.; Huff, M. E.; Thayer, M. M.; Cardoso, R. M.; Kassmann, C. J.; Lo, T. P.; Bruns, C. K.; Powers, E. T.; Kelly, J. W.; Getzoff, E. D.; Tainer, J. A. ALS mutants of human superoxide dismutase form fibrous aggregates via framework destabilization. *Journal of Molecular Biology* **2003,** *332*, (3), 601-15. DOI: 10.1016/s0022-2836(03)00889-1.
139. Wang, Q.; Johnson, J. L.; Agar, N. Y.; Agar, J. N. Protein aggregation and protein instability govern familial amyotrophic lateral sclerosis patient survival. *PLoS Biol* **2008,** *6*, (7), e170. DOI: 10.1371/journal.pbio.0060170.

140. Eisele, Y. S.; Monteiro, C.; Fearns, C.; Encalada, S. E.; Wiseman, R. L.; Powers, E. T.; Kelly, J. W. Targeting protein aggregation for the treatment of degenerative diseases. *Nature Reviews Drug Discovery* **2015,** *14*, (11), 759-80. DOI: 10.1038/nrd4593.
141. Colon, W.; Kelly, J. W. Partial Denaturation of Transthyretin Is Sufficient for Amyloid Fibril Formation in Vitro. *Biochemistry* **1992,** *31*, (36), 8654-8660. DOI: 10.1021/bi00151a036,.
142. Frederix, P. W.; Scott, G. G.; Abul-Haija, Y. M.; Kalafatovic, D.; Pappas, C. G.; Javid, N.; Hunt, N. T.; Ulijn, R. V.; Tuttle, T. Exploring the sequence space for (tri-)peptide self-assembly to design and discover new hydrogels. *Nature Chemistry* **2015,** *7*, (1), 30-7. DOI: 10.1038/nchem.2122.
143. Yan, X.; Li, J.; Mohwald, H. Self-assembly of hexagonal peptide microtubes and their optical waveguiding. *Advanced Materials* **2011,** *23*, (25), 2796-801. DOI: 10.1002/adma.201100353.
144. Chan, K. H.; Xue, B.; Robinson, R. C.; Hauser, C. A. E. Systematic Moiety Variations of Ultrashort Peptides Produce Profound Effects on Self-Assembly, Nanostructure Formation, Hydrogelation, and Phase Transition. *Scientific Reports* **2017,** *7*, (1), 12897. DOI: 10.1038/s41598-017-12694-9.
145. Chen, J.; Zhu, E.; Liu, J.; Zhang, S.; Lin, Z.; Duan, X.; Heinz, H.; Huang, Y.; De Yoreo, J. J. Building two-dimensional materials one row at a time: Avoiding the nucleation barrier. *Science* **2018,** *362*, (6419), 1135-1139. DOI: 10.1126/science.aau4146.
146. Adler-Abramovich, L.; Marco, P.; Arnon, Z. A.; Creasey, R. C.; Michaels, T. C.; Levin, A.; Scurr, D. J.; Roberts, C. J.; Knowles, T. P.; Tendler, S. J.; Gazit, E. Controlling the Physical Dimensions of Peptide Nanotubes by Supramolecular Polymer Coassembly. *ACS Nano* **2016,** *10*, (8), 7436-42. DOI: 10.1021/acsnano.6b01587.
147. Hartgerink, J. D.; Beniash, E.; Stupp, S. I. Self-Assembly and Mineralization of Peptide-Amphiphile Nanofibers. *Science* **2001,** *294*, (5547), 1684-1688.
148. Cui, H.; Pashuck, E. T.; Velichko, Y. S.; Weigand, S. J.; Cheetham, A. G.; Newcomb, C.; Stupp, S. I. Spontaneous and X-ray–Triggered Crystallization at Long Range in Self-Assembling Filament Networks. *Science* **2010,** *327*, (5965), 555-559.
149. Aida, T.; Meijer, E. W.; Stupp, S. I. Functional supramolecular polymers. *Science* **2012,** *335*, (6070), 813-7. DOI: 10.1126/science.1205962.
150. Silva, G. A.; Czeisler, C.; Niece, K. L.; Beniash, E.; Harrington, D. A.; Kessler, J. A.; Stupp, S. I. Selective differentiation of neural progenitor cells by high-epitope density nanofibers. *Science* **2004,** *303*, (5662), 1352-5. DOI: 10.1126/science.1093783.
151. Niece, K. L.; Hartgerink, J. D.; Donners, J. J.; Stupp, S. I. Self-assembly combining two bioactive peptide-amphiphile molecules into nanofibers by electrostatic attraction. *Journal of the American Chemical Society* **2003,** *125*, (24), 7146-7. DOI: 10.1021/ja028215r.
152. Hamley, I. W.; Dehsorkhi, A.; Castelletto, V. Coassembly in binary mixtures of peptide amphiphiles containing oppositely charged residues. *Langmuir* **2013,** *29*, (16), 5050-9. DOI: 10.1021/la400163q.
153. Leung, C. Y.; Palmer, L. C.; Kewalramani, S.; Qiao, B.; Stupp, S. I.; Olvera de la Cruz, M.; Bedzyk, M. J. Crystalline polymorphism induced by charge regulation in ionic membranes. *Proceedings of the National Academy of Sciences of the United States of America* **2013,** *110*, (41), 16309-14. DOI: 10.1073/pnas.1316150110.

154. Wang, D.; Hou, X.; Zhang, X.; Zhao, Y.; Ma, B.; Sun, Y.; Wang, J. Light and pH Controlled Hierarchical Co-assembly of Peptide Amphiphiles. *Langmuir* **2019**. DOI: 10.1021/acs.langmuir.9b01459.
155. Gao, C.; Li, H.; Li, Y.; Kewalramani, S.; Palmer, L. C.; Dravid, V. P.; Stupp, S. I.; Olvera de la Cruz, M.; Bedzyk, M. J. Electrostatic Control of Polymorphism in Charged Amphiphile Assemblies. *J Phys Chem B* **2017,** *121*, (7), 1623-1628. DOI: 10.1021/acs.jpcb.6b11602.
156. Albertazzi, L.; van der Zwaag, D.; Leenders, C. M.; Fitzner, R.; van der Hofstad, R. W.; Meijer, E. W. Probing exchange pathways in one-dimensional aggregates with super-resolution microscopy. *Science* **2014,** *344*, (6183), 491-5. DOI: 10.1126/science.1250945.
157. Ismail, A. A.; Mantsch, H. H. Salt bridge induced changes in the secondary structure of ionic polypeptides. *Biopolymers* **1992,** *32*, (9), 1181-6. DOI: 10.1002/bip.360320907.
158. Huerta-Viga, A.; Amirjalayer, S.; Domingos, S. R.; Meuzelaar, H.; Rupenyan, A.; Woutersen, S. The structure of salt bridges between Arg(+) and Glu(-) in peptides investigated with 2D-IR spectroscopy: Evidence for two distinct hydrogen-bond geometries. *Journal of Chemical Physics* **2015,** *142*, (21), 212444. DOI: 10.1063/1.4921064.
159. Kline, S. R. Reduction and analysis of SANS and USANS data using IGOR Pro. *Journal of Applied Crystallography* **2006,** *39*, (6), 895-900. DOI: 10.1107/s0021889806035059.
160. Monopoli, M. P.; Aberg, C.; Salvati, A.; Dawson, K. A. Biomolecular coronas provide the biological identity of nanosized materials. *Nature Nanotechnology* **2012,** *7*, (12), 779-86. DOI: 10.1038/nnano.2012.207.
161. Hadjidemetriou, M.; Kostarelos, K. Nanomedicine: Evolution of the nanoparticle corona. *Nature Nanotechnology* **2017,** *12*, (4), 288-290. DOI: 10.1038/nnano.2017.61.
162. Frohlich, E. The role of surface charge in cellular uptake and cytotoxicity of medical nanoparticles. *International Journal of Nanomedice* **2012,** *7*, 5577-91. DOI: 10.2147/IJN.S36111.
163. Elci, S. G.; Jiang, Y.; Yan, B.; Kim, S. T.; Saha, K.; Moyano, D. F.; Yesilbag Tonga, G.; Jackson, L. C.; Rotello, V. M.; Vachet, R. W. Surface Charge Controls the Suborgan Biodistributions of Gold Nanoparticles. *ACS Nano* **2016,** *10*, (5), 5536-42. DOI: 10.1021/acsnano.6b02086.
164. Wang, H.-X.; Zuo, Z.-Q.; Du, J.-Z.; Wang, Y.-C.; Sun, R.; Cao, Z.-T.; Ye, X.-D.; Wang, J.-L.; Leong, K. W.; Wang, J. Surface charge critically affects tumor penetration and therapeutic efficacy of cancer nanomedicines. *Nano Today* **2016,** *11*, (2), 133-144. DOI: 10.1016/j.nantod.2016.04.008.
165. Wang, Y.; Yao, S.; Meng, Q.; Yu, X.; Wang, X.; Cui, F. Gene expression profiling and mechanism study of neural stem cells response to surface chemistry. *Regenerative Biomaterials* **2014,** *1*, (1), 37-47. DOI: 10.1093/rb/rbu012.
166. Clemons, T. D.; Challenor, M.; Fitzgerald, M.; Dunlop, S. A.; Smith, N. M.; Iyer, K. S. Manipulating Cellular Interactions of Poly(glycidyl methacrylate) Nanoparticles Using Mixed Polymer Brushes. *ACS Macro Letters* **2016,** *5*, (10), 1132-1136. DOI: 10.1021/acsmacrolett.6b00613.
167. Yu, T.-T.; Cui, F.-Z.; Meng, Q.-Y.; Wang, J.; Wu, D.-C.; Zhang, J.; Kou, X.-X.; Yang, R.-L.; Liu, Y.; Zhang, Y. S.; Yang, F.; Zhou, Y.-H. Influence of Surface Chemistry on Adhesion and Osteo/Odontogenic Differentiation of Dental Pulp Stem Cells. *ACS*

*Biomaterials Science & Engineering* **2017,** *3*, (6), 1119-1128. DOI: 10.1021/acsbiomaterials.7b00274.

168. Karakoti, A. S.; Das, S.; Thevuthasan, S.; Seal, S. PEGylated inorganic nanoparticles. *Angewandte Chemie International Edition* **2011,** *50*, (9), 1980-94. DOI: 10.1002/anie.201002969.
169. Suk, J. S.; Xu, Q.; Kim, N.; Hanes, J.; Ensign, L. M. PEGylation as a strategy for improving nanoparticle-based drug and gene delivery. *Advanced Drug Delivery Reviews* **2016,** *99*, (Pt A), 28-51. DOI: 10.1016/j.addr.2015.09.012.
170. Webber, M. J.; Appel, E. A.; Vinciguerra, B.; Cortinas, A. B.; Thapa, L. S.; Jhunjhunwala, S.; Isaacs, L.; Langer, R.; Anderson, D. G. Supramolecular PEGylation of biopharmaceuticals. *Proceedings of the National Academy of Sciences of the United States of America* **2016,** *113*, (50), 14189-14194. DOI: 10.1073/pnas.1616639113.
171. Collier, J. H.; Messersmith, P. B. Self-Assembling Polymer–Peptide Conjugates: Nanostructural Tailoring. *Advanced Materials* **2004,** *16*, (11), 907-910. DOI: 10.1002/adma.200306379.
172. Hamley, I. W.; Ansari, I. A.; Castelletto, V.; Nuhn, H.; Rosler, A.; Klok, H. A. Solution self-assembly of hybrid block copolymers containing poly(ethylene glycol) and amphiphilic beta-strand peptide sequences. *Biomacromolecules* **2005,** *6*, (3), 1310-5. DOI: 10.1021/bm049286g.
173. Perinelli, D. R.; Campana, M.; Singh, I.; Vllasaliu, D.; Doutch, J.; Palmieri, G. F.; Casettari, L. PEGylation affects the self-assembling behaviour of amphiphilic octapeptides. *International Journal of Pharmaceutics* **2019,** *571*, 118752. DOI: 10.1016/j.ijpharm.2019.118752.
174. Cui, H.; Muraoka, T.; Cheetham, A. G.; Stupp, S. I. Self-assembly of giant peptide nanobelts. *Nano letters* **2009,** *9*, (3), 945-51. DOI: 10.1021/nl802813f.
175. Newcomb, C. J.; Sur, S.; Ortony, J. H.; Lee, O. S.; Matson, J. B.; Boekhoven, J.; Yu, J. M.; Schatz, G. C.; Stupp, S. I. Cell death versus cell survival instructed by supramolecular cohesion of nanostructures. *Nature Communications* **2014,** *5*, 3321. DOI: 10.1038/ncomms4321.
176. Ortony, J. H.; Newcomb, C. J.; Matson, J. B.; Palmer, L. C.; Doan, P. E.; Hoffman, B. M.; Stupp, S. I. Internal dynamics of a supramolecular nanofibre. *Nature materials* **2014,** *13*, (8), 812-6. DOI: 10.1038/nmat3979.
177. Gao, C.; Li, H.; Li, Y.; Kewalramani, S.; Palmer, L. C.; Dravid, V. P.; Stupp, S. I.; Olvera de la Cruz, M.; Bedzyk, M. J. Electrostatic Control of Polymorphism in Charged Amphiphile Assemblies. *Journal of Physical Chemistry B* **2017,** *121*, (7), 1623-1628. DOI: 10.1021/acs.jpcb.6b11602.
178. Iscen, A.; Schatz, G. C. Hofmeister Effects on Peptide Amphiphile Nanofiber Self-Assembly. *Journal of Physical Chemistry B* **2019,** *123*, (32), 7006-7013. DOI: 10.1021/acs.jpcb.9b05532.
179. Moyer, T. J.; Finbloom, J. A.; Chen, F.; Toft, D. J.; Cryns, V. L.; Stupp, S. I. pH and amphiphilic structure direct supramolecular behavior in biofunctional assemblies. *Journal of the American Chemical Society* **2014,** *136*, (42), 14746-52. DOI: 10.1021/ja5042429.
180. Behanna, H. A.; Donners, J. J.; Gordon, A. C.; Stupp, S. I. Coassembly of amphiphiles with opposite peptide polarities into nanofibers. *Journal of the American Chemical Society* **2005,** *127*, (4), 1193-200. DOI: 10.1021/ja044863u.

181. Toksoz, S.; Mammadov, R.; Tekinay, A. B.; Guler, M. O. Electrostatic effects on nanofiber formation of self-assembling peptide amphiphiles. *Journal of Colloid Interface Science* **2011,** *356*, (1), 131-7. DOI: 10.1016/j.jcis.2010.12.076.
182. Chen, C.; Wu, D.; Fu, W.; Li, Z. Peptide hydrogels assembled from nonionic alkyl-polypeptide amphiphiles prepared by ring-opening polymerization. *Biomacromolecules* **2013,** *14*, (8), 2494-8. DOI: 10.1021/bm4008259.
183. Wan, Y.; Wang, Z.; Sun, J.; Li, Z. Extremely Stable Supramolecular Hydrogels Assembled from Nonionic Peptide Amphiphiles. *Langmuir* **2016,** *32*, (30), 7512-8. DOI: 10.1021/acs.langmuir.6b00727.
184. Sur, S.; Tantakitti, F.; Matson, J. B.; Stupp, S. I. Epitope topography controls bioactivity in supramolecular nanofibers. *Biomaterials Science* **2015,** *3*, (3), 520-532. DOI: 10.1039/c4bm00326h.
185. Toft, D. J.; Moyer, T. J.; Standley, S. M.; Ruff, Y.; Ugolkov, A.; Stupp, S. I.; Cryns, V. L. Coassembled cytotoxic and pegylated peptide amphiphiles form filamentous nanostructures with potent antitumor activity in models of breast cancer. *ACS Nano* **2012,** *6*, (9), 7956-65. DOI: 10.1021/nn302503s.
186. Kenworthy, A. K.; Hristova, K.; Needham, D.; McIntosh, T. J. Range and magnitude of the steric pressure between bilayers containing phospholipids with covalently attached poly (ethylene glycol). *Biophysical Journal* **1995,** *68*, (5), 1921-1936. DOI: 10.1016/S0006-3495(95)80369-3.
187. Stuart, M. C. A.; van de Pas, J. C.; Engberts, J. B. F. N. The use of Nile Red to monitor the aggregation behavior in ternary surfactant-water-organic solvent systems. *Journal of Physical Organic Chemistry* **2005,** *18*, (9), 929-934. DOI: 10.1002/poc.919.
188. Grimsley, G. R.; Scholtz, J. M.; Pace, C. N. A summary of the measured pK values of the ionizable groups in folded proteins. *Protein Science* **2009,** *18*, (1), 247-51. DOI: 10.1002/pro.19.
189. Zhang, H.; Yu, M.; Song, A.; Song, Y.; Xin, X.; Shen, J.; Yuan, S. Modulating hierarchical self-assembly behavior of a peptide amphiphile/nonionic surfactant mixed system. *RSC Advances* **2016,** *6*, (11), 9186-9193. DOI: 10.1039/c5ra25437j.
190. Mukherjee, S.; Chowdhury, P.; Gai, F. Infrared study of the effect of hydration on the amide I band and aggregation properties of helical peptides. *Journal of Physical Chemistry B* **2007,** *111*, (17), 4596-602. DOI: 10.1021/jp0689060.
191. Tew, L. S.; Ching, J. Y.; Ngalim, S. H.; Khung, Y. L. Driving mesenchymal stem cell differentiation from self-assembled monolayers. *RSC Advances* **2018,** *8*, (12), 6551-6564. DOI: 10.1039/c7ra12234a.
192. Li, J. J.; Kawazoe, N.; Chen, G. Gold nanoparticles with different charge and moiety induce differential cell response on mesenchymal stem cell osteogenesis. *Biomaterials* **2015,** *54*, 226-36. DOI: 10.1016/j.biomaterials.2015.03.001.
193. Shrestha, S.; Mao, Z.; Fedutik, Y.; Gao, C. Influence of titanium dioxide nanorods with different surface chemistry on the differentiation of rat bone marrow mesenchymal stem cells. *Journal of Materials Chemistry B* **2016,** *4*, (43), 6955-6966. DOI: 10.1039/c6tb02149b.
194. Wittenauer, R.; Smith, L.; Aden, K. Background paper 6.12 osteoarthritis. *World Health Organisation* **2013**.

195. Malda, J.; Groll, J.; van Weeren, P. R. Rethinking articular cartilage regeneration based on a 250-year-old statement. *Nature Reviews Rheumatology* **2019,** *15*, (10), 571-572. DOI: 10.1038/s41584-019-0278-7.
196. Wang, W.; Rigueur, D.; Lyons, K. M. TGFbeta signaling in cartilage development and maintenance. *Birth Defects Research Part C: Embryo Today* **2014,** *102*, (1), 37-51. DOI: 10.1002/bdrc.21058.
197. Wynn, T. A.; Ramalingam, T. R. Mechanisms of fibrosis: therapeutic translation for fibrotic disease. *Nature Medicine* **2012,** *18*, (7), 1028-40. DOI: 10.1038/nm.2807.
198. Kelly, A.; Houston, S. A.; Sherwood, E.; Casulli, J.; Travis, M. A. Regulation of Innate and Adaptive Immunity by TGFbeta. *Advanced Immunology* **2017,** *134*, 137-233. DOI: 10.1016/bs.ai.2017.01.001.
199. Massague, J. TGFbeta in Cancer. *Cell* **2008,** *134*, (2), 215-30. DOI: 10.1016/j.cell.2008.07.001.
200. Holland, T. A.; Mikos, A. G. Advances in drug delivery for articular cartilage. *Journal of Controlled Release* **2003,** *86*, (1), 1-14. DOI: 10.1016/s0168-3659(02)00373-5.
201. van den Berg, W. B.; van Osch, G. J.; van der Kraan, P. M.; van Beuningen, H. M. Cartilage destruction and osteophytes in instability-induced murine osteoarthritis: role of TGFβ in osteophyte formation? *Agents and Actions* **1993,** *40*, (3-4), 215-219. DOI: 10.1007/BF01984064.
202. Hulth, A.; Johnell, O.; Miyazono, K.; Lindberg, L.; Heinegard, D.; Heldin, C. H. Effect of transforming growth factor-beta and platelet-derived growth factor-BB on articular cartilage in rats. *Journal of Orthopaedic Research* **1996,** *14*, (4), 547-53. DOI: 10.1002/jor.1100140408.
203. Wakefield, L. M.; Winokur, T.; Hollands, R.; Christopherson, K.; Levinson, A.; Sporn, M. Recombinant latent transforming growth factor beta 1 has a longer plasma half-life in rats than active transforming growth factor beta 1, and a different tissue distribution. *The Journal of Clinical Investigation* **1990,** *86*, (6), 1976-1984. DOI: 10.1172/JCI114932.
204. Patel, J. M.; Saleh, K. S.; Burdick, J. A.; Mauck, R. L. Bioactive factors for cartilage repair and regeneration: Improving delivery, retention, and activity. *Acta Biomaterialia* **2019,** *93*, 222-238. DOI: 10.1016/j.actbio.2019.01.061.
205. Chou, C. H.; Cheng, W. T.; Lin, C. C.; Chang, C. H.; Tsai, C. C.; Lin, F. H. TGF-beta1 immobilized tri-co-polymer for articular cartilage tissue engineering. *Journal of Biomedical Materials Research Part B: Applied Biomaterials* **2006,** *77*, (2), 338-48. DOI: 10.1002/jbm.b.30432.
206. Sridhar, B. V.; Doyle, N. R.; Randolph, M. A.; Anseth, K. S. Covalently tethered TGF-beta1 with encapsulated chondrocytes in a PEG hydrogel system enhances extracellular matrix production. *Journal of Biomedical Materials Research, Part A* **2014,** *102*, (12), 4464-72. DOI: 10.1002/jbm.a.35115.
207. Kim, J.; Lin, B.; Kim, S.; Choi, B.; Evseenko, D.; Lee, M. TGF-beta1 conjugated chitosan collagen hydrogels induce chondrogenic differentiation of human synovium-derived stem cells. *Journal of Biological Engineering* **2015,** *9*, (1), 1. DOI: 10.1186/1754-1611-9-1.
208. Hunziker, E. B. Growth-factor-induced healing of partial-thickness defects in adult articular cartilage. *Osteoarthritis and Cartilage* **2001,** *9*, (1), 22-32. DOI: 10.1053/joca.2000.0346.

209. Re'em, T.; Kaminer-Israeli, Y.; Ruvinov, E.; Cohen, S. Chondrogenesis of hMSC in affinity-bound TGF-beta scaffolds. *Biomaterials* **2012,** *33*, (3), 751-61. DOI: 10.1016/j.biomaterials.2011.10.007.
210. Chen, J.; Li, Y.; Wang, B.; Yang, J.; Heng, B. C.; Yang, Z.; Ge, Z.; Lin, J. TGF-β1 affinity peptides incorporated within a chitosan sponge scaffold can significantly enhance cartilage regeneration. *Journal of Materials Chemistry B* **2018,** *6*, (4), 675-687. DOI: 10.1039/c7tb02132a.
211. Wu, G.; Xiao, M.; Xiao, J.; Guo, L.; Ke, Y.; Li, H.; Fang, L.; Deng, C.; Liao, H. Elastic polyurethane bearing pendant TGF-beta1 affinity peptide for potential tissue engineering applications. *Materials Science & Engineering, C: Materials for Biological Applications* **2018,** *83*, 67-77. DOI: 10.1016/j.msec.2017.10.006.
212. Jiang, H.; Guler, M. O.; Stupp, S. I. The internal structure of self-assembled peptide amphiphiles nanofibers. *Soft Matter* **2007,** *3*, (4). DOI: 10.1039/b614426h.
213. Beniash, E.; Hartgerink, J. D.; Storrie, H.; Stendahl, J. C.; Stupp, S. I. Self-assembling peptide amphiphile nanofiber matrices for cell entrapment. *Acta Biomaterialia* **2005,** *1*, (4), 387-97. DOI: 10.1016/j.actbio.2005.04.002.
214. Webber, M. J.; Tongers, J.; Renault, M. A.; Roncalli, J. G.; Losordo, D. W.; Stupp, S. I. Development of bioactive peptide amphiphiles for therapeutic cell delivery. *Acta Biomaterialia* **2010,** *6*, (1), 3-11. DOI: 10.1016/j.actbio.2009.07.031.
215. Geiger, T.; Clarke, S. Deamidation, isomerization, and racemization at asparaginyl and aspartyl residues in peptides. Succinimide-linked reactions that contribute to protein degradation. *Journal of Biological Chemistry* **1987,** *262*, (2), 785-794.
216. Yang, H.; Zubarev, R. A. Mass spectrometric analysis of asparagine deamidation and aspartate isomerization in polypeptides. *Electrophoresis* **2010,** *31*, (11), 1764-72. DOI: 10.1002/elps.201000027.
217. Pasqualini, R.; Koivunen, E.; Kain, R.; Lahdenranta, J.; Sakamoto, M.; Stryhn, A.; Ashmun, R. A.; Shapiro, L. H.; Arap, W.; Ruoslahti, E. Aminopeptidase N is a receptor for tumor-homing peptides and a target for inhibiting angiogenesis. *Cancer Research* **2000,** *60*, (3), 722-727.
218. Bahnson, E. S.; Kassam, H. A.; Moyer, T. J.; Jiang, W.; Morgan, C. E.; Vercammen, J. M.; Jiang, Q.; Flynn, M. E.; Stupp, S. I.; Kibbe, M. R. Targeted nitric oxide delivery by supramolecular nanofibers for the prevention of restenosis after arterial injury. *Antioxidants Redox Signaling* **2016,** *24*, (8), 401-418. DOI: 10.1089/ars.2015.6363.
219. Concepcion, J.; Witte, K.; Wartchow, C.; Choo, S.; Yao, D.; Persson, H.; Wei, J.; Li, P.; Heidecker, B.; Ma, W. Label-free detection of biomolecular interactions using BioLayer interferometry for kinetic characterization. *Combinatorial Chemistry & High Throughput Screening* **2009,** *12*, (8), 791-800. DOI: 10.2174/138620709789104915.
220. Kurcinski, M.; Jamroz, M.; Blaszczyk, M.; Kolinski, A.; Kmiecik, S. CABS-dock web server for the flexible docking of peptides to proteins without prior knowledge of the binding site. *Nucleic Acids Research* **2015,** *43*, (W1), W419-W424. DOI: 10.1093/nar/gkv456.
221. Rifkin, D. B. Latent transforming growth factor-beta (TGF-beta) binding proteins: orchestrators of TGF-beta availability. *Journal of Biological Chemistry* **2005,** *280*, (9), 7409-12. DOI: 10.1074/jbc.R400029200.

222. Shi, M.; Zhu, J.; Wang, R.; Chen, X.; Mi, L.; Walz, T.; Springer, T. A. Latent TGF-beta structure and activation. *Nature* **2011,** *474*, (7351), 343-9. DOI: 10.1038/nature10152.
223. Trott, O.; Olson, A. J. AutoDock Vina: improving the speed and accuracy of docking with a new scoring function, efficient optimization, and multithreading. *Journal of Computational Chemistry* **2010,** *31*, (2), 455-61. DOI: 10.1002/jcc.21334.
224. Aggeli, A.; Bell, M.; Boden, N.; Keen, J.; Knowles, P.; McLeish, T.; Pitkeathly, M.; Radford, S. Responsive gels formed by the spontaneous self-assembly of peptides into polymeric β-sheet tapes. *Nature* **1997,** *386*, (6622), 259-262. DOI: 10.1038/386259a0.
225. Yao, Y.; Wang, Y. ATDC5: an excellent in vitro model cell line for skeletal development. *Journal of Cellular Biochemistry* **2013,** *114*, (6), 1223-1229. DOI: 10.1002/jcb.24467.
226. Farndale, R. W.; Sayers, C. A.; Barrett, A. J. A direct spectrophotometric microassay for sulfated glycosaminoglycans in cartilage cultures. *Connective Tissue Research* **1982,** *9*, (4), 247-8. DOI: 10.3109/03008208209160269.
227. Price, A. J.; Alvand, A.; Troelsen, A.; Katz, J. N.; Hooper, G.; Gray, A.; Carr, A.; Beard, D. Knee replacement. *The lancet* **2018,** *392*, (10158), 1672-1682. DOI: 10.1016/S0140-6736(18)32344-4.
228. Bayliss, L. E.; Culliford, D.; Monk, A. P.; Glyn-Jones, S.; Prieto-Alhambra, D.; Judge, A.; Cooper, C.; Carr, A. J.; Arden, N. K.; Beard, D. J.; Price, A. J. The effect of patient age at intervention on risk of implant revision after total replacement of the hip or knee: a population-based cohort study. *The lancet* **2017,** *389*, (10077), 1424-1430. DOI: 10.1016/s0140-6736(17)30059-4.
229. Delanois, R. E.; Mistry, J. B.; Gwam, C. U.; Mohamed, N. S.; Choksi, U. S.; Mont, M. A. Current Epidemiology of Revision Total Knee Arthroplasty in the United States. *Journal of Arthroplasty* **2017,** *32*, (9), 2663-2668. DOI: 10.1016/j.arth.2017.03.066.
230. Armiento, A. R.; Stoddart, M. J.; Alini, M.; Eglin, D. Biomaterials for articular cartilage tissue engineering: Learning from biology. *Acta Biomaterialia* **2018,** *65*, 1-20. DOI: 10.1016/j.actbio.2017.11.021.
231. Redondo, M. L.; Beer, A. J.; Yanke, A. B. Cartilage Restoration: Microfracture and Osteochondral Autograft Transplantation. *Journal of Knee Surgery* **2018,** *31*, (3), 231-238. DOI: 10.1055/s-0037-1618592.
232. Bae, D. K.; Yoon, K. H.; Song, S. J. Cartilage healing after microfracture in osteoarthritic knees. *Arthroscopy* **2006,** *22*, (4), 367-74. DOI: 10.1016/j.arthro.2006.01.015.
233. Kreuz, P. C.; Steinwachs, M. R.; Erggelet, C.; Krause, S. J.; Konrad, G.; Uhl, M.; Sudkamp, N. Results after microfracture of full-thickness chondral defects in different compartments in the knee. *Osteoarthritis Cartilage* **2006,** *14*, (11), 1119-25. DOI: 10.1016/j.joca.2006.05.003.
234. Minas, T.; Von Keudell, A.; Bryant, T.; Gomoll, A. H. The John Insall Award: A minimum 10-year outcome study of autologous chondrocyte implantation. *Clinical Orthopaedics and Related Research* **2014,** *472*, (1), 41-51. DOI: 10.1007/s11999-013-3146-9.
235. Marlovits, S.; Aldrian, S.; Wondrasch, B.; Zak, L.; Albrecht, C.; Welsch, G.; Trattnig, S. Clinical and radiological outcomes 5 years after matrix-induced autologous chondrocyte implantation in patients with symptomatic, traumatic chondral defects. *American Journal of Sports Medicine* **2012,** *40*, (10), 2273-80. DOI: 10.1177/0363546512457008.

236. Davies, R. L.; Kuiper, N. J. Regenerative Medicine: A Review of the Evolution of Autologous Chondrocyte Implantation (ACI) Therapy. *Bioengineering (Basel)* **2019,** *6*, (1), 22. DOI: 10.3390/bioengineering6010022.
237. Negoro, T.; Takagaki, Y.; Okura, H.; Matsuyama, A. Trends in clinical trials for articular cartilage repair by cell therapy. *npj Regenerative Medicine* **2018,** *3*, (1), 17. DOI: 10.1038/s41536-018-0055-2.
238. Andriolo, L.; Reale, D.; Di Martino, A.; Boffa, A.; Zaffagnini, S.; Filardo, G. Cell-Free Scaffolds in Cartilage Knee Surgery: A Systematic Review and Meta-Analysis of Clinical Evidence. *Cartilage* **2019**, 1-16. DOI: 10.1177/1947603519852406.
239. Eslahi, N.; Abdorahim, M.; Simchi, A. Smart Polymeric Hydrogels for Cartilage Tissue Engineering: A Review on the Chemistry and Biological Functions. *Biomacromolecules* **2016,** *17*, (11), 3441-3463. DOI: 10.1021/acs.biomac.6b01235.
240. Bian, L.; Guvendiren, M.; Mauck, R. L.; Burdick, J. A. Hydrogels that mimic developmentally relevant matrix and N-cadherin interactions enhance MSC chondrogenesis. *Proceedings of the National Academy of Sciences of the United States of America* **2013,** *110*, (25), 10117-22. DOI: 10.1073/pnas.1214100110.
241. Yang, R.; Wang, X.; Liu, S.; Zhang, W.; Wang, P.; Liu, X.; Ren, Y.; Tan, X.; Chi, B. Bioinspired poly (γ-glutamic acid) Hydrogels for Enhanced Chondrogenesis of Bone Marrow-Derived Mesenchymal Stem Cells. *International Journal of Biological Macromolecules* **2019**. DOI: 10.1016/j.ijbiomac.2019.09.104.
242. Wang, D. A.; Varghese, S.; Sharma, B.; Strehin, I.; Fermanian, S.; Gorham, J.; Fairbrother, D. H.; Cascio, B.; Elisseeff, J. H. Multifunctional chondroitin sulphate for cartilage tissue-biomaterial integration. *Nature Materials* **2007,** *6*, (5), 385-92. DOI: 10.1038/nmat1890.
243. Kim, I. L.; Pfeifer, C. G.; Fisher, M. B.; Saxena, V.; Meloni, G. R.; Kwon, M. Y.; Kim, M.; Steinberg, D. R.; Mauck, R. L.; Burdick, J. A. Fibrous Scaffolds with Varied Fiber Chemistry and Growth Factor Delivery Promote Repair in a Porcine Cartilage Defect Model. *Tissue Engineering Part A* **2015,** *21*, (21-22), 2680-90. DOI: 10.1089/ten.tea.2015.0150.
244. Spain, T. L.; Agrawal, C. M.; Athanasiou, K. A. New technique to extend the useful life of a biodegradable cartilage implant. *Tissue Engineering* **1998,** *4*, (4), 343-52. DOI: 10.1089/ten.1998.4.343.
245. Liu, M.; Zeng, X.; Ma, C.; Yi, H.; Ali, Z.; Mou, X.; Li, S.; Deng, Y.; He, N. Injectable hydrogels for cartilage and bone tissue engineering. *Bone Research* **2017,** *5*, 17014. DOI: 10.1038/boneres.2017.14.
246. Yang, D.; Xiao, J.; Wang, B.; Li, L.; Kong, X.; Liao, J. The immune reaction and degradation fate of scaffold in cartilage/bone tissue engineering. *Materials Science & Engineering, C: Materials for Biological Applications* **2019,** *104*, 109927. DOI: 10.1016/j.msec.2019.109927.
247. Zhou, F.; Hong, Y.; Zhang, X.; Yang, L.; Li, J.; Jiang, D.; Bunpetch, V.; Hu, Y.; Ouyang, H.; Zhang, S. Tough hydrogel with enhanced tissue integration and in situ forming capability for osteochondral defect repair. *Applied Materials Today* **2018,** *13*, 32-44. DOI: 10.1016/j.apmt.2018.08.005.
248. Deng, C.; Chang, J.; Wu, C. Bioactive scaffolds for osteochondral regeneration. *Journal of Orthopaedic Translation* **2018**. DOI: 10.1016/j.jot.2018.11.006.

249. Niece, K. L.; Czeisler, C.; Sahni, V.; Tysseling-Mattiace, V.; Pashuck, E. T.; Kessler, J. A.; Stupp, S. I. Modification of gelation kinetics in bioactive peptide amphiphiles. *Biomaterials* **2008,** *29*, (34), 4501-9. DOI: 10.1016/j.biomaterials.2008.07.049.
250. Yu, Z.; Tantakitti, F.; Yu, T.; Palmer, L. C.; Schatz, G. C.; Stupp, S. I. Simultaneous covalent and noncovalent hybrid polymerizations. *Science* **2016,** *351*, (6272), 497-502. DOI: 10.1126/science.aad4091.
251. Levorson, E. J.; Hu, O.; Mountziaris, P. M.; Kasper, F. K.; Mikos, A. G. Cell-derived polymer/extracellular matrix composite scaffolds for cartilage regeneration, Part 2: construct devitalization and determination of chondroinductive capacity. *Tissue Eng Part C: Methods* **2014,** *20*, (4), 358-72. DOI: 10.1089/ten.tec.2013.0288.
252. Setayeshmehr, M.; Esfandiari, E.; Rafieinia, M.; Hashemibeni, B.; Taheri-Kafrani, A.; Samadikuchaksaraei, A.; Kaplan, D. L.; Moroni, L.; Joghataei, M. T. Hybrid and Composite Scaffolds Based on Extracellular Matrices for Cartilage Tissue Engineering. *Tissue Engineering Part B: Reviews* **2019,** *25*, (3), 202-224. DOI: 10.1089/ten.TEB.2018.0245.
253. Zhu, D.; Wang, H.; Trinh, P.; Heilshorn, S. C.; Yang, F. Elastin-like protein-hyaluronic acid (ELP-HA) hydrogels with decoupled mechanical and biochemical cues for cartilage regeneration. *Biomaterials* **2017,** *127*, 132-140. DOI: 10.1016/j.biomaterials.2017.02.010.
254. Lewis, J. A.; Freeman, R.; Carrow, J. K.; Clemons, T. D.; Palmer, L. C.; Stupp, S. I. Transforming Growth Factor β-1 Binding by Peptide Amphiphile Hydrogels. *ACS Biomaterials Science & Engineering* **2020**. DOI: 10.1021/acsbiomaterials.0c00679.
255. Lisignoli, G.; Cristino, S.; Piacentini, A.; Toneguzzi, S.; Grassi, F.; Cavallo, C.; Zini, N.; Solimando, L.; Mario Maraldi, N.; Facchini, A. Cellular and molecular events during chondrogenesis of human mesenchymal stromal cells grown in a three-dimensional hyaluronan based scaffold. *Biomaterials* **2005,** *26*, (28), 5677-86. DOI: 10.1016/j.biomaterials.2005.02.031.
256. Daly, A. C.; Riley, L.; Segura, T.; Burdick, J. A. Hydrogel microparticles for biomedical applications. *Nature Reviews Materials* **2019,** *5*, (1), 20-43. DOI: 10.1038/s41578-019-0148-6.
257. Lu, Y.; Markel, M. D.; Swain, C.; Kaplan, L. D. Development of partial thickness articular cartilage injury in an ovine model. *Journal of Orthopaedic Research* **2006,** *24*, (10), 1974-82. DOI: 10.1002/jor.20249.
258. Moran, C. J.; Ramesh, A.; Brama, P. A.; O'Byrne, J. M.; O'Brien, F. J.; Levingstone, T. J. The benefits and limitations of animal models for translational research in cartilage repair. *Journal of Experimental Orthopaedics* **2016,** *3*, (1), 1. DOI: 10.1186/s40634-015-0037-x.
259. Cook, J. L.; Hung, C. T.; Kuroki, K.; Stoker, A. M.; Cook, C. R.; Pfeiffer, F. M.; Sherman, S. L.; Stannard, J. P. Animal models of cartilage repair. *Bone & Joint Research* **2014,** *3*, (4), 89-94. DOI: 10.1302/2046-3758.34.2000238.
260. Schmitz, R. J.; Wang, H. M.; Polprasert, D. R.; Kraft, R. A.; Pietrosimone, B. G. Evaluation of knee cartilage thickness: A comparison between ultrasound and magnetic resonance imaging methods. *Knee* **2017,** *24*, (2), 217-223. DOI: 10.1016/j.knee.2016.10.004.
261. Cross, M. W.; Frisbie, D. D.; McIlwraith, C. W. A comparative study of articular cartilage thickness in the stifle of animal species used in human pre-clinical studies compared to

articular cartilage thickness in the human knee. *Veterinary and Comparative Orthopaedics and Traumatology* **2018,** *19*, (03), 142-146. DOI: 10.1055/s-0038-1632990.

262. Roth, K. E.; Betz, S.; Schmidtmann, I.; Maier, G. S.; Ludwig, H. R.; Vogl, T.; Theisen, A.; Brochhausen, C.; Gotz, H.; Drees, P.; Rompe, J. D.; Kurth, A. A. Biological responses to individualized small titanium implants for the treatment of focal full-thickness knee cartilage defects in a sheep model. *Knee* **2020**. DOI: 10.1016/j.knee.2020.03.012.
263. Ruvinov, E.; Tavor Re'em, T.; Witte, F.; Cohen, S. Articular cartilage regeneration using acellular bioactive affinity-binding alginate hydrogel: A 6-month study in a mini-pig model of osteochondral defects. *Journal of Orthopaedic Translation* **2019,** *16*, 40-52. DOI: 10.1016/j.jot.2018.08.003.
264. Fisher, M. B.; Belkin, N. S.; Milby, A. H.; Henning, E. A.; Bostrom, M.; Kim, M.; Pfeifer, C.; Meloni, G.; Dodge, G. R.; Burdick, J. A.; Schaer, T. P.; Steinberg, D. R.; Mauck, R. L. Cartilage repair and subchondral bone remodeling in response to focal lesions in a mini-pig model: implications for tissue engineering. *Tissue Engineering Part A* **2015,** *21*, (3-4), 850-60. DOI: 10.1089/ten.TEA.2014.0384.
265. Mohan, N.; Gupta, V.; Sridharan, B. P.; Mellott, A. J.; Easley, J. T.; Palmer, R. H.; Galbraith, R. A.; Key, V. H.; Berkland, C. J.; Detamore, M. S. Microsphere-based gradient implants for osteochondral regeneration: a long-term study in sheep. *Regenerative Medicine* **2015,** *10*, (6), 709-28. DOI: 10.2217/rme.15.38.
266. van den Borne, M. P.; Raijmakers, N. J.; Vanlauwe, J.; Victor, J.; de Jong, S. N.; Bellemans, J.; Saris, D. B.; International Cartilage Repair, S. International Cartilage Repair Society (ICRS) and Oswestry macroscopic cartilage evaluation scores validated for use in Autologous Chondrocyte Implantation (ACI) and microfracture. *Osteoarthritis Cartilage* **2007,** *15*, (12), 1397-402. DOI: 10.1016/j.joca.2007.05.005.
267. Janeway, C.; Murphy, K. P.; Travers, P.; Walport, M., *Janeway's Immunobiology*. 2008.
268. O'Driscoll, S. W.; Keeley, F. W.; Salter, R. B. The chondrogenic potential of free autogenous periosteal grafts for biological resurfacing of major full-thickness defects in joint surfaces under the influence of continuous passive motion. An experimental investigation in the rabbit. *Journal of Bone and Joint Surgery* **1986,** *68*, (7), 1017-35.
269. Tsuchida, A. I.; Beekhuizen, M.; Rutgers, M.; van Osch, G. J.; Bekkers, J. E.; Bot, A. G.; Geurts, B.; Dhert, W. J.; Saris, D. B.; Creemers, L. B. Interleukin-6 is elevated in synovial fluid of patients with focal cartilage defects and stimulates cartilage matrix production in an in vitro regeneration model. *Arthritis Research and Therapy* **2012,** *14*, (6), R262. DOI: 10.1186/ar4107.
270. Gabay, C. Interleukin-6 and chronic inflammation. *Arthritis Research & Therapy* **2006,** *8*, S3. DOI: 10.1186/ar1917.
271. Jablonski, C. L.; Leonard, C.; Salo, P.; Krawetz, R. J. CCL2 but not CCR2 is required for spontaneous articular cartilage regeneration post-injury. *Journal of Orthopaedic Research* **2019**. DOI: 10.1002/jor.24444.
272. Iannone, F.; De Bari, C.; Dell'Accio, F.; Covelli, M.; Cantatore, F. P.; Patella, V.; Lo Bianco, G.; Lapadula, G. Interleukin-10 and interleukin-10 receptor in human osteoarthritic and healthy chondrocytes. *Clinical & Experimental Rheumatology* **2001,** *19*, (2), 139-45.

273. Burdick, J. A.; Chung, C.; Jia, X.; Randolph, M. A.; Langer, R. Controlled degradation and mechanical behavior of photopolymerized hyaluronic acid networks. *Biomacromolecules* **2005,** *6*, (1), 386-91. DOI: 10.1021/bm049508a.
274. Cui, H.; Muraoka, T.; Cheetham, A. G.; Stupp, S. I. Self-assembly of giant peptide nanobelts. *Nano Letters* **2009,** *9*, (3), 945-951. DOI: 10.1021/nl802813f.
275. Kastin, A., *Handbook of biologically active peptides*. Academic press: 2013.
276. Mnatsakanyan, R.; Markoutsa, S.; Walbrunn, K.; Roos, A.; Verhelst, S. H. L.; Zahedi, R. P. Proteome-wide detection of S-nitrosylation targets and motifs using bioorthogonal cleavable-linker-based enrichment and switch technique. *Nature Communications* **2019,** *10*, (1), 2195. DOI: 10.1038/s41467-019-10182-4.
277. Murphy, W.; Black, J.; Hastings, G. W., *Handbook of biomaterial properties*. Springer: 2016.
278. Nazli, S. A.; Loeser, R. F.; Chubinskaya, S.; Willey, J. S.; Yammani, R. R. High fat-diet and saturated fatty acid palmitate inhibits IGF-1 function in chondrocytes. *Osteoarthritis and Cartilage* **2017,** *25*, (9), 1516-1521. DOI: 10.1016/j.joca.2017.05.011.
279. Teixeira, J. H.; Pereira, C. L.; Almeida, M. I.; Teixeira, G. Q.; Gonçalves, R. M.; Barbosa, M. A.; Santos, S. G. Articular Repair/Regeneration in Healthy and Inflammatory Conditions: From Advanced In Vitro to In Vivo Models. *Advanced Functional Materials* **2020**. DOI: 10.1002/adfm.201909523.
280. Koh, R. H.; Jin, Y.; Kim, J.; Hwang, N. S. Inflammation-Modulating Hydrogels for Osteoarthritis Cartilage Tissue Engineering. *Cells* **2020,** *9*, (2). DOI: 10.3390/cells9020419.
281. Bury, M. I.; Fuller, N. J.; Meisner, J. W.; Hofer, M. D.; Webber, M. J.; Chow, L. W.; Prasad, S.; Thaker, H.; Yue, X.; Menon, V. S.; Diaz, E. C.; Stupp, S. I.; Cheng, E. Y.; Sharma, A. K. The promotion of functional urinary bladder regeneration using anti-inflammatory nanofibers. *Biomaterials* **2014,** *35*, (34), 9311-21. DOI: 10.1016/j.biomaterials.2014.07.057.

# VITA


## Jacob A. Lewis

(847) 313-5863 | jacoblewis2014@u.northwestern.edu


## EDUCATION

| | |
|---|---|
| **Northwestern University** | September 2014- |
| **McCormick School of Engineering, Evanston, IL** | July 2020 |
| Biomedical Engineering PhD candidate | |
| Master of Science | December 2018 |
| Management for Scientists and Engineers Certificate, Kellogg School | August 2018 |
| **University of California Berkeley,** | August 2009- |
| **College of Engineering, Berkeley, CA** | May 2013 |
| Bioengineering and Materials Science Engineering, Bachelor of Science | |

## PUBLICATIONS

1. **Lewis, J.A**., Garcia, M.B., Rani, L., and Wildsoet, C.F. Intact Globe Inflation Testing of Changes in Scleral Mechanics in Myopia and Recovery. *Experimental Eye Research.* 2014. 127, 42-48.
2. Freeman, R., Stephanopoulos, N., Álvarez, Z., **Lewis, J.A.**, et al. Instructing Cells with Programmable Peptide DNA Hybrids. *Nature Communications.* 2017. *8*, 15982.
3. Freeman, R., Han, M., Álvarez, Z., **Lewis, J. A.**, et al. Reversible Self-Assembly of Superstructured Networks. *Science.* 2018. 362(6416), 808-813.
4. Serrano, C. M., Freeman, R., Godbe, J., **Lewis, J. A.**, & Stupp, S. I. DNA-Peptide Amphiphile Nanofibers Enhance Aptamer Function. ACS Applied Bio Materials, 2019. 2(7), 2955-2963.
5. Kossover, O.*, Cohen, N.*, **Lewis, J. A**.*, Berkovitch, Y., Peled, E., & Seliktar, D. Growth Factor Delivery for the Repair of a Critical Size Tibia Defect Using an Acellular, Biodegradable Polyethylene Glycol–Albumin Hydrogel Implant. *ACS Biomaterials Science & Engineering*. 2020. 6(1) 100-111.
6. Godbe, J.M., Freeman, R., Burbulla, L. F., **Lewis, J.A.**, Krainc, D., & Stupp, S. I. Gelator Length Precisely Tunes Supramolecular Hydrogel Stiffness and Neuronal Phenotype in 3D Culture. *ACS Biomaterials Science & Engineering.* 2020. 6(2) 1196-1207.
7. Wester, J.R.*, **Lewis, J.A.***, Freeman, R.*, Sai, H., Palmer, L.C., Henrich, S.E., Stupp, S.I., Supramolecular Exchange Among Assemblies of Opposite Charge Leads to Hierarchical Structures. *Journal of the American Chemical Society.* 142(28) 12216-12225.
8. **Lewis, J.A**., Freeman, R., Carrow, J.K., Clemmons, T.R., Palmer, L.C., Stupp, S.I., Transforming Growth Factor β-1 Binding by Peptide Amphiphile Hydrogels. *ACS Biomaterials Science & Engineering.* 2020. In press
9. **Lewis, J.A**.*, Freeman, R.*, Clemmons, T.R., Godbe, J.M., Stupp, S.I. Self-Assembly of Nonionic Peptide Amphiphiles. *In preparation*

10. **Lewis, J.A**., Nemke, B., Lu, Y., McClendon, M.T., Mullen, M., Ravuri, S.K., Huard, J., Markel, M.D., Stupp, S.I. A Supramolecular-Covalent Hybrid Material for Cartilage Repair in a Large-Animal Model. *In preparation*

*Equally contributing authors

## SELECTED PRESENTATIONS

| | |
|---|---|
| **Lewis, J.A.,** Garcia, M., and Wildsoet, C.F. The Effect of Induced Myopia on the Creep Response of Whole Eyes. Summer Undergraduate Research Conference, UC Berkeley. Berkeley, CA (oral) | August 2012 |
| **Lewis, J.A.,** Garcia, M., and Wildsoet, C.F. The Effect of Induced Myopia on the Creep Response of Whole Chick Eyes. The Association for Research in Vision and Ophthalmology Annual Conference. Seattle, WA (poster) | May 2013 |
| **Lewis, J.A.,** Seliktar, D. PEGylated Protein Hydrogels for BMP-2 Delivery for Bone Regeneration. Whitaker Fellows Enrichment Seminar. Rome, IT (oral) | March 2014 |
| **Lewis, J.A.,** Seliktar, D. BMP-2 Release from PEGylated Fibrinogen and PEGylated Albumin Hydrogels. Nano-Israel Conference. Tel Aviv, IL (Poster) | March 2014 |
| **Lewis, J.A.,** PEGlyated Peptide Amphiphiles for Binding TGFβ-1. BME Research Day, Northwestern University. Evanston, IL (Poster) | May 2017 |
| **Lewis, J.A.,** et al. A Supramolecular Hybrid Material for Cartilage Engineering in an Ovine Model. Vail Scientific Summit. Vail, CO (Poster) | August 2018 |
| **Lewis, J.A**., et al. Peptide Amphiphile-Hyaluronic Acid Composites for Cartilage Regeneration in a Large-Animal Model. Biomedical Engineering Society Annual Meeting. Atlanta, GA (Oral) | October 2018 |
| **Lewis, J.A.,** Supramolecular Materials and Their Use in Musculoskeletal Regeneration and Cartilage Repair. University of Wisconsin BME Department Seminar. Madison, WI (Oral) | March 2019 |
| **Lewis, J.A.** et al., Covalent-Supramolecular Polymer Hybrids for Cartilage Repair. Material Research Society Spring Meeting. Phoenix, AZ (Oral) | April 2019 |
| **Lewis, J.A.** et al., Covalent-Supramolecular Polymer Hybrids for Cartilage Repair. Vail Scientific Summit. Vail, CO (Poster) | August 2019 |

## RESEARCH EXPERIENCE

Stupp Laboratory, Northwestern University, Evanston, IL November 2014-Present

*Supramolecular-Covalent Hybrid Materials for Cartilage Repair in a Large Animal Model*

- Designed peptide amphiphile – hyaluronic acid hybrid material to improve tissue regeneration in cartilage defects
- Optimized material composition based on mechanical toughness, swelling, protein retention, and degradation
- Evaluated viability and differentiation of mesenchymal stem cells encapsulated in hydrogels
- Coordinating inter-university collaboration to evaluate material-induced cartilage regeneration, tested in 30 sheep

*PA Materials with Improved Growth Factor Binding for Musculoskeletal Regeneration*

- Synthesized peptide amphiphile system for improved synthesis of signals that bind bioactive growth factors
- Quantified growth factor release by ELISA and binding kinetics by interferometry
- Demonstrated differential effect of changes in self-assembled structure on growth factor binding and chondrogenesis
- Characterized effect of materials charge on self-assembled morphology and osteogenic differentiation

*Hierarchical Self-Assembly of Dynamic Peptide Amphiphile Superstructures*

- Investigated hierarchical assembly of peptides by x-ray scattering, electron microscopy, and optical spectroscopy
- Synthesized and characterized DNA-peptide conjugates for tunable self-assembly and bioactivity

Seliktar Laboratory, Technion – Israel Institute of Technology, Haifa, Israel August 2013 – June 2014

- Manufactured protein-polymer hydrogels for slow release of growth factor for bone regeneration
- Characterized hydrogel properties and evaluated bone formation in rat model

Wildsoet Laboratory, UC Berkeley School of Optometry, Berkeley, CA August 2011-August 2013

- Designed system to optically measure displacement on surface of pressurized eye *in vitro*
- Evaluated the effect of myopia on the creep properties of intact sclera using over 100 animal eyes

## TEACHING AND LEADERSHIP

Personnel Coordinator, Graduate Leadership Advocacy Council September 2018 – Present

Oversee, organize, and train 50 department representatives to graduate student representative body

Mentor, Science Club, Boys and Girls Clubs of Chicago January 2017 – June 2018

Led after-school mentorship of 4 middle-school students to conduct fun and engaging scientific investigations.

Teaching Assistant, Systems Physiology March 2017 – June 2017

Lectured weekly to class of 80 students, assisted students in office hours as only course TA
Completed Mentored Discussion of Teaching program to improve pedagogical techniques

## AWARDS, FELLOWSHIPS, AND GRANTS

| | |
|---|---|
| National Science Foundation Graduate Research Fellowship | June 2015-May 2018 |
| Whitaker Fellowship: awarded for yearlong international research project | August 2013-June 2014 |
| Outstanding TA award – Northwestern BME department | May 2018 |